

Underground decision making; where to grow, when to branch

Theodora van den Berg

Theodora van den Berg

Underground decision making; where to grow, when to branch

PhD thesis, Utrecht University

Cover: *Root data*, design by Alfred J. Arulandhu & Thea van den Berg

Printing: Ridderprint | www.ridderprint.nl

ISBN: 978-94-6458-313-7

Underground decision making; where to grow, when to branch

**Ondergrondse beslissingen,
welke kant op te groeien en wanneer te vertakken
(met een samenvatting in het Nederlands)**

Proefschrift

ter verkrijging van de graad van doctor aan de
Universiteit Utrecht
op gezag van de
rector magnificus, prof.dr. H.R.B.M. Kummeling,
ingevolge het besluit van het college voor promoties
in het openbaar te verdedigen op

maandag 27 juni 2022 des middags te 2.15 uur

door

Theodora van den Berg

geboren op 2 februari 1987
te Wilnis

Promotoren:

Prof. dr. R.J. de Boer

Prof. dr. K.H.W.J. ten Tusscher

Dit proefschrift werd mogelijk gemaakt met financiële steun van de Nederlandse Organisatie voor Wetenschappelijk Onderzoek (NWO)

Thesis assessment committee:

Prof. dr. R.M.H. Merks

Prof. dr. D. Weijers

Prof. dr. I. Blilou

Prof. dr. R.J. Morris

Dr. V.V. Mironova

Contents

Chapter 1	Introduction	1
1.1	Preface	2
1.2	Plant roots	3
1.3	Dynamic modelling	8
1.4	Thesis outline	9
Chapter 2	Auxin Information Processing; Partners and Interactions beyond the Usual Suspects	13
2.1	Introduction	15
2.2	The Auxin–Plethora Division of Labour; A Separation of Timescales	17
2.3	Halotropism as a Case Study of a Graded-Signal Tropism; Auxin Computations in the Reflux Loop	19
2.4	Auxin Signalling in Phyllotaxis; Same yet Different	21
2.5	Pin Polarity in Gradients; Different yet Same	23
2.6	Conclusions and Outlook	24
Chapter 3	A reflux-and-growth mechanism explains oscillatory patterning of lateral root branching sites	27
3.1	Introduction	29
3.2	Results	31
3.3	Discussion	44
3.4	Star methods	47
3.5	Supplemental information	64
Chapter 4	Meristem growth dynamics shape lateral root priming morphospace	75
4.1	Introduction	77
4.2	Results	79
4.3	Discussion	89
4.4	Material and methods	91
4.5	Supplemental information	92
Chapter 5	Modeling halotropism: a key role for root tip architecture and reflux loop remodeling in redistributing auxin	95
5.1	Introduction	97
5.2	Results	99
5.3	Discussion	109
5.4	Materials and Methods	111
5.5	Supplementary information	118
Chapter 6	Halotropism requires phospholipase Dζ1-mediated modulation of cellular polarity of auxin transport carriers	125
6.1	Introduction	127
6.2	Methods	129
6.3	Results	132
6.4	Discussion	142
6.5	Supporting information	146

Chapter 7	Discussion	155
7.1	Summary	156
7.2	The many roles of auxin in emergent decision making in plant roots	159
7.3	The dynamic interaction between models and experiments and the rise of data	163
7.4	Conclusion	165
	References	167
	Samenvatting	189
	Curriculum vitae	195
	List of publications	196
	Acknowledgements	197

1

Introduction

“Never say there is nothing beautiful in the world anymore. There is always something to make you wonder in the shape of a tree, the trembling of a leaf” – Albert Sweitzer

1.1 Preface

Decision making in developmental systems is a highly dynamic and complex process, numerous individual entities, be it genes, cells or tissues, need to somehow give a coordinated response. This decision making starts from an embryonic state, when one or a few precursor cells proliferate and via coordinated differentiation give rise to a functioning tissue, and continues throughout an organism's lifetime to ensure survival and ultimately reproduction. Developmental decision making requires an intricate balance between robustness and flexibility. Organisms need robustness to avoid possible detrimental effects of genetic or environmental perturbations that hamper fitness, yet simultaneously require substantial plasticity to enable adaptation of phenotype or behaviour in response to different conditions.

1.1.1 Robust development

Developmental robustness could be defined as the persistence of a phenotypic trait given a perturbation, being either environmental fluctuations, gene expression, developmental noise or genetic mutations. The evolution of multicellular organisms with increasingly complex body plans has been paralleled by an increasing complexity in the regulation of developmental genes ensuring complex yet robust development (Levine and Tjian, 2003, Davidson, 2006). Deciphering the regulatory mechanisms that drive the spatio-temporal gene expression patterns underlying developmental programs and the causes for their robustness has been the aim of many studies. For example, in mammals the direction of the body axis is determined by a symmetry breaking patterning event (Tam and Loebel, 2007, Zhang and Hiiragi, 2018), that is later on in development followed by the patterning of the somites (Panganiban et al., 1997, Bessho et al., 2003). As originally proposed by Cooke and Zeeman (Cooke and Zeeman, 1976), somites form through a clock-and-wavefront mechanism in which a cell autonomous gene oscillator combined with a morphogen gradient enables the sequential translation of temporal oscillations into a spatially periodic pattern. In animals, symmetry, regularity and scaling of somites and the structures that derive from it are crucial for motility and fitness, and hence many mechanisms exist enhancing robustness of somitogenesis. As an example, it has been shown that synchronization of individual cell's oscillations is an important means to reduce developmental noise (Horikawa et al., 2006). Like animals, plants also use spatio-temporal gene expression to establish their main body axis and the subsequent patterning of the developing embryo (Hardtke and Berleth, 1998, Hamann et al., 1999, Laux et al., 2004). Nonetheless, in contrast to most animals that have completed their body plan after embryogenesis, plants continually add new body parts throughout their life and hence continuously deploy major developmental patterning processes. Next to growth and patterning of the main shoot and root, lateral shoots and roots will emerge from the main organs in a spatio-temporally repetitive pattern that particularly for roots bears some resemblance to somitogenesis (Jonsson et al., 2006, Prusinkiewicz and Lindenmayer, 2012, Biedron and Banasiak, 2018). The continuous addition of modular structures makes plants morphologically robust, not per se in terms of exact symmetry or high regularity, yet in enabling repair or replacement of chewed at wounded organs and the presence of a flexible outgrowth potential that can respond to environmental conditions. The redundancy in plants is not limited to the morphological level as plants are polyploid and have the unique ability to deal with large numbers of gene copies, through hybridization or even whole genome duplication, enabled by a plant specific gene silencing mechanism (Ha et al., 2009, Ding and Chen, 2018). Polyploidy has been shown to not only positively affect evolvability but also plasticity and the redundancy in plant morphology and genetics has been

suggested to be compensatory for their sessile life style and lack of movement (Harper, 1980, Dubcovsky and Dvorak, 2007, Wei et al., 2019, Fox et al., 2020).

1.1.2 Yet a flexible body

Combining robust development with adaptive phenotypic plasticity is arguably the most complex in plants due to their complete dependence on their local environment combined with an extensive post embryonic development. Where animals might adjust the size of their fixed number of somites based on body height or available food sources, plants develop and adjust the numbers and growth rate of their lateral outgrowths continuously throughout their life. For example, for the plant's root system, conditions do not only change globally but also locally; plant roots encounter patches of nutrients, beneficial bacteria, water or repellent substances and are able to adjust their growth rate and direction and branching pattern accordingly. As a case in point, gene expression downstream of nutrient level signalling enables plant roots to adjust their growth rate and root hair density (Muller and Schmidt, 2004, Salazar-Henao et al., 2016). Understanding the mechanisms of root growth and branching and the integration of environmental signals into such programs that drive their phenotypic plasticity is of crucial importance to improve future agricultural yield. In this thesis we study how plant roots 'decide' where to grow and when to branch. We explore how plant roots integrate environmental signals yet balance these signals with the need for a robust body plan in the context of lateral root branching and growth direction of the root.

1.2 Plant roots

1.2.1 Evolution of plant roots

After colonising land, plants evolved rhizoids, root like structures, during Early Devonian Times (c. 400 million years ago) that facilitated attachment to the surface as an early adaptation to the land environment (Raven and Edwards, 2001). The single celled rhizoids exhibit root like functions such as anchorage and uptake of water and nutrients, yet structurally most closely resemble modern root hairs. Fossil evidence indicates that true roots, as known in current extant plants, with a self-renewing meristem, gravitropic response and a root cap, emerged first in vascular plants (Kenrick and Strullu-Derrien, 2014). The roots of vascular plants appear to have acquired these traits that facilitate below ground growth in a step wise manner, with growth towards the gravity vector and a self-renewing meristematic region preceding the appearance of root hairs and a root cap (Hetherington and Dolan, 2018). One of the initial acquired traits of roots, gravitropic growth is not only beneficial for anchorage of the plant but is also essential for reaching nutrients and water (Seago Jr and Fernando, 2013). Although all land plant roots exhibit a form of gravitropism, only seed-bearing plants evolved a fast and efficient gravitropic response while earlier diverging plant species have a slower and less efficient response to gravity. The fast efficient gravitropic response thus specifically evolved in plants that colonised dry land as part of their seed mediated independence of a water rich environment, further underpinning the argument of the importance of gravitropism for plant resource acquisition (Linkies et al., 2010, Kenrick and Strullu-Derrien, 2014). A recent study by (Zhang et al., 2019) showed that two main components are responsible for the fast gravitropic response: 1) root architecture with gravity sensing starch cells in the root tip away from the elongation zone of the root, 2) efficient transport of the plant hormone auxin in the root tip (Zhang et al., 2019). Interestingly, the role of auxin transport is not limited to the emergence of fast gravitropism, it has recently been shown that evolutionary innovation in the auxin transporter family PIN-FORMED has been essential for the

evolutionary trajectory of flowering plants in facilitating developmental patterning and flowering (Zhang et al., 2020). Besides gravitropism vascular plant roots exhibit a range of tropic responses, phototropism (Kutschera and Briggs, 2012), hydrotropism (Shkolnik et al., 2016), halotropism (Galvan-Ampudia et al., 2013), and thigmotropism (Massa and Gilroy, 2003). The evolutionary origin of these responses remains thus far unknown. Nonetheless, most of these tropisms, except for hydrotropism, are auxin mediated indicating a possible coevolution with gravitropism and innovations in auxin transport.

Another crucial transition in root evolution was the capacity to branch, and in this way provide optimal anchorage and nutrient and water foraging potential. The exact origin of root branching is debated, however a similar trend as in gravitropism toward higher plasticity in later evolved plant lineages can be observed. More ancient roots of the lycophyte clade can only form a lateral root by splitting their main roots, ferns have a number of cells that can form a lateral root and finally angiosperms have dedicated cell files that could potentially form lateral roots at all positions on the main root (Motte and Beekman, 2019).

During their conquest of land, plants not only evolved to become adapted to life on dry land, but their close interaction with their environment also drastically changed Earth's climate by altering the carbon cycle and oxygen status (Kenrick and Strullu-Derrien, 2014, Dahl and Arens, 2020). The presence of land plants also led to the formation of new habitats for other species and shaped landscapes and weathering conditions (Gibling and Davies, 2012, Labandeira, 2013, Quirk et al., 2015). These strong abiotic and biotic interaction of plants with their environment is believed to be a major driver of evolution and biodiversity, as was already postulated by Charles Darwin (Darwin, 1859). In addition to shaping their environment, the body plan of individual plants themselves are strongly shaped by their environment. Enabled by the evolution of more plastic root branching mechanisms and sophisticated tropisms, plant roots adapt their branching patterns and growth directions to the presence of beneficial microbes, nutrients and abiotic stress conditions such as salt or drought.

1.2.3 *Arabidopsis thaliana* as a model organism

Understanding the basic developmental processes of plant roots and the adjustment of growth and branching in response to changing environmental conditions have been an ongoing focus in plant research. To gain insight in root developmental processes the model plant *Arabidopsis thaliana* has been extensively studied. *Arabidopsis* is a member of the *Brassicaceae* family, and although not a crop species itself, insights from *Arabidopsis* research have been successfully applied to crop species due to the close evolutionary relationship between all flowering plants (Sauquet et al., 2017). The root of *Arabidopsis* is highly regular in organization and has a relatively simple structure, combined with its short life cycle, up to 750 natural varieties and compatibility with laboratory growth conditions, this has made *Arabidopsis* a very useful model plant.

In the last decades studies on the *Arabidopsis* root have provided numerous insights on its radial patterning into distinct cell types, its longitudinal developmental zonation governing growth and terminal differentiation of cells and the hormonal-genetic control of these processes. *Arabidopsis* has a so-called taproot system, consisting of a persistently maintained main root with lateral roots branching from this main root (Figure 1.1A). The individual roots are cone shaped and consist of different tissues that are organised in a radial pattern (Dolan et al., 1993, Scheres et al., 2002). In the middle of the root are multiple layers of vasculature cells surrounded by 4 layers of outer tissue, pericycle, endodermis, cortex and epidermis, respectively (Figure 1.1A). Finally, in the root tip the

epidermis is surrounded by multiple layers of lateral root cap cells that shed off when they mature, leaving more shoot ward parts of the root with the epidermis as outer layer (Bennett et al., 2010). The root cap protects the stem cell region, columella and meristem, in the most distal part of the root.

Research in *Arabidopsis* has shown that plant hormones play a critical role in root growth, development and adaptive responses. A critical player is the phytohormone auxin that influences virtually all processes in growth and development. The most well-known auxin control pathway is via nuclear signalling and encompasses a transduction network with 2 main classes of regulatory factors, the Auxin Response Factors (ARFs) (Ulmasov et al., 1999a, Boer et al., 2014) and the transcriptional repressors Aux/IAAs (Causier et al., 2012). At low cellular auxin levels, activating ARFs heterodimerize with Aux/IAA, preventing them from activating gene expression. High auxin levels induce degradation of Aux/IAA via interaction with the TIR1/AFB complex, thus promoting the release of ARFs⁺ and enabling induction of target gene expression (Kepinski and Leyser, 2005, Calderon Villalobos et al., 2012). Apart from AUX/IAA-auxin and AUX/IAA-ARF binding affinity, auxin dosage sensitivity can be further tuned through the presence of negative, non-auxin sensitive ARFs competing with the positive regulatory ARFs (Weijers and Jurgens, 2004, Weijers et al., 2005, Vernoux et al., 2011). In addition to AUX/IAA-ARF nuclear signalling, additional non-canonical nuclear pathways have been identified, such as the ARF variant ETTIN, which lacks an AUX/IAA binding domain but instead exhibits an auxin dependent dimerization with the INDEHISCENT (IND) transcription factor (Simonini et al., 2016).

Finally, only recently, using new technological advances, it has been possible to demonstrate that auxin signalling is not limited to relatively slow differential gene expression, but that cytoplasmic auxin sensors exist enabling very fast (30s) responses (Fendrych et al., 2018). This rapid auxin response pathway was shown to involve cytoplasmic TIR1 and the cyclic nucleotide-gated ion channel CNGC14 which upon inducing Ca²⁺ influx leads to plasma membrane depolarization.

The spatio-temporal distribution of auxin is impacted by active long range transport by the PIN-FORMED family (PINs) (Okada et al., 1991, Bennett et al., 1995, Friml et al., 2002b) and AUX/LAX family (Bennett et al., 1996). Interestingly, auxin itself, through a non-canonical pathway involving kinases, has been shown to adjust the levels and activity of its own transporter PIN (Barbosa et al., 2014, Dubey et al., 2021) and also to influence the expression levels of AUX/LAX (Laskowski et al., 2006). Auxin transporters exhibit a tissue and developmental zonation specific pattern. Additionally, particularly in case of the exporting PINs they are localized on the cell membrane in a polar orientation facilitating directional transport. Specifically, the PINs in the vasculature tissue are oriented mainly downward, while the outer tissues have PINs with upward orientation and additionally above the meristem also slightly inwards. Combined this causes a flow of auxin that can be described as a reversed fountain (Grieneisen et al., 2007).

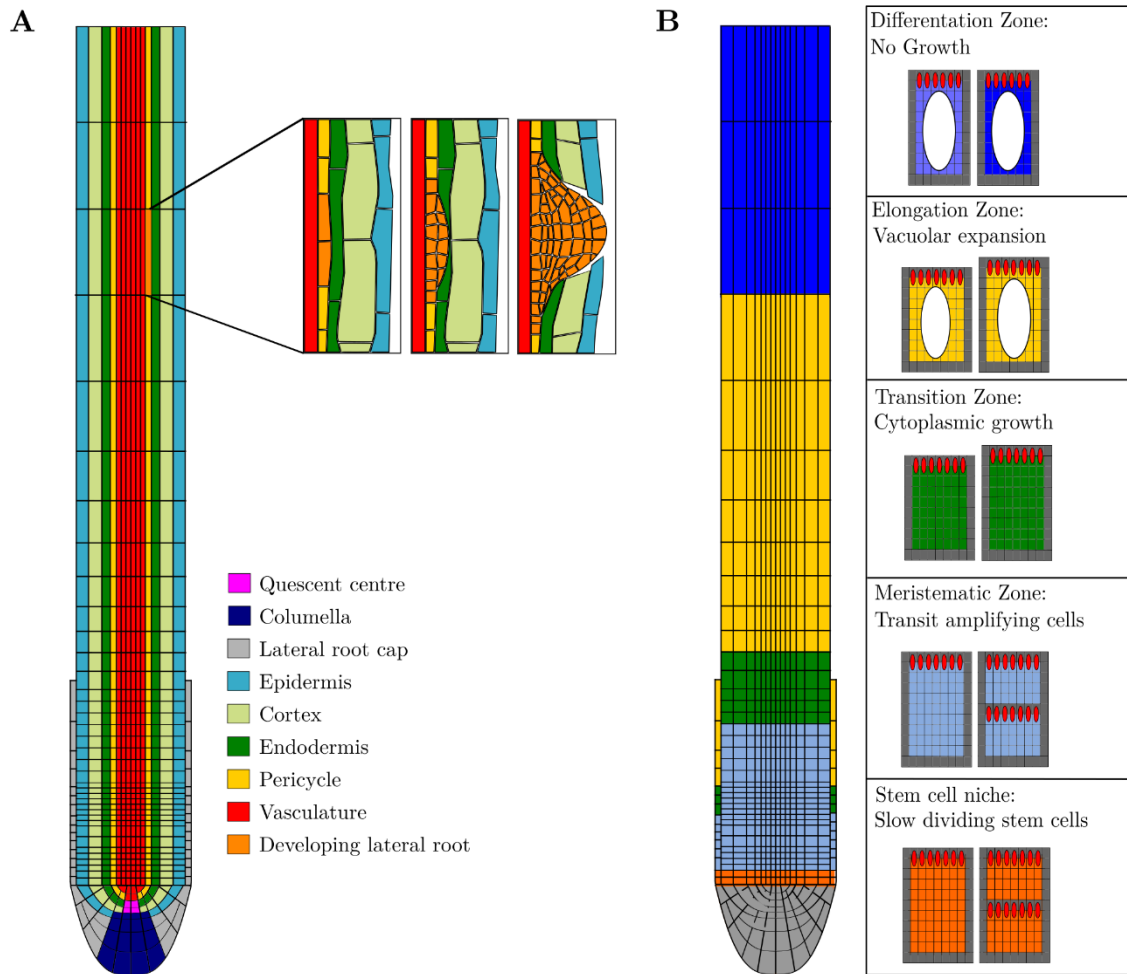


Figure 1.1. Overview of different root tissues and developmental zones in *Arabidopsis thaliana*. **A.** Idealized root architecture with different root tissue, with in the root tip: root cap (grey), columella (blue), quiescent centre (purple) and in the upper part: lateral root cap (dark grey), epidermis (cyan), cortex (light green), endodermis (dark green), pericycle (yellow) and vasculature tissue (red). Inset shows different stages of a developing lateral root, ranging from a lateral root founder cell (left) to an emerging lateral root (right) **B.** Different root developmental zones, stem cell zone (orange), meristematic zone (light blue), transition zone (dark green), elongation zone (yellow) and differentiation zone (dark blue).

1.2.2 The many messages of auxin in root development and adaptation

The specific orientation of the auxin transporters generate auxin maxima and gradients that are instructive for development (Grieneisen et al., 2007). First of all, auxin is involved in determining cellular fate and shape, for example, in the outer epidermal tissue cell files some cell files form root hairs while others do not. Although all epidermal files are derived from a few stem cells, spatial patterning by auxin causes a highly regular pattern in hair and non-hair cell with distinct gene expression profiles (Jones et al., 2009). In the case of *Arabidopsis*, these hair and non-hair cells are patterned into distinct cell files, but also other patterns exist (Datta et al., 2011). Additionally, within cells the position of the hairs depends on the auxin gradient, and adjusting the gradient, by flattening or changing the orientation, will bias the root hair positioning (Fischer et al., 2006, Ikeda et al., 2009). Similarly, in the longitudinal plane, auxin maxima and gradients determine the size and location of developmental zones with the highest levels of auxin around the quiescent centre (QC) in the root tip maintaining the undifferentiated state of the stem cells in and around the QC (Sabatini et al., 1999,

Blilou et al., 2005). The auxin gradient tapering off from the QC instructs the position and size of the meristematic zone where cells divide upon doubling their size, and the transition zone where cells grow but no longer divide. Size of the root meristem is a major determinant of root growth rate. Above the transition zone, auxin levels rise again and cells enter the elongation zone where they expand rapidly via vacuolar growth after which they enter the differentiation zone (Figure 1.1B). The developmental patterning of the main root is facilitated by transcription factors, such as the PLETHORAs (Galinha et al., 2007, Grieneisen et al., 2007, Tian et al., 2014, Mahonen et al., 2014, Salvi et al., 2020). Additionally the interaction with other phytohormones such as cytokinin (Dello Ioio et al., 2007, Bielach et al., 2012), gibberellin (Ubeda-Tomas et al., 2008), ethylene (Saini et al., 2013) and brassinosteroids (Hardtke et al., 2007) are known to affect root developmental zonation either directly or through impacting auxin.

Auxin is also a major player in the development of lateral roots. In *Arabidopsis*, lateral roots emerge from a specific cell file of the pericycle, the xylem-pole-pericycle (XPP) that exhibits long term cell division potential (Beeckman et al., 2001, Himanen et al., 2004). The first step of lateral root formation is the priming of competent cells for future lateral formation. Priming is characterised by regular oscillations in auxin and auxin response genes, and occurs at the shootward boundary of the meristem in the vasculature tissue (De Smet et al., 2007, Laskowski and Ten Tusscher, 2017). The signal travels then to adjacent pericycle cells where one or multiple cells become primed. It has previously been shown that auxin produced in the lateral root cap is necessary to ensure an oscillation amplitude sufficient for stable prebranch site formation, and also mutations in auxin transporters or biosynthesis have been shown to hamper prebranch site formation (De Rybel et al., 2012, Xuan et al., 2015, Xuan et al., 2016). The oscillatory nature of the priming signal was found to correlate to the shedding of the lateral root cap (Xuan et al., 2016) and several mechanisms, such as a clock-and-wavefront model and a Turing-type patterning mechanism, have been proposed to pattern the priming sites (Laskowski and Ten Tusscher, 2017). Cells can become so-called prebranch sites competent of future lateral root formation after being successfully primed in the early elongation zone, enabling them to form domains with stably maintained auxin signalling (Moreno-Risueno et al., 2010, Xuan et al., 2015, Xuan et al., 2016). Prebranch sites are through growth displaced towards the differentiation zone and continue to develop into lateral root founder cells (LRFC). During these first stages the auxin importer AUX1 facilitates an increase in auxin content in the prebranch and later LRF cells (Marchant et al., 2002, Laskowski et al., 2008). The resulting increased level of auxin is necessary to guide the process of nuclear migration and asymmetric divisions that form the new lateral root (De Smet et al., 2007, De Rybel et al., 2010, Berckmans et al., 2011). Interestingly, even the reduction in endodermal volume to relieve the mechanical constraint on the developing lateral root in the neighbouring pericycle tissue is auxin signalling dependent (Vermeer et al., 2014).

The role of auxin is not limited to dictating developmental status and cell fate but also the rate at which development and growth occurs. Mutations or environmental conditions impacting auxin levels may influence the fraction of prebranch sites that develop into fully emerged lateral roots within a certain time window, implying an impact on lateral root developmental rate (reviewed by (Cavallari et al., 2021). Indeed, the influence of auxin on cellular division, expansion and differentiation rates has been reported to be dosage dependent (Mahonen et al., 2014), and for example the effect of auxin on cellular elongation rate is at the basis of most root tropic responses. Here, preferential accumulation of auxin at 1 side of the root in the elongation zone, causes elongation rates to locally drop, resulting in asymmetric growth and root bending towards the side of high auxin and low growth rate. Root tropism are mainly facilitated by changes in auxin transporters, for example, during gravitropism an orientation

away from gravity will induce movement of starch granules which cause the repolarisation of PIN transporters (Kleine-Vehn et al., 2010).

In addition to aiding cell fate decisions, plants thus use auxin to decide at what rate to grow, in which direction to grow, and where to branch, begging the question of how they decide what to decide on. It is these decisions questions that are at the core of the work described in this thesis.

1.3 Dynamic modelling

Developmental systems can be studied at multiple spatial scales, ranging from organism, via tissues, and cells down to the molecular level. The different scales of an organism are not only a matter of zooming in and out, instead the activity of entities at a certain level can drive behaviour of entities at higher and lower levels. For example, cell level behaviour, whether a cell grows, divides or differentiates is driven by the state of its gene regulatory network and vice versa growth and division through diluting or stochastically distributing cell content affect gene regulatory network state. Similarly, tissue level behaviour or ‘decision making’ arises from the collective behaviour of the cells within the tissue and the interaction between them, but also feeds back on the conditions and hence subsequent behaviour of these cells. In addition to this wide range of spatial scales, developmental patterning processes also encompass a broad range of temporal scales. The separate, experimental, study of structures, be it molecules, cells or tissues in an organism will provide detailed insights in their appearance and behaviour, yet is often unable to capture the overall dynamical interactions and emergent behaviour of the system of interest as a whole as experiments are typically limited to one or two spatial and temporal scales.

Models have played a major role in unravelling complex multi-scale patterning processes and the mechanisms underlying their robustness. In animals a famous example is the previously discussed clock-and-wavefront driven somitogenesis (Cooke and Zeeman, 1976), where computational models have helped discover important roles for cell motility, cell-cell signalling and cell-cell adhesion in enhancing patterning robustness (Lewis, 2003, Horikawa et al., 2006, Armstrong et al., 2009, Uriu et al., 2010, Hester et al., 2011). Similarly, multiscale modelling has helped to understand how plants decode temporal and spatial signals into a coherent response. For example, phyllotaxis, the sequential initiation of lateral organs at the apical shoot meristem has been extensively analysed using modelling (Douady and Couder, 1996, Mitchison, 1977, Veen and Lindenmayer, 1977). Phyllotaxis was found to arise in a self-organized manner from the interplay between tissue growth, polar auxin transport and auxin biosynthesis together driving the patterning of auxin maxima guiding lateral organ outgrowth (Reinhardt et al., 2003, Vernoux et al., 2011). Recently, with improved experimental resolution for measuring auxin dynamics, the role of auxin in providing spatial and temporal cues was further confirmed (Galvan-Ampudia et al., 2020), showing that cell fate changes respond to a time-integrated rather than instantaneous auxin signal. In roots modelling has been used to elucidate how auxin can simultaneously facilitate a direct effect on cellular developmental rates and also affect the developmental zonation via PLT. Using a model that explicitly incorporates space and time it was shown how protein stability and the presence of plasmodesmata facilitate the seemingly contrastingly dual role of auxin through a separation of time scales (Mahonen et al., 2014). In another study by Laskowski et al. (2008), it was shown that bending-driven induction of lateral roots at the outer bend can be explained from an increase in auxin levels resulting from the increased cell sizes at the outer bend. The increased auxin subsequently drives a positive feedback that further enhances auxin levels in these cells thereby triggering lateral root formation (Laskowski et al., 2008).

1.4 Thesis outline

In this thesis we study decision making in plant roots specifically for the cases of prepatterning of lateral root competent sites and directional root growth by using multi-level computational models. Using these models we aim to understand how the combination of root architecture, developmental processes and hormone production and transport can drive decision making in plant roots and furthermore how environmental factors can impinge on the decision making process. To validate our model findings *in planta* we extensively collaborated with experimental groups. While the author of this thesis was involved in the set up and data analysis of the experiments, the experimental work was performed by members of the collaborating groups.

Both lateral root branching and directional growth have the plant hormone auxin as a major player. Even more so it has been suggested that tropisms, specifically the auxin asymmetry occurring during tropisms, influences the prepatterning of lateral roots, suggesting potential links between these two processes. Still, whether the effect of gravitropism is on sidedness or also frequency of lateral root patterning is debated (Kircher and Schopfer, 2016). The role of auxin in plant development is sometimes seemingly conflicting, for example, the observation that auxin can drive developmental rates and thereby drive root bending raises the question how this can occur without disturbing the also auxin-dependent developmental zonation (Mahonen et al., 2014). Additionally, auxin signalling output is often more specific than can be explained by tissue or cell specific signalling cascade and the involvement of auxin itself in setting up and regulating its own gene expression patterns and levels makes it complex to understand how auxin specificity arises. Therefore, in **chapter 2** we first focus on how the use of dynamical models and the additional consideration of spatial and temporal effects can aid the understanding of how plant roots decide on what decision to make using the plant hormone auxin.

In **chapter 3** we study the prepatterning of lateral root branching with the aim to elucidate the mechanism underlying the periodic auxin peaks observed during lateral root priming. Thus far, no satisfactory mechanism explaining these auxin oscillations had been proposed. Based on existing knowledge on the importance of auxin production (Strader and Bartel, 2011, Xuan et al., 2015), transport (De Smet et al., 2007, Moreno-Risueno et al., 2010, Xuan et al., 2015, Xuan et al., 2016), signalling in the vasculature (De Smet et al., 2007) and strong correlations with root growth (Jensen et al., 1998, Xuan et al., 2016), we started with the hypothesis that both the auxin reflux loop and growth are essential factors for lateral root priming. We used a multilevel model of plant root growth and auxin dynamics to investigate this hypothesis and pin down how this mechanism differs from earlier proposed priming mechanisms, most importantly the clock-and-wavefront model or a Turing pattern. Afterwards we set out to confirm our findings *in planta* in collaboration with the groups of Ben Scheres, Viola Willemsen and Tom Beeckman.

In **chapter 4** we then build upon our understanding of priming to study how dynamic changes induced by development or environmental factors influence the priming rate and the spacing between prebranch sites. Understanding the mechanisms of priming and the way environmental factors can impinge on the processes can help to understand to what extent main and lateral root adjustments in response to soil conditions might be coordinately caused by changes in main root growth and hence the prepatterning of the lateral roots and to what extent separate mechanisms are involved in adjustment of main and lateral root growth. We aimed to map the available morphospace for lateral roots in numbers and spacing and from there deduce how interdependencies between root meristem

size and cellular division rates might shape access to this morphospace. Finally, we discuss how the dynamic changes in priming and the resulting root system architecture could potentially affect RSA during abiotic stresses and varying nutrient conditions.

In **chapter 5** we shift our focus from decision making in lateral root branching to directional responses. Previous research had demonstrated a reduction in auxin transporters at the root side facing a salt gradient, followed by an auxin asymmetry and root bending away from a salt gradient (Galvan-Ampudia et al., 2013). An open question remained whether the observed auxin transporter asymmetry was causal and sufficient to explain the observed auxin asymmetry and root bending. By using root models with different root architecture and auxin transporter dynamics we aimed to understand how a salt gradient can be translated into a robust and timely directional auxin asymmetry able to drive adaptive root bending away from the salt. In both chapter 5 and 6 we tried to capture the dynamic nature of a tropic response in plant roots, the effect of transient responses, feedback and how these effects are translated into the timing and extent of the bending response in the plant root. We collaborated with the group of Christa Testerink to experimentally validate model predictions and build a realistic model of root halotropism.

The findings in chapter 5 elucidated how roots can temporally deviate from the gravity vector and overrule the gravitropic response. In **chapter 6** we further explore how plant roots integrated signals of gravitropism and halotropism, using a case study of the *pld ζ1* mutant to study the effect of cellular PIN2 levels and distribution on setting up an instructive auxin asymmetry and how PIN2 influences the opposing effects of gravitropism and halotropism.

Finally in **chapter 7** we integrated the findings of chapter 2 to 6 and discuss how the results of this thesis are connected to each other, how the findings can aid the understanding of plant root development and what future routes are there to explore. We extend our discussion by looking at the role of models in plant biology and the interaction of models with experiments and finally summarize the main conclusions of this thesis.

2

Auxin Information Processing; Partners and Interactions beyond the Usual Suspects

Thea van den Berg and Kirsten H. ten Tusscher

International Journal of Molecular Sciences (2017)

Abstract

Auxin plays a major role in a variety of processes involved in plant developmental patterning and its adaptation to environmental conditions. Therefore, an important question is how specificity in auxin signalling is achieved, that is, how a single signalling molecule can carry so many different types of information. In recent years, many studies on auxin specificity have been published, unravelling increasingly more details on differential auxin sensitivity, expression domains and downstream partners of the auxin receptors (transport inhibitor response 1 (TIR1) and other auxin signaling F-box proteins (AFB)), transcriptional repressors that are degraded in response to auxin (AUX/IAA) and downstream auxin response factors (ARF) that together constitute the plant's major auxin response pathways. These data are critical to explain how, in the same cells, different auxin levels may trigger different responses, as well as how in different spatial or temporal contexts similar auxin signals converge to different responses. However, these insights do not yet answer more complex questions regarding auxin specificity. As an example, they leave open the question of how similar sized auxin changes at similar locations result in different responses depending on the duration and spatial extent of the fluctuation in auxin levels. Similarly, it leaves unanswered how, in the case of certain tropisms, small differences in signal strength at both sides of a plant organ are converted into an instructive auxin asymmetry that enables a robust tropic response. Finally, it does not explain how, in certain cases, substantially different auxin levels become translated into similar cellular responses, while in other cases similar auxin levels, even when combined with similar auxin response machinery, may trigger different responses. In this review, we illustrate how considering the regulatory networks and contexts in which auxin signalling takes place helps answer these types of fundamental questions.

2.1 Introduction

The plant hormone auxin plays an important role in a wide range of developmental processes (Saini et al., 2013) as well as in a wide range of adaptive responses to environmental conditions (Fu and Wang, 2011, Kazan, 2013). Well known examples are the auxin-dependent control of cell division and differentiation rates (Dello Ioio et al., 2008), as well as the auxin maxima-dependent patterning of stem cell niches in the main root (Grieneisen et al., 2007, Petersson et al., 2009) and shoot (Vernoux et al., 2000) as well as new lateral organs (Benková et al., 2003, Heisler et al., 2005, De Smet et al., 2007), and the pre-patterning of the plant's vasculature network (Sachs, 1981, Sachs, 1991). Likewise, in most tropisms, the oriented growth of plant organs towards or away from a particular signal is guided by an instructive auxin asymmetry (Liscum and Briggs, 1996, Friml et al., 2002a, Swarup et al., 2005) and remodeling of overall plant root architecture in response to environmental conditions involves changes in auxin distribution patterns (Nacry et al., 2005, Krouk et al., 2010). This knowledge begs the question as to how a single hormone signal can convey so many different types of information. A large body of research, aimed at answering how specificity in auxin signalling arises, focuses on the different types of auxin receptors (TIR/AFB), Aux/IAA repressors and auxin response factors (ARFs) (Tiwari et al., 2003, Strader and Zhao, 2016) that together form the plant's major auxin signalling pathway. In *Arabidopsis*, a total of 6 TIR/AFB auxin receptors (Mockaitis and Estelle, 2008), 29 AUX/IAA repressors and 23 ARFs have been identified (Liscum and Reed, 2002), suggesting that part of the specificity in auxin signalling may depend on the specific auxin signalling molecules applied in a specific context. Research in this direction has uncovered differential sensitivity of distinct AUX/IAAs to auxin (Villalobos et al., 2012, Shimizu-Mitao and Kakimoto, 2014) specialised expression domains of different IAAs and ARFs (Weijers et al., 2005, Rademacher et al., 2011), as well as specificity differences between ARFs in the binding of auxin response elements in the promoters of downstream target genes (Boer et al., 2014). This knowledge enables one to answer certain questions on auxin specificity. As an example, if distinct modules with distinct auxin sensitivities are present within the same tissue, this explains how responses can vary with different levels of auxin. Indeed, the consecutive activation of the IAA28/ARF5,6,7,8,19, the IAA14/ARF7,19 and the IAA12/ARF5 auxin response modules involved in lateral root formation (De Rybel et al., 2012) may be related to an increase in auxin levels generated by the currently active module as well as feedbacks between the different modules (Goh et al., 2012, Lavenus et al., 2013). Similarly, the expression of different auxin response modules with similar auxin sensitivity in different tissues enables us to explain how an identical auxin signal conveys different information in different contexts (Rademacher et al., 2011). Intriguingly, auxin itself appears to often be involved in setting up these auxin response domains (Benková et al., 2003).

However, the insights on differential auxin sensitivity, expression domains, and downstream targets of different TIR/AFB, AUX/IAA and ARF types are insufficient to answer more complicated questions on auxin specificity. As an example, similar changes in auxin levels, occurring in the same tissues, may need to lead to different responses. To illustrate this, consider a cell at the proximal boundary of the root meristem and the transition zone that experiences an elevation in auxin level. How should this cell interpret this elevation in auxin level?

Auxin, combined with PLETHORA (PLT) transcription factors and antagonized by cytokinin, is a major determinant of meristem size (Dello Ioio et al., 2008, Mahonen et al., 2014). Thus, the auxin increase could imply that meristem size is expanding and hence that, rather than losing meristematic identity and starting to elongate and differentiate, the cell should stay meristematic. Or it could rather imply that the plant organ is undergoing a tropic response and the cell should respond by reducing the

elongation rate to support root bending. Alternatively, the elevated auxin level could also inform the cell that it finds itself in the middle of the upward phase of a lateral root priming event. Arguably, gravity responses are likely to be primarily controlled by epidermal auxin asymmetries, while lateral root priming involves auxin oscillations occurring specifically in the protoxylem and overlaying pericycle, and only meristem expansion may be governed by a tissue wide expansion of the auxin gradient. Still, this would require that an epidermal cell can at least distinguish between epidermis dominated asymmetric or rather tissue wide auxin elevations, while pericycle cells should be able to determine whether auxin elevations are pericycle specific or not. Intuitively, for us humans with a mind programmed for pattern recognition, it is clear that the response of the cell critically depends on the duration of the auxin elevation as well as to what extent other cells are experiencing the same or different changes in auxin levels. In the case of a meristem expansion, a persistent root wide change in auxin occurs, whereas in the case of tropism a transient asymmetric change in auxin takes place, while finally in the case of priming a transient more or less symmetric increase in auxin takes place that may be limited to the vasculature (Figure 2.1). However, it is far less clear how an individual plant cell is to obtain and decode this information on temporal and spatial aspects of auxin dynamics. Indeed, neither differential sensitivities nor differential expression domains of auxin response modules are sufficient to explain this. As another example, differential sensitivities and domains also do not enable us to explain how certain processes can be sensitive for relative rather than absolute changes in auxin levels, eliciting similar responses for widely different auxin levels.

In this review, we argue that to unravel such more complex auxin specificity problems, it is critical to consider the regulatory networks and functional context in which auxin signalling takes place. We will discuss several example studies in which such an approach was successfully applied. The common denominator between and central to the success of these studies is the combination of experiments with computational modelling. Generally speaking, the power of computational models lies in their capability to integrate knowledge obtained on different types of processes, playing out at different spatio-temporal scales, and investigate the types of feedback and emergent properties that these processes together give rise to. In addition, models allow us to vary the processes taken into consideration, their interactions and their conditions, enabling us to narrow down the core processes responsible for a biological property. Specifically, in the context of auxin sensitivity, by integrating auxin controlled processes playing out at different space and timescales, models enable, or even force us to investigate how these processes may functionally co-exist. In addition, they enable us to investigate the consequences of auxin-dependent feedback and auxin concentration ranges.

In the following sections, we discuss how using a modelling approach, studies have found major roles for feedback, differences in time scales, spatial patterning, auxin dependence of auxin transports and players other than the TIR/AFB, AUX/IAA and ARF factors. For example, we illustrate how a recent study demonstrated that auxin can simultaneously and without conflict control both stable developmental zonation and transient tropisms, by applying a division of labour separating the long developmental from the short tropism timescales (Mahonen et al., 2014). We end with the suggestion that plants are likely to have an as-yet uncharacterized machinery that enables them to respond similarly to a change in auxin levels across a wide range of auxin concentrations, similar to the maintained sensitivity of bacterial chemotaxis (Adler, 1966).

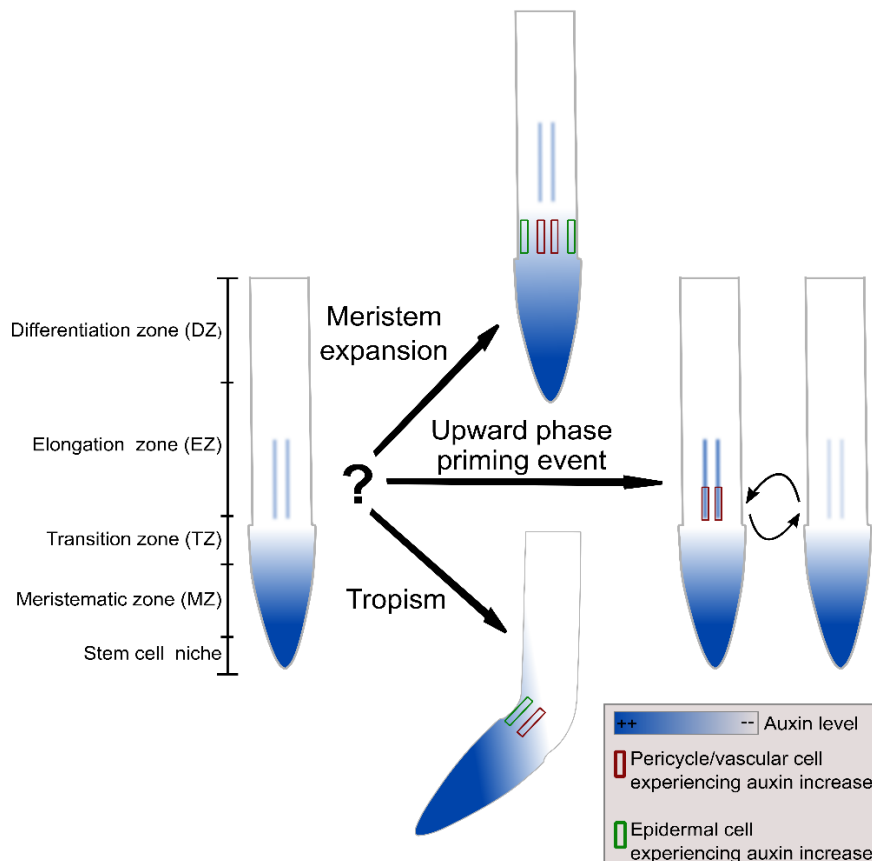


Figure 2.1. How can an individual plant cell deduce sufficient information from a locally perceived auxin increase? An increase in auxin experienced by an individual cell may reflect a long-term, tissue wide increase in auxin that will result in meristem expansion (upper graph, perceived in both epidermal and vascular cells), alternatively it may represent the upward phase of the oscillatory lateral root priming process (middle graph, predominantly perceived in vascular cells) and finally it may arise from tropism (lower graph, perceived in epidermal and possibly vascular cells). Thus, for an individual epidermal or vascular cell, a perceived auxin increase may arise from at least two of these three different situations, for which a different response is required.

2.2 The Auxin–Plethora Division of Labour; A Separation of Timescales

Two hallmarks of plant life are their lifelong continuation of growth and developmental programs and their ability to alter their development in response to environmental conditions. Combining these two characteristics requires dynamic adjustment of developmental programs to a changing environment, yet at the same time stably maintain a meristematic zone and ordered differentiation. Intriguingly, auxin is often involved in controlling both of these seemingly contradictory demands (Liscum and Briggs, 1996, Swarup et al., 2005, Dello Ioio et al., 2008). As an example, in the plant root, a gradient of auxin controls developmental zonation, with highest auxin levels corresponding to the quiescent center (QC) and surrounding stem cell niche (SCN), and gradually declining levels occurring throughout the rest of the meristem, elongation and differentiation zones (Grieneisen et al., 2007, Petersson et al., 2009, Ishida et al., 2010, Perrot-Rechenmann, 2010). At the same time, auxin affects the rates at which division, elongation and differentiation in these different zones occur (Evans et al., 1994). For instance, during gravitropism, when roots grow towards gravity, an asymmetric auxin accumulation leads to a single sided reduction in elongation rates that causes bending of the root towards the gravity vector (Mullen et al., 1998). In terms of auxin specificity, the question thus is how a transient auxin asymmetry can cause a growth asymmetry yet not perturb the developmental zonation that also appears to be controlled by auxin levels. Assuming that auxin would both alone and directly

dictate the developmental stage of a cell and at what rate processes involved in this stage are conducted, implies that an auxin asymmetry involved in tropic responses would perturb the root's developmental zonation. Therefore, it seems counterintuitive that auxin can control both stable developmental zonation and fast, transient tropisms. It has already been known for a long time that a family of transcription factors called the PLETHORAs (PLT) transcription factors play an important role in plant development (Galinha et al., 2007). Interestingly, these *PLT* genes are induced by auxin and expressed in a longitudinal gradient resembling the auxin gradient (Aida et al., 2004); furthermore, these PLTs are a main determinant for root developmental zonation (Galinha et al., 2007). To unravel the relative roles of auxin and PLTs and how these may together enable specificity, Mähönen et al. combined experiments with modeling. First, they demonstrated that while auxin directly affects the rates of division, expansion and differentiation, it appears to affect zonation only indirectly (Mahonen et al., 2014). Indeed, ectopic expression experiments demonstrated that PLT levels cell-autonomously control whether cells behave as stem cells, transit amplifying or differentiating cells. In line with this, increasing or reducing native *PLT* expression was shown to expand or reduce meristem size, respectively. Furthermore, they demonstrated that only prolonged exposure to high auxin levels induces *PLT* expression. Incorporating these findings into a multi-scale model of root growth predicts transcription close to the QC where auxin levels are high, thus resulting in a limited PLT protein domain rather than a gradient. The observation that in clonal expression experiments PLT proteins are present slightly outside their transcription domain led the authors to hypothesize that PLT proteins can move through the plasmodesmata that connect the cytoplasm of neighboring cells. Incorporating plasmodesmatal movement into the model demonstrated that a significant expansion of the PLT protein domain beyond its transcriptional domain could indeed arise, provided that PLT protein turnover is sufficiently slow. This can be understood from the fact that movement of PLT proteins through plasmodesmata is slow (order of magnitude of displacement of few cell diameters per 24 h); consequently, proteins will travel only a small distance if they are degraded too fast (half-life of less than 10 h). The authors subsequently experimentally confirmed this predicted importance of PLT protein stability for gradient formation. Finally, by using the model to virtually close the plasmodesmata, it was shown that stable proteins still formed a gradient beyond their transcriptional domain, albeit with a shorter length scale. When cells grow and divide, they become pushed out of the high auxin domain to which *PLT* transcription is limited. However, as a result of high PLT protein stability, protein levels do not immediately drop to very low levels in the absence of de novo transcription and translation PLT levels will drop gradually over time, causing PLT levels to reflect the amount of time or rather the number of cell divisions that have passed since the cell has left the *PLT* transcriptional domain, a process called mitotic segregation (Ibanes et al., 2006). Again, this finding was confirmed experimentally; this indicates that while auxin induces *PLT* transcription, the PLT protein gradient is not a simple readout of the auxin gradient. Instead, *PLT* transcription shows a slow response to high auxin levels, and the resulting spatially limited transcription domain is converted into a protein gradient through the slow processes of mitotic segregation and cell-to-cell movement.

As a consequence, the PLT gradient depends only on the root tip auxin maximum. In addition, the auxin and PLT gradients have different temporal dynamics. Auxin patterns respond directly to changes in expression levels, and the polar orientation of their cellular exporters, the PIN proteins. In contrast, PLT patterns change only in response to prolonged changes in the auxin maximum. Mahonen et al. demonstrated that this partial independence of the auxin and PLT gradients combined with their different timescales is critical for enabling auxin to govern both fast adaptation to environmental conditions and stable developmental zonation (Mahonen et al., 2014). Upon simulated gravitropism, the change in columella PIN polarity leads to the rapid generation of an auxin asymmetry driving gravitropic bending. At the same time, the PLT gradient remains constant, enabling it to maintain a

stable boundary between the meristem and elongation zone that is necessary for a temporally ordered, and tissue-wide coordinated progression of cell differentiation (Figure 2.2).

Auxin can thus fulfill two seemingly conflicting tasks by performing one directly, and the other indirectly using a partner that only partly depends on auxin and has substantially slower dynamics.

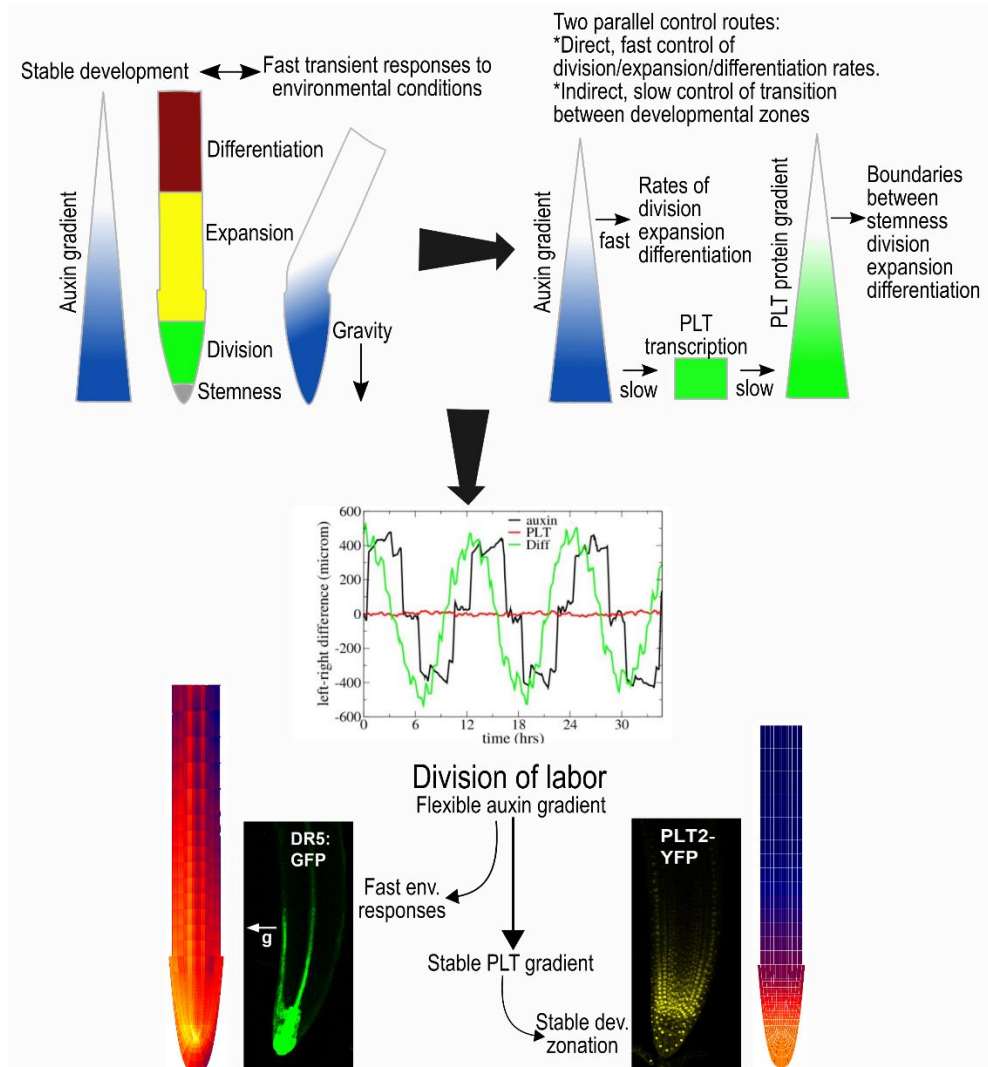


Figure 2.2. The auxin–PLETHORA (PLT) division of labour (Mahonen et al., 2014). If auxin were to directly control both rates and developmental zones, transient auxin asymmetries occurring during tropisms would perturb developmental zonation (upper left panel). PLT gradients result from auxin gradients through slow induction for high auxin levels, slow division and slow cell-to-cell movement (upper right panel). The control of rates by auxin and of zones by PLTs enables fast adaptation to tropic cues while maintaining stable PLT-mediated zonation (middle panel). Experiments confirmed the model predictions of the division of labor by the partial independence of the auxin and PLT gradients (lower panel).

2.3 Halotropism as a Case Study of a Graded-Signal Tropism; Auxin Computations in the Reflux Loop

Tropisms form an important aspect of plant adaptation, enabling individual plant organs to grow away or towards particular cues. In all tropisms but hydrotropism (Shkolnik et al., 2016), the bending of plant organs is orchestrated through an asymmetric auxin pattern that causes asymmetric growth rates (Friml et al., 2002b, Kutschera and Briggs, 2012, Galvan-Ampudia et al., 2013). A major question in

tropism research is thus how different environmental stimuli become translated into an instructive auxin asymmetry.

For plant roots, the most studied tropism is gravitropism, the orientation of the root towards the gravity vector. Specialised root tip columella cells containing starch granules, called statoliths, play a major role in gravitropism. Upon re-orientation of the root, the statoliths sediment on the new downward face of the cells (Eshel and Beeckman, 2013), causing a change in the pattern of PIN3 and PIN7 proteins from an apolar localisation at all membrane faces to a polar orientation on the now downward face of the columella cells (Friml et al., 2002b, Kleine-Vehn et al., 2010). As a consequence, auxin flux is biased to the lower side of the root, causing an elevation of auxin at the lower side and a decrease of auxin at the upper side of the root (Ottenschläger et al., 2003, Monshausen et al., 2011). Importantly, in gravitropism, individual cells, through statolith sedimentation and subsequent PIN repolarization, can sense the direction of and respond directionally to the gravity signal. As a consequence, all columella cells, independent of whether they are on the upward or downward side of the root, coherently polarize their auxin transport towards the lower side, thereby directly generating a clear and robust auxin asymmetry. In plant shoots, the most studied tropism is phototropism, the orientation of the shoot towards light. At the light exposed side, plant cells respond by reducing ATP-binding cassette B19 (ABCB19)-mediated downward auxin transport and enhancing PIN3-mediated lateral auxin transport, thus locally accumulating auxin, while at the shaded side no such response occurs. As a consequence, an auxin asymmetry directly arises from the differential reception of and response to the signal at the two sides of the plant hypocotyl (Christie and Murphy, 2013).

A completely different situation arises in a recently discovered root tropism, halotropism, where roots bend away from elevated salt concentrations (Sun et al., 2008, Galvan-Ampudia et al., 2013). Since salt readily diffuses through the medium -experimental agar or soil- roots will generally be exposed to a relatively shallow gradient of salt, rather than experiencing salt only on one side. For example, in the study of Galvan-Ampudia et al. across root salt concentration, differences are in the order of only 5–10% (Galvan-Ampudia et al., 2013). A similar, graded signal distribution may occur in hydrotropism (Cassab et al., 2013). As roots experience a salt gradient, this logically implies that cells at the different sides of the root mount a similar response, albeit with cells at the side experiencing more salt a slightly stronger one. Furthermore, it seems unlikely that individual cells are capable of detecting the direction of the salt gradient and responding to it directionally. Thus, the question then is how relatively small differences in salt levels, and hence response strength at the two sides of the root, eventually become translated into a clear-cut overall asymmetry in auxin. To achieve this, cells at different sides of the root should somehow communicate to integrate information from different sides of the root and determine at which side salt concentrations are highest.

While this specific question has thus far not been addressed, results of a recent study by Van den Berg et al. provide interesting suggestions (van den Berg et al., 2016). In this study, it was shown that the earlier identified asymmetry in the PIN2 auxin exporter (Galvan-Ampudia et al., 2013) is insufficient to fully explain halotropism-induced root bending. The authors used a simulation model to demonstrate that the auxin dependence of the auxin resistant 1 (AUX1) auxin importer and the PIN2 exporter are critical for amplifying the small auxin asymmetry generated by the initial PIN2 asymmetry. Put simply, on the side with highest salt levels, less PIN2 leads to less auxin transport upward on that side, thereby decreasing local auxin levels, which subsequently leads to a further decrease in PIN2 as well as AUX1, etc. As a consequence, increasingly less auxin is transported upward on the more salt-exposed side. The auxin not transported at the side with the highest salt levels is subsequently rerouted to the other side. Initially, only small amounts of auxin will be rerouted;

nonetheless, the higher auxin levels, resulting from the rerouting, will amplify AUX1 and PIN2 levels through positive feedback and subsequently increase in auxin rerouting (van den Berg et al., 2016). While the study of Van den Berg et al. does not yet address what generates the initial PIN2 asymmetry, it does point to the important role of auxin feedback on its own transporters as effective amplifiers of initial auxin differences. This opens up the interesting possibility that if the very first response to a graded environmental signal involves qualitatively similar yet quantitatively slightly different changes in auxin transport or signalling, the root tip reflux loop combined with the auxin feedback on auxin transporters may suffice to amplify these initial differences into a full auxin asymmetry (Figure 2.3).

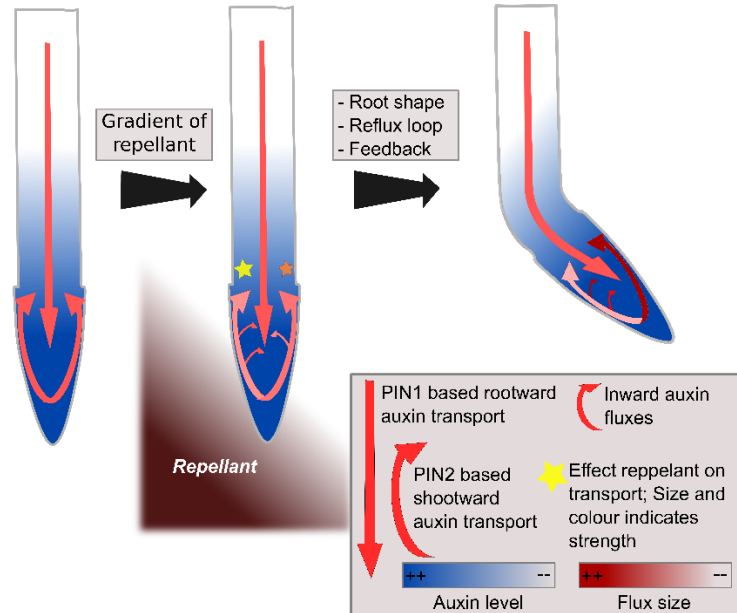


Figure 2.3. Hypothetical model of left–right sensing in plants during tropisms. A gradient of repellent, for example diffusing NaCl, causes a stress response at both sides of the root, though somewhat stronger at one side than the other, causing modulations in the reflux loop (middle panel). Subsequent positive feedback of auxin on its own transporters combined with root tip architecture and reflux loop properties amplify initial differences into a clear instructive auxin asymmetry, enabling bending (van den Berg et al., 2016) (right panel).

2.4. Auxin Signalling in Phyllotaxis; Same yet Different

At the shoot apex, the regular formation of new leaf primordia is preceded by the formation of auxin maxima that arise in the vicinity of the shoot meristem where auxin levels are lower. It has long been established that dynamic repolarization of the auxin exporting PIN1 proteins play a major role in the repetitive generation of these auxin maxima (Okada et al., 1991). However, for a long time, an open question remained to what extent pattern formation involved only spatio-temporal differences in auxin concentration levels between primordia and central meristem, and to what extent changes in auxin sensitivity and/or downstream targets may also be involved. Ultimately, the impact of auxin signalling on patterning is a product of the local auxin levels and the local auxin sensitivity.

Interestingly, a large-scale expression analysis of the AUX/IAA and ARF factors active in the shoot apical meristem region revealed that similar factors are active across the meristem region albeit with lower levels occurring in the central meristem than in the periphery and young primordia (Vernoux et al., 2011). Thus, neither differential sensitivity nor different domains of different players involved can explain the distinct developmental trajectories of the central region that remains meristematic and the peripheral regions that repetitively produce new leaf organs. This implies that these different developmental fates solely rely on differences in auxin levels and sensing occurring in the different

regions. As a consequence, robust patterning requires the persistent generation of significant differences in auxin levels and sensing between these different regions.

Given the observed difference in AUX/IAA and ARF levels between central meristem and periphery, Vernoux et al. (2011) applied a modelling approach to investigate the potential significance of these concentration differences for robust auxin-driven patterning. A key aspect of the model is that it incorporates gene expression-activating ARFs that can be repressed by AUX/IAA and derepressed by auxin, but also the less frequently considered autonomously acting repressive ARFs (Figure 2.4A). Importantly, activating and repressive ARFs compete for the same finite number of binding sites upstream of target genes (Ulmasov et al., 1999b). Finally, activating ARFs are assumed to cooperatively affect gene expression. As a consequence, while gene expression linearly declines with the number of repressive ARFs it supralinearly increases with the number of activating ARFs (Figure 2.4B). Using the model, the authors could thus demonstrate that if the number of activating and repressive ARFs increases similarly, downstream gene expression increases (Figure 2.4C). This enabled them to explain how the lower levels of ARFs and AUX/IAA occurring in the centre of the meristem result in lower auxin sensitivity than the higher levels occurring in the periphery and the primordia. This differential sensitivity was subsequently experimentally confirmed. Furthermore, the spatial correlation between low auxin levels and low auxin sensitivity in the centre and high auxin levels and auxin sensitivity in the periphery was shown to contribute to the robustness of phyllotactic patterning (Vernoux et al., 2011). While not addressed in this study, one can imagine that by making AUX/IAA and ARF levels auxin dependent, sensitivity to auxin becomes correlated with auxin levels.

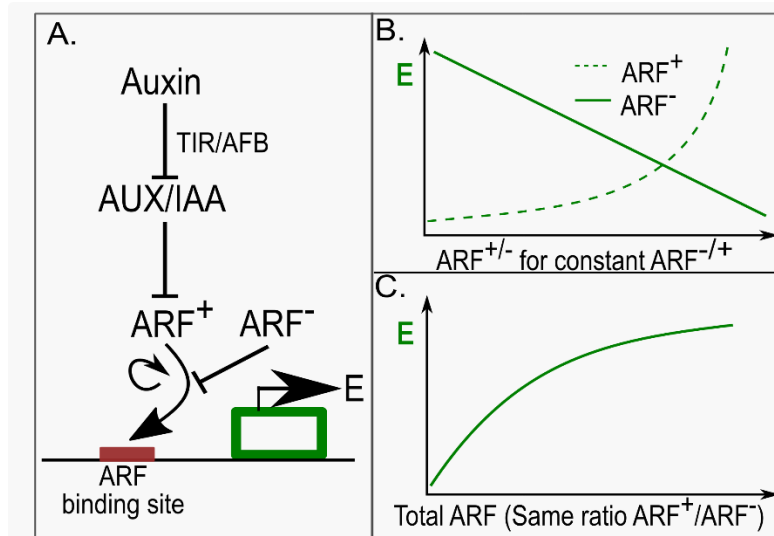


Figure 2.4. In phyllotaxis, different amounts of ARFs result in differential auxin sensitivity (Vernoux et al., 2011). (A) Auxin response network, with auxin de-repressing the AUX/IAA repressed activating ARFs (ARF^+), activating and repressive ARFs (ARF^-) competing for the same auxin response elements (ARE) upstream of auxin responsive genes, and gene expression levels (E) cooperatively depending on activating ARFs; Lines ending with arrowheads indicate positive regulatory interactions, lines ending with a horizontal line indicate negative regulatory interactions; (B) Gene expression in response to different levels of repressive and activating ARFs, for constant amounts of activating and repressive ARFs respectively. The non-linear response to activating ARFs arises from their cooperative effects on gene expression; (C) Gene expression levels in response to different amounts of activating and repressive ARFs for a constant ratio between the activating and repressive ARFs.

2.5 Pin Polarity in Gradients; Different yet Same

The ability to generate well defined auxin maxima, gradients and paths critically depends on the polar localisation of the auxin exporting PIN proteins (Blilou et al., 2005, Wisniewska et al., 2006, Grieneisen et al., 2007). It is generally assumed that, at least to a certain extent, the polar membrane localisation of PIN proteins depends on auxin (Figure 2.5A). Unfortunately, how exactly these polar patterns arise remains unclear. Earlier hypotheses on the role of the auxin binding protein 1 (ABP1) protein in sensing auxin levels (Xu et al., 2010) and the role of auxin-dependent cycling of PIN proteins to and from the membrane (Robert et al., 2010) in setting up PIN polarity have become heavily disputed due to recent studies (Gao et al., 2015, Jásik et al., 2016). Because of this yet incomplete understanding, models for PIN polarity dynamics have mostly been formulated in phenomenological terms. Depending on whether the aim was to explain patterns of shoot phyllotaxis or leaf veination, up-the-gradient or with-the-flux feedbacks of auxin levels or transport on PIN levels have been proposed (Heisler and Jönsson, 2006, Stoma et al., 2008, Bayer et al., 2009). In the former, PIN levels are assumed to increase on membranes oriented to neighbouring cells with high auxin levels; in the latter, PIN levels are assumed to increase in the direction of largest transport flux.

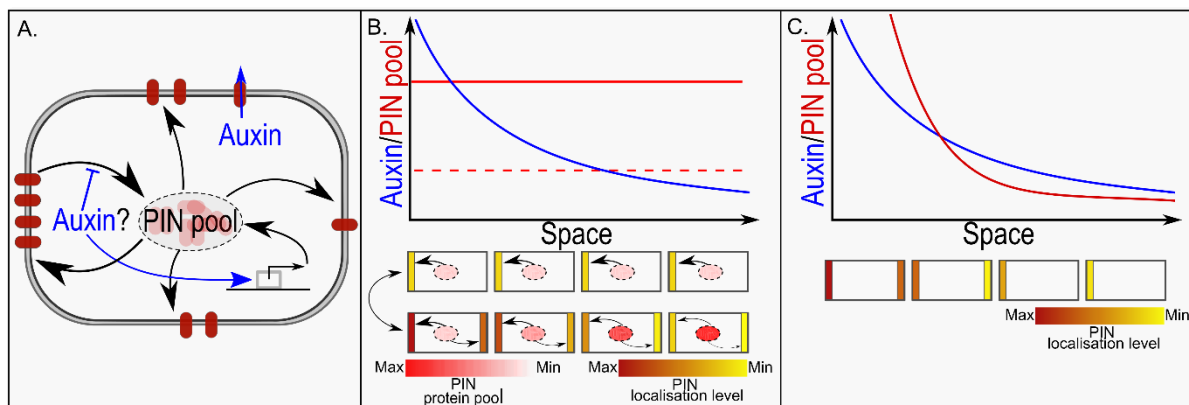


Figure 2.5. In PIN polarisation, the cellular PIN pool size determines graded versus all-or-none polarisation. (A) Gene expression is a major determinant of overall cellular PIN pool size. Individual membrane compartments derive their PINs from this single shared PIN pool, and PINs not deposited on the membrane together constitute the remaining cytoplasmic PIN pool; (B) The upper graph shows a hypothetical auxin gradient across a one-dimensional tissue. We assume an up-the-gradient type of feedback on PIN localisation. If the overall cellular PIN pool is small, all-or-none polarisation occurs and all cells show the same polarity pattern with high amounts of PINs on the highest concentration facing membrane and low or absent PINs on the lowest concentration facing membrane, and few PINs left in the cytoplasmic PIN pool (middle figure). If the overall cellular PIN pool is large, PIN levels on each individual membrane depend on the auxin level they experience, resulting in a graded polarity pattern with amount of polarity and amount of PINs on highest and lowest concentration facing membranes increasing along the gradient, and amount of PINs remaining in the cytoplasmic gradient decreasing along the gradient (lower figure); (C) The upper graph shows again a hypothetical auxin gradient that now induces a gradient in overall cellular PIN pool sizes. For small PIN pools, all-or-none polarisation occurs; for larger PIN pools, polarisation becomes graded with auxin levels, while for very large PIN pools, apolar PIN patterns arise.

Detailed mathematical analysis of a large range of PIN polarity models showed that, independent of assuming either with-the-flux or up-the-gradient feedback, the type of PIN polarisation patterns arising strongly depended on the size of the cellular PIN pool and the extent to which all PIN proteins are deposited on the membrane (van Berkel et al., 2013). If the amount of PIN proteins in a cell is assumed to be large relative to the amount of PINs that will be localised on the membrane, PIN levels are not limiting. As a consequence, different membranes of the same cell are not competing for PINs, and each membrane can adapt its PIN levels to local auxin or auxin flux levels. Under these conditions, graded PIN polarity patterns arise: if auxin levels or fluxes differ more across a cell, the cellular PIN

patterns will polarise more strongly. Thus, along a non-linear auxin gradient, cellular polarisation increases with the steepness of the gradient. Furthermore, as individual membranes respond to their local auxin or flux level, even along a linear auxin gradient resulting in similar polarisation levels, average PIN levels will follow auxin or flux levels. Indeed, if one adds to these models the realistic assumption that membrane compartments can only contain a finite amount of PINs, large unlimiting levels of PINs combined with very high auxin levels generate apolar PIN patterns (Figure 2.5B). If, in contrast, we assume a finite pool of PIN proteins that for a large part will be positioned on the membrane, PIN proteins become limiting. In this case, the different membrane compartments of the cell compete for PINs; putting more PIN proteins on one membrane automatically means that less PINs will be available for other membranes. Due to positive feedback, more and more PINs will be put on the membrane facing the highest auxin levels or auxin flux levels, and less and less on the other membranes, resulting in full-blown polarisation, independent of the average levels or size of across-cell differences in auxin or auxin flux that the cells were experiencing. This all-or-none polarisation allows cells in different parts of the tissue, experiencing different average flux strengths or concentrations, as well as different across-cell differences in fluxes or concentrations, to build a similar PIN polarity pattern (van Berkel et al., 2013) (Figure 2.5B).

The above demonstrates two things relevant for auxin specificity. First, if the cellular PIN pool to a large extent is localised on the membrane, different auxin levels or fluxes can produce similar PIN polarity patterns. Second, by regulating PIN pool size, similar gradients in auxin levels or fluxes can generate different PIN patterns: all cells polarised similarly, or cellular polarisation changing along the gradient (Figure 2.5C). In this context, it is noteworthy that auxin, both directly and via regulating the PLT transcription factors, upregulated *PIN* expression levels (Blilou et al., 2005, Vieten et al., 2005).

2.6 Conclusions and Outlook

The plant hormone auxin plays a critical role in a wide range of developmental and adaptive processes. Understanding these processes, at an individual level as well as in relation to one another, requires that we understand how auxin can regulate so many distinct processes. Logically speaking, a single signal, such as auxin, can only convey distinct or even contradicting information by collaborating with other factors. Traditionally, specificity of auxin signalling is considered in terms of differential sensitivity, expression domains or downstream targets of auxin signal transduction pathways. In this article, we argued that other partnerships beyond these usual suspects as well as the context and regulatory networks in which auxin signalling takes place are critical to consider. To support this argument, we demonstrated a series of insights on auxin specificity obtained in recent studies.

While we discussed only a limited number of examples in this review, we expect that the type of partnerships pointed out is more common. For instance, in the last example of PIN polarity, we discussed how different auxin signals can generate similar responses. Because of the finiteness of available PIN proteins, under certain conditions different tissue-level auxin gradients can become translated into similar patterns of PIN polarity (van Berkel et al., 2013). We suspect that something similar should hold for temporal auxin changes; under certain conditions, different changes in auxin levels are capable of eliciting the same response, provided that the temporal direction and relative amount of auxin change, increase or decrease, are similar. As an example, while it is still debated whether lateral root priming involves periodic changes in auxin levels or merely auxin responses (Laskowski and Ten Tusscher, 2017), one would expect that different environmental conditions or different root developmental ages affect root tip auxin levels as well as baseline and maximum levels

of these auxin oscillations. Still, effective lateral root priming should occur under all these conditions. This requires a machinery capable of sensing relative changes in auxin levels rather than absolute auxin levels. Sensitivity to relative changes is well-known from bacterial chemotaxis, in which bacteria are capable of sensing a directional relative difference in chemotactic cue across a wide range of concentrations. The mechanistic basis of this capacity to sense relative differences lies in the presence of a slow timescale negative feedback from average concentration levels to proteins responsible for sensitivity, resulting in a normalisation of sensitivity to average concentration levels (Adler, 1966, Adler, 1969, Parkinson, 1993). We expect that for sensing relative auxin changes, the TIR/AFB-AUX/IAA-ARF system may play an important role. As the study by Vernoux et al. showed, absolute levels of the AUX/IAAs, ARF repressors and ARF activators may impact the sensitivity for auxin (Vernoux et al., 2011). Extrapolating from their results, one can imagine a system in which AUX/IAA and ARF levels depend on long-term auxin levels, causing increased sensitivity to changes in auxin for persistently high auxin levels. Alternatively, auxin sensitivity could also be modulated by affecting the levels of the more upstream TIR1/AFB factors, as was, for example, shown for bacterial infections (Navarro et al., 2006).

In this review, we solely focused on auxin as a critically important plant hormone; however, many more hormones (Vert et al., 2008, Antoniadis et al., 2015), peptides (Matsuzaki et al., 2010), and small RNAs (Yoon et al., 2010) are involved in developmental patterning. Therefore, auxin specificity may also arise from combining similar auxin signals with different types or levels of other signalling molecules. A major factor to consider in this context is cytokinin, for which differential patterns have been clearly established (Antoniadis et al., 2015). Nevertheless, this will shift the question to what causes these differential cytokinin patterns. Given the highly intertwined nature of auxin and cytokinin signalling, production, degradation and transport, auxin itself is likely involved in controlling cytokinin patterning (Chandler and Werr, 2015). More general, many of the signalling molecules involved in development, either directly or indirectly, have an effect on and are at the same time affected by auxin (Cruz-Ramirez et al., 2012, Whitford et al., 2012, Moubayidin et al., 2013). Therefore, a complete and in-depth understanding of auxin specificity will require a further elucidation of the regulatory interactions and mutual patterning of auxin with other hormones and signalling molecules. Similar to the studies described here, we expect a major role for computational modeling in unraveling how such complex signalling and patterning networks endow the auxin signal with its specificity.

Acknowledgements

This work was supported by the Netherlands Scientific Organization (Nederlandse Organisatie voor Wetenschappelijk Onderzoek) grant number 864.14.003 to Thea van den Berg and Kirsten ten Tusscher.

3

A reflux-and-growth mechanism explains oscillatory patterning of lateral root branching sites

Thea van den Berg, Kavya Yalamanchili, Hugues de Gernier, Joana Santos Teixeira, Tom Beeckman, Ben Scheres, Viola Willemsen and Kirsten ten Tusscher

Developmental Cell (2021)

Abstract

Modular, repetitive structures are a key component of complex multi-cellular body plans across the tree of life. Typically, these structures are prepatterned by temporal oscillations in gene expression or signaling. While for vertebrate somitogenesis and arthropod segmentation a clock-and-wavefront mechanism was identified and plant leaf phyllotaxis arises from a Turing-type patterning, the mechanism underlying lateral root patterning has remained elusive.

To resolve this enigma we combined computational modelling with in planta experiments. Intriguingly, auxin oscillations automatically emerge in our model from the interplay between a reflux loop generated auxin loading zone, and stem cell driven growth dynamics generating periodic cell size variations. In contrast to clock-and-wavefront and Turing patterning, the uncovered mechanism predicts both frequency and spacing of lateral root forming sites to positively correlate with root meristem growth. We validate this prediction experimentally. Combined, our model and experimental results support that a novel periodic patterning mechanism underlies lateral root priming.

3.1. Introduction

In multi-cellular organisms, developmental processes are not only responsible for generating a multitude of cell types from genetically identical cells, but also for the spatial organization of cell types, tissues and organs into functional body plans. In many multi-cellular organisms, at least part of the body plan is of modular, repetitive nature. Well-known examples are the segments of annelids and arthropods (Davis and Patel, 1999), the somites (Conlon et al., 1995, Palmeirim et al., 1997, Dubrulle and Pourquié, 2002), and appendages of vertebrates (Saunders, 1948, Dolle et al., 1989, McGinnis and Krumlauf, 1992) as well as the phytomers of plants (Reinhardt et al., 2003, Smith et al., 2006), trichome patterning on plant leaves (John C. Larkin et al., 1999, Ishida et al., 2008) and placement of hair cells on roots (Galway et al., 1994, Ishida et al., 2008). Plant root system architecture is also repetitive, but on top of this, displays high plasticity, ensuring access to water and nutrients under a wide range of different conditions (Rogers and Benfey, 2015, Eshel and Beeckman, 2013). As a consequence, under natural conditions the regular nature of the root system architecture may become obscured (Gruber et al., 2013). In the model plant *Arabidopsis thaliana* it has been shown that the earliest step in the formation of new lateral roots, essential for the formation of a branched root architecture, is highly regular (De Smet et al., 2007, Moreno-Risueno et al., 2010). Lateral root (LR) formation starts with the priming of subsets of pericycle cells to gain competence for the future formation of LRs (De Smet et al., 2007, Moreno-Risueno et al., 2010). Priming is characterized by temporal oscillations in auxin signaling and gene expression in the root transition zone with an as yet unknown primary cause. Primed sites will through growth become transformed into a spatially repetitive pattern of competent sites for LR formation (De Smet et al., 2007, Moreno-Risueno et al., 2010, Xuan et al., 2015, Xuan et al., 2016).

Mathematical modelling has played a key role in unravelling the mechanisms underlying periodic developmental patterning processes. In 1952 Turing demonstrated that interactions between a slowly diffusing activator and a more rapidly diffusing inhibitor substance could give rise to regular periodic patterning (Turing, 1952). In case of polar tissue outgrowth such Turing type patterning mechanisms give rise to the periodic production of new pattern elements. While originally proposed for phyllotaxis (Saunders, 1992), and for a long time difficult to substantiate experimentally, Turing type patterns are now generally accepted to underly vertebrate appendage (Newman and Frisch, 1979) and digit patterning (Raspopovic et al., 2014), and hair (Sick et al., 2006, Plikus et al., 2008), feather (Jiang et al., 1999, Shyer et al., 2017) and skin pigmentation patterning (Yamaguchi et al., 2007). Additionally, a Turing-like substrate depletion mechanism in which up-the-gradient polarization of auxin exporting PIN proteins locally enhances, and at a longer range depletes, auxin levels has been shown to underly phyllotaxis (Reinhardt et al., 2003, Jonsson et al., 2006, Sick et al., 2006). Of similar significance is the clock-and-wavefront mechanism first proposed by Cooke and Zeeman in 1976 (Cooke and Zeeman, 1976). This model proposes that underlying somitogenesis is a cell-autonomous oscillatory clock combined with a wavefront dictating when and where these temporal oscillations become translated into a periodic pattern. The clock-and-wavefront model has received substantial experimental support, identifying the clock as a set of genetically encoded negative feedbacks resulting in gene expression oscillations (Panganiban et al., 1997, Bessho et al., 2003, Dequeant et al., 2006, Sarrazin et al., 2012). Based on the observation of periodic variations in gene expression coinciding with variations in auxin signaling, Moreno-Risueno (2010) proposed that a clock-and-wavefront mechanism analogous to that observed in vertebrate somitogenesis underlies periodic priming (Moreno-Risueno et al., 2010). As an alternative possibility a Turing-type mechanism, similar to that used in vertebrate appendage patterning and phyllotaxis has been proposed (Laskowski and Ten Tusscher, 2017). Thus far, for neither mechanism substantial proof has been provided.

So far, no single loss-of-function mutations have been identified that completely abolish LR formation at or preceding the founder cell stage, while mutations blocking LR formation at later stages have been identified (DiDonato et al., 2004). Interestingly, a strong repression of LR formation occurs in the dark, known to affect sugar transport and consequently root growth dynamics (Jensen et al., 1998). Additionally, studies have demonstrated an important role for the synthesis of the auxin precursor indole-3-butyric acid (IBA) in the lateral root cap (LRC) in determining the amplitude of priming oscillations (Strader and Bartel, 2011, Xuan et al., 2015) and reported a reduced production of LRs for mutations in auxin transporting proteins such as PIN2 (Xuan et al., 2016), LAX3 (Swarup et al., 2008, Lewis et al., 2011) and AUX1 (De Smet et al., 2007, Lewis et al., 2011, Xuan et al., 2015). Auxin perception in the vasculature was furthermore shown to be critical for LR formation (De Smet et al., 2007). Finally, recent studies reported a strong spatio-temporal coincidence of repetitive LRC apoptosis and priming events (Xuan et al., 2016) as well as a key role for growth related cell-wall remodeling (Wachsman et al., 2020). Together, these studies indicate the importance of auxin production, transport and perception while also hinting at a key role for growth dynamics.

Here we hypothesized that the interplay between the auxin reflux loop and growth dynamics gives rise to regular auxin oscillations. To investigate this hypothesis we combined computational modelling and in planta experiments. Excitingly, incorporating auxin transport and growth dynamics into a novel multi-scale realistic root model automatically led to the emergence of repetitive auxin peaks. Moreover, these auxin oscillations originated in the elongation zone (EZ) protoxylem and were subsequently transmitted to the pericycle, consistent with experimental observations (De Smet et al., 2007). Specifically, we found that root tip anatomy and reflux loop properties result in an auxin loading zone at the start of the EZ, with preferential loading in large narrow vasculature cells. Additionally, we showed how root growth dynamics in the meristem, by causing alternations in the sizes of cells arriving at the transition zone (TZ), causes substantial variation in auxin loading potential, resulting in auxin level oscillations. In contrast to a Turing mechanism or a clock-and-wavefront mechanism the ‘reflux-and-growth’ mechanism discovered here predicts that both the frequency and spatial spacing of priming events depend on meristem cell production and hence tissue growth rate. Our in planta experiments confirmed these model predictions. Combined, our findings support that a hitherto undescribed mechanism for periodic pattern formation underlies LR priming. Our in planta experiments uncovered similar correlations for actual formed LRs as for the priming sites, indicating the importance of early priming events for actual root branching patterns.

3.2. Results

3.2.1 Priming emerges from combined root auxin transport and growth dynamics

To investigate the role of root tip auxin reflux and growth dynamics in the generation of auxin oscillations, we developed a novel computational model, incorporating an anatomically realistic root topology and detailed auxin dynamics. The model incorporates cell type and zone specific patterns of the auxin exporting PIN membrane proteins as well as the auxin importing AUX/LAX membrane proteins, as well as passive cellular auxin import, auxin production and degradation, and a shoot-derived influx of auxin. Additionally the model incorporates realistic root growth dynamics consisting of slow stem cell (SC) divisions near the quiescent centre (QC), subsequent clonal expansion of more rapidly dividing transit amplifying (TA) cells (Bizet et al., 2015, Rahni and Birnbaum, 2019) as well as expansion and differentiation dynamics (Fig 1A). As a consequence, after originating from a SC division, individual cells sequentially transition these distinct zones as younger cells formed rootward of them push them away from the SC niche. Additionally, individual cells undergo dynamic cell size changes. While growing in between divisions cells gradually increase in size, halving their size upon division, and when undergoing expansion they undergo a much more rapid size increase that ends as cells start their terminal differentiation.

Since we are focusing on LR priming, in which protoxylem and xylem pole pericycle play critical roles, our two-dimensional model represents a longitudinal cross-section through the protoxylem poles. To include critical aspects of *in planta* three dimensional auxin fluxes (el-Showk et al., 2015) in addition to the predominant basally oriented active auxin transport, we also incorporated outward oriented, protoxylem directed PIN transport in the vasculature (Fig. S3.1A).

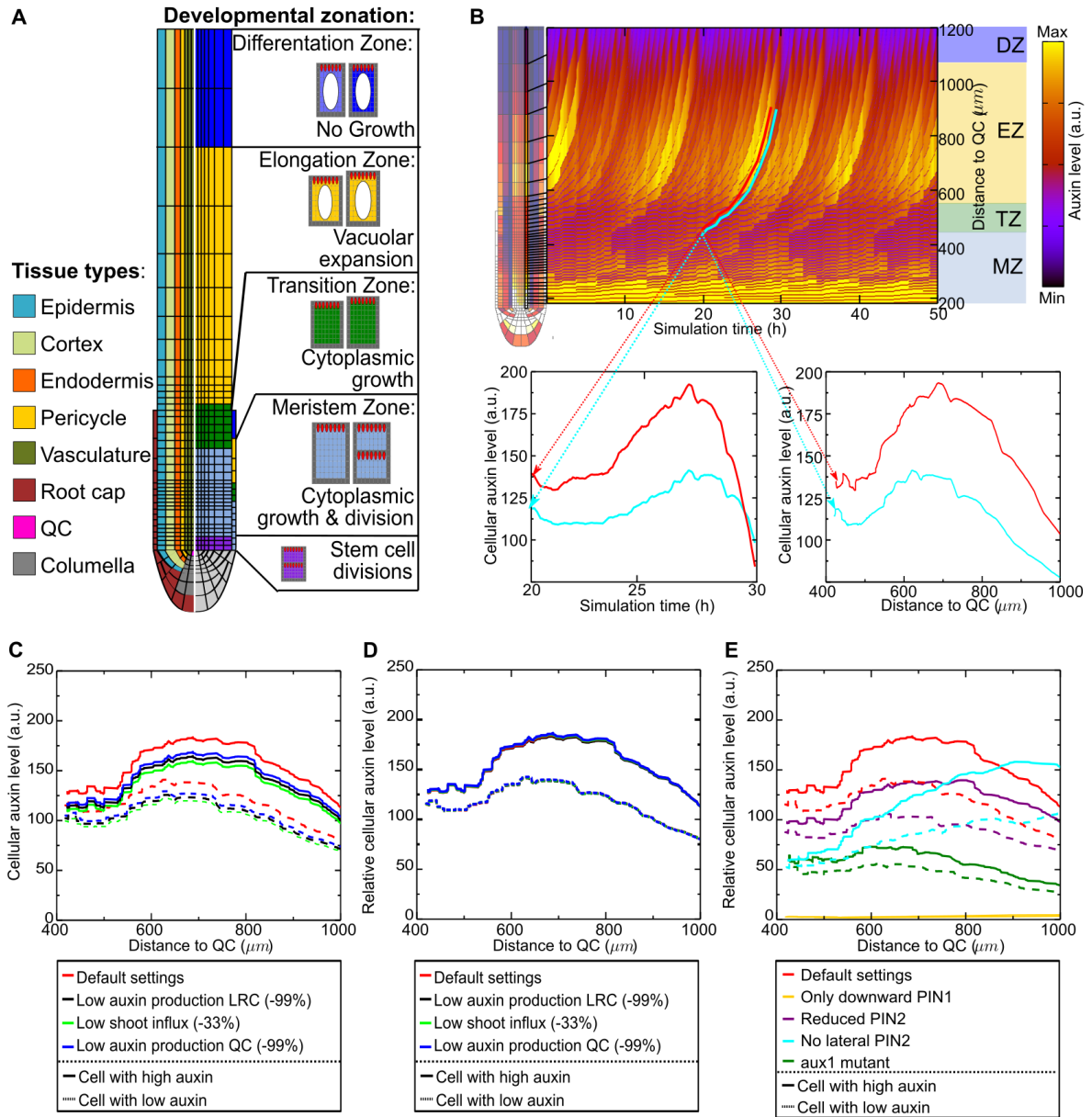


Figure 3.1. Auxin oscillations automatically emerge from a growing root model. A) Overview of root model with tissue types (left) and division, expansion and differentiation zones (right). B) Model auxin dynamics. Top: Kymograph displaying snapshots of auxin levels in a longitudinal line inside the vasculature at 100s intervals, Bottom: Auxin levels in a high (red line) and a subsequent low auxin (cyan) experiencing cell as a function of time (left) and space (right), cells were followed from entrance in the TZ to exit to DZ. C) Spatial auxin profile for different auxin production settings for a cell experiencing high (solid line) and low (dotted line) auxin. Auxin production settings were altered to obtain a similar reduction in total auxin for the 3 different cases. D) Same spatial auxin profile for different auxin production settings as shown in C but now with auxin levels normalized against total root tip auxin content. E) Spatial auxin profile for altered reflux loop settings, for a cell experiencing high (solid line) and low auxin (dotted line) with cellular auxin levels normalized for total auxin content. Simulations shown are default simulation (red, as shown in B), simulation with only downward PIN1 in vasculature (yellow), 50% reduction in PIN2 in LRC, epidermis and cortex without changing the relative strength of basal and lateral transport (purple), absent lateral PIN in LRC, epidermis and cortex from TZ shootward (cyan) and an aux1 mutant with a 90% reduction in AUX/LAX gene-expression (green).

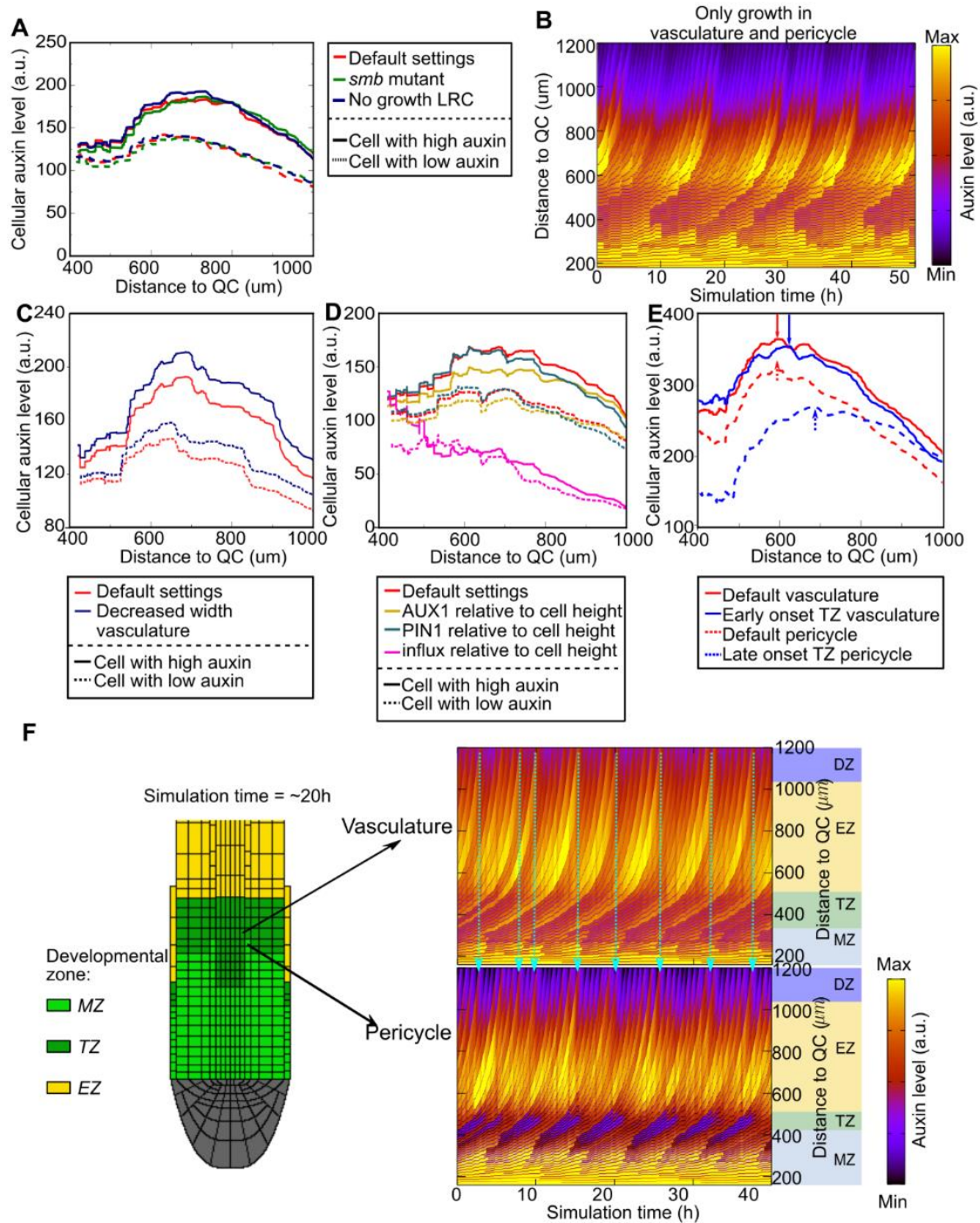


Figure 3.2. Role of root cap and vascular growth dynamics in priming. A) Normalized temporal auxin dynamics for a simulated *smb* mutant and absence of LRC growth. B) Kymograph for a simulation in which only vasculature and pericycle grow. Auxin scale is normalized to maximum observed auxin levels, in Fig. S3.2B the same scale as in Fig. 3.1B is used. C) Normalized auxin dynamics for reduced width of vasculature cell files. This simulation with decreased vasculature cell width was performed with 1 extra vasculature file to avoid simultaneously altering overall vascular tissue width and hence root architecture. D) Auxin dynamics for relative to cell height normalized active auxin import (AUX1), active export (PIN) or passive import. Normalization of transport for cell height was applied to vasculature cells in the TZ, EZ and DZ. Cellular auxin levels were normalized for total auxin content to allow comparison between the different simulations. E) Normalized auxin dynamics for tissue specific TZ onset of the vasculature and pericycle, only cells experiencing high auxin are shown. Arrows indicate the spatial position of the auxin maximum. F) Root zonation (left) and kymographs of vasculature (upper) and pericycle (lower) for the same simulation with tissue specific TZ onset as shown in E. Cyan arrows indicate priming onset in vasculature and transmission to neighboring pericycle. See also Figure S3.2.

Surprisingly, regular temporal variations in auxin levels automatically emerged in this model (Fig. 3.1B, Video S3.1). Even more noteworthy, these oscillations predominantly occur in the vasculature (Fig. 3.1B) and pericycle (Fig. S3.1B) of the TZ and early EZ, precisely where priming is experimentally found to occur (De Smet et al., 2007). Indeed, as is clear from the root tip auxin patterns, highest auxin levels occur in the vascular tissues (Fig. S3.1B).

3.2.2 Auxin availability can shape oscillation amplitude

Previous research indicated the importance of auxin production for priming amplitude (Dubrovsky et al., 2008, Strader and Bartel, 2011, De Rybel et al., 2012, Xuan et al., 2015). For example, LRC specific production of the auxin precursor IBA was found to significantly enhance the amplitude of priming oscillations (Strader and Bartel, 2011, Xuan et al., 2015). To investigate the consistency of the priming mechanism occurring in our model with these observations, simulations with reduced LRC auxin production were performed. Consistent with experimental results, oscillation amplitude was reduced (Fig. 3.1C) while frequency was unaffected (Fig. S3.1C). Importantly, similar reductions in stem cell region auxin production or shoot auxin influx resulted in similar reductions in oscillation amplitude (Fig. 3.1C, S3.1C), indicating that overall auxin availability rather than its location of origin is relevant for oscillation amplitude. Furthermore, when normalizing auxin levels against total root tip auxin content (Fig. 3.1D), we find that amplitude changes can be fully ascribed to changes in overall auxin availability.

3.2.3 Root tip reflux loop can define a TZ/EZ auxin loading domain

While shoot influx and local auxin production control root tip auxin availability, spatio-temporal auxin patterning strongly depends on auxin transport (Grieneisen et al., 2007, Band et al., 2014). Previous experimental research has reported reduced LR production for mutations in PIN2 (Xuan et al., 2016), LAX3 (Swarup et al., 2008, Lewis et al., 2011) and AUX1 (De Smet et al., 2007, Lewis et al., 2011, Xuan et al., 2015). To assess the importance of the root tip auxin reflux loop for the auxin oscillations uncovered in our novel model, simulations with modified PIN and AUX/LAX expression patterns were performed. First, we simulated auxin dynamics in the presence of only vascular localized, rootward oriented PINs, representing a *pin2* null mutant in absence of other PINs taking over upward transport. This resulted in a nearly complete abolishment of auxin oscillations even when normalized against the significantly reduced total root auxin content (Fig. 3.1E, S3.1D). Next, we investigated auxin patterning when PIN2 levels were reduced by 2/3, which caused (normalized) oscillation amplitude to decrease with 33% (Fig. 3.1E, S3.1D). If instead we maintain PIN2 levels yet remove lateral inward oriented PIN2 in the epidermis, oscillations decrease in amplitude and shift shootward (Fig. 3.1E, S3.1D). Finally, we simulated an *aux1* mutant, resulting in a 67% decrease of (normalized) auxin oscillation amplitude (Fig. 3.1E, S3.1D), consistent with earlier observations that absence of AUX1 expression in the LRC strongly reduces oscillation amplitude (De Smet et al., 2007, Xuan et al., 2016). Combined, these results suggest that PIN2 and AUX1 mediated upward transport through the LRC and epidermis, and subsequent inward transport towards the vasculature are essential for auxin oscillations in the vasculature of the TZ and EZ. Noteworthy, the previously proposed LRC apoptosis driven priming mechanism relies on a similar upward and inward auxin transport route (Xuan et al., 2016).

3.2.4 Growth of vasculature and pericycle is a key component of the auxin oscillation model

Previous experimental results demonstrated a strong correlation between periodic LRC apoptosis and oscillatory LR priming (Xuan et al., 2016). To test the causal nature of this correlation in our model, simulations mimicking defects in LRC growth dynamics were performed. Outcomes show that auxin oscillations persist albeit at reduced amplitude both in a simulated *sombrero* (*smb*) mutant (Fig. 3.2A, S3.2A), as well as in complete absence of LRC growth dynamics (Fig. 3.2A, S3.2A). These results suggest that other coordinated growth processes may be responsible for the correlation between LRC apoptosis and auxin oscillations but not LRC shedding itself. To further explore this, we systematically simulated the consequences of growth dynamics in a subset of tissues while not applying growth elsewhere. Growth of vasculature and pericycle tissue was found necessary and sufficient for auxin oscillations, while growth of other tissue layers merely contributes to oscillation amplitude (Fig. 3.2B, S3.2B). To further support our finding that only growth of the to be primed tissues is required we performed simulation in a minimal 1D model with a single row of growing cells with similar SC niche driven growth dynamics as used in the full model. The results show that mild auxin oscillations arise that are augmented when adding an auxin loading zone (Fig. S3.2C).

3.2.5 Growth induced cell size increases can drive auxin loading into vasculature cells

Auxin availability and a functional reflux loop explain how auxin becomes transported upward to the TZ/early EZ, but do not yet explain why vascular and pericycle growth are essential for this process, nor why auxin oscillations predominantly occur in these tissues. Indeed, while the lateral, outward oriented vascular PIN pattern explains the within-vasculature preference for the outermost, protoxylem cell file, it does not explain the preferential loading of auxin in the vasculature per se. Particularly since this loading pattern implies that the auxin transported in the reflux loop passes from the LRC, through epidermis and ground tissue, to the vasculature, and, albeit with somewhat different amplitude and location, still occurs in absence of inward oriented PIN2 in the epidermis, root cap and cortex.

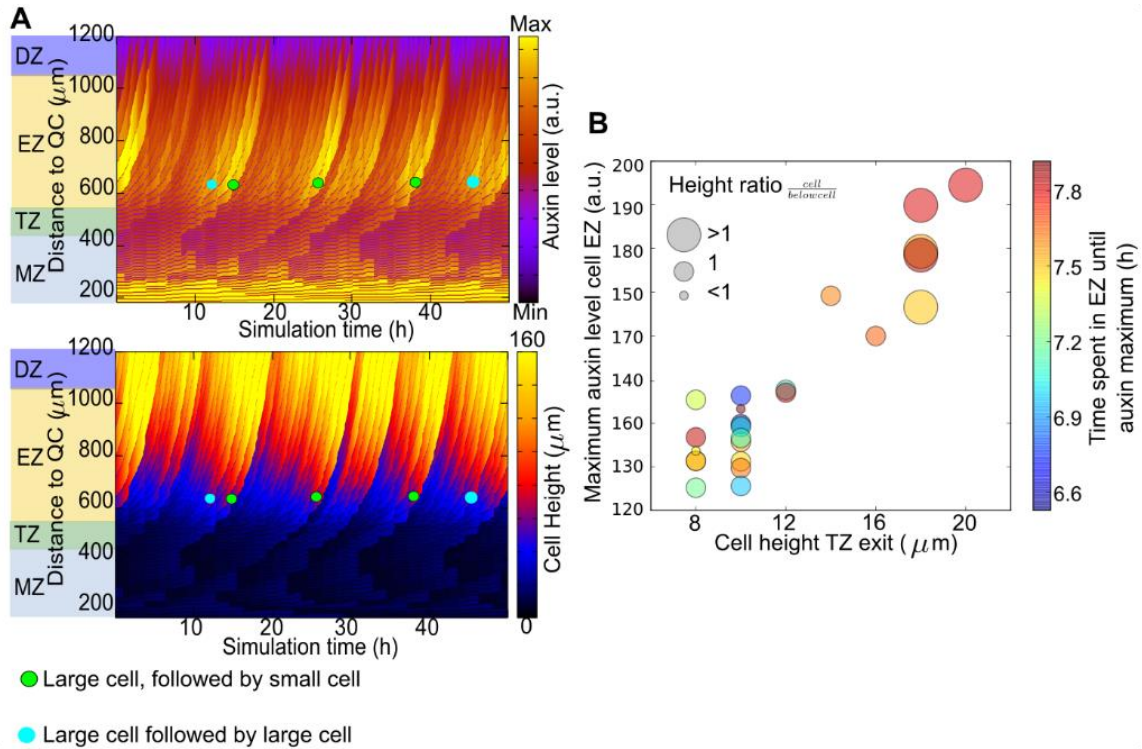


Figure 3.3. Priming arises in abutting large-small cell pairs. A) Kymograph showing auxin (upper) and cell sizes (lower), green dot indicates a large cell followed by a small cell and blue dot a large cell followed by another large cell. B) Maximum auxin levels as a function of cell height upon TZ entrance for simulation shown in A. Cells entering the EZ between 10-30h of simulation time are shown. Colors indicate the time spent in the EZ until the maximal auxin level is reached. Circle size indicates the ratio between the cell's size and that of the cell below it.

We hypothesized that cell growth causes auxin increase through an enhanced auxin influx/efflux ratio: While the typically apolar active and passive auxin import increases with membrane surface area and hence cell size, the predominant polar localization of PIN exporters on non-growing rootward (PIN1) and shootward (PIN2) membranes causes a relative decrease in auxin efflux with increasing cell sizes. Notably, these effects will be more prominent for narrow vasculature cells that undergo the largest increase in surface to volume ratio. Decreasing the width of only vascular tissue in our model further enhances auxin oscillation amplitude (Fig. 3.2C), corroborating this hypothesis. Simulations normalizing either active AUX1 mediated auxin influx, passive membrane-based auxin influx or active PIN mediated auxin efflux with cell height indicate that auxin oscillations are predominantly driven by a size-dependent increase in passive auxin uptake (Fig. 3.2D).

3.2.6 An explanation for progress of priming from vasculature to pericycle

In experiments, priming is initially observed in protoxylem cells, with the signal subsequently being passed on, and in case of successful priming, maintained in pericycle cells (De Smet et al., 2007). In our default settings, priming occurs simultaneously in the protoxylem and neighboring pericycle, with the two tissues experiencing only mildly different maximum auxin levels (Fig. S3.1B). However, in planta, protoxylem, protophloem and metaphloem cells stop dividing closest to the root tip, while neighboring pericycle cells do so considerably further shootward (Lavrekha et al., 2017). These different dynamics will result in large protoxylem cells next to smaller pericycle cells at the start of the TZ. After incorporating these characteristics into our model we observed auxin elevations to first occur in the vasculature, and subsequently being passed on to abutting pericycle cells (Fig. 3.2E, 3.2F), in line with experimental data (De Smet et al., 2007). Notably, the differential onset of cell expansion

enhances vascular oscillation amplitude while reducing that of the pericycle and allows for a partial maintenance of the priming signal (Fig. 3.2E, 3.2F). Thus, our model naturally produces the correct location and order of events in LR priming, as an emergent property of incorporating increasingly realistic root growth dynamics.

3.2.7 Priming occurs in large cells followed by smaller cells

Our results thus far indicate that priming arises from the preferential loading of auxin in large, rapidly expanding vascular cells, but do not yet explain what causes its periodic nature. To decipher the mechanism underlying the periodic nature of the observed auxin oscillations, we first compared kymographs depicting intracellular auxin levels with those showing cell size (Fig. 3.3A). Additionally, we correlated cell size and auxin loading dynamics (Fig. 3.3B). In both kymographs and plot we observe a strong correlation between cell size upon entering the EZ and maximum attained auxin levels, confirming our earlier results on the importance of cell size for auxin uptake. In addition to cell height, we observed a weaker but significant correlation for cellular auxin levels with EZ residence time. This can be understood from the fact that EZ residence time affects loading time as well as the amount of cell size increase occurring inside this loading zone (Methods, Fig. S3.6).

Next, we focused on the periodicity in auxin loading and its predominant relation to cell size. In the kymographs we see that maximum auxin loading occurs in the latest, largest arriving cells of a group of incrementally larger and more auxin loading cells, with this group being terminated by newer, smaller cells arriving (Fig. 3.3A). These smaller cells, which by growing slower cause a slower displacement of shootward cells, enhance the EZ residence time of larger cells, thereby further boosting their size dependent auxin loading (Methods, Fig. 3.3B). As maximum auxin loading thus occurs on the boundary of large and small cells arriving at the EZ, we can effectively trace the temporal dynamics of priming by focusing on the periodic occurrence of directly abutting large-small cell pairs (Fig. 3.3B: >1 ratio for cell height/cell height below cell).

The sequential increase in cell size terminating with a small cell starting of a new sequence observed in our model was previously observed for cortical cells in a detailed root tip tracking study (von Wangenheim et al., 2017). Unfortunately, direct validation of the priming mechanism uncovered here by concurrently measuring detailed cell size and auxin dynamics *in planta* is impossible with current techniques, particularly for the narrow shaped and internally localized vasculature. Similarly, validation through tracing back LR forming sites to earlier, only transiently present, cell size differences or spatio-temporally targeted interference with the formation of large-small cell pairs, or their cell-size dependent auxin loading is technically unfeasible. Therefore, we decided to further unravel how root growth dynamics determines priming characteristics in order to arrive at a series of experimentally testable predictions on the relation between root growth and priming features.

3.2.8 Priming arises from abutting clones in a defined spatiotemporal window

First, simulations were performed varying different components of overall root growth: TA cellular division rate, meristem size (i.e. number of dividing cells), and cellular elongation rate. Results show that both increases in TA division rate (for a given meristem size) and meristem size (for a given TA division rate) enhance priming frequency (Fig. 3.4A, 3.4B, S3.3A, S3.3B, Video S3.2a, Video S3.2b). In contrast, increases in elongation rate enhance priming amplitude (Fig. 3.4C, Video S3.2c) but not frequency (Fig. 3.4D). Thus, overall meristem cell production, determined by both division frequency and meristem size, dictates priming frequency.

Next we set out to unravel how meristem cell production determines priming dynamics, i.e. the periodic formation of large-small cell pairs. For this we need to consider that plant root growth is directionally organized, with rootward oriented, slowly dividing stem cells generating transit amplifying (TA) daughter cells that enter the meristem (Bizet et al., 2015, Lavrekha et al., 2017, Rahni and Birnbaum, 2019). These TA cells undergo multiple rounds of rapid, approximately synchronized divisions, forming an expanding clone of sibling cells (von Wangenheim et al., 2017, Rahni and Birnbaum, 2019). Due to the formation of newer, out-of-phase, clones, older clones move shootward relative to the QC, out of the meristem.

Formation of a large-small cell pair requires that for two abutting, out-of-phase clones the rootward clone divides once more after the last division of the top clone. The chances at any given meristem location for two such abutting clones to occur depend on clone density. As a measure for the number of clones fitting in the meristem, we take the number of divisions a cell can undergo before leaving the meristem, given by $\log_2(\text{meristem size})$ (Beemster and Baskin, 1998) (Fig. 3.5A). Thus, clone density scales with $\log_2(\text{meristem size})/\text{meristem size}$, indicating that as MZ size increases, clone density decreases and clone size increases (Fig. 3.5B).

Additionally, to produce a large-small cell pair at the TZ, the final division in the top clone has to occur sufficiently early for it to have time to grow large, yet not so early that it undergoes another division and becomes small again. Thus this final division should occur in a *limited spatial window*, defined by the position cells occupy when at a distance of $1-(1-\alpha)$ cell cycle from the TZ, with α sufficiently small. Indeed, tracing back primed cells to the position of their final divisions reveals a restricted spatial window, with a value for α of 0.25 (Fig. 3.5C). Larger meristems result in a faster cumulative displacement of cells, translating this temporal window into a spatial window (in number of cells) that increases linearly with meristem size (Fig. 3.5D) (see Methods).

Given that per meristem position the chances for two out-of-phase clones scales with $\log_2(\text{meristem size})/\text{meristem size}$, and priming requires the top clone to divide within a spatial window which size scales with meristem size, priming frequency should scale with $\log_2(\text{meristem size})$, consistent with our simulations showing a sublinear increase with meristem size (Fig. 3.4B, 3.5D). However, this only takes into account the chance for two abutting clones to occur at a position at which this could potentially lead to formation of a large-small cell pair. For this to actually occur, the topmost clone should divide at this position, which occurrence scales with TA division frequency (Fig. 3.4A, 3.5E). Overall priming frequency thus depends on the product of division rate with $\log_2(\text{meristem size})$.

By definition, the spacing between primed sites (PS) is equal to the number of cells passing by in between priming events, and hence equals cell production divided by priming frequency. A sub-linear dependence of priming frequency on meristem size (Fig. 3.4B), implies that as meristem size (and hence production) increases, PS spacing should increase as well. Indeed, in our simulations we see a strong positive correlation between PS spacing and meristem size (Fig. 3.6A). On the contrary, since increases in division frequency almost fully translate to increases in priming rate (Fig. 3.4A) (Methods), we expect no significant correlation between PS spacing and division rate, Indeed simulations confirm that this correlation was not significant (Fig. 3.6B).

Summarizing, our model predicts a positive correlation between priming frequency and meristem size as well as division rate (Fig. 3.4A, 3.4B), and between PS spacing and meristem size (Fig. 3.6A). To more compactly represent our findings we translate these predictions into a positive correlation

between priming frequency and spacing with cell production (product of meristem size and cell division rate) (Fig. 3.6C, 3.6D). Additional advantage of this compression is that we can now display all data points combined, rather than using only a subset of datapoints with similar meristem size when plotting priming as a function of division rate, or vice versa (i.e., Fig. 3.4A, 3.4B).

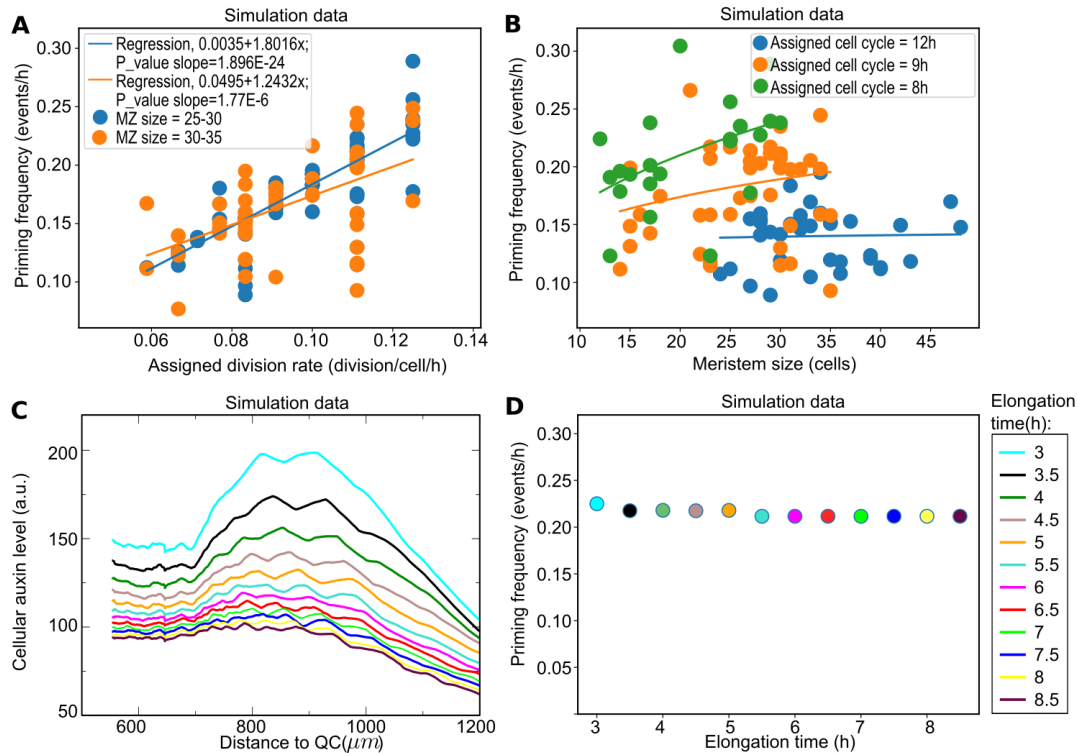


Figure 3.4 Priming frequency and amplitude as a function of growth parameters. A) Simulation data of priming frequency as a function of TA division rate for meristem sizes between 25-30 or 30-35 cells. Per meristem range and TA division rate, SC division rates were varied between 0.2-0.67 times TA division rate. Data were fitted using linear regression. B) Simulation data of priming frequency as a function of meristem size, for cell cycles of 12h, 9h or 8h (corresponding to division rates of 0.083, 0.11 and 0.125, respectively). SC division rates were varied as in A. Data were fitted to a power-law distribution. C) Simulation data of priming amplitude as a function of elongation time. D) Simulation data of priming frequency as a function of elongation time for the same simulations as shown in C. See legend next to panel D for the elongation time corresponding to the different line colors. See also Figure S3.3.

3.2.9 Validation of the reflux-and-growth priming mechanism

Our reflux-and-growth model thus predicts a positive relationship between both priming frequency and spacing and cell production (Fig 6E and 6F, green lines). As a next validation step, we compared these predictions against those of alternative models, and investigate which model predictions are supported best by the experimental data. A first alternative model is the clock-and-wavefront model (Moreno-Risueno et al., 2010), generally accepted to underlie the segmentation of the vertebrate body axis into somites (Conlon et al., 1995, Palmeirim et al., 1997, Jiang et al., 2000, Dubrulle et al., 2001, Baker et al., 2006). Following to the clock-and-wavefront paradigm, oscillation frequency (and thus presumably priming frequency and LR production rate) depends on the frequency of the cell-autonomous clock, generated by a delayed negative feedback motif, and would be independent of meristematic cell production (Fig. 3.6E, black line). In contrast, wavelength (i.e. PS spacing) depends on the amount of growth in between clock periods and would hence scale with production (Fig. 3.6F, black line).

Another theoretically possible mechanism that has been proposed for LR priming is the Turing mechanism (Turing, 1952, Laskowski and Ten Tusscher, 2017). In a polarly growing tissue such as the root, the continuous increase of tissue size would result in the periodic production of new peaks each time tissue size has increased with the wavelength of the Turing pattern. This causes LR production rate to linearly depend on growth rate and hence cell production (Fig. 3.6E, red line). The wavelength itself depends on the interaction and transport parameters together giving rise to the Turing pattern, and are independent of cell production (Fig. 3.6F, red line).

To investigate whether *in planta* priming dynamics support the reflux-and-growth priming mechanism uncovered here we set up experiments aimed at inducing a range of different meristem cell production rates and resulting priming dynamics. To this end, we compared plants grown under control conditions with plants treated with the growth hormones, gibberellic acid (GA), and two different levels of brassinosteroids (BR), to induce variation in relevant growth parameters and thereby priming (Ubeda-Tomas et al., 2008, Gonzalez-Garcia et al., 2011). Importantly, while these hormonal treatments through cross-talk may interfere with auxin levels and/or signaling, both our model and experimental data (Xuan et al., 2016, Perianez-Rodriguez et al., 2021) indicate that this only directly affects oscillation amplitude, not frequency. This enables us to focus on the direct and indirect effects of these hormone treatments on meristem growth dynamics and its relation with priming dynamics.

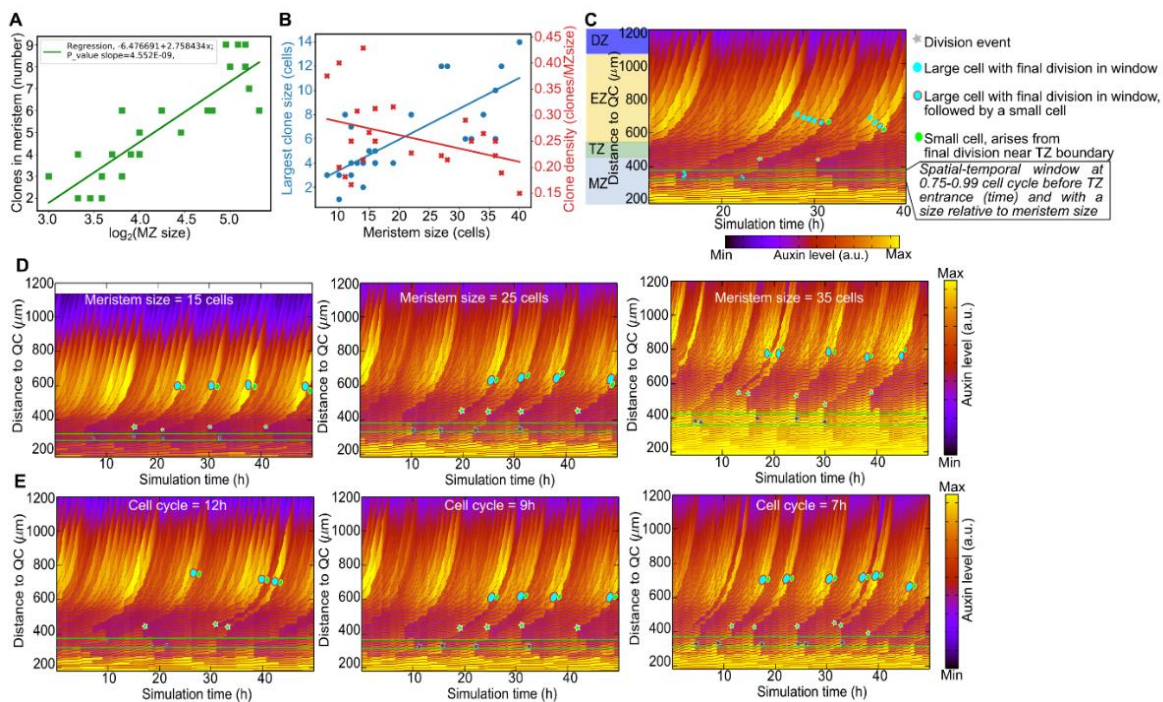


Figure 3.5. Priming arises from asynchronous clones with final divisions in a limited spatio-temporal window. A) Clone number as a function of \log_2 (MZ size). Data were fitted using linear regression. B) Clone size (blue) and density (red) as a function of MZ size. Data were fitted using linear regression. C) Zoomed in kymograph showing that cells with a final division in the indicated spatial window arrive large in TZ, and when followed by a small, recently divided cell obtain highest auxin levels. Window is indicated as area between horizontal green lines. D) Size of window in which final divisions lead to priming for incrementally increasing MZ sizes, from left to right 15, 25 and 35 cells in MZ. Cyan cells indicate cells divided in window followed by a recently divided cell (indicated green). E) Number of divisions within window that lead to priming for incrementally increasing TA division rates, from left to right 0.08 div/cell/h (cell cycle = 12h), 0.11 div/cell/h (cell cycle = 9h) and 0.14 div/cell/h (cell cycle = 7h).

To achieve this we designed an experimental set-up following priming zone auxin oscillations in time through recording activity of a DR5::LUC transgene (Moreno-Risueno et al., 2010), while growth parameters were tracked in parallel. Overall, sizes of actively dividing meristems range from ~12 to ~48 cortical cells (~4 fold range) (Fig. 3.6G, S3.4A), cell production rates from 1.23 to 3.2 (~2.5 fold range) (Fig. 3.6G, S3.4B), priming frequency from 0.2 to 0.87 events per hour (~4.5 fold range) (Fig. 3.6H, S3.4C) and priming site spacing from 1 to 8 cells (~8 fold range) (Fig. 3.6H, S3.4D). Thus, significant variations in growth parameters as well as priming characteristics were successfully generated using the selected treatments.

Our experimental perturbation data show a significant positive correlation between both priming frequency and PS spacing with cell production (Fig. 3.7A, 3.7B, S3.5A, S3.5B), as well as similar relations between frequency and spacing with meristem size and division frequency (Fig. S3.5C, S3.5D, S3.5E, S3.5F). This enables us to falsify both Turing based and clock-and-wave front driven priming mechanisms and support the newly discovered reflux-and-growth priming mechanism.

3.2.10 Distinct vascular division dynamics significantly contribute to priming frequency

Interestingly, despite our model simulations covering active meristem sizes and division rates over a range similar to those measured experimentally, priming frequencies and PS spacing distances observed in our model differ approximately ~4 fold from those experimentally measured (compare Fig. 3.6C and 3.6D with, 3.7A and 3.7B). Given that the model does correctly simulate correlations between priming frequency, PS spacing and meristem cell production, we reasoned that while the priming mechanism found in our model is correct, some quantitative aspect must differ from the *in planta* situation.

Additionally to the aforementioned early onset of differentiation in the protoxylem relative to the pericycle (Lavrekha et al., 2017), two recent studies measuring *Arabidopsis* root cell division dynamics found that transit amplifying division frequencies in stele cells are approximately 1.5 times higher as compared to cortical cells (Lavrekha et al., 2017, Rahni and Birnbaum, 2019). This implies that our measured cortical cell production and division rates significantly underestimate the rate of vascular divisions driving priming dynamics. Additionally, one of these studies reported that while cellular division rates were higher, the frequency of division events within the stele was lower and cell length larger, indicating fewer, larger cells (Lavrekha et al., 2017). Incorporating these three vasculature specific features into our model resulted in a substantial increase in priming frequency and decrease in PS spacing (Fig. 3.7C, 3.7D, red versus green data), maintaining the previously found relationships while significantly improving the quantitative agreement between model and experimental data (Fig. S3.5G and S3.5H).

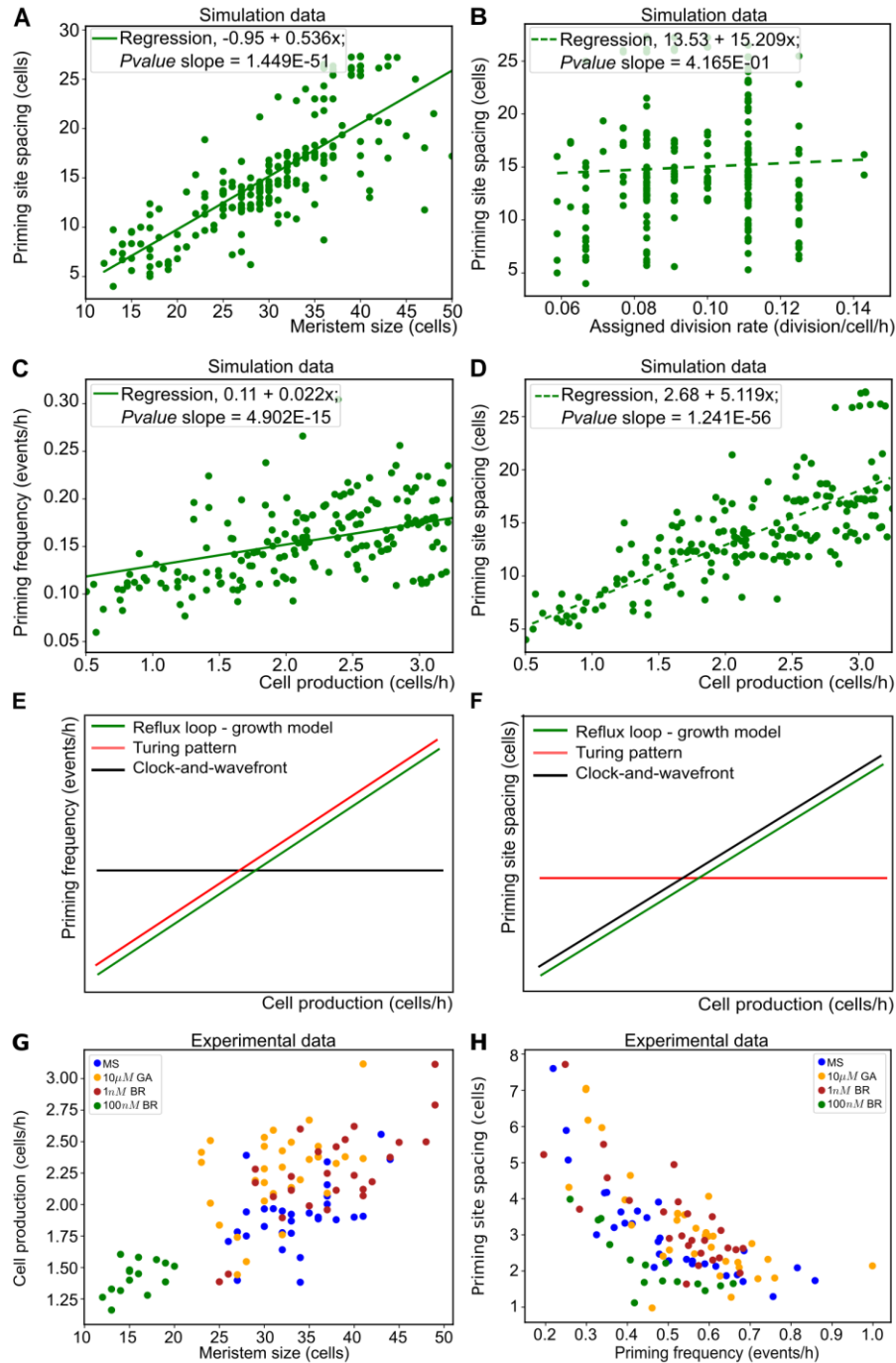


Figure 3.6. PS spacing and frequency as a function of division rate and MZ size. A) Simulation data for priming site spacing as a function of MZ size. Data were fitted using linear regression. B) Simulation data for PS spacing as a function of division frequency. Data were fitted using linear regression was performed. C) Simulation data for priming frequency as a function of cell production for simulations with varying meristem size and division frequency. Data were fitted using linear. D) Simulation data for priming site spacing as a function of cell production for simulations with varying meristem size and division frequency. Data were fitted using linear regression. E) Predicted relationship for priming frequency with cell production for reflux-and-growth, Turing pattern and clock-and-wavefront models. F) Predicted relationship for PS spacing with cell production for reflux-and-growth, Turing pattern and clock-and-wavefront models. G) Experimentally measured cell production as a function of meristem size. Data points from both control and 3 different hormone treatments are shown, with color indicating the treatment. H) Experimentally measured priming frequency as a function of priming site spacing, from the same experiments as shown in G. To measure priming dynamics, plants carrying a DR5:LUC construct were used. See also Figure S3.4.

3.2.11 Actual LR frequency and PS spacing scale in similar manner with cell production

For plant fitness, it is not the frequency and spacing of priming events, but the actual formation and spacing of LRs that is relevant. A major question thus is to which extent our model is capable of explaining LR patterning. To establish this, an additional series of experiments was performed, using similar perturbations as before, but now counting the numbers of and distances between LRs as well as LR primordia, using the early-expressed LR specific PLT3 reporter (Du and Scheres, 2017). Figure 7E and 7F shows that a similar positive correlation between LR formation frequency and LR spacing and cell production was found as for PS frequency and spacing. Thus, with our unravelling of the mechanisms underlying LR priming, also meaningful predictions for actual LR patterning can be made.

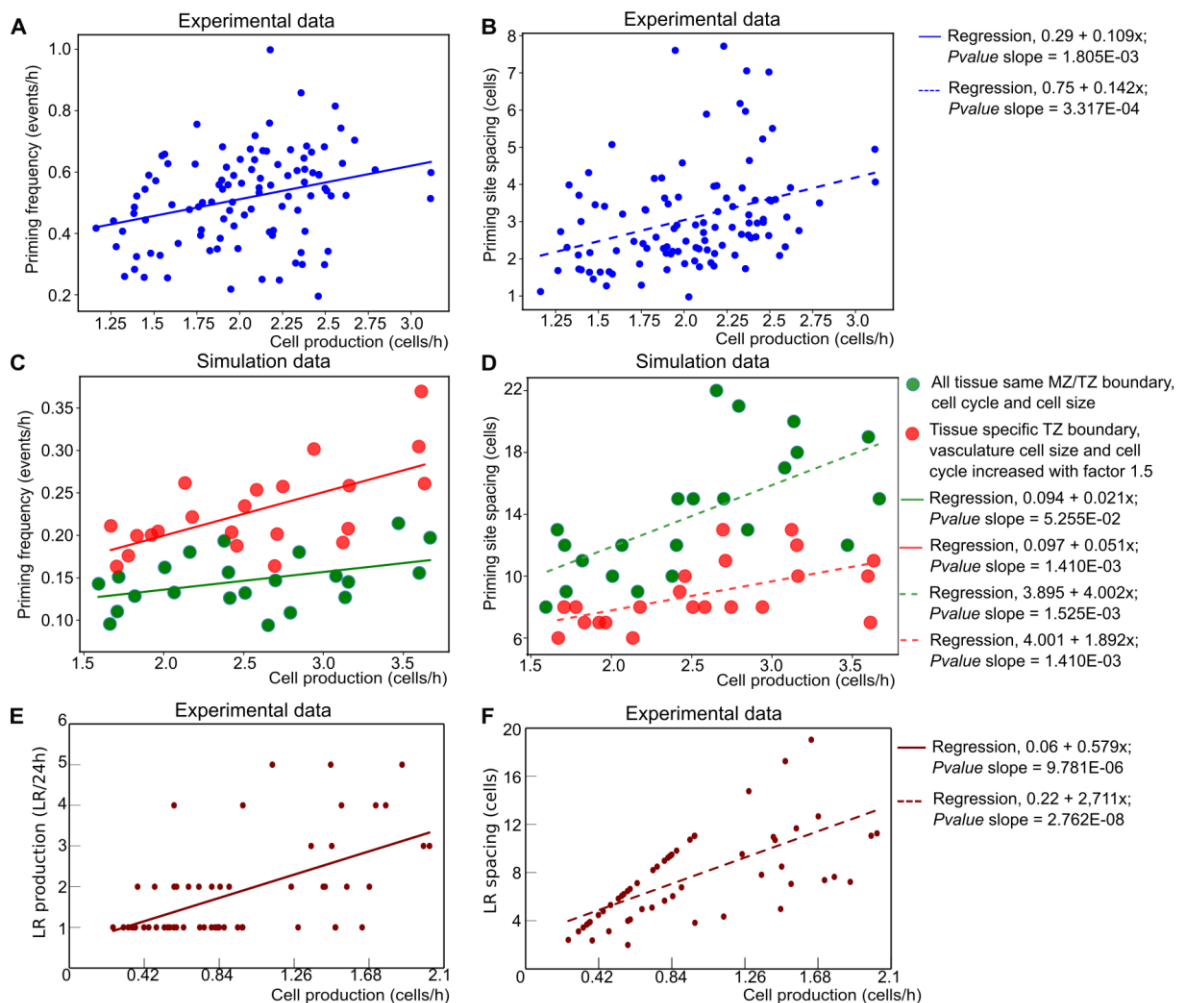


Figure 3.7. Priming frequency and PS spacing as a function of cell production. A, B) Experimentally measured priming frequency (A) and PS spacing (B) as a function of cell production. Data points from both the control and the three different hormone treatments are shown, now without using different colors to differentiate treatments. To measure priming dynamics, plants carrying a *DR5::LUC* construct were used. C, D) Priming frequency (C) and PS spacing (D) as a function of cell production in simulations incorporating cell type specific zonation, increased vascular division rate and cell height. E, F) Number of LRs per day (E) and LR spacing (F) as a function of cell production. Data points from both the control and the three different hormone treatments are shown. To measure LR formation dynamics, plants carrying a *PLT3::GUS* construct were used. Data in A-F were fitted using linear regression. See also Figure S3.5.

3.3 Discussion

At first glance, the root system of a plant does not necessarily appear highly regular (Gruber et al., 2013), yet the initial step of LR formation, LR priming, has been shown to have a repetitive nature. During LR priming, periodic oscillations in the plant hormone auxin and its downstream effects prepattern subsets of pericycle cells to become competent for future LR formation (De Smet et al., 2007, Moreno-Risueno et al., 2010, Xuan et al., 2015, Xuan et al., 2016). Later stages of lateral root formation have successfully been unraveled. As an example the transition from 2 primed protoxylem sites to a single sided stable founder cell has been shown to arise from a competition for auxin (signaling) (el-Showk et al., 2015) that can be biased by environmental factors such as water availability promoting auxin signaling intensity (Orosa-Puente et al., 2018). Thus far, the mechanistic basis of lateral root priming has remained unclear.

In this study we aimed to uncover the mechanism underlying LR priming. Inspired by the reported importance of auxin transport as well as the strong correlation with root cap apoptosis, root growth and cell wall remodeling (Jensen et al., 1998, Xuan et al., 2016, Wachsman et al., 2020) we hypothesized that priming arises from an interplay between root tip auxin transport and growth dynamics. To test this idea, we developed a novel multi-scale root growth model enabling us to simultaneously track auxin and auxin signaling dynamics at the single cell, tissue and whole root organ level, while independently varying different aspects of auxin and growth dynamics. Analyzing our novel growth model, we uncovered that the root tip auxin reflux loop creates an auxin loading domain at the start of the EZ. Additionally, we elucidated how their narrow shape and early onset of elongation provides vasculature cells with the highest auxin loading potential, causing preferential auxin accumulation in these cells. Next we showed how priming occurs in the final, largest cell of a series of increasingly large vasculature cells, and is followed by a significantly smaller cell. We then went on to demonstrate how the typical root tip growth dynamics results in the periodic production of large-small cell pairs. Specifically, we elucidate how stem cell driven growth dynamics results in the sequential production of out-of-phase clones of sibling cells, and hence out-of-phase dividing neighboring cells. Combined we thus uncovered a novel reflux-and-growth mechanism for periodic LR priming. To link this model to experiments, we derived predictions stating that both cell division rate and meristem size, and hence meristem cell production rate determines priming frequency as well as PS spacing.

To validate these model predictions, we measured spatio-temporal dynamics of priming site and LR formation using perturbations that allowed us to extract information on the influence of individual model parameters by deconvolution of effects. In agreement with our model predictions but not with those of competing models, we observed a significant positive correlation of both priming frequency and spacing with meristem cell production rate. Our results thus present a novel framework explaining the periodic nature of LR priming in dicot plant roots that highlights the role of cell size differences in auxin-based patterning. As such it bears resemblance to an earlier study demonstrating how lateral root bending, through enlarging cells at the outer curve of the bend, could induce lateral root formation (Laskowski et al., 2008).

As a further support of the mechanism we propose here, agreement between model outcomes and experimental data further increased when incorporating additional biological detail into our model. When accounting for the differences in distance relative to the QC from where cells stop dividing (Lavrekha et al., 2017), our model automatically reproduces the start of priming in the protoxylem file (De Smet et al., 2007), and the subsequent transmission of the signal to the pericycle, where founder

cell formation occurs (Dubrovsky et al., 2006). On a similar note, incorporating the experimentally observed larger size and higher division frequency of vascular cells (Lavrekha et al., 2017, Rahni and Birnbaum, 2019) significantly improved quantitative agreement between model and data. Additionally, the predicted periodic pattern of gradually increasing sizes of cells arriving at the transition zone with the final largest cell followed by the first smallest cell of a new sequence has been measured for cortical cells in a detailed root tip tracking study (von Wangenheim et al., 2017).

Compared to prebranch site spacing actual root system architecture is often considerably less regular (Gruber et al., 2013). Stochasticity (Laskowski, 2013), root curvature (Kircher and Schopfer, 2016, Richter et al., 2009), environmental conditions (Bao et al., 2014, Gruber et al., 2013), and competition between neighboring primed sites (Bielach et al., 2012, Hofhuis et al., 2013, Toyokura et al., 2019) all mold prebranch site patterns into actual root system architecture.

Indeed, we observed ~4 fold lower LR numbers and ~4 fold increase in LR spacing as compared to priming site numbers and spacing (Fig. 3.7A, B and Fig. 3.7E, F). Although differences may partly arise from data being obtained in separate experiments under slightly different conditions, the size of the difference suggests many priming events do not result in LR formation. While earlier studies reported a near 100% translation from priming events to LR formation (Xuan et al., 2015, Xuan et al., 2016), much lower success rates were reported in experiments using a similar intermittent light regime and no additional sucrose as we applied here (Kircher and Schopfer, 2018). Combined, this underlines the extensive reserve potential and plasticity in root architecture development under more natural growth conditions. Nevertheless, our in planta experiments demonstrate that for actual formed LRs a similar dependence of frequency and spacing on meristem growth rate exists as was found for prebranch sites. Thus, at least for idealized experimental conditions, qualitative spatio-temporal characteristics of priming and prebranch site patterning translate into those for LRs.

In addition to the predictions of our model being borne out by our experimental correlations, the priming mechanism uncovered here agrees with a large range of experimental data. We demonstrated how reduction of LRC auxin production (Xuan et al., 2015), and mutations in auxin transporters (De Smet et al., 2007, Swarup et al., 2008, Lewis et al., 2011, Xuan et al., 2015, Xuan et al., 2016) significantly reduce oscillation amplitude, explaining the reduced observed prebranch site numbers from a decreased chance for priming to lead to prebranch site formation. Also, the predicted importance of cell elongation for oscillation amplitude (Fig. 3.4C, 3.4D) is supported by recent experimental findings reporting reduced LR formation for roots with shorter elongated cells (Alarcon et al., 2019), or reduced potential for cell wall modification (Wachsman et al., 2020). Additionally, the central role of growth uncovered here explains why in absence of light and hence growth, no LR formation takes place (Jensen et al., 1998). The observed relationship between LR formation and cell production is furthermore supported by studies varying nutrient levels, where a decrease in main root size (and hence cell production) translated to reduced LR numbers and a higher LR density (Pérez-Torres et al., 2008, Gruber et al., 2013). Our findings furthermore suggest that the previously found correlation between LRC apoptosis and priming may arise from the coordination between root cap apoptosis and meristem growth dynamics, consistent with a recent study demonstrating this coordination (Shi et al., 2018) and the observed persistence of priming in the apoptosis defective *smb* mutant (Xuan et al., 2016). Finally, findings indicating that mutations in pericycle specific cell cycle regulators affect the frequency of LR formation corroborate the importance of cell growth and division dynamics in determining LR formation (Nieuwland et al., 2009).

Lateral roots are an important determinant of both dicot taproot and monocot fibrous root architectures, Available data indicate a common pericycle origin of these lateral roots, while depending on the species also cortical and endodermal cell layers may contribute to lateral root formation(Xiao et al., 2019). Intriguingly, depending on the species the auxin maxima preceding lateral root formation may form at either the protoxylem (e.g. Arabidopsis) or protophloem (e.g. maize) vascular pole (Jansen et al., 2012), possibly as a result of differently oriented radial auxin transport. In either case formation of the auxin maxima critically depends on auxin transport, and vascular priming signals are transmitted to the pericycle. Combined with the fact that the priming mechanism uncovered here depends on the basics of stem cell driven root growth, that is shared between all higher, true roots containing plants, this suggests that while radial patterning may be species specific, oscillatory longitudinal auxin patterning is likely largely conserved. Indeed, our model results indicate that changes in root tip size, shape and number or number of cortical layers do not change priming dynamics (Fig. S3.6I).

In summary, our work presents evidence that LR priming is driven by a non-canonical mechanism for periodic pattern formation that is distinguishable from other known periodic patterning mechanism such as a clock-and-wavefront model or a Turing pattern.

3.3.1 Limitations of this study

A limitation of the current study is that the lateral root priming mechanism we uncovered *in silico* could not be experimentally validated in a direct manner and instead required a more indirect validation of model predictions. Direct validation of the priming mechanism through perturbation would require interfering with either the dynamic formation of periodic cell size differences or with the cell size dependence of auxin uptake. It is to our knowledge currently not feasible to perturb the relationships between time available for growth and attained cell size, or of cell surface area with passive uptake capacity *in planta* in a targeted, systematic manner (note that we did perform these experiments *in silico*, confirming our hypothesis (Methods, Fig. S3.6)). An alternative direct validation of the priming mechanism by measuring a correlation between the periodic formation of large-small cell pairs in the early EZ and auxin oscillations or subsequent lateral root formation would require the dynamic monitoring of transient cell size differences either simultaneous with auxin dynamics or combined with tracing these to lateral root development. Again, there are technical limitations on dynamic measurements of vascular cell sizes due to the narrow shape and internal tissue localization of the vasculature.

Acknowledgments

We thank Joop Vermeer for financial support of K.Y. Rutger Hermsen for advice on statistical analysis and Jan Kees van Amerongen for management of computational facilities. TvdB and KtT were funded by grant nr 864.14.003 of the Dutch Organization for Scientific Research (Nederlandse Organisatie voor Wetenschappelijk Onderzoek, NWO), H.G and T.B by a grant G022516N of The Research Foundation - Flanders (FWO), J.S.T was funded by grant nr 737.016.012 of NWO, K.Y is funded by VIDI grant nr 864.13.008 of NWO.

3.4 STAR METHODS

KEY RESOURCES TABLE

REAGENT or RESOURCE	SOURCE	IDENTIFIER
Chemicals, Peptides, and Recombinant Proteins		
SCRI Renaissance 2200 (SR2200)	Renaissance Chemicals	N/A
D-Luciferin	Duchefa Biochemie	Cat# L1349
Gibberellic acid A3	Duchefa Biochemie	Cat# G0907
24-Epibrassinolide	Duchefa Biochemie	Cat # E0940
Murashige & Skoog basal salts Medium	Duchefa Biochemie	Cat# M0222
Plant-agar	Duchefa Biochemie	Cat# P1001
MES Monohydrate	Duchefa Biochemie	Cat# M1503
Na ₂ HPO ₄ ·2H ₂ O	Merck	Cat# 106580
NaH ₂ PO ₄ ·H ₂ O	Merck	Cat# 106346
K ₃ Fe(CN) ₆	Merck	Cat# 104973
K ₄ Fe(CN) ₆ ·3H ₂ O	Merck	Cat# 104984
Triton X100	Sigma-Aldrich	Cat# 9002-93-1
X-GlcA Cyclohexylammonium Salt	Duchefa Biochemie	Cat# X1405
N-dimethyl-formamide	Sigma-Aldrich	Cat# D4551
Dimethyl sulfoxide	Sigma-Aldrich	Cat# D5879
TWEEN® 80	Sigma-Aldrich	Cat# P5188
Experimental Models: Organisms/Strains		
<i>Arabidopsis: pPLT3::GUS</i>	Du and Scheres, 2017	N/A
<i>Arabidopsis: DR5::Luciferase</i>	Moreno-Risueno et al., 2010	N/A
Software and Algorithms		
Fiji	https://fiji.sc/	RRID:SCR_002285
Cell-o-Tape	https://www.nottingham.ac.uk/research/groups/cvl/software/cellotape.aspx	N/A
KymoResliceWide	https://github.com/ekatrucha/KymoResliceWide	N/A
Growing root model	http://bioinformatics.bio.uu.nl/khwjtuss/PrimingRoot	N/A
Other		
Nunc™ Cell-Culture Treated Multidishes	Thermo Scientific	Cat# 167063

3.4.1 RESOURCE AVAILABILITY

Lead Contact

Further information and requests for resources and reagents should be directed to and will be fulfilled by the Lead Contact, Kirsten ten Tusscher (k.h.w.j.tentusscher@uu.nl).

Materials Availability

This study did not generate new unique reagents or materials

Data and Code Availability

The code and datasets generated during this study are available at [<http://bioinformatics.bio.uu.nl/khwjtuss/PrimingRoot>].

3.4.2 EXPERIMENTAL MODEL AND SUBJECT DETAILS

Plant material

Arabidopsis thaliana accession Col-0 was used in this work. The transgenic *Arabidopsis thaliana* lines used were described previously: pPLT3::GUS (Du and Scheres, 2017) and DR5::LUC (Moreno-Risueno et al., 2010, Xuan et al., 2016). Seeds were surface sterilized with gaseous chlorine produced in a sealed container with 80ml bleach supplemented with 3ml of 37% hydrochloric acid for 2 hours. Seeds were sown on growth medium consisting of half-strength Murashige Skoog salts (½ MS) with 1 - 1.5% agar for lateral root number assay and luciferase assay respectively. Seeds were then stratified at 4°C for 2 days in the dark and transferred to growth chamber at 22°C for germination under long day conditions (16 h light/8 h dark photoperiod) in oriented Petri dishes (15 degree to vertical plane).

3.4.3. METHOD DETAILS

3.4.3.1 Experimental methods

Hormone Treatments

Seeds were sterilized, plated and seedlings were grown as described in the plant material subsection. The seedlings were transferred with tweezers onto solid ½ MS medium plates containing Gibberellic acid (GA) at a final concentration of 10µM or Brassinosteroid (24-Epibrassinolide) (BR) at a final concentration of 1nM or 100nM. As control the seedlings were transferred to ½ MS medium without any supplements. For the lateral root number assay the total duration of the hormonal treatment was 6 days. Quantification of lateral roots was performed over a 4 day period, starting 2 days after transfer to the treatment plates to avoid measuring initial, transfer induced stress response rather than hormonal responses. For the luciferase assay the hormonal treatment period was 66 hours, Luciferase imaging of the root began 48 hours after transfer to the treatment plates (more details can be found in the respective sections below).

Histology and Microscopy

Histochemical staining of promoter-driven β-glucuronidase (GUS) activity was performed as described previously (Willemsen et al., 1998) with modifications. In brief, a strip of filter paper soaked in GUS staining solution (0.5 mg/ml X-gluc dissolved in n-dimethyl-formamide, 0.1% Triton X-100, 0.5 mM K₄Fe(CN)₆·H₂O, 0.5 mM K₃Fe(CN)₆, and 50 mM sodium phosphate buffer, pH 7.2) was placed on the root section of interest and incubated at 37°C in the dark for 2 hours. Stained primordia were counted under a Carl Zeiss Stemi SV6 Stereomicroscope. For meristem and cortical cell size

analysis, roots were stained and fixed in SCRI Renaissance 2200 Staining Solution (0.1% (v/v) SR2200, 1% (v/v) DMSO, 0.05% (w/v) Triton X-100, 5% (w/v) glycerol, 4% (w/v) para-formaldehyde in PBS buffer (pH 8.0) and stored at 4°C before imaging as described previously (Kerstens et al., 2020). Images were acquired using a Zeiss LSM 710 confocal laser scanning microscope with 40X objective with laser lines and setting as described previously (Kerstens et al., 2020). Images were analyzed with Fiji (Schindelin et al., 2012).

Lateral root number assay

PLT3::GUS seedlings grown on ½ MS plates for 5 days were transferred onto respective treatment/control plates. 2 days after transfer, the root tips of the seedlings were labelled and the plates were scanned using Epson Expression 11000XL every 24hrs for 4 consecutive days. Displacement of root tips indicated by consecutive marks was used to determine root growth per day. At the end of the treatment period, the number of lateral root primordia/ emerged lateral roots formed per day were quantified by counting the GUS stained primordia in each labelled section.

Luciferase assay

DR5::LUC seeds were plated on ½ MS medium and grown for 5 days before transferring onto compartmented plates (Nunc™ Thermo Scientific™) containing two hormonal treatments randomly selected from a paired design. The next day, we sprayed the seedlings with a 1 mM D-Luciferin solution (dissolved in 0.01% Tween80, 0.1% DMSO) in order to reveal their DR5::LUC expression. 24 hours after spraying in vivo luminescence signal was monitored for 18 hours using the Nightshade LB 985 (Berthold) system adapted for live-imaging of vertically growing Arabidopsis seedlings by (Xuan et al., 2018).

Similar to an approach previously followed by Kircher and Schopfer, we measured in vivo DR5:LUC luminescence in plants exposed to intermittent periods of darkness (allowing luminescence recording) and light (simulating normal growth chamber conditions)(Kircher and Schopfer, 2018). Specifically, for a period of 18h we applied 22 min cycles in which plants were exposed to 14 min light, and to 8 min of darkness, recording DR5::LUC expression for the final 3 min of darkness, DR5::LUC expression was recorded using an integrated charge-coupled device (CCD) camera, acquired the emitted signal with a 5 minutes exposure time and a 2x2 binning resolution. During the 14 minutes of light exposure, we simulated the growth chamber light intensity using the Nightshade LED panels. After imaging roots were stained and fixed in SR2200 Staining Solution to perform analysis on primary root meristem.

Kymograph analysis

Stack images from microscopy analysis were analyzed by making a kymograph using the KymoResliceWide plugin for FiJi (<https://github.com/ekatrakha/KymoResliceWide>). A line matching the width of an individual root was drawn on the root in the last time frame of the movie, the plugin was used with ‘average’ settings to avoid temporal differences in the stacks to influence the outcome of the analysis. A space scale was added while processing the kymograph (Figure S3.6A).

ImageJ/Fiji cannot handle different scales in x and y direction therefor only a space scale was added, while a time scale was manually added based on the duration of the experimental recording. Brightness and contrast was adjusted per individual root to allow visual identification of priming events. Since no

conclusions are drawn from or analysis is based on priming amplitudes, adjusting settings per individual root did not affect our analysis of priming frequency and spacing.

Kymograph analysis, root growth

To measure root growth rate over the 18h period of the recording a line was drawn perpendicular to the position of the root tip at the end of recording (Figure.S3.6B, red line). Subsequently, a straight line was drawn from this first line to the position the root tip occupied at the start of the recording (Figure.S3.6B, cyan line), with the total size of this line representing overall root tip displacement and hence overall root growth. Dividing this root growth over the time of the recording results in a root growth rate. Root growth rate measurements were afterwards divided over the average adult (expanded) cell size of the respective root to obtain root growth rate expressed in cell numbers/h.

Kymograph analysis, priming site spacing

To determine priming site spacing a line was drawn corresponding to the position of the t=18h time frame (Figure S3.6C, yellow dotted line), using a line width of 3 pixels to enhance resolution. Start and end position of this line are determined by the position of the TZ/EZ border (location where priming occurs, recognizable as the second diagonal line from the left in the kymograph) at the start (Figure S3.6C, red line) and end of the recording period. We have thus defined, for a particular time point, a spatial domain in which we can determine the spacing of priming events.

To determine spacing, we plot DR5:LUC intensity along the defined spatial domain (Figure S3.6D). To measure actual priming site spacing rather than pre-branch site spacing priming events that do not result in maintained high pixel intensity but instead fade out were artificially enhanced with a white line to allow measurement at the t=18h position in the kymograph (Figure S3.6D).

An intensity plot over space was obtained and was used to determine the priming site spacing (Figure S3.6E). Priming site spacing (PSS) per root was calculated in the following way:

$$\text{PSS (mm)} = (\text{peak}_{\text{last(mm)}} - \text{peak}_{\text{first(mm)}} - \text{peaks}_{\text{num}} * \text{size}_{\text{cell}}) / (\text{peaks}_{\text{num}} - 1)$$

Where $\text{peak}_{\text{last(h)}}$ and $\text{peak}_{\text{first(h)}}$ are the positions in space of the last and first DR5:LUC intensity peak respectively, $\text{peaks}_{\text{num}}$ are the number of peaks counted and $\text{size}_{\text{cell}}$ refers to the average adult cell size of the respective root. The $-\text{peaks}_{\text{num}} * \text{size}_{\text{cell}}$ serves to subtract from the total distance between first and last priming event the space occupied by priming events themselves, thus restricting inter priming distance calculation to in between non-primed cells. The above formula calculates the PSS in mm, by dividing this distance afterwards over adult cell size of the corresponding root we compute PSS in cell numbers.

Kymograph analysis, priming frequency

To independently determine priming frequency we need to determine the number of priming events occurring along the time axis. However, since the resolution of the time axis is considerably lower than that of the space axis, projecting priming events on the time-axis will likely results in highly noisy priming frequency data. As an alternative approach, to make use of the higher resolution in the spatial dimension, we first draw a diagonal line following the position of the root tip over time (Figure.S3.6G, yellow line), We set the scale of this spatio-temporal root tip trajectory line to the 18h of the recording period. Next, we draw a line parallel to this line, corresponding to the displacement over time of the end EZ/start DZ where priming events are most clearly visible (Methods Fig 1G, yellow dashed line). The time scale of this line (mm to h conversion) is obtained from the root tip line. We have thus

defined, for a particular spatial trajectory, a temporal domain in which we can determine priming frequency.

To determine frequency DR5:LUC intensity was plotted along the defined temporal domain, again fading out priming events where artificially enhanced to determine frequency of priming rather than pre-branch site formation (Figure S3.6F).

The priming period (inverse of priming frequency) per root was calculated as follows:

$$\text{Priming period (h)} = (\text{peak}_{\text{last(h)}} - \text{peak}_{\text{first(h)}}) / (\text{peaks}_{\text{num}} - 1)$$

Where $\text{peak}_{\text{last(h)}}$ and $\text{peak}_{\text{first(h)}}$ are the occurrence in time of the last and first DR5:LUC intensity peak respectively, $\text{peaks}_{\text{num}}$ are the number of peaks counted.

In total n=132 roots were grown and imaged (MS, n=33; 10 μ m GA, n=31; 1nm BR n=32 and 100nm BR n=36), n=104 were analysed. Data from 28 roots was excluded from analysis due to various reasons: growing out of the imaging plane (n=5), heavy curling (n=3), curling and touching of neighboring root (n=14), lack of growth (n=2), lack of resolution (n=4). Roots treated with 100nm BR were more prone to curling and hence touching of neighboring roots. Of the total of n=28 excluded roots, n=19 were treated with 100nm BR, n=5 with 10 μ m GA, n=1 with 1nm BR and n=3 were on control medium.

Measuring active meristem size

Meristem imaging was done as mentioned in the histology and microscopy section. To measure meristem size and mature cortical cell sizes, Fiji/Image J was used (Schindelin et al., 2012), applying the Cell-0-tape macro for cell size measurements (French et al., 2012). Previous research has demonstrated that due to the stopping of cell division and onset of cell elongation, the boundary of the actively dividing meristem corresponds to the position in graph plotting cell size as a function of distance from the QC where cell size increase starts to accelerate (Hayashi et al., 2013, Ivanov and Dubrovsky, 2013). Therefore, to determine active meristem size, we plot cortical cell size as a function of position, doing this for both cortical cell files. We defined the meristem boundary as the position where the slope of cell size changes from neutral to positive (Figure.S3.6H green line). If we obtain different meristem boundary positions from the two cortical cell files, an average meristem boundary position was computed.

All n=104 roots that were used for kymograph analysis were also used for active meristem size measurements.

Determining cell production and division frequency

To determine (cortical) cell production rate, the number of (cortical) cells produced by the meristem per hour, we divide the measured root growth rate (in μ m/h) (see section *Kymograph analysis, root growth*) over the mature cortical cell size (in μ m).

Next, to determine (cortical) cell division frequency, the number of cell divisions per hour, we divide the obtained cell production rate (in cells/h) over the number of meristematic cortical cells (see section *Measuring active meristem size*).

3.4.3.2 Computational methods

General model description

We developed a novel multi-scale model for root growth and development, using as a basis a combination of our earlier root models that either incorporated a realistic root tip architecture (van den Berg et al., 2016) or root growth dynamics (Mahonen et al., 2014), similar to what we recently published (Salvi et al., 2020). As a critical extension thereof, we incorporated in more detail root meristem activity, including realistic cell division patterns with slow stem cell (SC) divisions near the quiescent center (QC) and subsequent clonal expansion of more rapidly dividing transit amplifying (TA) cells (Fig. 3.1A) (Bizet et al., 2015, Rahni and Birnbaum, 2019). Like our earlier models, the model incorporates cell type specific and zonation dependent gene expression and polarity patterns of AUX/LAX auxin importers and PIN exporters (Fig S3.1A), developmental zone specific cellular growth, division, expansion and differentiation dynamics (Fig. 3.1A), cell level control of gene expression, and sub cellular, grid level, simulation of auxin dynamics. With respect to gene expression, the model only incorporates the auxin-dependent gene expression of AUX/LAX.

Tissue lay-out

In the current study we aimed to investigate the interplay between auxin transport and root growth dynamics. Work by us and others has demonstrated the importance of a realistic root tip layout, as compared to a simplified rectangular root topology, for root tip auxin patterning (Cruz-Ramirez et al., 2012, van den Berg et al., 2016). Thus, we need to incorporate in our model an anatomically realistic, wedge-shaped root tip layout encased in a lateral root cap (LRC). At the same time, our research goal requires the incorporation of root growth dynamics. However, since the development of a full mechanical model of root growth dynamics is outside the scope of the present paper, the aim was to use the previously applied simplistic method of simulating root growth dynamics in which cells grow by adding a row of grid points and shifting upward all more shootward cells (Mahonen et al., 2014). While this root growth algorithm can be easily applied in a square root topology in which all cells are stacked in straight columns, this approach is less easily extended to the curved regions of the root tip. Therefore, as a compromise, we limited the size of the curved part of our root topology and ignored cell growth and divisions there, simulating growth dynamics only in the straight part of the root architecture. We reasoned that this is a justified approximation since it only ignores growth dynamics of the columella and lowermost parts of the RC, which do not contribute to root tip meristem growth dynamics. The root layout was simulated on a grid of $224 \times 2255 \mu\text{m}^2$ with a spatial resolution of $2 \mu\text{m}$. A total of 8 different cell types were incorporated in the model, with cell type specific widths incorporated based on experimental data and earlier modelling studies (Laskowski et al., 2008, van den Berg et al., 2016). In figure 3.1A, left side of root, moving from outermost to innermost these are: RC and LRC (maroon, $8 \mu\text{m}$ in straight part root), epidermal (blue, $18 \mu\text{m}$), cortical (light green, $20 \mu\text{m}$), endodermal (orange, $12 \mu\text{m}$), pericycle (yellow, $8 \mu\text{m}$) and 3 vasculature files (dark green, $6 \mu\text{m}$). Finally, the vasculature converges on the QC (pink) and below the QC are the columella cells (grey) (Fig. 3.1A).

To simulate developmental zonation dynamics, our model root is subdivided into 4 distinct developmental zones, moving from the root tip shootward these are: meristematic zone (MZ), with cytoplasmic growth and cell division; transition zone (TZ), with cytoplasmic growth but without further cell division; elongation zone (EZ), with vacuolar expansion; and differentiation zone (DZ), in which cells undergo terminal differentiation without growing further (Fig. 3.1A, right part of root). In the model used in this study, to simplify matters, the position of zonation boundaries were defined in

terms of distance from the QC rather than made dependent on auxin (Grieneisen et al., 2007), PLT (Mahonen et al., 2014) or combined PLT and cytokinin signaling (Salvi et al., 2020) gradients. Boundary positions were set such that the combined meristem and transition zone contains an average number of 40 cells for default simulations (average size 1.5 times the 8 μm they have just after division). The rootward 75% of these cells belong to MZ and will proliferate while the shootward 25% belong to the TZ, exhibiting cytoplasmic growth but no longer dividing. The EZ contains between 7-10 cells with a height between 20 and 174 μm and the DZ contains 8-12 cell with an size of 175 μm . PIN expression and polarity patterns as well as AUX1/LAX patterns were incorporated based on tissue type and developmental zone, in agreement with experimental data (Bennett et al., 1996, Swarup et al., 2001, Péret et al., 2012, Swarup et al., 2005) and similar to earlier modeling studies (Grieneisen et al., 2007, Laskowski et al., 2008, Mahonen et al., 2014, Salvi et al., 2020) (Fig. S3.1A). This pattern of auxin transporters results in reverse fountain auxin reflux pattern with maximum levels in the QC (Grieneisen et al., 2007) (Fig. S3.1A).

Auxin dynamics

Auxin metabolism, passive and active transport across the membrane, and intracellular and intra-apoplast diffusion were implemented on a subcellular, grid point level in a similar manner as in earlier studies (Grieneisen et al., 2007, Mahonen et al., 2014, van den Berg et al., 2016).

For a cytoplasmic grid point i,j ($A_{i,j}$) surrounded by n wall (A_{wall}) and m cytoplasmic (A_{cell}) grid points the equation is as follows:

$$\frac{\partial A_{i,j}}{\partial t} = p_A + D_{cell} \frac{\partial^2}{\partial x^2} (\sum_{l=0}^m A_{cell} - A_{i,j}) + \sum_{k=0}^n ((i_{pas} + i_{AUX/LAX}) A_{wall,k}) - \sum((e_{PIN} + e_b) A_{wall}) - d_A A_{i,j} \quad (1)$$

Here, p_A is the auxin production rate, d_A is the auxin degradation rate, and D_{cell} is the diffusion rate of auxin inside a cell. $i_{pas+act}$ is the combined passive, diffusional and active, AUX/LAX mediated influx of auxin from walls to cytoplasm, e_{PIN} represents active, PIN mediated export of auxin from cytoplasm to walls, and active transport by other not explicitly modeled exporters such as ABCBs is captured in e_b . For an apoplastic grid point i,j ($A_{i,j}$) surrounded by n wall (A_{wall}) and m cytoplasmic (A_{cell}) grid points the equation is as follows:

$$\frac{\partial A_{i,j}}{\partial t} = D_{wall} \frac{\partial^2}{\partial x^2} (\sum_{k=0}^n A_{wall,k} - A_{i,j}) - \sum_{l=0}^m ((i_{pas+act}) A_{cell,l}) + \sum((e_{PIN} + e_b) A_{cell}) \quad (2)$$

With D_{wall} representing the auxin diffusion rate in the apoplast.

Auxin production

While historically, root auxin levels were assumed to almost solely depend on shoot delivered auxin, more recent data show the importance of root localized regions of high auxin production, particularly once roots have passed a particular developmental age (Bhalerao et al., 2002). We incorporated elevated auxin production occurring in cells surrounding the QC as well as in the columella and LRC cells (Fig. 3.1E), assigning these cells with higher values of p_A (Table S3.1). Finally, to ensure that despite grid based modeling of auxin dynamics, the overall auxin production of an individual cell is independent of cell size we normalized p_A as $p_A = p^* \frac{height_{cell}}{height_{MZcell}}$.

Where $height_{cell}$ is the actual height of the cell and $height_{MZcell}$ is the initial height of a meristematic cell.

Boundary conditions

To simulate auxin exchange with the not explicitly modeled shoot, we incorporate an auxin influx (*inf*) into the top wall of the topmost endodermal and stele cells, while including an auxin efflux (*eff*) from the top walls of all other cell files with the strength of *eff* determined by the amount of influx and AUX/LAX on the lower membrane of the top cells. This approach is similar to that used in previous root tip models (Grieneisen et al., 2007, Mahonen et al., 2014, van den Berg et al., 2016, Di Mambro et al., 2017, Salvi et al., 2020)

AUX/LAX pattern

For simplicity active auxin import was described using a single lumped AUX/LAX import term. To define the lumped expression domain we defined an AUX/LAX prepattern that represents the sum of experimentally reported expression domains of AUX/LAX genes (Bennett et al., 1996, Swarup et al., 2001, Péret et al., 2012, Swarup et al., 2005) (Fig. S3.1A). Active AUX/LAX mediated influx is described as: $i_{AUX/LAX} = v_{up} * AUX/LAX_{pat} * AUX/LAX_{gen}$ where v_{up} is the auxin uptake rate of AUX/LAX, AUX/LAX_{pat} is the pre-pattern describing the maximum membrane level of the auxin importers as a function of zone, cell type and membrane face and AUX/LAX_{gen} is the cell level gene expression of AUX/LAX. AUX/LAX expression is auxin dependent (Laskowski et al., 2006, Laskowski et al., 2008), and we recently showed that this auxin dependence plays an important role in root tropisms (van den Berg et al., 2016). Assuming a saturating dependence of AUX/LAX expression on auxin levels we write:

$$\frac{dAUX/LAX_{gene}}{dt} = \frac{max_{AUX/LAX} * Auxin^2_{MeanCell}}{Auxin^2_{MeanCell} + km^2_{AUX/LAX}} - d_{AUX/LAX} AUX/LAX_{gene} \quad (3)$$

Here, $max_{AUX/LAX}$ is the maximal gene expression rate of AUX/LAX, $km_{AUX/LAX}$ is the auxin level at which the rate of AUX/LAX expression is half maximal, AUX/LAX proteins are degraded with rate $d_{AUX/LAX}$, and $Auxin_{MeanCell}$ is the average cellular auxin level.

PIN expression and localization

Similar to our earlier studies, we model active auxin export from cells as consisting of a major PIN protein mediated component (e_{pin}) and a minor additional component (e_b) that can be thought of as ABCB/PGP mediated auxin export. For simplicity (e_b) is assumed to be equal for all cells and to have an apolar membrane pattern. Similar to $i_{AUX/LAX}$, e_{PIN} is implemented to depend on uptake rate, polarity pattern and gene expression levels in the following way: $e_{PIN} = v_{out} * PIN_{pat} * PIN_{gen}$ where v_{out} is the rate of PIN mediated auxin transport, PIN_{pat} the PIN pre-patterning describing the maximum membrane level of the auxin importers as a function of zone, cell type and membrane face and PIN_{gen} the gene expression level of PIN. With regards to PIN mediated transport, tissue type and zonation dependent PIN pre-patterns are incorporated based on experimental data and similar to those used in earlier models (Fig. S3.1A) (Grieneisen et al., 2007, Laskowski et al., 2008, Mahonen et al., 2014, van den Berg et al., 2016). Previous research has shown the critical importance of protoxylem and xylem pole pericycle in LR priming. The initial priming signal was shown to only occur at the two protoxylem poles, not in other vascular files, and to be transmitted specifically to

overlying pericycle cells in which subsequent LR development occurs (De Smet et al., 2007). Since we aim to model LR priming, we choose for our 2D model to represent a longitudinal cross-section through the protoxylem poles. To achieve this we implemented a vascular PIN pattern emulating critical aspects of the *in planta* present three dimensional auxin fluxes that result in the directing of auxin towards the protoxylem poles, ensuring protoxylem pole priming only (el-Showk et al., 2015). Specifically, we included in addition to the predominant basally oriented active auxin transport, outward oriented, protoxylem directed PIN transport (Fig. S3.1A).

Relative to earlier models changes were made in the PIN1 polarity pattern in the MZ, based on recent experimental data demonstrating a relatively apolar distribution of PIN1 in the lowermost regions of the root (Omelyanchuk et al., 2016) (Fig. S3.1A). This change resulted in a broader, more robust auxin maximum, more consistent with experimentally observed auxin patterns. For simplicity, regulation of and resulting changes in PIN gene expression levels were ignored.

Growth dynamics

Earlier data on Arabidopsis root growth dynamics (Beemster and Baskin, 1998) suggested that cell cycle durations in the root meristem (RAM) are in the order of 20 hours. These cell cycle durations were based on measured cumulative cell flux dynamics at the end of the meristem with the assumption that all, approximately 30-35, rows of cells within the meristem divide at a similar rate. In our earlier model, cellular growth dynamics were based on these estimated rates (Mahonen et al., 2014). However, more recent data suggest that cell divisions occur in only a limited, rootward region of the meristem containing 15-20 cell rows (Wendrich et al., 2017, Rahni and Birnbaum, 2019). Cells in the remaining more shootward part of the meristem grow slowly, while not or hardly dividing, until switching to rapid vacuolar expansion driven growth in the elongation zone (Delo Ioio et al., 2008, Novak et al., 2016). Division rates measured within the lowermost, actively dividing part of the meristem were found up to 3 hours per cell cycle (Campilho et al., 2006, Rahni and Birnbaum, 2019, von Wangenheim et al., 2017). To account for these recent insights, we incorporated in the current model transit amplifying division rates in the range between 8 and 20h. In addition, we also explicitly incorporated a proper meristem zone (MZ) in which cells actively divide and a shootward MZ part, which we will refer to as a transition zone (TZ) in which we ignore rare cell divisions and only simulate slow cytoplasmic cell growth (Fig. 3.1A).

Individual cells start in the MZ where they grow with rate $r_{\text{growthMZ}}/\mu\text{m}$ and divide when they have doubled their size. When leaving the MZ, cells enter the TZ where they still grow with $r_{\text{growthMZ}}/\mu\text{m}$ but no longer divide. Upon entering the EZ, cells start to expand with rate $r_{\text{growthEZ}}/\mu\text{m}$ until a maximum cell height of $175\mu\text{m}$ is reached and cells enter the DZ. MZ and EZ growth rates are per μm , resulting in higher per cell growth rates for larger cells and constant elemental growth rates, consistent with experimental observations (Beemster and Baskin, 1998). Given the discrete, grid based nature of our model, cellular growth is executed in discrete steps during which a single row of grid points is added to the height of a cell. The time interval at which these discrete growth event occurs follows from the cellular growth rate in the following manner: if $(\text{time}) \leq \text{time}_{\text{prevgrowthstep}} + (1/(r_{\text{growthMZ/EZ}} * \text{cellheight}))$ add row of gridpoints. Concentrations of auxins and proteins are corrected for these instantaneous cellular volume increases in case of cytoplasmic growth, but not in case of vacuolar driven cell expansion where cytoplasmic volume is assumed to stay constant. Upon division, cells are divided into two equally sized daughter cells that inherit transporter patterns and concentrations of cellular components of their mother cell. All tissues grow in the described manner. In the LRC developmental zones are shorter and cellular apoptosis occurs when cells reach a fixed

position from the root tip, corresponding with the start of EZ of other tissue types (Fig.3.1A). To ensure an approximately constant size of the simulated tissue, a constant sized simulation domain encompassing the simulated tissue is defined and the most shootward cells are removed if their shootward cell wall is within 2 grid points of the simulation domain upper boundary.

Model variations, auxin availability and transport

To investigate the impact of root tip auxin transport and auxin availability, simulations with altered expression and/or localization of auxin importers and exporters or altered auxin production were performed (Fig 3.1C, 3.1D, 3.1E). Alterations in transporter levels, auxin production rates or shoot auxin influx rates were applied by simply multiplying default parameter values with a scaling parameter α , using $\alpha > 1$ in case of increase and $\alpha < 1$ in case of decrease of transporter or production levels. Alterations were often applied in a tissue and zone specific manner, applying $\alpha \neq 1$ only in specific regions of the root tip (Table S3.2).

Model variations, altered tissue specific growth dynamics

For adjustment in growth dynamics for LRC tissue (Fig 3.2A) we assumed that the location of LRC shedding was more shootward to mimic a *smb* mutant while keeping all other settings the same. For simulations with absence of growth in specific tissue (Fig. 3.2A, 3.2B), simulations were run to equilibrium. After this, for assigned tissues no growth, division and expansion dynamics were simulated while all other tissue would continue growth as in default conditions.

Model variations, auxin transport relative to cell height

To determine the mechanism underlying the cell expansion driven increases in cellular auxin levels we performed additional simulations investigating the roles of auxin export and import and effective changes therein as a consequence of cell expansion. Since passive auxin uptake occurs across the membrane, which surface area increases with cell height passive transport automatically increases with cell height. This increase will thus also occur *in planta*. Additionally, for the apolar AUX/LAX-mediated active auxin import we did not incorporate a cell size increase mediated dilution of membrane transporter levels in our default model settings. Constant membrane levels with an increased membrane area result in larger cellular AUX/LAX levels, therefore, also active auxin import increases with cell height in our model. It is unclear whether *in planta* also such an increase occurs, which would imply an upregulation of AUX/LAX production proportionate to membrane area. Finally, PIN proteins typically are highly abundant on shootward/rootward membranes, with significantly lower levels and/or occupying smaller membrane fractions of lateral membranes. Nonetheless, analogous to the situation for AUX/LAX, the strong increase in lateral membrane length during growth results in an implicit upregulation of total lateral PIN levels elongation. Again it is unclear whether this increase occurs *in planta*, or rather total lateral PIN levels are maintained and smeared out over a larger area.

To investigate the relevance of these size-dependent increases in passive and active auxin import and export for auxin loading, in a subset of simulations we prevented this increase through normalizing these auxin fluxes for cell height in the TZ, EZ and DZ of stele cell files by multiplying them with a factor $\frac{MZ_{cellheight}}{cellheight}$ for $cellheight > 2.2 * MZ_{cellheight}$, where $MZ_{cellheight} (= 8 \mu m)$ and $2 * MZ_{cellheight} (= 16 \mu m)$ is the average cell height in the TZ just before expansion starts. Since plant cells elongate in length this normalization for transport was only applied for the lateral membranes. Furthermore, in case of

normalization of passive import, since auxin levels in the EZ strongly depend on this passive influx we restricted the normalization to 25% of the total passive influx capacity to prevent a total auxin collapse in the simulations.

Model variations, tissue specific zonation

In our default simulations cell growth, division and expansion dynamics are perfectly synchronized within and across cell files. However, in planta between tissue types differences in zonation dynamics, cell cycle durations and cell sizes have been observed (Beemster and Baskin, 1998, Lavrekha et al., 2017, Rahni and Birnbaum, 2019). Stele protoxylem and protophloem cells start expanding relatively close to the root tip (~150 μm), whereas pericycle protoxylem and protophloem cells stop divisions furthest from the root tip (~250 μm) (Lavrekha et al., 2017, Rahni and Birnbaum, 2019). Additionally, vasculature cell cycles are faster than cell cycles in the outer tissues (16h vasculature versus 22h cortex) ((Lavrekha et al., 2017), supplemental information) and vasculature cells have an increased height compared to outer tissue (1.5-2 times larger on average) (Lavrekha et al., 2017, Rahni and Birnbaum, 2019).

To investigate the consequences for priming of these cell type specific differences, we implemented a tissue type dependent location of the MZ-TZ boundary, transit amplifying division rates and cell sizes, both alone and in combination in our model. For the MZ-TZ boundary vasculature division ceases at 55% of the total meristem length, pericycle at 85% of meristem length and all other tissue at 75% of meristem length, for division rates we increased vascular TA division rates by a factor of 1.5, and for cell sizes we increased vascular cell sizes by a factor of 1.5.

Since plants cells have cell walls which they share with their neighboring cells, cells are unable to slide past one another and instead maintain their neighborhood of surrounding cells. This begs the question how vasculature cells can have a more rapid cell cycle, implying a larger doubling rate and hence elemental growth rate, compared to other cells. Adding to this a larger cell size (doubling in less time) aggravates this matter even further. However, while outer cell files curve out laterally from the QC (Fig 3.1A) and straighten out further shootward, vasculature cell files originate atop of the QC and follow a straight trajectory. We thus hypothesized that the curvature of non-vascular cell files would result in a longer pathlength, that in absence of compensation would result in a higher cumulative displacement at the end of the MZ for these cell files. This would imply that higher vascular growth rates serve to compensate for the longer pathlength. To investigate this matter, we analyzed 10 meristems of 7-day old *Arabidopsis* roots grown on 1/2MS medium that were used for the lateral root number assay, we applied the Fuji plugin cell-o-tape to measure the length of the cell file from QC to EZ for a cortical and vasculature file and divided the difference of the cell file lengths through the average cortical cell size in the first 4 layers above the QC. The results indicate that a cortical cell file length is 12-20 μm longer than stele file length, translating to roughly to 2.5-3 cells of 5 μm . This indicates that ~1-2 division evens have occurred in the cortical cell file before vasculature divisions start.

We combined these findings with the data from Lavrekha 2017 et al regarding cell cycle and cell size values for cortex and stele cells to analytically test whether the differences in division rate and cell size indeed serve to compensate differences in cell file length and result in overall synchronized cumulative displacement from cell growth (Lavrekha et al., 2017).

For stele cells we model the cumulative displacement as function of time as:

$$MZ_{position}(t) = 2\frac{t}{tTA} + 2\frac{t-tSC}{tTA} + 2\frac{t-2*tSC}{tTA}$$

Where $MZ_{position}$ is the position of a cell in a meristem expressed in cortical cell size, the terms are the growth contribution by TA division from released SC assuming that a maximum of 3 SC divisions occur in the time window that an individual cell spends in the MZ. When assuming a 1.5 times larger cell height.

For the cortical cell files starting with 4 instead of 1 cell, we applied the following formula:

$$MZ_{position}(t) = -3 + 4 * 2\frac{t}{tTA} + 2\frac{t-tSC}{tTA} + 2\frac{t-2*tSC}{tTA}$$

Here the -3 term represents the 3 cells already present when counting from the QC in the cortical but not the vasculature cell file, to ensure we are comparing positions of cells with an initially corresponding position over time. Additionally, the $-1.5tTA_{cort}$ term represents that given the presence of 4 instead of 1 cell relative to the last SC division already 1 TA division has passed and hence a new SC division is due at time $t=tSC-tTA$. For stem cell cell cycles we applied $tSC=60h$ and for TA cell cycles we applied $tTA_{stele}=16h$ and $tTA_{cort}=22h$ for stele and cortex respectively (Lavrekha et al., 2017, Rahni and Birnbaum, 2019).

When plotting the above formulas while not incorporating the larger size of vascular cells nor their faster TA division (using the same value as for the cortex), we see that the head start provided by the curvature of the cortical cell file results in a substantially faster displacement of cortical versus vasculature cells (Figure S3.6I, yellow vs brown line). When incorporating in the vasculature formula either the larger cell size (Figure S3.6I, purple line) or the faster division rates this difference in displacement decreases (Figure S3.6I, grey line). Only when incorporating both aspects a highly similar displacement graph as compared to the cortex arises (Figure S3.6I, red line). These findings confirm our hypothesis, supporting that the larger vasculature cell size and faster division rates serve to compensate for the longer cell file length in the cortex due to curvature.

Since in our model growth dynamics are only applied outside of the curved region (see section Tissue layout), applying a faster division and hence growth rate in the vasculature would induce biologically unrealistic sliding in our model. To avoid this sliding, several adjustments to the model growth dynamics were made. First, under default conditions, per update step cells in the MZ could undergo either growth or division, leading to a small growth disadvantage of faster dividing cells. To avoid this, cells were allowed to both grow and divide during the same time step. Secondly in our default simulations cells enter the EZ when their lower membrane is above the LRC, however, with different cell sizes in the meristem this might result in large cells not meeting this condition yet while a smaller neighboring cell already enters the EZ and starts to rapidly elongate. To achieve across cell file synchronously occurring rapid elongation, cells should in addition to their lower membrane being above the LRC, have only neighboring cells in the horizontal plane that all also fulfill the requirements to start elongation. Finally, we applied a compensation in the elongation rates for large cells. To understand this, we need to consider the following: In our discrete, grid-based model, cell walls take up 1 grid point. Therefore, modeling the situation of a large cell flanked by two smaller cells half its size, results in our model in practice in a large cell of height H flanked by two cells of height $(H-1)/2$, due to the 1 grid point cell wall separating these two smaller cells also taking up space. As a consequence, despite having a constant elemental growth rate, the presence of a non-expanding cell wall causes the 2 small cells to expand less rapidly than the one larger cell. To prevent this, we need to downscale expansion rates of larger cells, taking into account the number of non-growing cell walls potentially present in cell files containing smaller cells.

To achieve this we apply the following formula:

$$\Gamma_{\text{growthMZ/EZ}} * (\text{cellheight} - (\text{cellheight}/MZ_{\text{cellheight}} - 1) * 1.5)$$

giving a penalty for how often a meristematic cell size ($MZ_{\text{cellheight}}$) fits in the cell size and hence compensating for the number of walls small $MZ_{\text{cellheight}}$ sized cells would have that do not contribute to growth rate, the -1 is such that a $MZ_{\text{cellheight}}$ sized cell has no penalty.

Analysis methods: kymographs

To display and analyze simulated spatio-temporal auxin dynamics, we also generated model kymographs. Kymographs were created by taking snapshots of auxin patterns in a one grid point wide longitudinal cross section in the cell file of interest (typically outer vasculature or pericycle). To zoom in on the spatial domain relevant for priming, longitudinal snapshots run from the first dividing cell (~200 μm from root tip) to the position where cells are fully elongated (~1200 μm from the root tip). Snapshots were stored every 100 time steps (=20 seconds) and aligned according to their temporal sequence. Priming frequency was obtained by $\frac{\text{priming}-1}{\text{firsttime}}$, where priming is the observed number of priming events, time is the simulation time. A cell was considered to undergo priming (i.e. its passing through the EZ was counted as a priming event) when the auxin level of that cell at the start of the EZ was more than 110% of that of its immediate above and below neighboring cells. Priming site spacing was counted as the number of cells passing through in the time interval between 2 priming events, cells undergoing priming were excluded from the priming site spacing count.

Analysis methods: disentangling size, time and competition effects on auxin loading

Our results show that the auxin reflux loop creates an auxin loading zone in the transition zone/early elongation zone and that long narrow cells have an advantage in terms of auxin loading potential. Kymographs show that particularly large cells followed by a small cell have the largest auxin levels (Fig. 3.3A). At the start of the EZ (400 μm from the root tip), we see a periodic temporal sequence from small to large cells arriving at the EZ. Furthermore, we see that the cells that gain the highest auxin levels are those cells that arrive with the largest size at the EZ and that have the smallest cell following them (Fig. 3.3B).

Theoretically, having a small cell below you may contribute to the auxin level of the above large cell in a total of three ways. First, nearby cells may compete for auxin, and given the lower auxin loading potential of a small cell, the above larger cells may be enabled to load more auxin. Second, due to exponential growth dynamics a smaller cell causes less displacement of its upper neighbor, allowing this cell to reside longer in the auxin loading region, we will refer to this as residence time. This larger residence time will allow the above cell to load auxin for a larger time period, which may contribute to its overall auxin levels. Third, a larger residence time allows for a longer period of growth while inside this domain, so it will also allow the above cell to reach a larger size while in the auxin loading domain and may thus enhance auxin loading due to size.

To disentangle these potential effects of competition, residence time and cell size we performed a series of artificially controlled growth simulations. These artificial growth simulations were started from steady state conditions obtained under normal growth dynamics. For these simulations, controlled growth was applied as follows: 1 cell at the start of the elongation zone was monitored for

its cell size and auxin levels during the growth simulation, only the 10 cells of the meristem directly below the tracked cell were allowed to grow. For these 10 meristem cells linear growth was applied, meaning that cellular growth rates do not increase with cell size as is normally the case. These specific growth dynamics were maintained irrespective of whether cells are still in the meristem zone or enter the elongation zone during the time of the growth simulation. The non-standard linear growth dynamics were chosen for more easy control of growth rate and hence overall cumulative displacement generated by this growth domain as opposed to the standard exponential growth. Cells that are in the elongation zone from the start of the simulation onwards elongated with standard, exponential dynamics.

First to test whether cells compete for auxin (Fig. S3.6J, orange bottom box), we varied whether the below meristem cells divided or not. This allows us to investigate whether size dependent competition is relevant for auxin levels in the larger cells.

Next to assess the influence of residence time (Fig. S3.6J, orange-green middle box), we doubled the meristematic cell cycle duration essentially impacting cumulative displacement rate and hence residence time in the elongation zone. However, without additional measures, changing the time spent in the early elongation zone will also affect the growth time and hence the size the cell has when residing in this zone. To be able to investigate the impact of residence time independent of cell size, elongation rates need to be adjusted such that a constant final cell size is reached at a fixed distance from the root tip. To achieve this, cells in the elongation zone were tracked and their actual height, $height_{act}$ is compared with the target height, $height_{tar}$ that would normally be achieved under default growth rates. The ratio between these two heights is next used to determine a modified root growth rate:

$$rgrowth_{EZ,corrected} = rgrowth_{EZ} * \frac{height_{tar}}{height_{act}}$$

This corrected growth rate is subsequently applied, resulting in $height_{act}$ converging to $height_{tar}$. In this way growth rate variations in the below MZ are compensated by changes in the growth rate in EZ. The target cell height is determined as follows: $height_{tar} = height_{start} + (rgrowth_{EZ})^{t_{growth}}$, where $height_{start}$ is the cell size at the start of the simulation and t_{growth} is the time a cell would need to reach the current position under default displacement velocity.

Finally to assess the effect of cell size on auxin loading (Figure S3.6J, green, upper box), we doubled the elongation time while keeping all other settings, including final cell size constant, enabling us to investigate the impact of expansion rate and hence cell size attained within the TZ independent of changes in residence time.

The results of the 3 above described simulations were compared to a default growth simulations where meristem cells grow but not divide at a doubling rate of 7h and cells in the elongation zone reach their final cell size in 7h (Fig S3.6J, black line). The comparison shows that auxin loading hardly depends on the size of the neighboring below cell, suggesting that reduced competition for auxin does not play a significant role (Fig S3.6J, orange line). A modest increase in auxin loading can be observed for increased residence time (Green/orange line). Finally, we see a significant reduction in auxin loading for a more slowly expanding, and hence smaller cells (green line). Thus, the impact of a smaller below cell arises predominantly from the above cell having more time to grow and hence reaching larger sizes and more auxin loading potential, and to a lesser extent from the above cell spending more time in the auxin loading domain (Figure S3.6J).

Analysis methods: Mathematical derivation of dependence priming on division frequency and meristem size

Following Beemster and Baskin (1998) the residence time of a cell in the meristem (T_{res}) as a function of cell cycle duration ($T_{cellcycle}$) and meristem size (MZ_{size}) can be written as: $T_{res} = T_{cellcycle} * \log_2(MZ_{size})$, which basically states that the time it takes for a cell to leave the meristem is the product of the time needed for the cell to divide times the number of divisions needed to generate the number of cells in the meristem. Since each round of division, cell numbers double the latter equals $\log_2(MZ_{size})$. From this equation it follows that the number of divisions a cell (n_{div}) undergoes before leaving the meristem equals: $n_{div} = \frac{T_{res}}{T_{cellcycle}} = \log_2(MZ_{size})$.

In the limit case where stem cells divide at the same rate as transit amplifying cells, each round of division of a TA cell also a new clone originates at the SC. Under these conditions the number of divisions a cell undergoes before leaving the meristem equals the number of clones generated by the SC within that period that fill up the meristem from the SC up until this cell that is just about to leave the meristem. Thus an upper boundary for the number of clones fitting in the meristem is the number of divisions a cell can undergo before leaving the meristem, $\log_2(MZ_{size})$.

Clone density can then be written as: clone density = $\frac{\log_2(MZ_{size})}{MZ_{size}}$.

For a priming event to occur a large-small cell pair needs to arrive in the transition zone. In order to arrive large in the transition zone a cell needs to have undergone its last division as long as possible ago, yet not undergo one further division. This defines a temporal window of $(1 - \alpha)$ cell cycle before reaching the transition zone (less than $(1 - \alpha)$ cell cycle ago cells have not grown enough, equal or more than 1 cell cycle ago they will divide once more). This temporal window can be translated into a spatial window (in terms of number of cells) by again using the equation that Beemster and Baskin (1998) formulated for a cell's residence time in the meristem:

$$T_{res} = T_{cellcycle} * \log_2(MZ_{size}).$$

To calculate the size of the window we can write:

$$\begin{aligned} T_{res} - T_{cellcycle} &= T_{cellcycle} * \log_2(\beta_{low}) \rightarrow \beta_{low} = 2^{(T_{res} - T_{cellcycle})/T_{cellcycle}} \\ T_{res} - \alpha * T_{cellcycle} &= T_{cellcycle} * \log_2(\beta_{up}) \rightarrow \beta_{up} = 2^{(T_{res} - \alpha * T_{cellcycle})/T_{cellcycle}} \end{aligned}$$

Where β_{low} is the lower and β_{up} is the upper boundary of the window expressed in the number of meristem cells between this position and the QC and $(1 - \alpha)$ is the fraction of the cell cycle that still results in the arrival of a large cell at the TZ. By definition window size is then given by

$$window = \beta_{low} - \beta_{up} \text{ and hence } window = \frac{2^{(T_{res} - \alpha * T_{cellcycle})/T_{cellcycle}}}{2^{(T_{res} - T_{cellcycle})/T_{cellcycle}}}$$

substituting $T_{res} = T_{cellcycle} * \log_2(MZ_{size})$ subsequently results in:

$$window = 2^{(\log_2(MZ_{size}) - \alpha)} - 2^{(\log_2(MZ_{size}) - 1)}$$

The derived function window can be approximated as $window = \gamma * MZ_{size}$, which for the $\alpha=0.25$ derived from our simulations results in a value of $\gamma=0.34$ (Figure S3.6K). The spatial window defines the number of cell positions at which one last division will result in a cell that will be large enough to give rise to a priming event.

For priming to occur, a large cell needs to be followed by a small cell. Thus, rootward of the cell undergoing its last division in the spatial window, a further round of cell division should occur causing this cell to arrive small. For the lowermost position in this spatial window, at ~0.99 cell cycle, it automatically holds that the cell rootward of it, at a distance of 1 cell cycle of the end of the meristem, will undergo one more round of cell division before entering the TZ. For positions inside the window, the only possibility for that particular cell to divide for the last time yet the cell(s) directly below it to undergo one more division is if these cells are part of another out-of-phase dividing clone.

Combined this gives rise to the following formula for priming frequency:

For window is ≤ 1 : $P_{freq} = D_{freq}$

for window > 1 : $P_{freq} = D_{freq} * (1 + (window - 1) * async)$

here D_{freq} is the division frequency, for which holds $D_{freq} = \frac{1}{T_{cellcycle}}$, which sets a lower limit to the priming frequency in absence of asynchronous clones, $(window - 1)$ reflects that if asynchronous clones are present other positions in the window than this lowermost one (so $window - 1$) give room to alternative, out of phase final division events. Finally $async$ is an asynchronicity factor, that determines to what extent asynchronous divisions may occur at these additional positions provided by window size and is proportionate to clone density $= \frac{\log_2(MZ_{size})}{MZ_{size}}$ (see above).

Numerical integration and run-time performance

Auxin transport occurs at relatively high rates. As a consequence, standard Euler forward explicit integration schemes would require very small temporal integration steps ($\Delta t = 0.0001$). To simulate plant growth dynamics over a time course of one or several days, this would result in excessively long simulation run times. Therefore, similar to earlier modeling studies by us and others (Grieneisen et al., 2007, Mahonen et al., 2014) we used an alternating direction semi-implicit integration scheme for the auxin partial differential equations (Peaceman and Rachford, 1955), allowing us to use integration steps of 0.2s and a spatial integration step of $\Delta x = 2 \mu m$. The code of the model was written in C++, simulations were run on 24 to 36-core workstations with Intel Xeon E5-2687W processors, resulting in a typical run-time of 24 hours for a simulation representing 6 days of plant growth.

3.4.4 QUANTIFICATION AND STATISTICAL ANALYSIS

Statistical analysis and curve fitting were performed using python. Criteria for exclusion of experimental samples were described in the corresponding STAR methods. Statistical details of experiments (whenever present: n, mean, median, p-value) are in the figure legends of corresponding experiments.

Computational results

Robustness analysis

To test whether the observed behavior found here might be an artifact of modelling choices we performed an extensive robustness analysis. First, to ensure that the observed oscillations are not a result of changes in tissue total auxin content due to the culling of the most shootward cells as they are nearing the boundary of the simulation domain, we performed simulations in much larger simulation domains yet similar starting tissue sizes in which initially the simulation domain is not reached by the topmost cells (Fig. S3.6A). This enabled us to validate that oscillations occur also in absence of culling of shootward cells. Second, to ensure robustness against changes in precise root tip

architecture or division dynamics incorporated in the model, simulations were performed in an alternative root tip architecture with a more pointy root tip shape as previously used in our halotropism study (van den Berg et al., 2016) (Fig. S3.6B), in a root tip architecture in which all cells have a reduced width (Fig. S3.6C, left panel), in a root tip layout in which cells in the different cell files are staggered (Fig. S3.6D), in a root tip in which clones of sibling cells divide slightly asynchronously (Fig. S3.6E), and in a root tip where both different cell files are staggered and cells divide slightly asynchronous (Fig. S3.6F). In all cases, oscillation dynamics were found to robustly occur. Additionally, simulations were performed at an alternative spatial resolution (1 μm instead of the default 2 μm), again without resulting in changes in oscillation dynamics (Fig S3.6C, right panel). Next, we investigated whether the incorporated auxin-dependence of AUX/LAX expression, or rather ignoring the auxin-dependence of PIN expression affected oscillations. Again, both removing AUX/LAX auxin dependence or instead incorporating PIN auxin dependence had no significant effect on oscillation dynamics (Fig. S3.6G, S3.6H). Finally, we performed simulations for a root tip model incorporating multiple layers of cortical cell layers as frequently encountered in plant species other than *Arabidopsis thaliana* demonstrating that also this does not influence priming dynamics (Fig. S3.6I). We thus conclude that the observed oscillations in auxin levels are not a direct result of particular choices in model assumptions, simplifications or implementation.

In the main manuscript, as part of our investigation of the mechanism underlying oscillations we have varied auxin production rates and locations, PIN and AUX1 transporter efficiencies and patterns, meristem sizes, and cell division and elongation rates. In all cases, periodic auxin oscillations were observed. Changes in auxin parameters merely affected oscillation amplitude but not frequency, as for example shown in Figure 3.1C and 3.1D. Similarly, changes in elongation rate also affected oscillation amplitude but not frequency, as demonstrated in Figure 3.4. In contrast, changes in meristem size and division rate affected priming frequency and spacing, as described. Only when the auxin reflux loop was fully abolished (Fig 3.1E, yellow line) or vascular cells were not allowed to grow (Fig S3.2B) simulations did not display periodic auxin oscillations.

3.5 Supplemental information

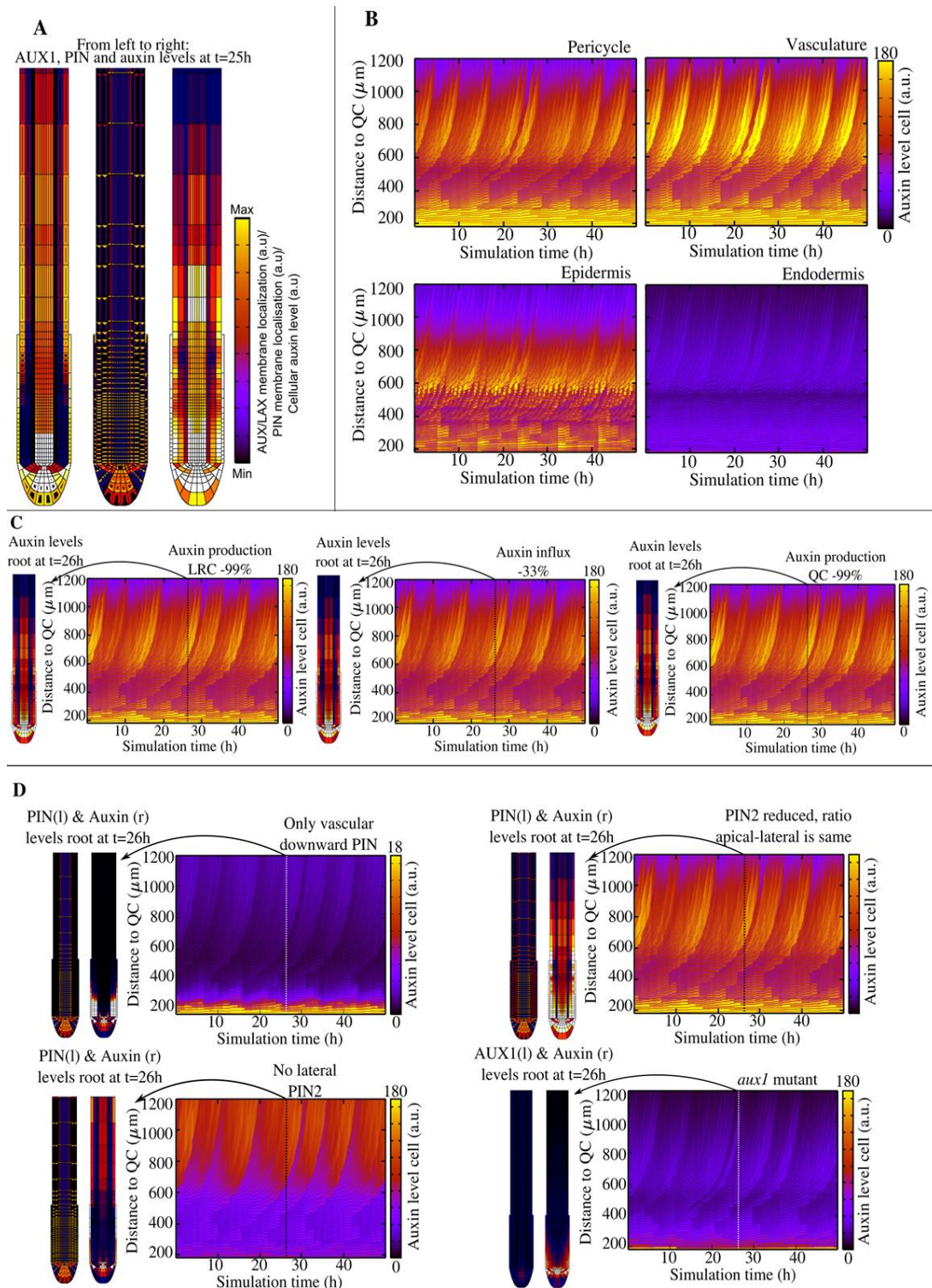


Figure S3.1; Auxin oscillations automatically emerge in a growing root model. Related to Figure 3.1. A.) Model output for default parameter settings, from left to right: snapshots of AUX/LAX and PIN membrane patterns and cellular auxin levels; Color scale indicates relative levels of these properties. B.) Kymographs for pericycle, vasculature, epidermis and endodermis auxin levels for default parameter settings. Color scale indicates cellular auxin levels for all 4 kymographs. C.) Snapshot of auxin pattern at 26h simulation time and (vasculature) kymographs for reduced auxin availability. D.) Snapshot of transporters (PIN or AUX/LAX) and auxin patterns at 26h simulation time and kymographs for simulations with altered reflux loop settings. Auxin color bars were scaled per simulation for visualization purposes.

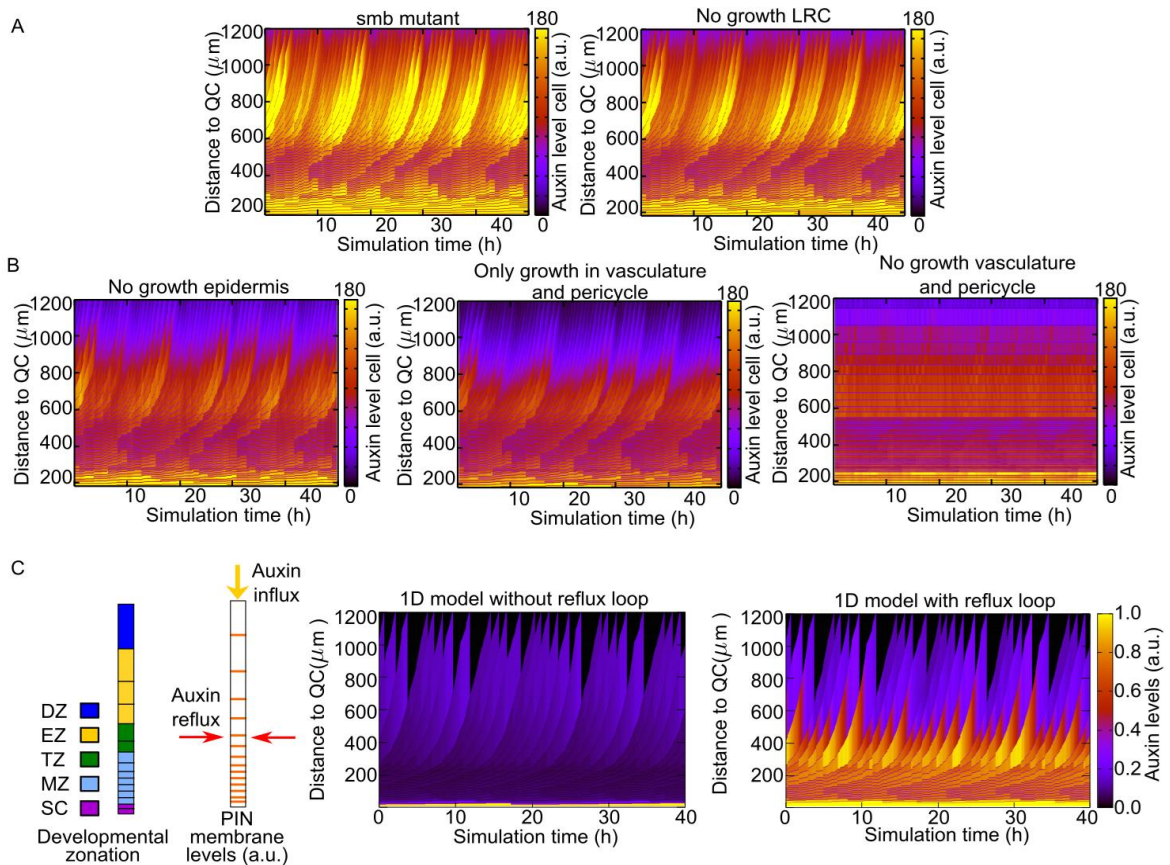


Figure S3.2; Role of root cap and vascular growth dynamics in priming. Related to Figure 3.2.A) Kymographs of vascular auxin levels for a simulated *smb* mutant and absence of LRC growth. B) Kymographs for simulations without growth in epidermis (left), only growth in vasculature and pericycle (middle) and only growth in epidermis, cortex and endodermis (right). For comparison purposes, the auxin scale bar is kept constant relative to the simulation in which all tissues grow (Fig 3.1B). C) Simulation data for a simplified 1D model. From left to right: schematic depiction of the developmental zonation, PIN1 pattern and lateral auxin influx mimicking a reflux loop that generates an auxin loading zone at the MZ/EZ boundary (tissue width is amplified for ease of visualization), kymograph for 1D model without lateral auxin influx and kymograph for 1D model incorporating lateral auxin influx.

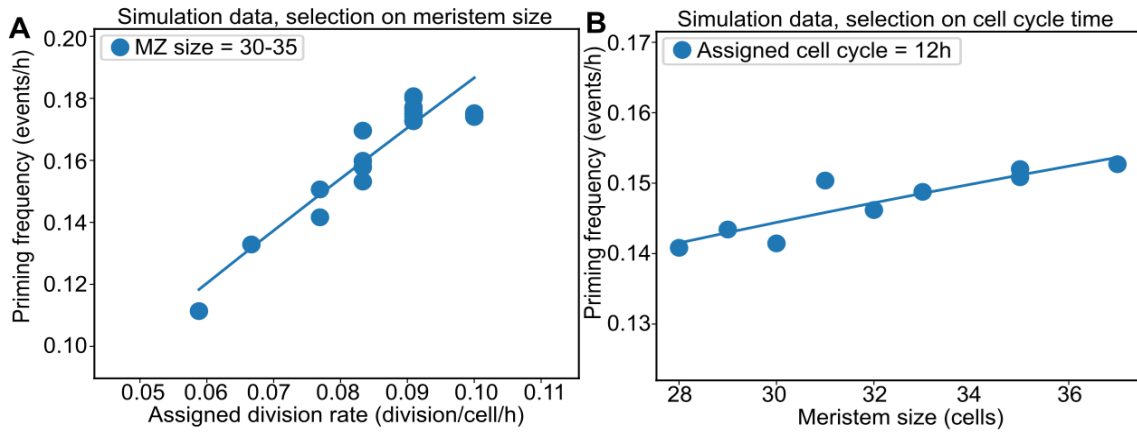


Figure S3.3; PS spacing and frequency as a function of division rate and MZ size. Related to Figure 3.4. A,B) Simulations performed with varying division rate (A) or varying MZ size (B) while keeping stem cell division constant.

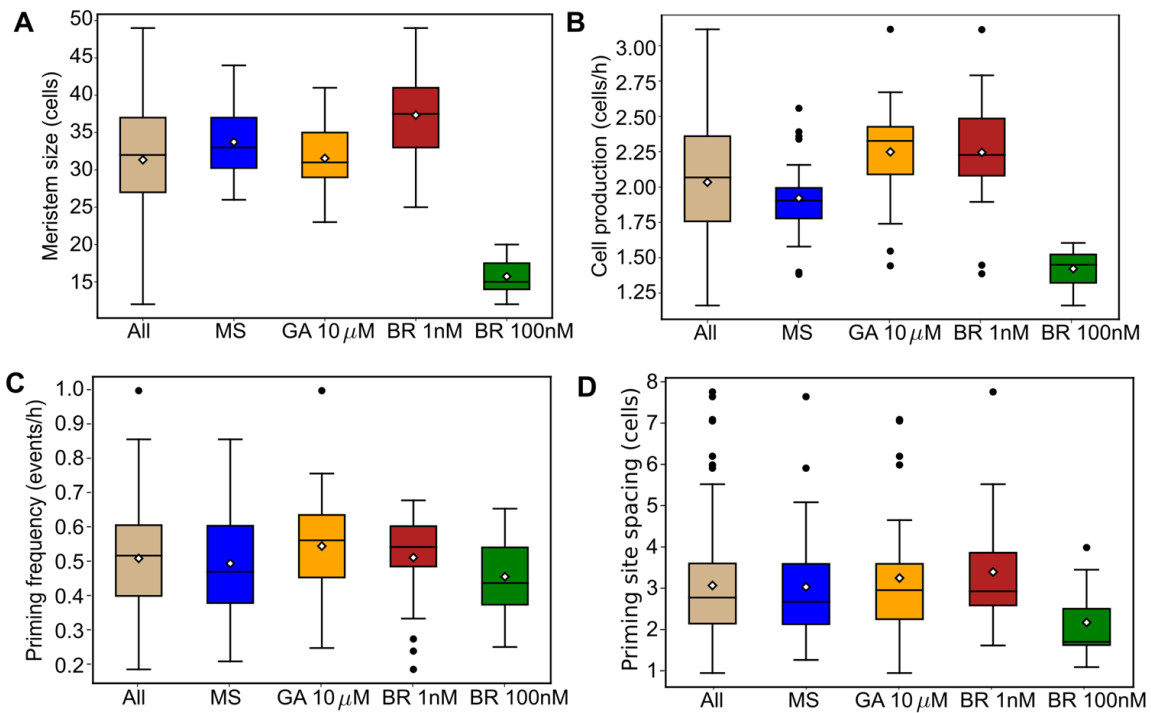


Figure S3.4; Distribution of measurements for growth and priming parameters. Related to Figure 3.6. A-D) Boxplot of experimental measurements for MZ size (A), cell production (B), priming frequency (C), and priming site spacing (D) and cell division rate (G). Color indicates data set, all data combined (brown, $n=104$), control/MS (blue, $n=30$), 10mM GA (yellow, $n=26$), 1nM BR (red, $n=31$) and 100 nM BR (green, $n=17$). Boxes cover lower to upper quartile values, black line indicates median and white square mean, whiskers indicate the total range of the data and black dots indicates outliers.

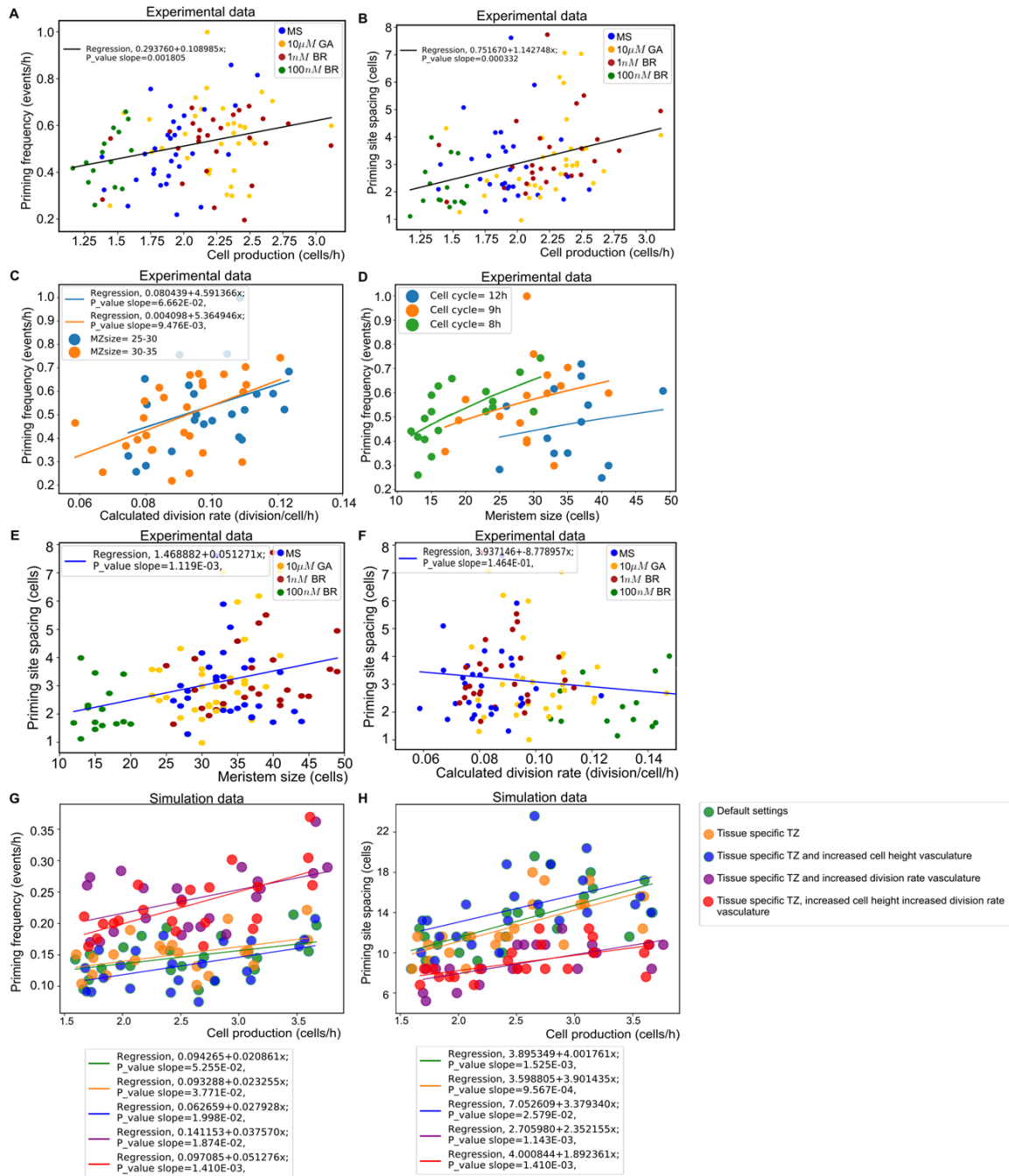


Figure S3.5; Priming frequency and spacing as a function of cell production. Related to Figure 3.7. A, B) Experimentally measured priming frequency (A) and PS spacing (B) as a function of cell production. Data points are colored to indicate the different treatments. C) Experimentally measured priming frequency as a function of division rate. To avoid confounding effects, subsets of data containing only plants with a similar MZ size were used. Data points from both the control and the three different hormone treatments are used. D) Experimentally measured priming frequency as a function of meristem size. To avoid confounding effects, subsets of data containing only plants with a similar division rate were used. Data points from both the control and the three different hormone treatments are used. E) Priming site spacing as a function of MZ size for experiments. Data points are colored to indicate the different treatments. F) PS spacing as a function of division frequency for experiments. Data points are colored to indicate the different treatments. G, H) Model priming frequency (G) and PS spacing (H) as a function of cell production. Vasculature specific details were incorporated into the model alone or in combination, and results were compared to those for default model settings (green line). In A, B, E, F the combined data of different treatments were fitted to a single linear regression line. In C, D, G, H, data was fitted using linear regression per color-indicated subset

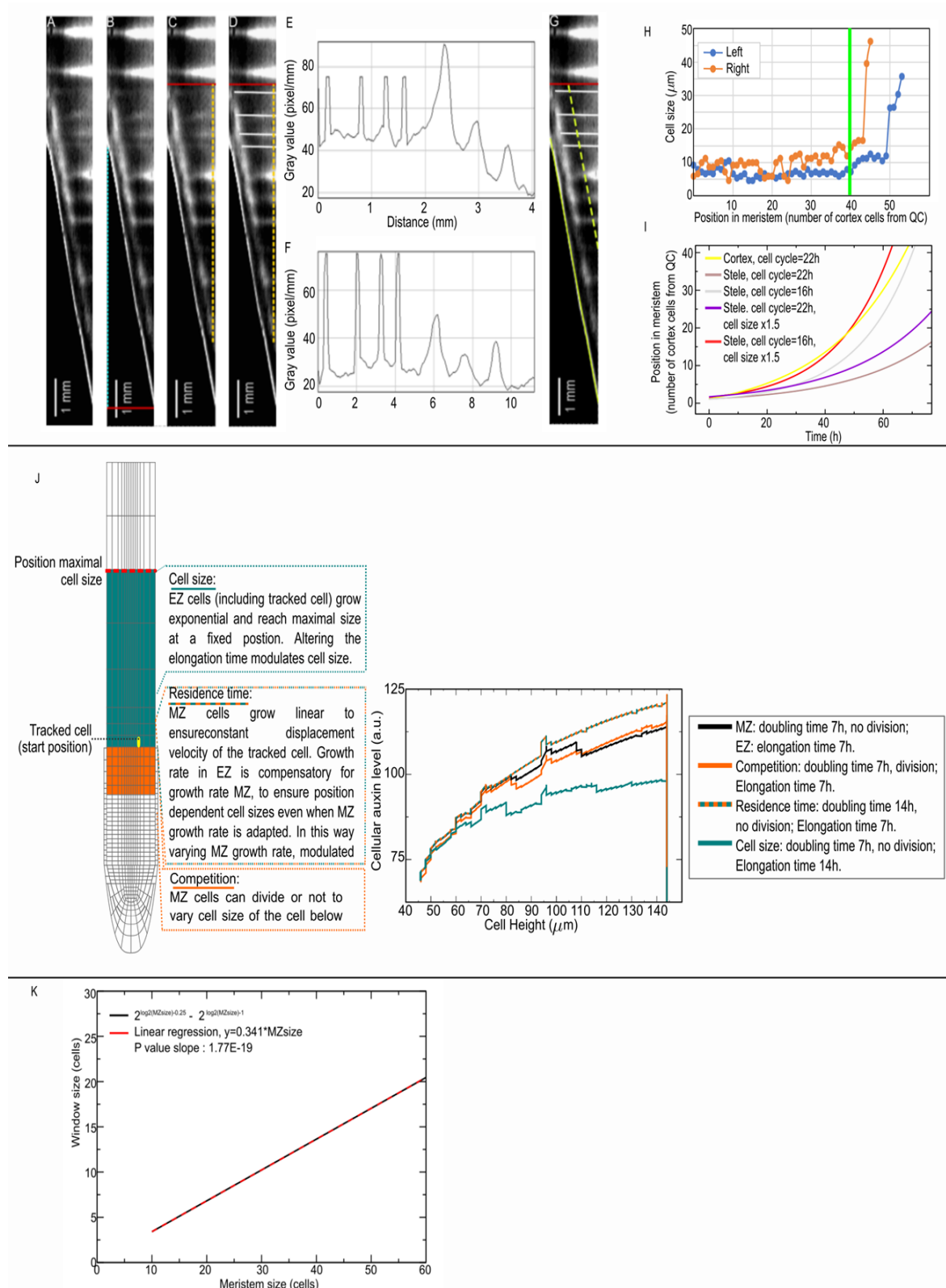


Figure S3.6; Experimental and analysis methods. Related to STAR methods. A) Example kymograph B) Growth was measured through a line (cyan) running from the location of the root tip at the start to the end of the imaging period (red line indicates root tip location at the end of imaging). C) PSS was determined by measuring intensity on a line matching the last time frame (18h) of imaging (dotted yellow line), a line perpendicular to the location of the TZ at the start of imaging was taking as the start of the measurements. D) To account for all priming events, fading priming events were enhanced with a white line. E) Intensity values along the yellow line shown in D for analysis of the spacing of the primed sites. F) Intensity values along the yellow line in G for analysis of the timing of priming events. G) Priming frequency was measured

by obtaining a space-time scale from the root tip growth (solid yellow line) and measuring intensity from a line in the EZ exactly parallel to the root tip. TZ location at the start of imaging (red line) was taken as the start of measurements. H) Example meristem analysis, cell size from two cortical files on either side of the root were measured and plotted against their position from the stem cell. The point where in both cortical cell files cell size start to increase was taken as a measure of the end of the active meristem. I) Cumulative displacement of cortical and stele cell files with cortical cell cycle =22h and stele cell cycle = 16h and cell size scaled such that cortical cell size =1 and stele cell size =1.5. Cortical cell displacement in meristem when applying cortex formula and cell cycles (yellow). Stele cell displacement applying stele formula combined with cortical cell cycle and cell size(brown), stele cell cycle and cortical cell size (grey), cortical cell cycle and stele cell size (purple) and stele cell cycle and cell size(red). J) Importance of cell size, residence time and competition for auxin loading. Artificially controlled growth experiment to disentangle potential effects of competition (Left bottom box), residence time (Left middle box) and cell size (Left upper box). Auxin level in the last cell of the MZ was tracked and a default simulation (Black line) was compared to the following variations: Cells in MZ below the tracked cell divided, enabling to investigate the influence of competition based on neighbor cell size (Orange line). Cells in the MZ grew slower, increasing the residence time of the tracked cell (Green-orange line). Elongation time was varied while keeping all other settings constant, enabling to investigate the impact of expansion rate and hence cell size attained within the TZ independent of changes in residence time (Green line). K) Window size(black line) as a function of meristem size. Linear regression line (dotted red) with $a=0.341$ and $p=1.77E-19$.

Table S3.1 Auxin parameters. Related to STAR methods

Parameter	Description	Value	Dimension
p_A	Basal auxin production rate	0.0015	s^{-1}
QC_{p_A}	QC auxin production rate	$50 * p_A$	s^{-1}
$Col_{p_A}^I$	Columella auxin production rate	$15 * p_A$	s^{-1}
LRC_{p_A}	LRC auxin production rate	$10 * p_A$	s^{-1}
inf	Shoot influx	0.96	$\mu m s^{-1}$
d_A	Auxin degradation rate	0.000725	[auxin] s^{-1}
D_{cell}	Cytoplasmic diffusion rate	600	$\mu m^2 s^{-1}$
D_{wall}	Apoplasmic diffusion rate	40	$\mu m^2 s^{-1}$
i_{pas}	Passive influx	2.5	$\mu m s^{-1}$
v_{up}	Active influx rate	0.07	$\mu m s^{-1} [AUX/LAX]^{-1}$
$\frac{max_{AUX}}{LAX}$	Maximal AUX/LAX expression rate	0.01	[auxin] s^{-1}
$\frac{km_{AUX}}{LAX}$	Saturation constant AUX/LAX expression	50	[auxin]
X/LAX	AUX/LAX degradation rate	0.0001	s^{-1}
e_b	Non-PIN mediated export rate	1	$\mu m s^{-1}$
v_{out}	Active efflux rate	0.2	$\mu m s^{-1} [PIN]^{-1}$
PIN_{gen}	Cellular PIN expression levels	100	[]

Table S3.2; Auxin availability and transport. Related to STAR methods.

Description	Parameter	Affected tissue	α
Low auxin production LRC (Fig 3.1C)	LRC_{p_A}	LRC	0.01
Low shoot influx (Fig 3.1C)		-	0.667
Low auxin production QC (Fig 3.1C)	QC_{p_A}	QC	0.01
Only downward PIN1 (Fig 3.1D)	PIN_{prepat}	All except vasculature and pericycle	0.0
<i>Aux1</i> mutant (Fig 3.1D)	AUX/LAX_{pat}	All	0.1
Reduced PIN2 (Fig 3.1D)	PIN_{prepat}	EZ/DZ, LRC, epidermis and cortex	0.5
Extra AUX1 vasculature (Fig 3.1E)	AUX/LAX_{pat}	Vasculature	2.0
Extra AUX1 epidermis (Fig 3.1E)	AUX/LAX_{pat}	Epidermis	2.0
Only shootward PIN2(Fig 3.1E)	PIN_{prepat}	TZ/EZ/DZ, LRC, epidermis and cortex (lateral membranes)	0

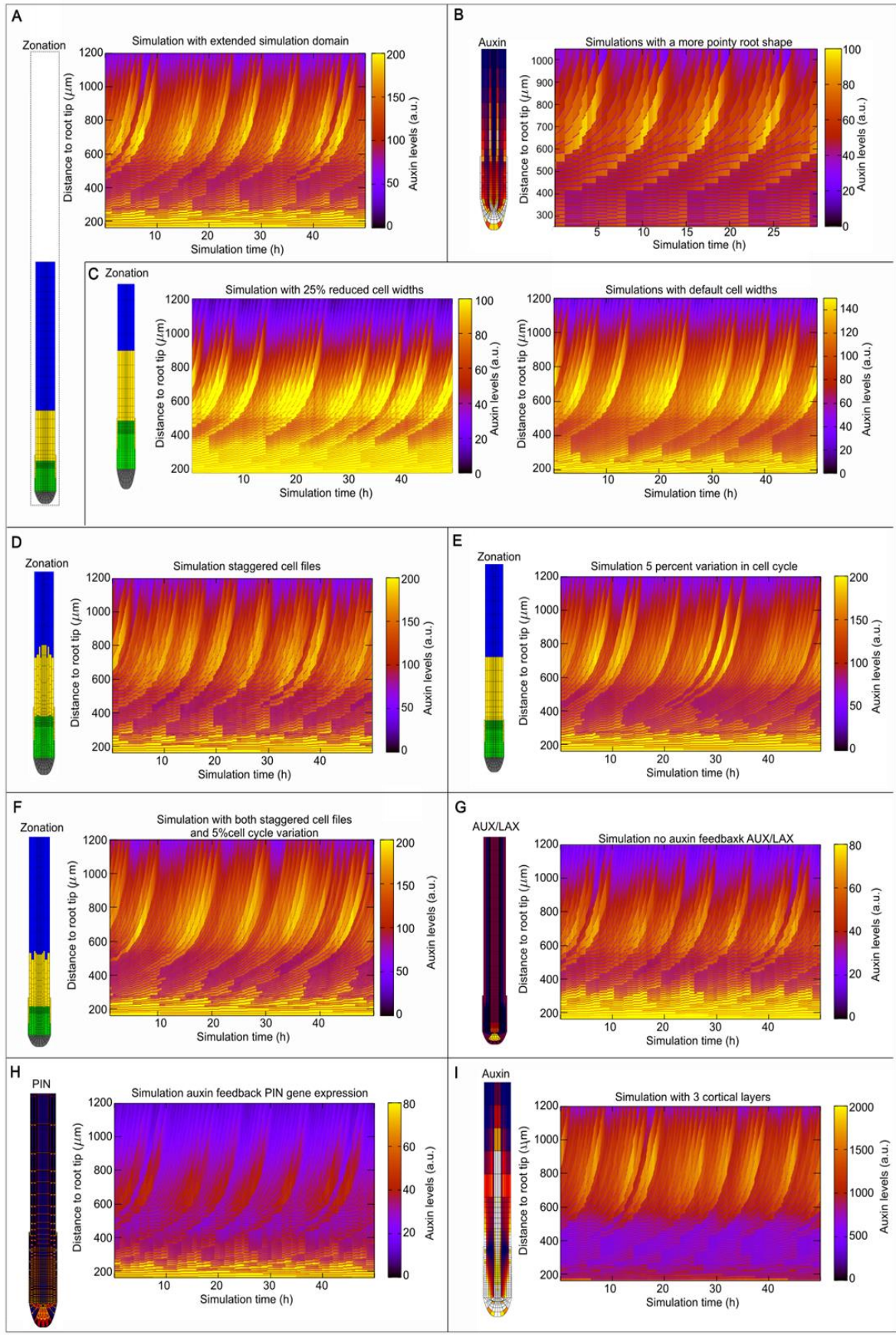


Figure 3.7; Robustness analysis computational methods. Related to STAR Methods. A) Simulation with extended simulation domain, border around root snap shot (left) indicates simulation domain. B) Simulation with an alternative, more pointy, root shape. Only cells in the straight part of the model grow and divide. C) Simulation with all widths reduced with 25%, relative cell width between tissue was maintained (left panel). Due to instability issues resulting from the very narrow vasculature width under default settings, these simulations were performed at a spacestep of 1 μm instead of default 2 μm . Additionally, auxin influx and production were reduced 2 fold to correct for the extra production and influx due to the decreased spacestep. For comparison purposes, we performed a simulation with default cell widths, but same changes of 1 μm spacestep and reduced influx and production illustrating that temporal dynamics of oscillations are independent of cell widths. D) Simulation with staggered cell files, to obtain staggering simulation was performed with different initial cell sizes per cell file. E) Simulation with 5 percent variation in cell cycle time between cells. F) Simulation with both staggered cell files and 5 percent variation in cell cycle time between cells. G) Simulation without auxin dependent AUX/LAX expression. H) Simulation with auxin dependent PIN expression. I) Simulation with 3 cortical cell files instead of the default 1 cortical cell files.

Video S3.1: Auxin oscillations automatically emerge in a growing root model. Related to Figure 3.1. Growing root model with cellular auxin levels (left), 1 pixel wide snapshots of the root's vasculature are displayed in the kymograph (right) over the time course of the simulation.

<https://ars.els-cdn.com/content/image/1-s2.0-S153458072100561X-mmc2.mp4>

Video S3.2a: Priming frequency increases with increasing division rate. Related to Figure 3.4.

Root simulations with varying cell cycle duration (inverse of division rate) while keeping meristem size constant. From left to right: cell cycle 6h (division rate = 0.1667 h^{-1}), cell cycle 9h (division rate = 0.11 h^{-1}) and cell cycle 12h (division rate = 0.183 h^{-1}).

<https://ars.els-cdn.com/content/image/1-s2.0-S153458072100561X-mmc3.mp4>

Video S3.2b: Priming frequency increases with increasing meristem size. Related to Figure 3.4.

Root simulations with varying meristem sizes while keeping division rate constant. From left to right: 12 meristem cells, 25 meristem cells and 40 meristem cells. Note that meristem cell counts only represent actively dividing cells, TZ cells were not counted as part of the meristem. Also note that for increasing MZ sizes in our model oscillation amplitude decreases. This is due to the reduced time for elongation in the loading zone resulting from the higher cumulative displacement caused by larger cell numbers. In planta, elongation rates appear to be compensated for higher division rates or meristem sizes, reducing this effect.

<https://ars.els-cdn.com/content/image/1-s2.0-S153458072100561X-mmc4.mp4>

Video S3.2c: Priming amplitude but not frequency is influenced by elongation rate. Related to Figure 3.4.

Root simulations with varying elongation durations (inverse of elongation rate) while keeping cell cycle time and meristem size constant. From left to right: elongation time 5.5h (elongation rate = 0.18 h^{-1}), elongation time 7.5h (elongation rate = 0.13 h^{-1}) and elongation time 9.5h (elongation rate = 0.105 h^{-1}).

<https://ars.els-cdn.com/content/image/1-s2.0-S153458072100561X-mmc5.mp4>

4

Meristem growth dynamics shape lateral root priming morphospace

Thea van den Berg, Kavya Yalamanchili, Jacob P. Rutten, Hugues de Gernier, Tom Beeckman, Ben Scheres, Viola Willemsen, Joop Vermeer and Kirsten ten Tusscher

Abstract

We have previously shown that lateral root priming emerges from root meristem growth dynamics, as a consequence any adjustment in growth or growth related processes will be translated into changes in priming site numbers and density. Here we break down overall cell production rate into its constituent parts, and decipher the distinct effects of meristem size, stem cell and transit amplifying division rates on priming dynamics. We analytically derive the priming morphospace, the combined priming frequency and density as a function of root meristem growth, with cell division rate and meristem size shaping the lower and upper boundary of this morphospace and meristem clone density determining the actual position occupied between these boundaries. Additionally, we demonstrate that *in planta* interdependencies between meristem size, stem cell and transit amplifying division rate constrain the use of this morphospace and favor high priming site numbers and densities. Together these findings elucidate how growth parameters are translated into priming site numbers and densities and how transitions in growth dynamics cause a shift in position within the priming morphospace. This translation from growth to priming dynamics enables us to explain the observed speed up in priming frequency during the first days after germination.

Finally, although priming is followed by several developmental check points before the emergence of an actual lateral root, we argue that it is likely that changes in growth parameters during abiotic stress or varying nutrient conditions that affect priming site number and density, at least partly, explain the observed environmental induced root system architecture remodeling.

4.1. Introduction

Plant roots, often referred to as the ‘hidden half’ of the plant, are essential for water uptake, nutrient acquisition and anchorage. To ensure plant survival and fitness, the length of the main root (MR), length, angle, numbers and density of lateral roots (LR), all display a high plasticity in response to environmental conditions (Gruber et al., 2013, Koevoets et al., 2016, Shahzad and Amtmann, 2017). A stunning example of this extensive plasticity is the diametrically opposite root architectures generated by genetically identical plants in response to either nitrate or phosphate starvation, resulting in either steep rooting or shallow surface foraging architectures (Linkohr et al., 2002). Additionally, abiotic stress, such as, salinity and heavy metals are known to induce changes in LR density and numbers as well as in MR growth (Julkowska and Testerink, 2015, Khare et al., 2017).

In plants with a taproot system architecture, such as *Arabidopsis thaliana*, root system architecture (RSA) arises from the continuous formation of LRs branching off of the MR. LR development involves a sequence of processes, ranging from the priming of competent cells for future LR formation to the actual emergence of a LR from within the MR and is subsequent further outgrowth (Banda et al., 2019, Du and Scheres, 2018). Changes in developmental stage and environmental conditions impinge via signalling cascades on several stages of LR development, inhibiting or promoting their further development and thereby resulting in altered number and density of LRs (Pérez-Torres et al., 2008, Zhang et al., 1999, Zhao et al., 2011). Nonetheless, these regulatory effects on the different stages of LR development are insufficient to fully explain the dynamic RSA adjustments observed during normal post germination root development or in response to abiotic stress or varying nutrient conditions. For example, during the first days after germination a strong increase in the rate of formation of LRs can be observed (Bhalerao et al., 2002) that cannot simply be explained from increases in auxin levels in the growing root tip meristems. Similarly during nutrient deprivation increases in LR density can be observed that display a strong but thus far unexplained correlation with decreases in MR length (Gruber et al., 2013).

Indeed, interestingly, these developmental, nutrient and stress induced changes in RSA almost always coincide with changes in MR growth (Gruber et al., 2013, Bhalerao et al., 2002) induced through changes in the hormonal-genetic signalling networks controlling growth parameters such as meristem size (Liu et al., 2015), cell division rate (Lai et al., 2007, Naulin et al., 2020, West et al., 2004, Yang et al., 2014) and/or stem cell activity (Ortega-Martinez et al., 2007, Sanchez-Calderon et al., 2005, Ticconi et al., 2009). We have recently shown that the very first stage of LR development, the priming of competent cells for future LR formation, can be understood as an emergent property of MR growth dynamics (van den Berg et al., 2021). Based on this we hypothesize that adjustments in RSA, at least partly, originate from MR growth induced adjustments in priming site numbers and density that are subsequently translated to numbers and densities of LR.

To investigate this hypothesis we make use of our previously developed computational root growth model for LR priming dynamics. In a previous study we used this model to reveal a reflux-and-growth mechanism for LR priming, with the root tip auxin reflux loop establishing an auxin loading zone at the start of the elongation zone and meristem growth inducing semi-periodic variations in cell sizes driving oscillations in cellular auxin loading potential (Figure 4.1). In reflux-and-growth driven LR priming the frequency and spacing of LR priming sites was found to positively correlate with root meristem cell production rate. We subsequently used *in planta* experiments to validate these predictions and distinguish these from previously proposed Turing or clock-and-wavefront LR priming mechanisms (van den Berg et al., 2021).

In the current study we use the availability of this theoretical framework for LR priming to determine a morphospace for LR priming sites, in terms of both numbers and density. We set out to determine how different root meristem growth related properties, meristem size, transit amplifying division rate, and stem cell division rate, together determine the position of an individual plant in this morphospace. Through comparing model outcomes with experimental data we were able to reverse engineer how *in planta* meristem growth dynamics shape the accessibility of this morphospace. Additionally, we deciphered how adjustments in MR growth related properties in response to environmental conditions move the plant's position in this LR priming morphospace. Finally, by understanding the translation of meristem size, division rate and stem cell activity to priming site numbers and density we were able to explain the developmental speed up in priming frequency during the first 6 days after germination.

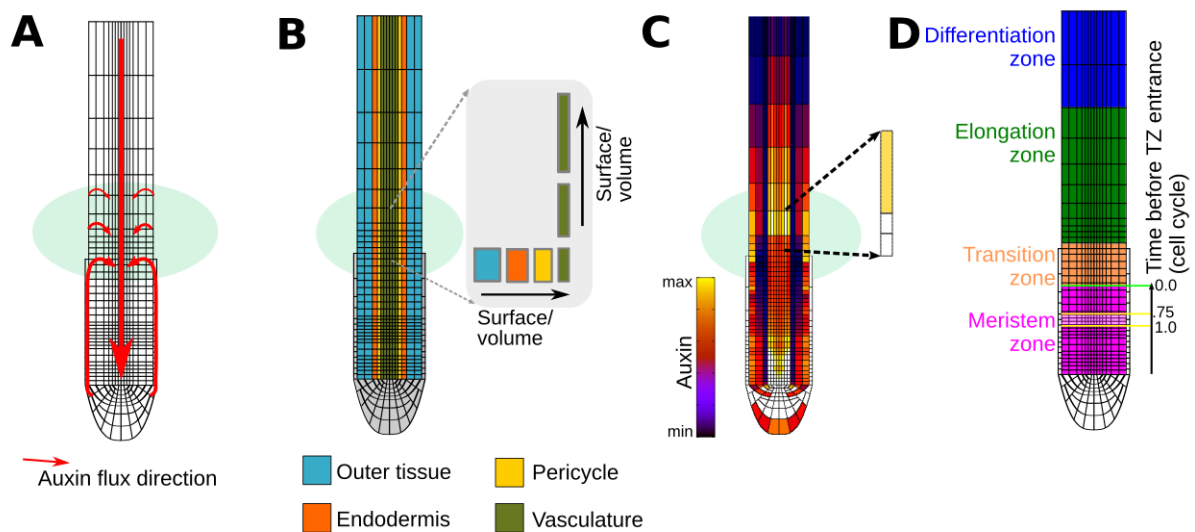


Figure 4.1. Overview the reflux-and-growth mechanism for LR priming. A) Auxin transport creates an auxin loading zone (green oval) at the start of the elongation zone. B) Large, narrow vasculature cells have an optimal surface to volume ratio for auxin loading, hence the priming signal will first and foremost occur in the vasculature. C). Large cells followed by a small cell have both a large surface for auxin loading and increased time for loading due to the reduced replacement resulting from the low growth rate of the small cell below. D) Large cells followed by a small cell occur when the upper cell has its final division in a spatial-temporal window 0.75-1 cell cycle before entrance into the transition zone, and the following cell has its final division above this window. The difference in timing between their last divisions will translate into differential growth time before arrival in the elongation zone and form a large-small cell pair.

4.2. Results

4.2.1 Priming frequency varies for similar meristem cell production output

In our previous study we have shown that a priming site arises in a large vasculature cell that is followed by a small cell, because large, narrow vasculature cells have an optimal surface to volume ratio to facilitate auxin loading and the following small cell provides extra loading time due to its relative slow growth (Figure 4.1B and 4.1C). Additionally, we showed that the number and density of these priming sites will depend on the product of 3 factors: 1) the size of the spatio-temporal window in which a final division event allows for long enough growth to cause a cell to arrive large at the elongation zone, 2) the level of asynchronicity in divisions that determines the chances of a directly below cell to divide once more and hence arrive small, 3) the actual frequency at which divisions occur. In chapter 3 we established that window size is proportionate to growth driven cell displacement rate, and hence meristem size, and could be described as $\beta * MZsize$. The division asynchronicity, or clone density, was shown to scale with the rounds of division a cell can undergo before leaving the meristem (the maximum number of clones fitting in a meristem) divided over the meristem size: $\sim \frac{\log_2(MZsize)}{MZsize}$, implying that clone density decreases with increasing meristem size. The product of window size and division asynchronicity thus is $\beta * \log_2(MZsize)$. Taken together the reflux-and-growth model predicts that priming frequency positively correlates with meristem size and division frequency. By subsequently dividing cell production: $\ln(2) * MZsize * divfreq$, the number of cells passing by per hour, over priming frequency we subsequently derived that the spacing between consecutive priming events positively correlates with only meristem size. Therefore, both priming frequency and spacing positively correlate with meristematic cell production rate (van den Berg et al., 2021) and Methods for analytical derivation (van den Berg et al., 2021).

Our experiments previously validated model predictions that both priming frequency, which can be rephrased as priming site production rate (PSP), and priming site spacing (PSS) increase with meristem cell production rate, thereby falsifying predictions from alternative, previously proposed models for priming. Still, we observe a large spread in PSP rate and PSS for similar cell production rates (Figure 4.2). This spread in data seems to vary for different cell production ranges for both experimental (Figure 4.2A and 4.2B) and simulation data (Figure 4.2C and 4.2D).

The spread in PSP and PSS for a particular meristematic cell output, suggests that our understanding of how meristem growth dynamics and output dictate priming frequency is incomplete.

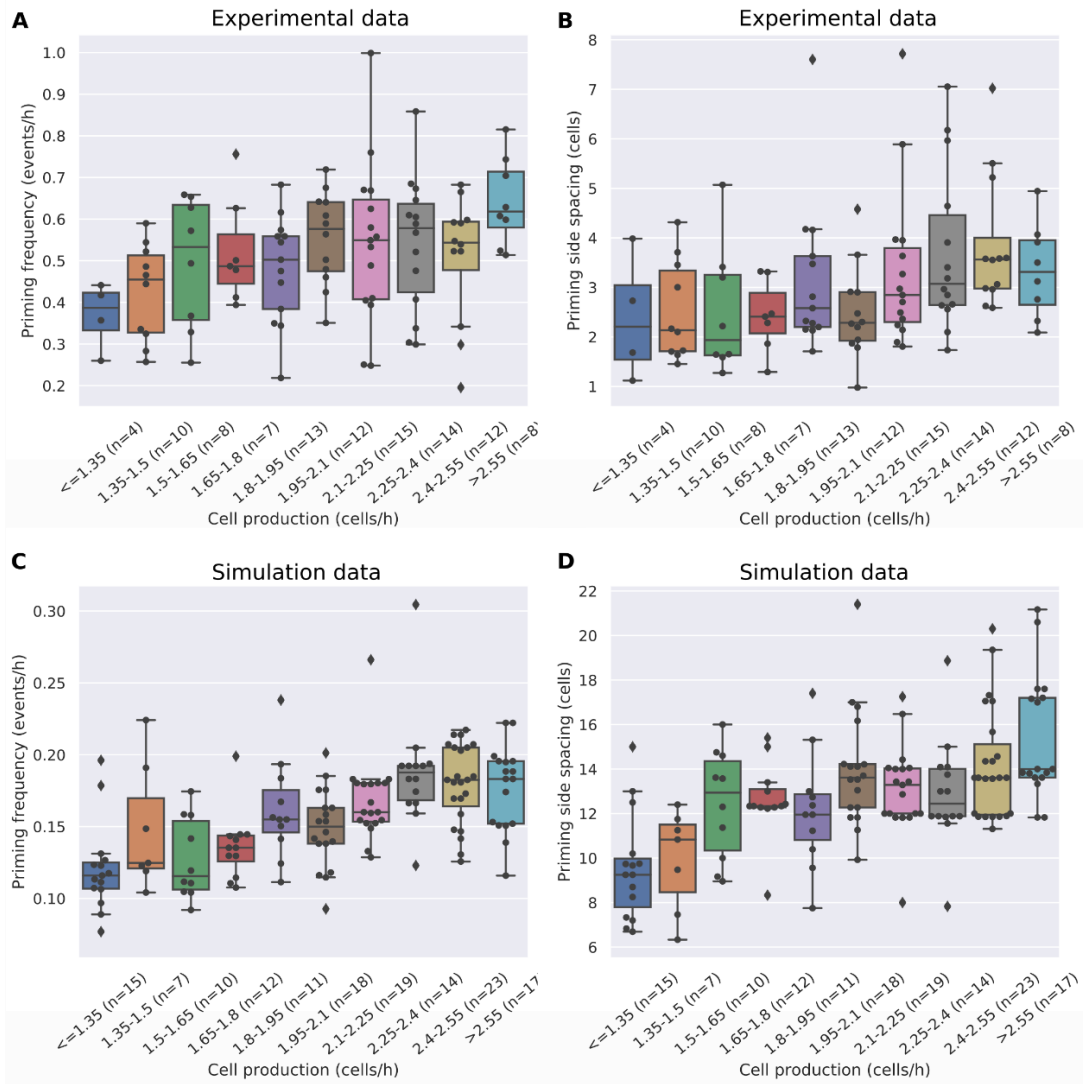


Figure 4.2. Priming site production and priming site spacing is variable within a cell production range, production range was 1.2-2.7 cells/h. A) Priming site production and B) Priming site spacing for experimental data ($n=104$), control/MS ($n=30$), GA 10 μ m ($n=26$), BR 1nm ($n=31$) and BR 100 nm ($n=17$). C) Priming site production and D) priming site spacing for simulation data.

4.2.2 Priming morphospace is bound by division frequency and meristem size

To further our understanding of how meristem growth dynamics affect priming dynamics we make use of the unique potential of models to simulate artificial “what if” scenarios not occurring *in planta*. Specifically, we compared the normal clonal division pattern, arising from stem cells dividing slower than transit amplifying cells, with at one extreme a situation in which all meristem cells divide synchronously and at the other extreme a situation in which all cells in the meristem divide at random, asynchronous times. In figure 4.3 we compare kymographs of these 3 different scenarios with all a similar cell production rate, depicting besides cellular auxin levels (Figure 4.3, top row) also cell heights (Figure 4.3, 2nd row), time since last division (Figure 4.3, third row), and distance from QC for this final division (Figure 4.3, bottom row). Independent of division dynamics, priming (Figure 4.3, top row, cells with highest auxin) occurs in the largest cells (Figure 4.3, 2nd row), that arose from dividing the longest ago before reaching the elongation zone (Figure 4.3, 3rd row), indicating that division dynamics do not affect priming mechanism. In contrast, division dynamics strongly impact the frequency at which priming occurs and the spacing between the priming sites, with the lowest

number of priming events occurring for fully synchronized divisions (Figure 4.3, left panels) and the highest number of priming events occurring for maximally asynchronous divisions (Figure 4.3, middle panels). These two scenarios thus enable us to define boundaries of the priming morphospace, the lower and upper limits of priming site production rate and the corresponding priming site spacing.

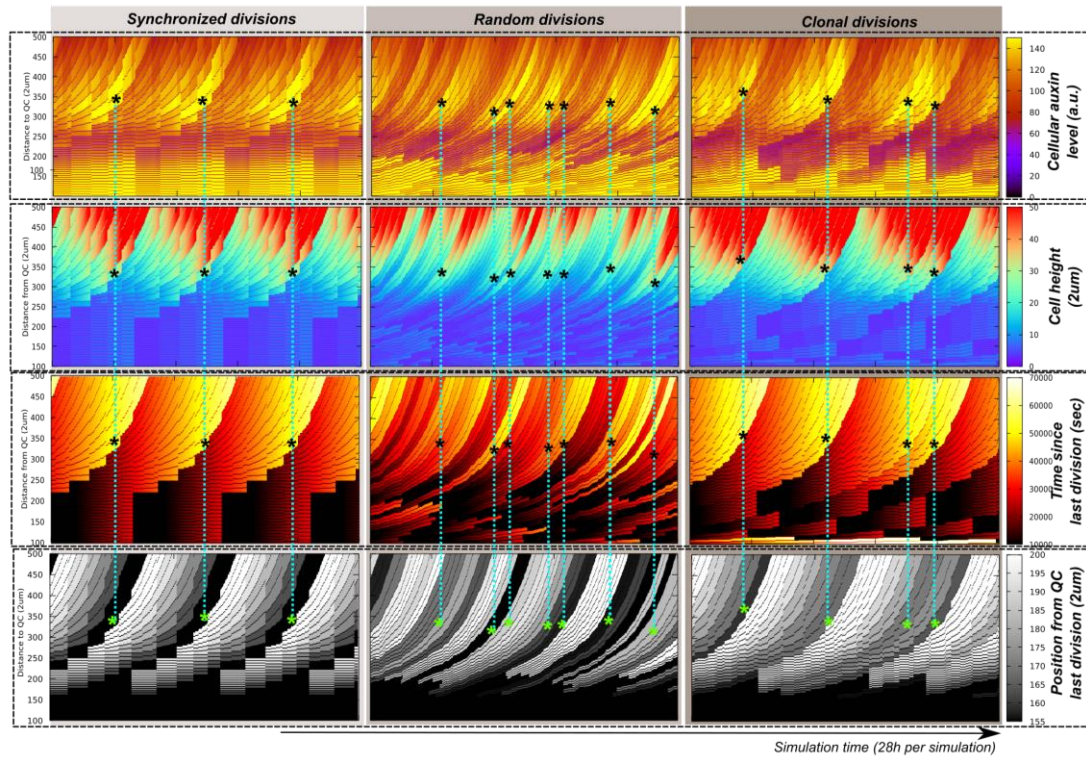


Figure 4.3. Simulations with a meristem size of ~ 25 and cell cycle of 8h, division patterns vary in the following way from left to right: synchronized divisions, random divisions and clonal divisions. Different rows depict a similar time frame per simulation and display different features of the cells, from top to bottom: Mean cellular auxin, Cell height (resolution 2µm), time since last division and position from QC at final division. Asterisks indicate primed cells and lines are for identifying primed cells in different rows.

To understand the low priming frequency under fully synchronous divisions we considered further the differences in priming dynamics. We observed that while for clonal and asynchronous divisions the final division of the primed cells occur within a spatial window, for synchronous divisions these final divisions appear to occur at a single location (Figure 4.3, bottom row). These differences can be understood as follows, in situations where not all divisions are synchronous we identified a spatio-temporal window in which a final division of a cell would enable it to arrive large in the elongation zone (Figure 4.1D), with out-of-sync cells below that cell having a final division above the spatial window causing these cells to arrive smaller in the EZ. If, however all divisions occur synchronously, the only possibility for generating a large-small cell pair, is if the top cell divides precisely at a distance covered in 1 cell cycle, causing that cell to have just left the division zone when the below cells undergo one more round of division. This implies that the lower boundary for priming frequency, occurring for fully synchronous divisions, is determined by the transit amplifying division frequency:

$$P_{\text{freq}(\text{min})} = TA_{\text{div}},$$

where P_{freq} is the priming frequency or priming site production rate per hour and TA_{div} is the cell division rate of the transit amplifying cells. Note that in this extreme scenario of fully synchronized divisions TA_{div} is equal to SC division rate. For fully synchronous divisions we thus predict

that priming frequency is independent of meristem size and equal to TA division rate, a prediction that is borne out by our model simulations (Figure 4.4A and 4.4C green triangles).

As priming site spacing follows from the ratio of cell production over priming frequency, maximum PSS for this situation can be described with $PSS_{(max)} = \frac{cellproduction}{TA_{div}}$, meaning that the number of cells exiting the meristem within 1 cell cycle determines the priming site spacing. Following Beemster & Baskin overall meristem cell production equals $\ln(2) * MZsize * divfreq$ (Beemster and Baskin, 1998), implying that maximum PSS spacing only depends on meristem size and not on TA division rate. Again, this is in agreement with simulation outcomes (Figure 4.4B and 4.4D, green triangles).

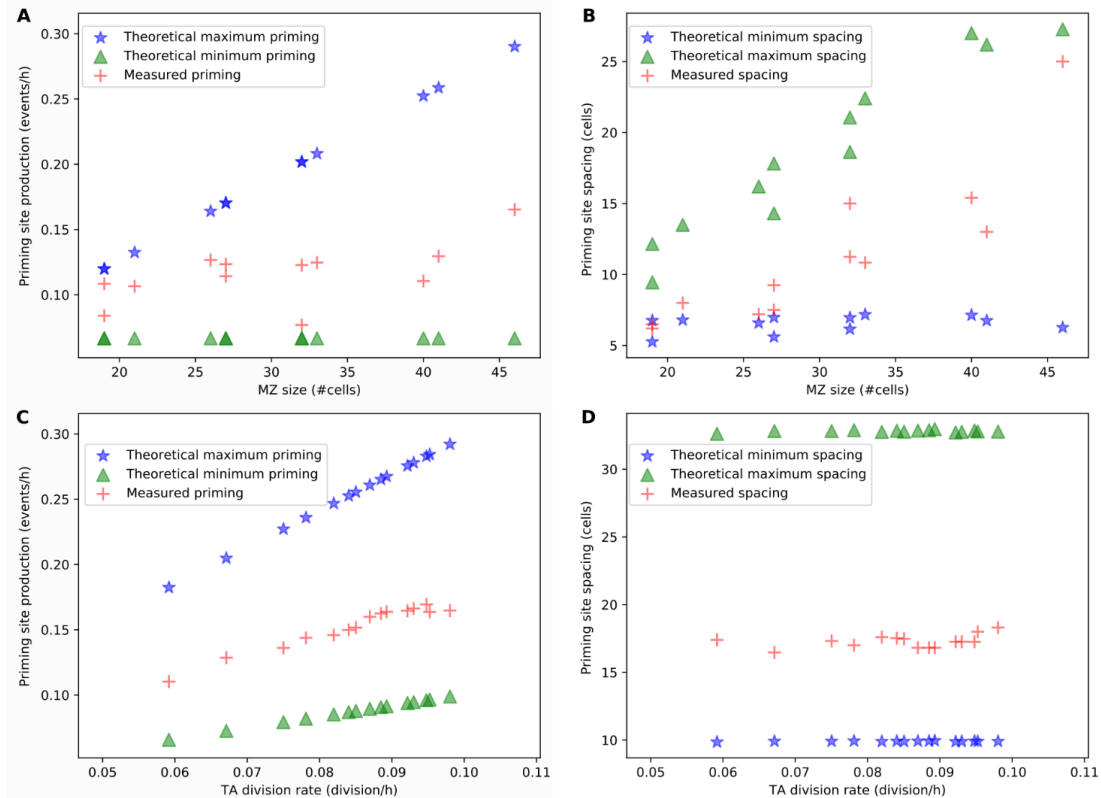


Figure 4.4. Priming morphospace, minimum (green triangle) and maximum (blue stars) priming site production rate and spacing determine the boundaries of the priming site morphospace. Simulated data (red plus) falls between the calculated boundaries. A) Priming site production as a function of meristem size, division rate was kept constant at 0.06cell/h. B) Priming site spacing as a function of meristem size, division rate was kept constant at 0.06cell/h. C) Priming site production as a function of cell division rate, meristem size was kept constant at 35 cells. D) Priming site spacing as a function of cell division rate, meristem size was kept constant at 35 cells.

To understand the other boundary of the priming morphospace, the maximum priming site production rate and minimum PSS, we need to consider the other extreme case in which all cells divide asynchronously. In this case the formation of a large-small cell pair can occur at all positions in the window. Since divisions are fully uncorrelated all cells having a final division in the window can have a lower neighbor that divides once more at a position above this spatial window. This implies that the upper boundary of priming frequency can be described as:

$$P_{freq(max)} = TA_{div} * window$$

with window size proportionate to MZ size ($\beta * MZ$) (Figure 4.4A and 4.4B, blue stars). To determine the lower boundary for PSS we again need to divide cell production over priming frequency:

$$PSS_{(min)} = \frac{cellproduction}{TA_{div} * window}$$

Since cell production can be described as $\ln(2) * MZsize * divfreq$ (Beemster and Baskin, 1998) and $window = \beta * MZsize$, the formula of $PSS_{(min)}$ evaluates to $\frac{\ln(2)}{\beta}$ and implies, that TA division frequency nor meristem size impact PSS when division are completely asynchronous (Figure 4.4B and 4.4D, blue stars).

In plant roots actual division dynamics are in between the above two extremes of fully synchronous versus fully asynchronous divisions, with slower stem cell divisions responsible for producing asynchronous clones of transit amplifying cells. The formation of large-small cell pairs in this clonal case can occur at the lowest position of the window, as for the fully synchronous case, and at window positions corresponding to the border between two subsequent clones where the upper clone divides for the last time within the window while the below clone divides once more above the window. From the above it finally follows that priming frequency can be described as:

$$P_{freq} = TA_{div} + TA_{div} * (window - 1) * async$$

where $async$ is a measure of clone density and $window > 1$. If all cells divide synchronously $async = 0$, for completely asynchronous divisions $async = 1$, while in case of clonal divisions $0 < async < 1$. Indeed, when analyzing a simulation data set for settings with clonal growth dynamics, measured priming frequencies and priming site densities fall between the predicted priming morphospace boundaries (Figure 4.4, red).

Our analysis and model simulations thus suggest that the observed variation in priming dynamics for similar cell production can be explained from similar cell production rates arising from different combinations of meristem size, TA and stem cell division rates, leading to a different position in priming morphospace.

4.2.3 *In planta* growth dynamics determines access to morphospace

To confirm the *in planta* validity of our upper and lower limit predictions for priming morphospace we reanalyzed our previously obtained experimental data (van den Berg et al., 2021) through plotting for each individual plant data point the observed priming frequency and PSS as well as the theoretically predicted minimum and maximum priming frequencies and PSS. While in our previous study we measured priming dynamics under control conditions as well as under a series of hormonal perturbations, we here restrict our analysis to the data obtained under control (MS) conditions. To perform our analysis we need to take into consideration that in contrast to our simulations *in planta* priming occurs at 2 non-synchronized xylem poles while the sidedness of a priming event cannot be derived from the relatively low resolution experimental observations. The priming site production increase due to non-synchronized xylem poles might depend on the cell production in the meristem, with lower cell production resulting in a lower chance for an asynchronized priming event to occur than for higher cell production rate ranges. Thus, to correct for *in planta* two sided priming, we tried a range 1.2-2 fold increase to compute the upper boundary of the priming site production and concomitant lower boundary of the priming site spacing. We found that any factor between 1.5-2 ensures a priming site morphospace that envelopes the priming frequency and spacing data over the whole range of cell production rates. Additionally, we take into account that priming occurs in the vasculature tissue with an average 1.5 times faster division rate as the cortex where cell production rate was measured (Lavrekha et al., 2017, Rahni and Birnbaum, 2019). Our results confirm that

experimentally observed priming frequency and PSS fall within the theoretically predicted priming morphospace boundaries (Figure 4.5A and 4.5B).

To compare *in planta* with model data, we performed simulations with a similar range of meristem sizes and cell production rates. Interestingly, when comparing simulation data with *in planta* data (Figure 4.5A-B versus 4.5C-D), *in planta* data seems concentrated towards the maximum predicted priming site production and minimum predicted PSS, especially for larger meristem sizes. The observed higher priming site production rate for larger meristems *in planta* suggests a higher level of asynchronicity. To verify whether *in planta* division asynchronicity is indeed larger than in our model we measured maximal clone sizes. For this we make use of the fact that the (near) synchronously divisions within a clone result in similar cell sizes while asynchronicity between clones should result in across clone size differences (see methods). In agreement with the higher priming frequency and smaller PSS observed *in planta*, the results show smaller maximum clone sizes and hence a higher asynchronicity *in planta*, particularly for larger meristems. *In planta* maximum clone size appears to remain constant over a broad range of meristem sizes while in simulations clone size increases with meristem size (Figure 4.5E). These results suggest that an increase in stem cell division frequency, with increasing meristem size may occur *in planta*, which was not incorporated in our model simulations. Furthermore, when computing TA division frequency from cell production and meristem size, *in planta* we observe decreasing division rates with increasing meristem size, while TA division rate in the model remains approximately constant with meristem size (Figure 4.5F).

It is the ratio of stem cell division rate versus transit amplifying division rate that determines the number of asynchronous clones within a meristem. Importantly, while both increasing stem cell division rates and decreasing transit amplifying division rates thus enhance asynchronicity they have differently sized and opposite direction effects on overall meristematic cell division rate and hence cell production, with increasing stem cell division rate moderately enhancing and decreasing transit amplifying division rate significantly decreasing cell production. We performed additional simulations to investigate how faster stem cell divisions, alone (Figure 4.5G and 4.5H, green) or combined with reduced TA division rates (Figure 4.5G and 4.5H yellow) may explain the differential *in planta* usage of priming morphospace and accompanying smaller clone sizes. Consistent with asynchronicity being

approximated by $\frac{SC_{freq} * \log_2(MZsize)}{TA_{freq}}$, and hence clone size with the inverse of this relation, an increase in stem cell division rate and decrease in transit amplifying division rate additively decrease the slope with which clone size increases with meristem size (Figure S4.1). Interestingly, an isolated increase in SC rate had a positive effect on the PS production rate for meristem sizes <35 while combined with a decrease in TA division rate instead an increase in PS production rate was observed for meristem >35 cells. Furthermore, the increased SC rate combined with a decreased TA division rate strongly increased the density of the priming sites by reducing the priming site spacing with 30-40% (Figure 4.5H).

These results can be understood as follows, for smaller meristem sizes for which priming frequency is not yet limited by large clones an increase in stem cell division rate enhances both clonal asynchronicity and increases overall division frequency, both enhancing priming frequency (Figure 4.5G and 4.5H, green, Figure S4.1C). For larger meristems clone size is limiting for priming frequency, thus while the increased stem cell rate might result in a few extra clones in the meristem the large clones limit the occurrence of independent divisions in the window. When in addition to increased stem cell rate the TA rate is decreased, average cell division rate and hence cell production is lowered (Figure S4.1C). As a consequence, the positive effect of increased clonal asynchronicity from

increased stem cell and decreased transit amplifying cell division rates on priming frequency is cancelled by the negative effect of a lower cell production rate on priming frequency for lower meristem sizes. In contrast for larger meristems, where priming is limited by large clone sizes and cell production is high already because of large meristem size (Figure S4.1C), the positive effect of more smaller clones outweighs that of the reduced cell production and results in an increase in priming frequency (Figure 4.5G, yellow). Additionally, the lower cell production rate resulting from the decreased TA rate results in a strong decrease in the priming site spacing and thus increases the density of the priming sites (Figure 4.5G, yellow).

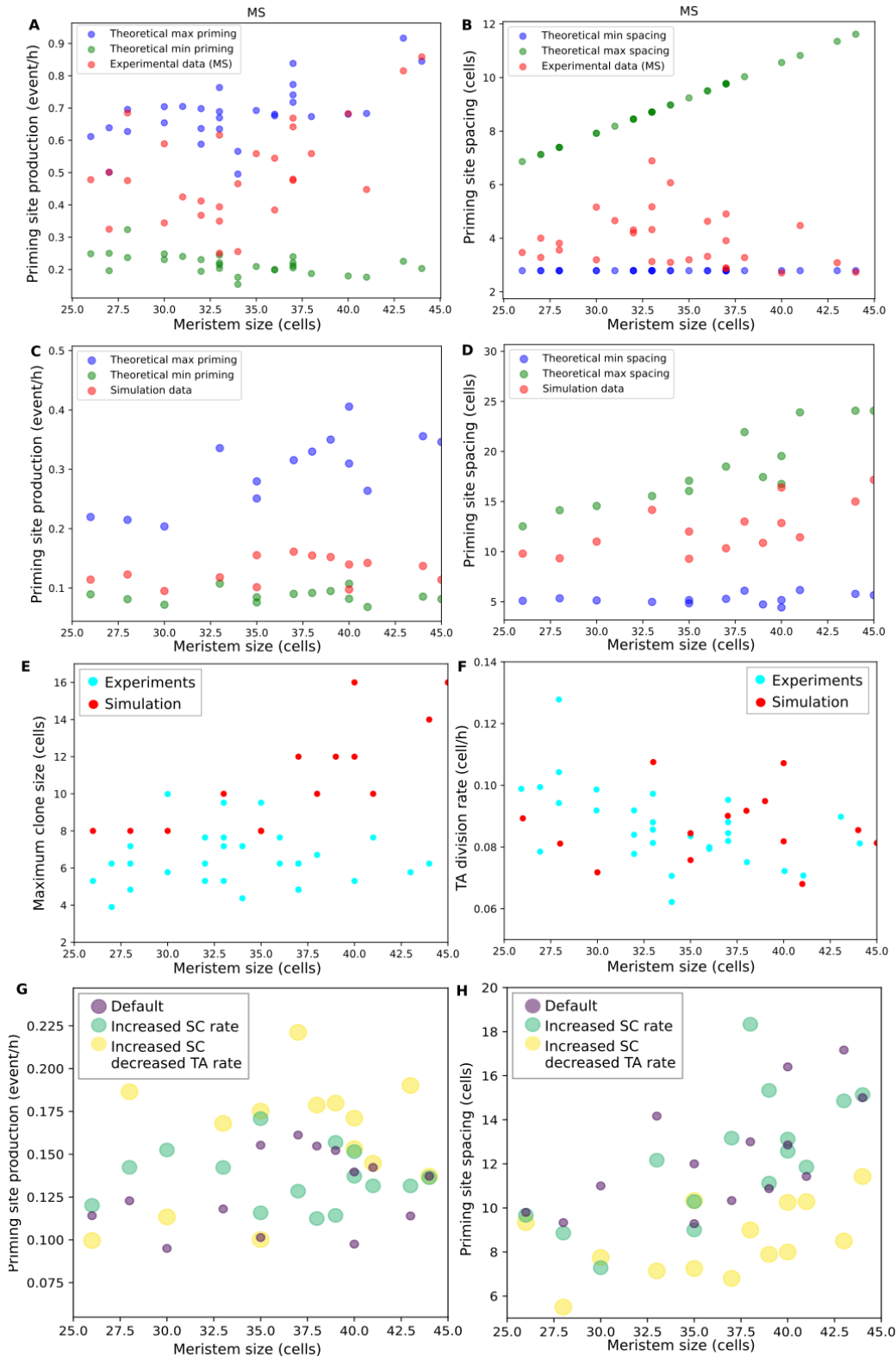


Figure 4.5. Position in the priming morphospace depends on the ratio between SC activity and TA division rate for a given meristem size. Minimal (green), maximal (blue) and data (red) for A) in planta priming site production rates, B) in planta priming site spacing, C) simulation priming site production rate and D) simulation priming site spacing. E) Maximal clone size and F) TA division rate for in planta (cyan) and simulation (red) data. G) Priming site production rate and H) priming site spacing for simulations with a default (purple), increased (30%) SC activity (green) or increased SC activity combined with a decreased TA division rate (~30%) (yellow).

Summarizing, our analysis suggests that *in planta* the interdependence of meristem growth characteristics, with TA division rate decreasing and SC division rate increasing with MZ size, result in a particular occupancy of priming morphospace biased towards high priming frequencies and low priming site spacing.

Additionally, they indicate that it is non-trivial to predict the effect of for example a TA division rate change on priming dynamics, and that for this also meristem size and SC division rates need to be taken into account.

4.2.4. Growth transitions induce movement through priming morphospace

In addition to meristem growth factors determining priming site numbers and density being interdependent, these are also highly dynamic during plant development. Indeed, coinciding with MR meristem growth related changes, be it during initial meristem set up, or as a result of abiotic stress or nutrient conditions, often a concomitant adjustment in LR numbers and density can be observed (Bhalerao et al., 2002, Gruber et al., 2013, Koevoets et al., 2016, Shahzad and Amtmann, 2017). As an example case, under calcium starvation it has been observed that MR length decreases and LR density increases (Gruber et al., 2013). When we simulate this with the assumption that the decrease in MR size results from a decrease in meristem size, we observe an increase in both priming site density and overall numbers consistent with the experimental observations (Figure 4.6). This implies that the experimentally observed changes in LR density may not require an explanation fully separate from the changes in MR size.

Importantly, for nitrogen starvation a less clear link between MR size and LR density was found (Gruber et al., 2013). Indeed, meristem size can change through a number of different mechanisms, such as an increase of the cytokinin response receptor ARR1 (Zhu et al., 2015) or down regulation of PIN transporters (Liu et al., 2015), increases in SC activity due to toxic stress (Timilsina et al., 2019), and reduction or increase of TA cell division rates (Lai et al., 2007, Naulin et al., 2020, West et al., 2004, Yang et al., 2014). Some of these mechanisms merely involve meristem size, while others involve, -indeed arise through- concomitant changes in SC or TA division rates. Our results indicate that it is the combination of meristem size, SC and TA rate that determines priming site production and spacing. As a consequence, in absence of data on all these parameters it is hard to predict how a change in meristem size will translate into a change in priming dynamics and indeed only in certain cases a clean increase in priming site density may be observed.

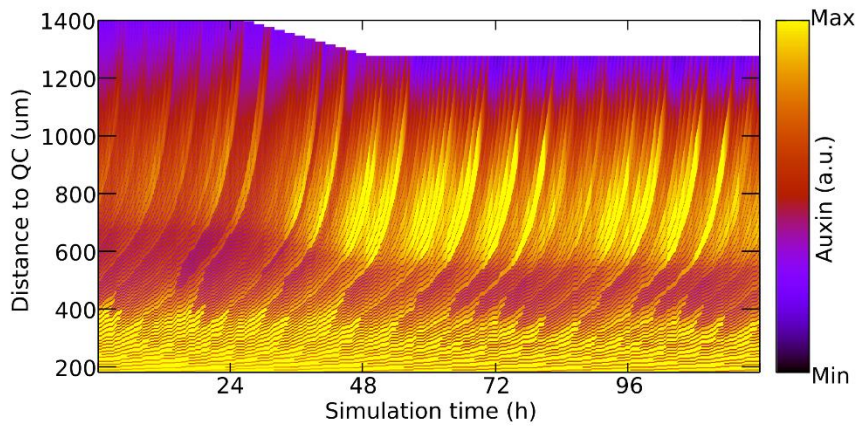


Figure 4.6. Kymograph for a simulation where a growth transition occurs with a 25% decrease in meristem size. Transition occurred over a time period of 24h, starting at $t=26h$.

One of the most profound growth transition occurs in the first days after germination (Bhalerao et al., 2002). The activation, expansion and subsequent stabilization of the root meristem coincides with the onset and subsequent speedup in priming frequency (Xuan et al., 2015). To test whether the increase in meristem size during the first 6 days after germination could be causal for the onset and increase in priming frequency, we mimicked a developing root through linearly increasing meristem size from 7 to 45 cells over a time course of 6 days, measuring the number of priming sites generated per day (Figure 4.7, white numbers). The results show an increase in priming frequency due to the meristem size driven increase in cell production that saturates as meristem size stabilizes.

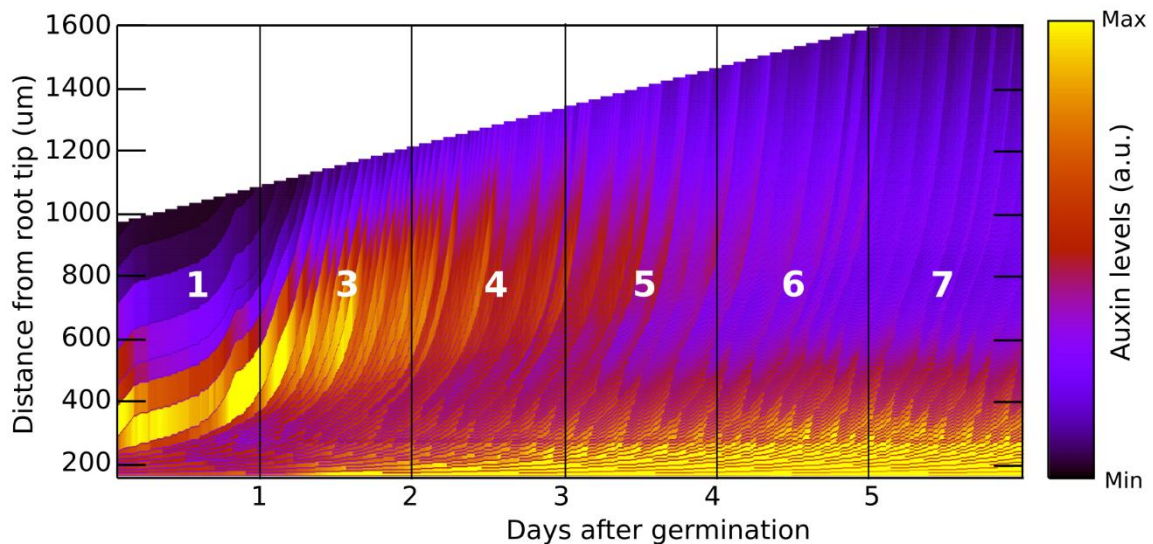


Figure 4.7. Kymographs for developing root after germination, meristem size increases from 7 to 45 cells in 5 days, cell cycle is 9h. Simulations were run until auxin equilibrium was reached before applying post germination meristem outgrowth. Meristem growth resulting in expansion from 5 to 45 meristem cells over the time course of 5 days was superimposed.

4.3. Discussion

LR priming involves the periodic oscillations of auxin and its downstream processes to prime cells for future LR formation. Priming has been shown to be a semi-regular process and although many factors can influence priming amplitude and therefore priming success, the frequency itself appears to be resilient with only growth-related factors inducing changes in frequency. In our previous study we showed that priming site numbers and density correlate with cell production due to their dependency on meristem size and division rate (van den Berg et al., 2021), however, when comparing within production range priming site numbers and density we here observed a large variation in outcome. Therefore in this study we aimed to elucidate the exact dynamics underlying LR priming and showed how meristem size, division rate and stem cell activity together define a morphospace for priming site numbers and density. We made use of the possibilities of a computational root model to test ‘what if’ scenarios and showed that in case of fully synchronised divisions, priming numbers will be limited by the division rate. Similarly, for fully asynchronised divisions priming site density is limited by the relative size of the priming window in the meristem and the number of cells produced per cell cycle. After determining the boundaries of the priming morphospace we showed that *in planta* high priming site numbers and density are favoured due to the interrelatedness of meristem growth factors meristem size, stem cell and transit amplifying division rates. Finally, we demonstrated that developmental transitions involving changes in meristem growth dynamics will induce movement in this priming morphospace that will depend on the initial state before the growth transitions.

In this study we have shown, although in an indirect manner, that *in planta* the ratio between stem cell and TA activity decreases with increasing meristem size and that this has a positive effect on priming site numbers and density. This increasing ratio thus ensures high priming site number and densities for meristem sizes where otherwise large clones would be expected with a low priming site frequency and density as a result.

Supporting this interdependence of root meristem growth factors, in a recent study we demonstrated that, through affecting the spread of PLETHORA transcription factors, master regulators of meristem function, stem cell division rate is an important determinant of root meristem size in addition to the previously identified importance of levels of auxin, cytokinin and PLETHORA expression (Rutten and Ten Tusscher, 2021, Salvi et al., 2020). Additionally environmental factors have been shown to impinge on stem cell activity by either decreasing (Zhang et al., 2010) or increasing (Chen et al., 2011, Vilarrasa-Blasi et al., 2014) their activity rate.

Next to environmental changes affecting stem cell activity, nutrient status as well as abiotic stress are also known to affect root growth through alterations in meristem size and division rate (Gruber et al., 2013, Koevoets et al., 2016). Nutrient status and abiotic stress also affect LR density and numbers, which is often considered a condition specific response that requires its own mechanistic explanation separate from the changes observed in MR growth dynamics. Based on our findings, we instead suggest that changes in LR numbers and density observed concomitantly with changes in MR growth could at least be partially explained by adjustments in priming dynamics that become translated to changes in LR numbers and density. When exploring this idea in our computational model we find that increased SC activity, decreased TA activity as well as meristem size reduction often lead to an increase in priming site density. We found that the effect of increased SC activity, either alone or in combination with decreased TA activity, on priming site production or spacing depended on the meristem size. While smaller meristems seem to increase priming site production upon increased SC activity, they lose this increase when a decrease in TA activity is additionally applied. In contrast,

larger meristems did not benefit from an isolated increase in SC activity, yet increased both priming site production and strongly increased LR density when TA activity was additionally decreased. This indicates that when assessing changes in RSA upon nutrient deprivation it is important to compare plants with similar cell production ranges, age and root length. For example, a study by Gruber et al. (2013) compared the effect of different nutrients on the MR and LR density. However, nutrient conditions were started at different plant ages, with some nutrients being applied at day 4 after germination while others were applied at day 7 after germination (Gruber et al., 2013). Since during the first 7 days after germination an increase in meristem size and cell production rate and a concomitant increase in priming site production can be observed (Bhalerao et al., 2002, Salvi et al., 2020, Xuan et al., 2015), we wonder to what extent differences in RSA adaptation to different nutrients may in fact arise from the difference in priming site dynamics at the moment nutrient conditions were varied.

Another interesting observation is that although we previously have shown that priming site production as well as priming site spacing increases with cell production and in this way the reflux-and-growth mechanism can be distinguished from a Turing pattern or clock-and-wavefront model (van den Berg et al., 2021), in our current study we show that although this global trend holds, cell production can be negatively correlated to priming site production when clone size is limiting (Figure 4.5G and S4.1C). This results from the emergent nature of priming, where meristem size and TA division rate both, in a non-linear way, contribute to priming site production as well as priming site spacing. It is the combination of meristem size and the ratio between stem cell and TA rate that will determine the relative contribution of cell production to either priming site production or priming site spacing (Figure 4.8). Any adjustment in one of these three parameters will induce a shift in this balance and hence influence the density and production of priming sites.

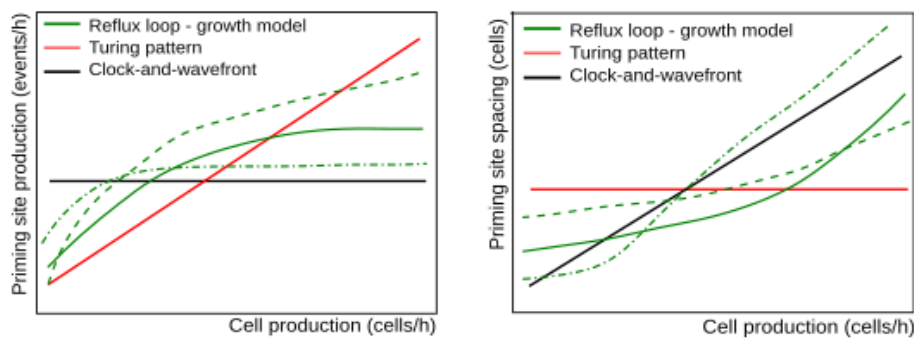


Figure 4.8. Priming site production (left) and priming site spacing (right) as a function of cell production for different models of lateral root priming. Turing pattern (red) predicts solely a linear change in priming site production while the clock-and-wavefront model predicts only a linear change in priming site spacing (black) in response to cell production variation. The reflux loop-growth model instead predicts a non-linear increase for both priming site production as well as priming site spacing, with the exact shape of the curve depending on the meristem size and the relative activity of TA versus SC division rate.

In summary the results of this study show how priming site numbers and density are shaped by *planta* meristem growth factors and their dependency on each other. The resulting dynamics can lead to behaviour that is often interpreted as a condition or stage specific response, such as increasing LR density when plants are nutrient deprived or an increase in priming site numbers during early development yet is likely to at least partially arise from changes in priming dynamics. Future research is needed to address to what extent changes in priming dynamics can explain changes in LR numbers and density, in order to establish what changes still require a separate, specific explanation.

4.4. Material and methods

4.4.1 Experimental methods

The experimental data used here was identical to the data obtained and described in chapter 3. Information regarding the experimental set up and data analysis for meristem size, division frequency, priming frequency and LR spacing can be found in chapter 3 (van den Berg et al., 2021).

For the current study one additional analysis was performed on the data to determine the maximal clone size in the meristem (van den Berg et al., 2021). To determine clone size, we make use of the fact that cells within a clone divide and grow near synchronously, resulting in within clone cell size similarity. First, cell sizes in the cortical cell file were obtained by using Cell-O-tape, a Fiji plugin, similar to the method used in chapter 3 to obtain meristem size. Next, clone size of the largest clone was determined by counting the number of neighbouring cells in the vertical plane with a similar cell height, starting to count from the top of the meristem downwards. Given the presence of two cortical cell files, the maximum largest clone size found from the two cell files was taken. However, similar trends were obtained if instead the average of the two largest clone sizes was taken (data not shown). To determine clone size, we define cell size similarity, taking into account that cell growth is exponential, and hence a small asynchronicity in cell division and growth within a clone result in larger absolute valued size differences late in the cell cycle when cells are larger as compared to early in the cell cycle. Therefore, we first derive for the cell currently under consideration its “position” in the cell cycle from the minimal cell height in the meristem, $Height_{min}$ and the cell division rate, $\frac{cellproduction}{ln(2)MZsize}$:

$$time_{current} = \frac{\log_2\left(\frac{height_{current}}{height_{min}}\right)}{divisionrate} + / - \frac{\gamma}{divisionrate},$$

where the first term calculates the cell’s position in the cell cycle and the second term allows for small variations in cell cycle position due to noise in cellular growth rate, we thus compute a small range of positions within the cell cycle, rather than a single position. γ was set between 0.75-1.5 but the exact value did not affect the outcome of the analysis.

Next, we used this range of positions in the cell cycle $time_{current}$ to evaluate the expected range of cell heights of the below cell if this cell would still belong to the same clone:

$$height_{target} = height_{min} * 2^{time_{current} * divisionrate}$$

If the height of the below cell falls within the calculated range for $height_{target}$, this procedure will be repeated for the next cell below without changing $time_{current}$. If instead the cell height of the below cell does not fall within the $height_{target}$ range it is assumed that this cell represents the topmost cell of a new clone and a new $time_{current}$ will be.

4.4.2 Computational methods

The model used for this study was previously described in chapter 3 (van den Berg et al., 2021). Default parameter settings as described in chapter 3 were used for all simulations. For this study one additional model output analysis was done to measure the maximum clone size at the end of the simulation. To do so, similar to the experimental analysis, groups of cells with similar cell height were counted starting from the end of the meristem. Due to the deterministic nature of the model cell height similarity was here defined as $CellHeight_i = CellHeight_j$, (i.e., identical cell height) were $CellHeight_i$ is the cell above and $CellHeight_j$ the below cell.

4.5 Supplemental information

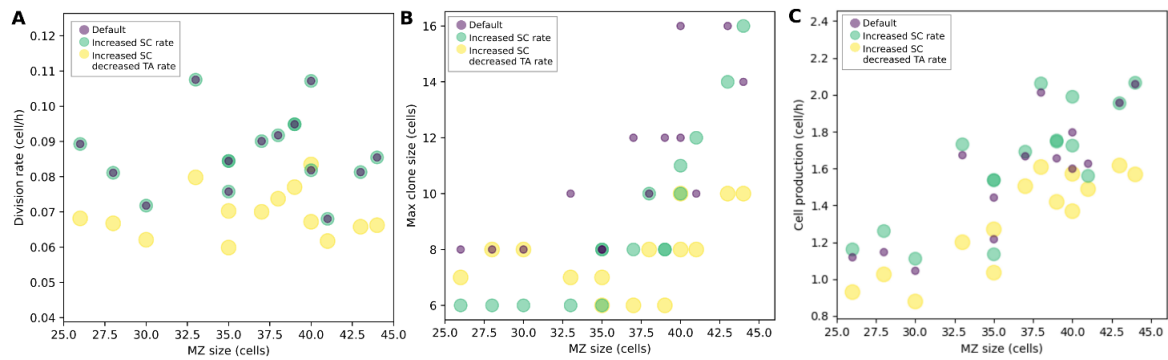


Figure S4.1. Changes in (A) division rate, (B) maximum clone size and (C) cell production as a function of meristem size in response to ~30% increase in SC division rate alone (green) or ~30% decrease in TA and 30% increase in SC division rate (yellow). Simulation results with default SC and TA division rates (purple) are added for reference.

5

Modeling halotropism: a key role for root tip architecture and reflux loop remodeling in redistributing auxin

**Thea van den Berg Ruud A. Korver Christa Testerink and
Kirsten H. W. J. ten Tusscher**

Development (2017)

Abstract

A key characteristic of plant development is its plasticity in response to various and dynamically changing environmental conditions. Tropisms contribute to this flexibility by allowing plant organs to grow from or towards environmental cues. Halotropism is a recently described tropism in which plant roots bend away from salt. During halotropism, as in most other tropisms, directional growth is generated through an asymmetric auxin distribution that generates differences in growth rate and hence induces bending. Here, we develop a detailed model of auxin transport in the *Arabidopsis* root tip and combine this with experiments to investigate the processes generating auxin asymmetry during halotropism. Our model points to the key role of root tip architecture in allowing the decrease in PIN2 at the salt-exposed side of the root to result in a re-routing of auxin to the opposite side. In addition, our model demonstrates how feedback of auxin on the auxin transporter AUX1 amplifies this auxin asymmetry, while a salt-induced transient increase in PIN1 levels increases the speed at which this occurs. Using AUX1-GFP imaging and *pin1* mutants, we experimentally confirmed these model predictions, thus expanding our knowledge of the cellular basis of halotropism.

5.1 Introduction

Plant development is characterized by a large degree of flexibility, termed developmental or phenotypic plasticity. As a result of their sessile nature, plants have very limited influence over the environmental conditions they find themselves in. As a consequence, plants had to evolve the capacity to survive in different environments as well as dynamically changing environmental conditions by making their developmental programs dependent on environmental signals. The resulting phenotypic plasticity enables plants to flexibly adjust to their environmental conditions. This developmental plasticity may influence overall architecture, for example, the layout of the root system, by influencing meristem size and hence the rate of root growth ((Aquea et al., 2012, Chapman et al., 2011, Jain et al., 2007, Liu et al., 2015, West et al., 2004) as well as the number of developing or outgrowing lateral roots (Jain et al., 2007). Another, perhaps more subtle, adaptation of plant development involves the directional growth of plant organs towards or away from a perceived stimulus, such as the gravity vector (Abas et al., 2006, Sukumar et al., 2009), light (Laxmi et al., 2008, Sassi et al., 2012, Wan et al., 2012) or nutrients (Niu et al., 2015). Recently, we described a new tropism, called halotropism, that entails the directional growth of plant roots away from salt (Galvan-Ampudia et al., 2013).

At the base of most plant tropisms lies an asymmetric distribution of the plant hormone auxin (Went, 1974) that generates asymmetric growth rates and thus causes bending. Auxin patterns are strongly determined by auxin transport. Auxin can enter cells both via passive diffusion as well as active transport mediated by the AUX/LAX family of importers (Rutschow et al., 2014, Swarup et al., 2008, Bennett et al., 1996). Auxin importers have a tissue-specific expression pattern (Swarup et al., 2005, Péret et al., 2012, Swarup et al., 2001, Bennett et al., 1996) leading to the preferential retention of auxin in particular tissues. Auxin can only leave cells via active transport, a process that is dominated by the PIN family of exporters (Friml et al., 2003, Paponov et al., 2005, Petrasek et al., 2006, Wisniewska et al., 2006). In addition to having tissue-specific expression domains, PIN proteins have a tissue and PIN-type-specific polar membrane pattern, leading to directional auxin transport fluxes (Benková et al., 2003, Friml et al., 2002b). In plant roots, a reverse fountain PIN pattern generates a symmetrical auxin gradient with a maximum close to the root tip (Blilou et al., 2005, Grieneisen et al., 2007). During root tropisms, bending is caused by an asymmetric elevation of auxin in the expansion zone that causes an asymmetric repression of expansion rates (Scheitz et al., 2013, Thimann, 1936).

The best studied tropism in plant roots is gravitropism. Upon a gravitropic stimulus, columella cell statoliths sediment onto the downward oriented membrane face (Eshel and Beeckman, 2013). Via an unidentified mechanism, this causes the polarization of the normally apolar PIN3 and PIN7 proteins onto the downward membrane (Friml et al., 2002a). As a consequence, most auxin arriving in the root tip now becomes transported towards the downward side. The auxin dependence of PIN2 membrane levels (Abas et al., 2006, Chen et al., 1998) and AUX1 gene expression levels (Laskowski et al., 2006, Laskowski et al., 2008) enable these transporters to amplify this initial auxin asymmetry and transport part of the excess auxin towards the expansion zone where it can affect expansion rates and induce root bending (Abas et al., 2006, Bennett et al., 1996, Chen et al., 1998, Luschnig et al., 1998, Muller et al., 1998, Swarup et al., 2001). Thus, while PIN3 and PIN7 appear to have a primary, asymmetry-inducing role, PIN2 and AUX1 appear to have a secondary, amplifying and transducing role (Eshel and Beeckman, 2013).

Intriguingly, we reported in an earlier study that the salt-induced auxin asymmetry causing halotropic root bending co-occurred with a reduction of epidermal PIN2 at the salt-exposed side of the root. No asymmetries in other PINs were reported. These data imply that PIN2, which has a mostly secondary

role in gravitropism (Abas et al., 2006, Kleine-Vehn et al., 2008, Wan et al., 2012), plays a primary, asymmetry-generating role in halotropism. The gravitropism induced polarity switch in PIN3 and PIN7 in the root tip, where all auxin fluxes converge, biases auxin transport in one direction. This causes an auxin increase at one side of the root and an auxin decrease at the opposite side as two sides of the same coin. In contrast, although it can be easily understood that the halotropism-induced reduction of epidermal PIN2 will lead to a decrease of auxin at the salt-exposed side, it is far less trivial to see how this should lead to a concomitant increase in auxin at the opposite side. As a consequence, currently two alternative scenarios remain possible. In the first, PIN2 is the sole auxin asymmetry generator, and the reduced transport of auxin at one side of the reflux loop somehow leads to a translocation of this auxin towards the opposite side of the reflux loop. Alternatively, another unidentified auxin asymmetry-generating source may be present under halotropism.

In the current study, we use a detailed model of auxin transport in the Arabidopsis root tip to investigate whether the measured changes in PIN2 are necessary and sufficient to explain the auxin asymmetries observed under halotropism. We combine our modeling with experiments aimed at unraveling the potential role of salt-induced changes in other PIN proteins in generating or amplifying auxin asymmetry, as well as to confirm predictions generated by our model. Our computer simulations reveal the crucial importance of taking into account a realistic wedge-shaped root tip architecture for studying root tropisms. In absence of this realistic architecture, a PIN2 reduction at the salt-exposed side fails to induce any auxin increase at the opposite side, while in its presence, a modest auxin increase is automatically induced. We show that this increase was enhanced substantially when taking into account the auxin dependence of AUX1 (Bennett et al., 1996) and PIN2 (Baster et al., 2013, Paciorek et al., 2005, Whitford et al., 2012). Furthermore, our model predicts that underlying this enhanced auxin asymmetry is an asymmetry in AUX1 and PIN2 patterns. We experimentally validate this prediction for AUX1, demonstrating that exposure to a salt gradient results in an elevation of AUX1 levels on the non-salt-exposed versus salt-exposed side. In addition, we experimentally demonstrate that exposure to a salt gradient induces a transient, symmetric upregulation of PIN1. Incorporating this in our model significantly amplifies the auxin asymmetry arising in the early phases of halotropism, thus speeding up the halotropic response. Finally, we experimentally validated this role of PIN1 in root halotropism, by showing that *pin1* mutants exhibit a delayed halotropic response.

Our study suggests that the observed changes in PIN2 are responsible for the primary generation of auxin asymmetry. This asymmetry is subsequently further enhanced by the feedback of auxin on PIN2 itself and AUX1, and effectively sped up by a transient upregulation of PIN1. Together, this provides the necessary and sufficient conditions for generating an auxin asymmetry capable of inducing effective root bending.

5.2 Results

5.2.1 Halotropic auxin asymmetry

To be able to judge whether the auxin asymmetries occurring in our simulations are sufficient to explain halotropic root bending, we first need to establish the amount of auxin asymmetry actually occurring during halotropism. For root tropisms, it is well known that auxin elevation leads to repression of cell expansion rates (Band et al., 2012, Mullen et al., 1998). However, it is less clear whether the concomitant decrease in auxin at the opposite side of the root contributes to growth rate asymmetry and bending by stimulating growth rate. Thus, we take a conservative approach, assuming that tropic bending is only caused by auxin elevation and growth inhibition.

In an earlier study (Galvan-Ampudia et al., 2013), we quantified the changes in DR5 and DII-Venus auxin reporter under halotropism. A ~20% reduction in DR5 and a ~20% increase in DII-Venus was found at the salt-exposed side, and a ~20% increase in DR5 and ~10% decrease in DII-Venus at the non-salt-exposed side. In an earlier study by Band et al. (2012), it was shown that during gravitropism a ~30% decrease in DII-Venus occurred on the lower side of the root and that this corresponds to an ~100% increase in auxin levels. Extrapolating these data, it was approximated that the change in DII-Venus observed during halotropism corresponds to a ~30-40% increase in auxin levels.

5.2.2 Root tip architecture

The key question of this study is whether and how a reduction of epidermal PIN2 at the salt-stressed side can cause a rerouting of auxin to the non-salt-exposed side of the root. We hypothesize that root tip architecture plays a key role in this process. To investigate this, we developed three alternative root tip architectures. In the first, the baseline model, a highly simplified rectangular representation was used, similar to previous studies (Grieneisen et al., 2007, Laskowski et al., 2008, Mahonen et al., 2014, Mironova et al., 2010) (Fig. 5.1A, left). In the second, extended model, a realistic wedge-shaped root tip architecture containing root cap tissue was applied (Fig. 5.1A, middle). This architecture somewhat resembles the root tip model used in Cruz-Ramírez et al. (2012). Differences are the narrower root tip architecture, the stronger curvature and resulting smaller left-right distances close to the root tip, and the decrease in number of vascular cell files close to the root tip in our model, that we believe more realistically represent Arabidopsis root tip topology. The third architecture (Fig. 5.1A, right) is a variant of the second, in which vascular cells and outer columella cells are increased in width. It should be noted that during root aging, typically all tissues increase in width (Zhu et al., 1998). We are not modeling root aging here, rather, we increased the width of only the internal tissues to specifically investigate the impact of left-right distances between epidermal and lateral root cap tissues for auxin rerouting. For further details we refer to the Materials and Methods section.

Note that while in the baseline model only vascular tissue connects directly to the quiescent center (QC) and epidermal, cortical and endodermal cell files end on the columella, in the extended model, these tissues all end in a curvature directly on or near the QC. Furthermore, in the extended model the columella tiers are directly connected to either the epidermis or the lateral root cap. Since these tissues have a predominantly upward orientation of PIN polarity, all columella tiers are thus connected to shootward-transporting tissue files. By contrast, in the baseline model columella cells are connected both to upward transporting epidermal and downward transporting cortical and endodermal tissue. These differences can be expected to subtly affect properties of the auxin reflux loop. Indeed, in Fig.

5.1B, it can be observed that in the extended model auxin levels are reduced in the columella, and elevated in the epidermal and outer vascular cell files (right) compared with the baseline model (left).

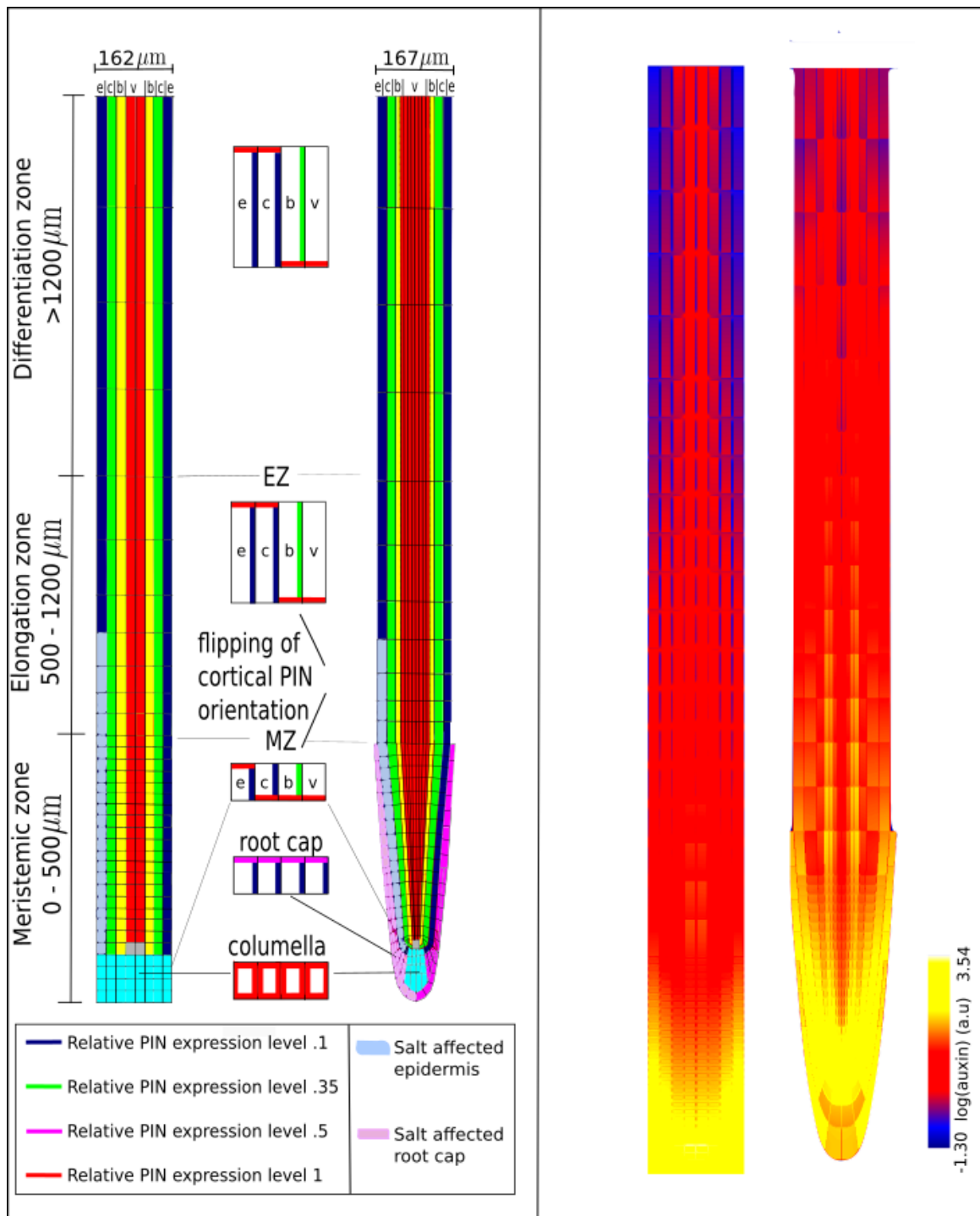


Figure 5.1. Overview of model tissue layout. (A) Layout of cell types, root zones and PIN polarity pattern in the baseline (left) and extended (middle) root models and a variant of the extended root model with larger left-right distances (right). Quiescent center (gray), columella (cyan), root cap (pink), epidermis (e, blue), cortex (c, green), border or endodermal cells (b, yellow) and vasculature (v, red). The root is divided into three zones, from bottom to top: meristem (MZ), elongation (EZ) and differentiation zone (DZ). Insets in the middle show the predefined PIN polarity pattern as present on the left side of the root in the different root zones (right side is a mirror image of the left side). An imposed salt gradient is assumed to influence PIN2 levels in lower left epidermal cells (light blue) and root cap cells (light pink). (B) Steady state non-salt stressed auxin pattern in the baseline model (left) and extended model (right).

5.2.3 Salt-induced changes in PIN2

To monitor salt-gradient-induced auxin rerouting, we plot the percentage change in epidermal auxin levels (Fig. 5.2A), overall root pattern of auxin levels (Fig. 5.2B) and auxin rerouting (Fig. 5.2C). In the latter, we measure in each root cell whether auxin levels are elevated by at least 1% in case of the rectangular root topology, or at least 10% in case of the wedge-shaped root topology. We record the earliest time point at which such an elevation occurs and depict this time with a color code, thus generating a map of temporal auxin rerouting.

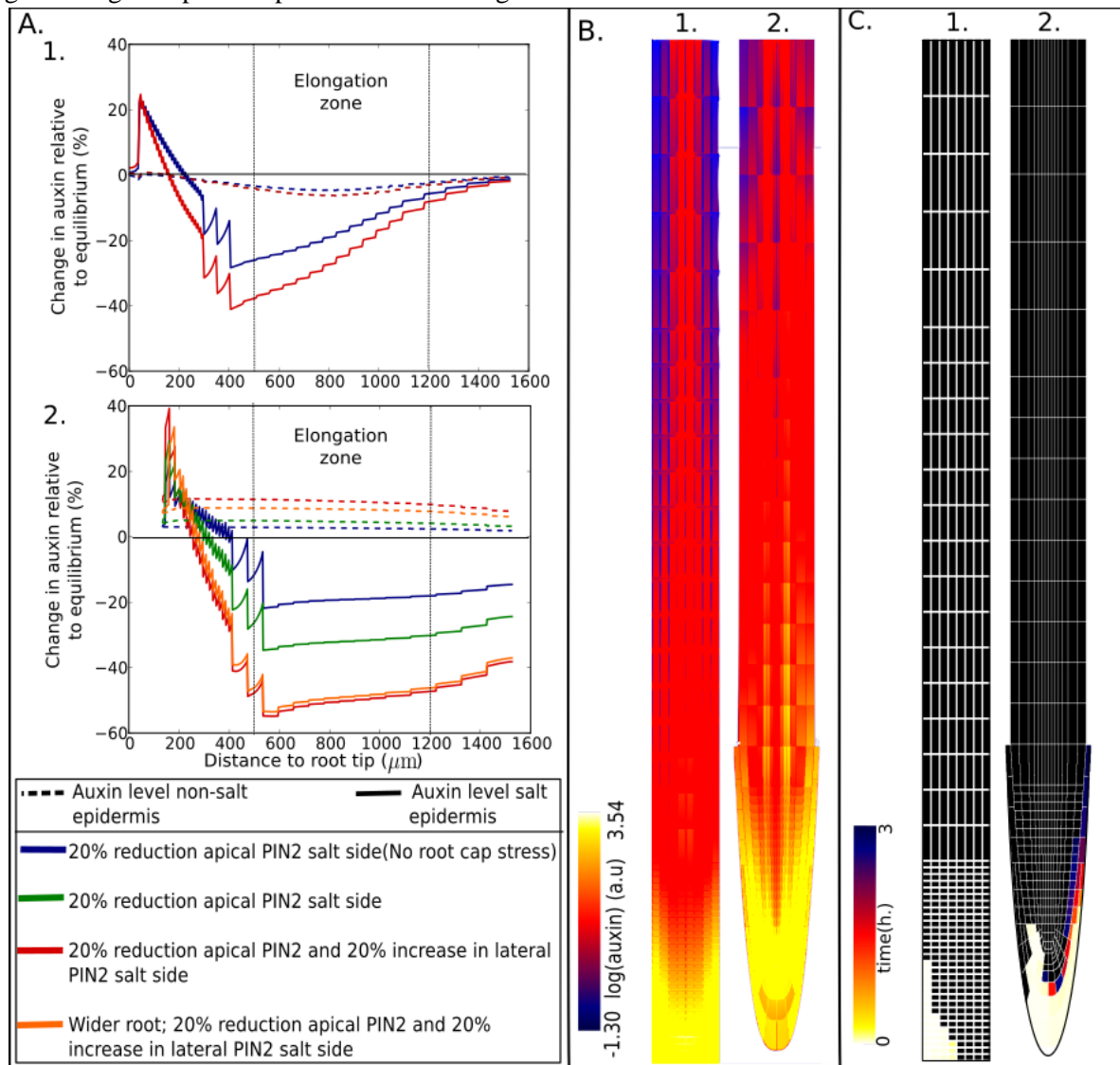


Figure 5.2. Influence of salt-induced changes in PIN2 protein levels. Salt stress was applied to the baseline and extended models, either by reducing only apical PIN2 levels or by also increasing lateral PIN2 levels. To investigate the impact of having a root cap, in the extended model, the reduction in apical PIN2 levels was applied only to epidermal cells, or to epidermal and root cap cells. To investigate the impact of distances between epidermal and root cap cells, results are also shown for an alternative realistic root tip architecture with increased left-right distances between epidermal and root cap cells, applying salt stress by decreasing apical and increasing lateral PIN2 levels. (A) Percentage changes in epidermal auxin levels on the salt-stressed and non-stressed side of the root relative to non-stressed conditions in the baseline (top) and extended (bottom) models. Location of the elongation zone is indicated. (B) Overall root tip auxin distributions for the scenario resulting in most auxin asymmetry in the baseline (left) and extended (right) models after 24 h of salt stress. (C) Auxin-rerouting maps for the scenario resulting in most auxin asymmetry in the baseline (left) and extended (right) model. For the baseline model, auxin rerouting was monitored by measuring the time at which at least a 1% increase in auxin levels occurred. For the extended model, a 10% auxin increase threshold was applied.

Halotropism simulations were started by applying a 20% reduction of apical PIN2 levels in epidermal cells on the salt stressed side of the baseline root model. This results in an asymmetric distribution of auxin (Fig. 5.2A, top and Fig. 5.2B, left). However, in contrast to experimental results where auxin decreases at the salt-stressed side and increases at the non-salt-stressed side, auxin decreases at both sides of the root. By mapping auxin rerouting, we see that halotropism results in a fast increase of auxin levels in the lowermost regions of the salt-exposed side (Fig. 5.2C, left). Clearly, the PIN2 reduction at the salt-exposed side results in a ‘traffic jam’, leading to auxin accumulation upstream of the transport blockage. No rerouting of auxin to the non-salt-exposed side occurs. Instead, the lower auxin levels at the non-exposed side imply that a reduction of overall reflux loop efficiency has occurred. Next, the same salt stress scenario was applied to our model extended with a realistic root tip architecture. Now, one can observe that besides a decrease of auxin at the salt-stressed side, auxin increases – albeit to a minor extent – at the non stressed side (Fig. 5.2A, bottom). Besides its modified root tip shape the extended model also contains root cap tissue. The rootcap has a similar PIN2 expression as the epidermis. It is therefore likely that the root cap PIN proteins are similarly affected by salt stress. When root cap stress is added to the model, the auxin increase at the non stressed side is augmented (Fig. 5.2A, bottom). Internalization of PIN2 from the apical membrane can hypothetically lead to elevated deposition of PIN2 on the lateral membrane. Indeed, our earlier data suggested a small increase in localization of PIN2 on the lateral inward membrane of cells at the salt-stressed side of the root (Galvan-Ampudia et al., 2013). Addition of this lateral upregulation in the extended model increases the auxin asymmetry (Fig. 5.2A, bottom; Fig. 5.2B, right), this was also the case when instead of a lateral upregulation, a basal upregulation of PIN2 was added (data not shown). However, when this same increase in lateral PIN2 was added to the baseline rectangular root model, the decrease in auxin on the non-salt-exposed side was even more severe (Fig. 5.2A, top). Thus, while lateral PIN proteins potentiate the translocation of auxin from the stressed to the non-stressed side in the realistic root tip architecture, in a rectangular root tip architecture this merely further cripples the effectiveness of the reflux loop.

Looking at the auxin rerouting map (Fig. 5.2C, right) for the wedge-shaped root, we observe a moderate rerouting of auxin to the lowermost parts of the non-salt-exposed side. Note, however, that for the wedge-shaped root, a threshold of 10% auxin increase is used for mapping auxin rerouting, whereas we used a 1% threshold value in the baseline square root model. Applying this lower threshold value in the wedge-shaped root model would reveal that auxin rerouting extends more shootward, consistent with the small increase in epidermal auxin levels (Fig. 5.2A, bottom; Fig. S5.1). The increase in auxin levels at the non-salt-exposed side of the root involves an initial rerouting against the normal direction of auxin transport as dictated by the polar PIN pattern of the reflux loop (Fig. 5.1A). This rerouting arises from auxin accumulating because of a lack of upward-oriented PIN2 transport, thereby increasing auxin uptake by the cells below it, now also causing accumulation in this cell, thus leading to the backward propagation of accumulated auxin. Only once the midline of the root is passed can this accumulated auxin join the normal direction of transport at the opposite non-salt-exposed side of the root. Our results suggest that a more realistic wedge-shaped root tip is essential for at least some of the accumulated auxin to reach this midline and become rerouted to the non-exposed side.

We hypothesized that the potential to re-route auxin to the non-exposed side critically depends on the shorter distance between left and right epidermis (and lateral root cap) tissue in the extended model compared with the baseline model. To test this, we use a variant of the extended model in which the root tip still has a wedge shape and contains a lateral root cap, but these distances have been increased

(Fig. 5.1A, right). This results in a reduction of the auxin increase at the non-salt-exposed side of the root (Fig. 5.2A, bottom), thus confirming our hypothesis.

Note that the maximum observed increase in auxin levels at the non-stressed side of the root are 12-14% (extended model, salt-stress induced decrease of apical and increase of lateral PIN2 levels). This is substantially less than the auxin increase observed during halotropism experiments.

5.2.4 AUX/LAX pattern and auxin feedback on its expression

Until now, influx of auxin from the walls into the cell was assumed to be equal for all cells. However, active import of auxin occurs by AUX/LAX membrane proteins, which exhibit a tissue-specific expression pattern (Bennett et al., 1996, Swarup et al., 2001, Péret et al., 2012). In gravitropism, AUX1 is essential for the adequate propagation of the initial auxin asymmetry (Bennett et al., 1996, Swarup et al., 2001). Therefore, we decided to investigate the potential role of AUX/LAX importers in halotropism. Focusing on the changes in auxin levels in the elongation zone of the root ($\geq 500 \mu\text{m}$ from root tip), incorporation of the AUX/LAX tissue-specific expression results in an increase of auxin levels on both sides of the root (Fig. 5.3A). This logically follows from the preferred retention of auxin in AUX/LAX-expressing cells, such as the epidermis. Overall, auxin asymmetry actually decreased as a result of AUX/LAX incorporation into our model. However, the expression of auxin importers is known to be positively regulated by auxin (Laskowski et al., 2006, Laskowski et al., 2008). This auxin dependence may allow AUX/LAX importers to respond to and amplify auxin asymmetry. Earlier *in silico* studies have demonstrated the patterning potential of auxin feeding back on its own transporters (Runions et al., 2014). Addition of this auxin dependence indeed led to an increase in asymmetry, specifically the non-stressed side increased in auxin level (Fig. 5.3A), resulting from a substantially increased rerouting of auxin to this side (compare Fig. 5.2C, right, and Fig. 5.3B). Indeed, auxin levels at the non-salt-exposed side now increased by $\sim 30\%$, which is close to the factor 1.3-1.4 increase we estimated to occur during halotropic root bending. Another difference is that compared with Fig. 5.1B, middle, and Fig. 5.2B, right, the auxin pattern in Fig. 5.3B more closely resembles experimentally measured patterns with low auxin levels in meristematic epidermal cells, and epidermal auxin levels increasing above the end of the root cap where the elongation zone starts (Band et al., 2014, Brunoud et al., 2012) (see also Fig. S5.2). Clearly, incorporating realistic AUX/LAX patterns is crucial for correctly simulating auxin patterns. Underlying the enhanced halotropic auxin asymmetry, we see that AUX/LAX expression decreased on the salt-exposed side and increased on the non-exposed side (Fig. 5.3B). This asymmetry in AUX/LAX expression is not restricted to the epidermis, as the auxin importers are also asymmetrically expressed in the vasculature (Fig. 5.3B). This vascular asymmetry is consistent with the observed asymmetry in auxin signaling in the vasculature in halotropism experiments (Galvan-Ampudia et al., 2013).

Next, we set out to experimentally validate the asymmetry in AUX/LAX expression predicted by our model, focusing on AUX1 as the major auxin importer involved in tropisms. We assessed AUX1 membrane occupancy patterns, assuming that AUX1 membrane occupancy is linearly related to AUX1 expression levels, as is the case in our model. Fig. 5.3C shows an AUX1 pattern in a control root, which is expected to have a symmetric AUX1 pattern. Note the apparent asymmetry in vascular AUX1 patterns, which is due to the protophloem cells not always lying symmetrically in the focal plane. While this is something that can be avoided in many studies, this is not the case in our study where we do not want to interfere with root orientation relative to the salt gradient. For these reasons, we focus on epidermal AUX1 patterns for which both sides are clearly visible (Fig. 5.3C). As can be seen in Fig. 5.3B, our model predicts AUX1 patterns to be symmetric close to the root tip, and start diverging

shootward from the rootcap. To test for such a spatial pattern, we measured AUX1 levels in the epidermal outer membranes, allowing us to assess the longitudinal AUX1 membrane pattern starting from the rootcap and going shootwards, and determine the development of left-right differences along this axis by computing ratios between non-exposed and salt-exposed sides (Fig. 5.3D). Consistent with our model predictions, close to the root cap, salt-exposed roots show an approximately symmetric AUX1 pattern comparable to that of control roots (ratio close to 1), whereas higher up, asymmetry builds up with the non-exposed side having higher AUX1 levels than the salt-exposed side (ratio close to 1.45). We tested for statistical significance of these findings by binning AUX1 ratios in 5000 μm spanning length segments for both salt-exposed and control roots, using a double-sided t-test to test per segment whether AUX1 ratios differ significantly. All segments were found to differ significantly (Table S1).

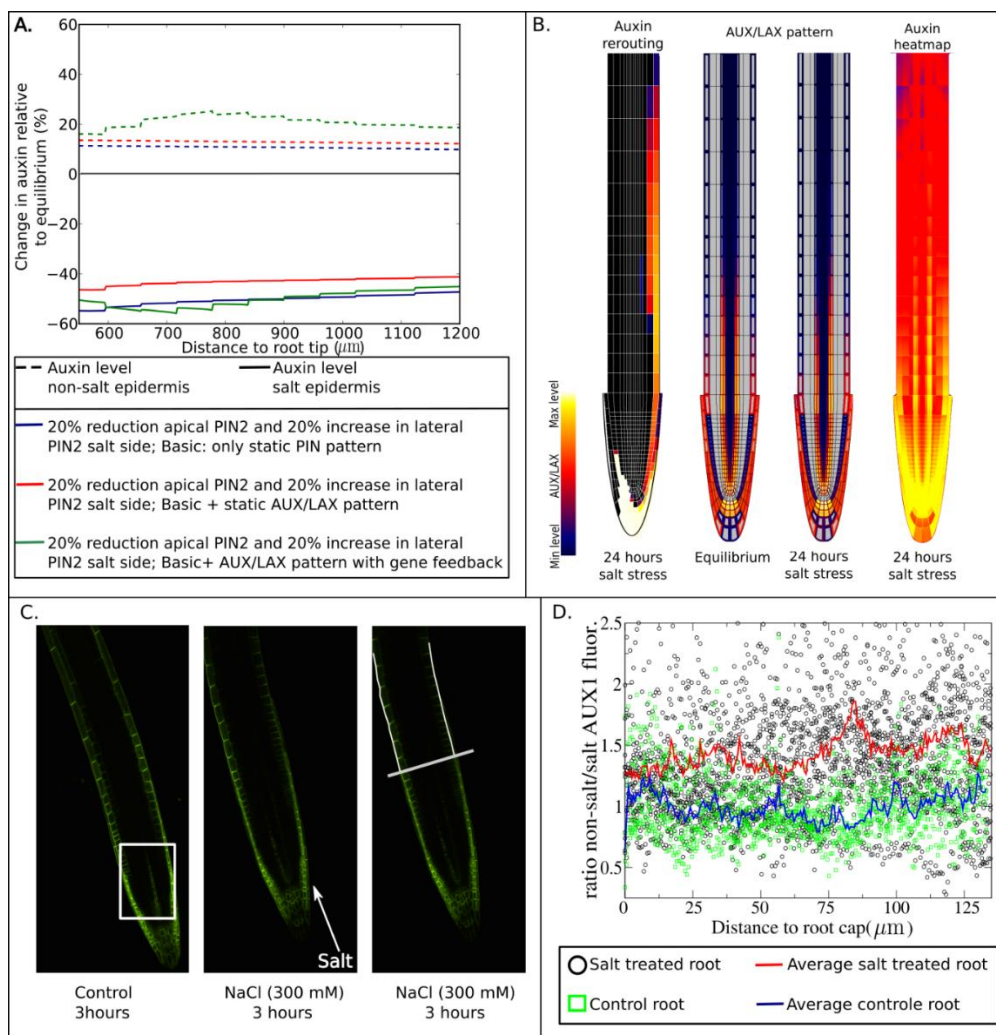


Figure 5.3. Role of auxin-dependent AUX/LAX. (A) Impact of AUX/LAX pattern and auxin feedback on AUX/LAX expression on epidermal auxin asymmetry 24 h after applying salt stress by reducing apical and increasing lateral PIN2 levels. (B) Auxin rerouting, change in AUX/LAX expression pattern and resulting auxin asymmetry in presence of auxin feedback on AUX/LAX expression. (C) AUX1-mVenus pattern in control root showing in the boxed region an asymmetric AUX1 fluorescence in the vasculature due to root orientation (left), and in a salt-exposed root showing generation of an asymmetric AUX1 pattern in the epidermis (middle). The right image shows a line transverse to the root length axis indicating the end of the lateral root cap, and two lines tracking the outer epidermal membranes in which AUX1 fluorescence levels are measured from the end of the root cap shootward. (D) Ratios of AUX1 fluorescence levels of the non-exposed to the salt-exposed side as a function of distance from the lateral root cap. Six roots were used for the control; for salt treatment, data from 12 roots were used. For details, see Materials and Methods.

5.2.5 Auxin feedback on PIN2 membrane levels

PIN proteins are constitutively cycling between the membrane and cytoplasmic vesicles. Experiments suggest that auxin may reduce the internalization of PINs, which would allow it to enhance its own export from the cell (Paciorek et al., 2005). However, effects are significantly stronger for synthetic than naturally occurring auxins (Paciorek et al., 2005, Rakusova et al., 2011). On the other hand, more indirect interactions involving SCF (TIR1/AFB)-auxin signaling and GOLVEN peptides, also appear to cause auxin-dependent regulation of PIN2 levels on the membrane (Baster et al., 2013, Whitford et al., 2012). When this feedback is added on top of the AUX/LAX pattern and feedback, the asymmetry in auxin is increased, especially in the lower part of the elongation zone, while auxin asymmetry in higher parts of the root decreased (Fig. S5.3A). Note that the concurrent asymmetry in PIN pattern underlying this (change in) auxin asymmetry is considerably smaller than the one observed for AUX/LAX, but again shows a decrease in the salt-exposed side and an increase on the non-exposed side (Fig. S5.3B).

5.2.6 Salt-induced upregulation of PIN1

In an earlier study, we performed a control experiment aimed at verifying whether applied salt concentrations would affect internalization of PIN proteins other than PIN2. Cellular PIN1, PIN2, and PIN3 levels were determined under uniform salt exposure (Galvan-Ampudia et al., 2013). Intriguingly, PIN1 and PIN3 were found to be significantly upregulated by salt. Since these PIN1 and PIN3 elevations were observed under uniform high-level salt exposure and measured at a single time point, we now investigated to what extent physiologically relevant changes in PIN1 and PIN3 membrane levels arise in response to a salt gradient over the course of time (Fig. 5.4A, Fig. S5.4).

We find that, consistent with the earlier observed increase in cellular PIN1 levels, membrane levels of PIN1 increase by ~22% (Fig. 5.4A left panels, Fig. S5.4A). However, the increase in PIN1 levels is transient. After 2 h of exposure, membrane levels of PIN1 had returned to its normal non-salt-stressed level (Fig. 5.4A, Fig. S5.4A). No indications for differences in PIN1 upregulation between the salt-exposed and non-exposed side of the root were found. Strikingly, in contrast to the earlier observed large increase in cellular PIN3 levels, membrane levels of PIN3 showed only a 4% transient upregulation (Fig. 5.4A, right panels, Fig. S5.4B). The observed salt-induced changes in PIN1 and PIN3 protein levels were similar for different membrane compartments as well as the intracellular compartment (Fig. S5.4), indicating that changes are not caused by changes in membrane-cycling dynamics. The difference in findings between current and earlier experiments is likely to be caused by the much higher concentration of salt applied when dipping the roots in uniform salt concentration, compared with the more subtle treatment of growing seedlings on a salt gradient (Fig. S5.4).

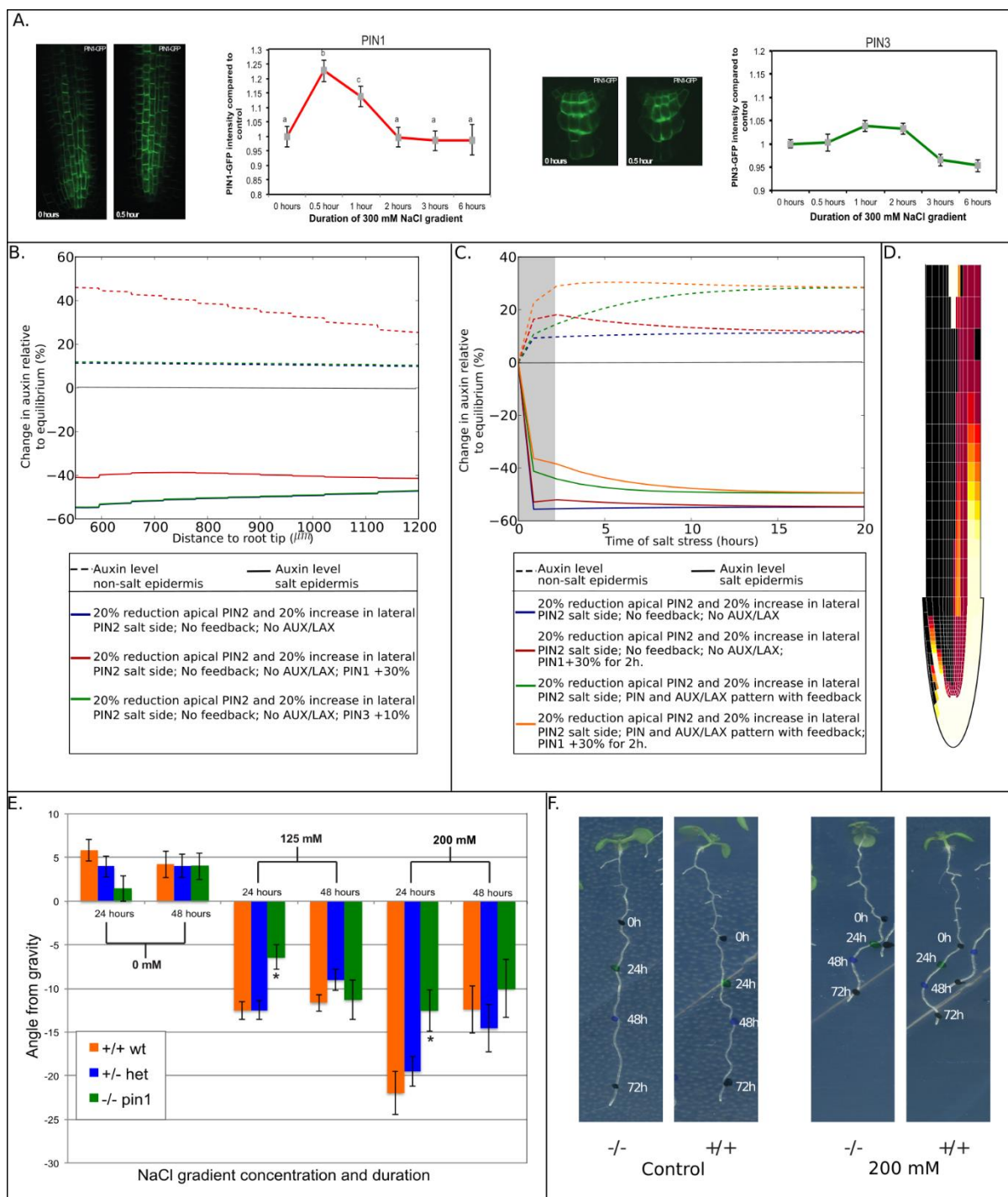


Figure 5.4. Influence of salt gradient-induced changes in PIN1 and PIN3 levels. Representative images of roots of *A. thaliana* seedlings expressing PIN1-GFP (A, left) or PIN3-GFP (A, right) in control conditions (0 h) and after 30 min of a 300 mM NaCl gradient (0.5 h). Quantification of total PIN1-GFP and PIN3-GFP intensity at different time points in *A. thaliana* stele root cells is shown in the graphs. Three independent biological replicates were used in which 2-6 roots were used per time point and 5 stele cells were analyzed per root. For PIN1, $n=90$ for 0 h; $n=25$ for 0.5 h; $n=55$ for 1 h and 2 h; $n=50$ for 3 h and 6 h; for PIN3, $n=70$ for 0 h; $n=20$ for 0.5 h; $n=60$ for 1 h; $n=55$ for 2 h; $n=40$ for 3 h; $n=35$ for 6 h. Letters indicate different significance groups as determined by multivariate ANOVA. PIN1 levels show a 22% increase relative to control after 30 min of exposure to a salt gradient, after 1 h, this increase is reduced to 14%, and after 2 h the PIN1 level showed no significant difference relative to the control condition. PIN3 protein levels increase 4% compared with control conditions after 1 h of exposure, after 3 h, levels dropped to a 5% decrease compared with control conditions. (B) Impact of persistent salt-induced upregulation of PIN1 or PIN3 on epidermal auxin asymmetry after 24 h of salt stress. For comparison purposes, auxin asymmetry in the absence of PIN1 and PIN3 regulation is also shown. Owing to the lack of effect of PIN3 upregulation,

control and PIN3 upregulation lines are superimposed. (C) Influence of transient PIN1 upregulation on the temporal dynamics of epidermal auxin asymmetry at a distance of 590 μm from the root tip. The 2 h period of PIN1 upregulation is indicated by the gray area. PIN1 upregulation is applied both in absence and presence of an AUX/LAX pattern and feedback of auxin on AUX/LAX expression and on PIN2 membrane occupancy. For comparison purposes, auxin asymmetry dynamics in the absence of transient PIN1 upregulation are also shown. (D) Auxin rerouting in the presence of transient PIN1 upregulation and auxin feedback on AUX/LAX expression and PIN2 membrane occupancy. (E) The *pin1* mutant shows a transient reduction in halotropism response after 24 h. Seeds from a heterozygous *pin1* parent were germinated on 0.5 MS plates and after 5 days exposed to a diagonal NaCl gradient. Seedlings that were homozygous for the *pin1* tDNA insertion ($-/-$) showed a reduced response to the NaCl gradient on both plates with a 125 mM and a 200 mM salt gradient compared with seedlings that were heterozygous ($+/-$) and seedlings homozygous for the wild-type (*Col-0*) allele ($+/+$). This reduction was observed after 24 h but not after 48 h. Two independent biological replicates were used in which 200 seedlings per treatment were quantified and genotyped. This resulted in $+/-$, $n=105$; $+/+$, $n=56$; $-/-$, $n=44$ for the 0 mM treatment. For the 125 mM treatment, the sample sizes were: $+/-$, $n=122$; $+/+$, $n=120$; $-/-$, $n=59$. For 200 mM, $+/-$, $n=93$; $+/+$, $n=71$; $-/-$, $n=45$. (F) Representative images of seedlings homozygous for the *pin1* wild-type allele ($+/+$) or seedlings homozygous for the tDNA insertion ($-/-$) on control plates or plates with a 200 mM NaCl gradient. Colored dots were placed at the root tip after 0 (1st black dot), 24 (green dot), 48 (blue dot) and 72 (2nd black dot) hours after applying the salt gradient. The angle from gravity after 24 h (the angle between the line from the first to the second dot and a line straight down) is significantly smaller in the example of the $-/-$ seedling on a 200 mM NaCl gradient compared with the wild-type seedlings.

Returning to our computational model, we investigated how the transient increases in PIN1 and PIN3 could contribute to generate auxin asymmetry. First, the influence of 30% and 10% elevations in PIN1 and PIN3 levels, respectively, were investigated in isolation, ignoring for a moment auxin feedback on auxin transporters and the transient nature of the PIN1 and PIN3 elevations. Elevation of PIN1 levels significantly enhances auxin asymmetry, in particular by elevating auxin at the non-salt-exposed side (Fig. 5.4B). In contrast, the small elevation of PIN3 has no observable effect on auxin asymmetry. Therefore, we restrict our further analysis to PIN1. Next, we added the transient nature of the increase in PIN1 to the model, both in isolation and in a setting incorporating the feedback of auxin on auxin transporters. We plotted the changes in epidermal auxin levels at the start of the elongation zone (590 μm from the root tip) as a function of time (Fig. 5.4C). Interestingly, we see an elevated auxin asymmetry relative to control conditions during the transient PIN1 elevation in absence of feedback (Fig. 5.4C, red versus blue lines), indicating that symmetric PIN1 elevation contributes to generation of auxin asymmetry. This increased asymmetry gradually disappears once PIN1 has returned to normal levels (Fig. 5.4C), indicating that a transient PIN1 increase has no persistent effect on auxin asymmetry. If we combine the transient PIN1 elevation with feedback on auxin transporters, we see that increases in PIN1 cause an asymmetry that is slightly larger than that generated by feedback alone (Fig. 5.4C, compare orange and green lines), and that in the presence of feedback, the PIN1-induced auxin asymmetry decreases more slowly (Fig. 5.4C, compare orange and red lines). Most importantly, the transient PIN1 increase enhances the auxin asymmetry present during the first hours of halotropism (compare speed of auxin rerouting in Fig. 5.3B and Fig. 5.4D). In addition to speeding up the build-up of auxin asymmetry, a transient PIN1 elevation also causes an overshoot in auxin asymmetry levels during the early phases of halotropism. This agrees with our earlier observation that auxin asymmetry is higher after 4 h than after 6 h of salt exposure (Galvan-Ampudia et al., 2013).

To test the computationally predicted importance of PIN1, we tested halotropic responses on a salt gradient over a 48 h time course in plants homozygous for the *pin1* tDNA insertion compared with plants having a single or double copy of the wild-type PIN1 allele. In Fig. 5.4E,F, we show the angle from gravity 24 h and 48 h after exposure to a 125 mM or 200 mM salt gradient or control conditions. For the 24 h time point, we see that for both salt concentrations, plant homozygous for the *pin1* tDNA insertion showed a significantly smaller angle from gravity relative to both heterozygotes and plants homozygous for the wild-type allele, indicative of a reduction of halotropic response strength in the absence of PIN1. After 48 h of exposure to a salt gradient, the homozygous *pin1* tDNA plants showed

similar angles. This demonstrates that PIN1 conveys only a transient increase in halotropic response strength that is no longer present at 48 h, consistent with our model predictions. Note that the decrease in angle from gravity from 24 to 48 h can be understood from gravitropic signaling becoming stronger, thus counteracting the halotropic growth away from gravity, consistent with our earlier finding (Galvan-Ampudia et al., 2013). The stronger decrease under higher salt concentrations is likely to arise from the higher initially attained angles more strongly inducing gravitropism.

5.2.7 Robustness of the results

In complex models such as these, testing the robustness of simulation outcome to specific model settings is of paramount importance to determine whether a general mechanism rather than an obscure, rare outcome has been found. To investigate the dependence on particular model assumptions, we varied a model assumption influencing the location of the main source of auxin in our model, which might potentially affect auxin patterns and fluxes and hence auxin asymmetry generated under halotropism. In the current model, all root cells have a small potential to produce auxin, and a major source of auxin is provided by influx from the shoot. However, recent data indicate that localized, root tip auxin production plays a major role in shaping the root's auxin pattern (Ljung et al., 2005, Stepanova et al., 2008). Therefore, as an alternative, we performed simulations in which shoot to root auxin flux was reduced by 50%, while auxin production was elevated 100-fold in the QC and in root cap cells, auxin production was increased 50-fold while decay was decreased by a factor of 2. Parameter settings were chosen such that for ease of comparison similar overall auxin content was achieved. Fig. S5.5 shows that this change in model setup results in a highly similar auxin asymmetry pattern compared with the default model settings. Thus, a shift in main auxin source from the shoot-root connection to the root tip does not impact our model outcome.

Next, to investigate the robustness of model outcome to parameter values, we varied most of our model parameters over a range of 50% decrease to 50% increase of their original values. In Fig. S5.6, we show the outcomes of our robustness analysis: for all tested parameters we observed limited quantitative variation in auxin asymmetry, while maintaining qualitatively similar outcomes. Based on these results, we conclude that model outcomes depend to a limited extent and in a smooth, linear fashion on parameter settings, thus implying the robustness of our model outcomes.

5.3 Discussion

We recently described halotropism as a new directional response of plants roots allowing them to grow away from salt (Galvan-Ampudia et al., 2013). In the current study, we used a detailed model of plant root auxin transport to investigate whether our earlier observations can account for halotropic root bending.

Our simulation study points to the crucial role of root tip architecture. We find that in a simplified rectangular root model, a reduction of PIN2 on the salt-exposed side merely results in the accumulation of auxin in the meristem. In contrast, in a realistic wedge-shaped tip architecture, the PIN2 decrease generates a small increase in auxin at the opposite root side. We showed that this potential to re-route auxin from the salt-exposed to the non-exposed side depends positively on the presence of a lateral root cap, the increase of lateral PIN proteins on the salt-exposed side, and a limited distance between epidermis and root cap of salt-exposed and non-exposed side. Together, this indicates that the potential for lateral transport of the auxin accumulating at the salt-exposed side is of crucial importance. In addition, we demonstrated an important role for positive feedback of auxin on its own transporters. Auxin-induced upregulation of AUX/LAX importers substantially elevated the auxin asymmetry generated by root tip architecture. The predicted asymmetry in AUX1 pattern resulting from this feedback was confirmed experimentally. Finally, we demonstrated that PIN1 is transiently upregulated under a salt gradient. While this transient change in PIN1 levels has no effect on long term auxin asymmetry, it significantly enhances the degree of auxin asymmetry during the early stages of salt stress. We speculate that generating auxin elevation at a faster rate is important to ensure root bending away from the salt before the tip of the root has started to grow into the salt-contaminated area. We experimentally validated this predicted role of PIN1 in halotropism.

In conclusion, our study shows that a decrease in PIN2 on the salt-exposed side can function as the primary generator of auxin asymmetry, but is not enough to generate a sufficiently large auxin asymmetry sufficiently fast. For this, the feedback of auxin on its own transporters and the transient salt-induced upregulation of PIN1 play a crucial role. Interestingly, in gravitropism, the *pin3* mutant is not agravitropic (Kleine-Vehn et al., 2010), starch mutants remain partly gravitropic (Caspar and Pickard, 1989), but both the *pin2* (Luschnig et al., 1998, Muller et al., 1998) and *aux1* (Bennett et al., 1996, Swarup et al., 2001) null mutants are agravitropic. Based on this it has been suggested that other, PIN3/7-independent mechanisms for gravitropism exist (Wolverton et al., 2002). Our study suggests that PIN2 may be a candidate for such a secondary asymmetry-generating mechanism, provided that gravitropism can somehow influence PIN2 directly.

Our study is an important step in unraveling the mechanistic basis of halotropism. It can be computed that in the experiments we performed here and earlier (Galvan-Ampudia et al., 2013), the differences in salt concentration at both sides of the root are in the order of 4-9.5%. Thus, future studies should be aimed at deciphering how such small asymmetries in auxin levels can become translated into a single-sided PIN2 response and how this might be related to the seemingly contradictory findings of an initial increase in PIN2 levels soon after the application of salt stress, as observed by Zwiewka et al. (2015) and the reduction in PIN2 levels after 6 h of salt stress, as we reported earlier (Galvan-Ampudia et al., 2013).

In addition, future studies should be aimed at deciphering the interplay between different tropisms. Interestingly, we found here that the auxin asymmetry generated during halotropism is substantially smaller than that during gravitropism. However, salt has been shown to suppress the gravitropism-

induced degradation of PIN2 (Galvan-Ampudia et al., 2013) while enhancing the degradation of starch (Sun et al., 2008), explaining why halotropism can at least temporarily overcome gravitropism. In our earlier study, we demonstrated that at low salt concentrations halotropism is insufficiently strong to override gravitropism, while for higher salt concentrations, the eventual takeover of halotropic by gravitropic growth depends on salt concentrations (Galvan-Ampudia et al., 2013), suggesting a quantitative tug of war between the two tropisms. Given the important role of PIN2 and AUX1 in both gravitropism (Abas et al., 2006, Bennett et al., 1996, Chen et al., 1998, Luschnig et al., 1998, Muller et al., 1998, Swarup et al., 2001) and halotropism (this study), and the important role of PIN2 in phototropism (Wan et al., 2012), these proteins probably represent the signaling nexus at which different tropism pathways converge and signal integration occurs.

A final important question for future research is how tropisms can function in different developmental or environmental conditions, corresponding to different overall auxin levels. For robust tropic responses to occur, this might imply that tropisms generate and plant cells respond to relative rather than absolute changes in auxin levels – an issue that so far has not been investigated.

5.4. Material and methods

5.4.1 Summary of the computational model

We use a spatially extended, grid-based model of the Arabidopsis root, similar to earlier models (Grieneisen et al., 2007, Laskowski et al., 2008, Mahonen et al., 2014). The model incorporates a root tissue architecture with subcellular resolution, cell type and developmental zone-specific spatial expression domains and polarity patterns for the auxin-exporting PIN proteins and the auxin-importing AUX/LAX genes, auxin transport within cells and cell walls and across membranes, and feedback of auxin levels on PIN membrane occupation as well as on AUX/LAX gene expression. The source code for the simulation models can be downloaded from <http://bioinformatics.bio.uu.nl/khwjtuss/HaloRoot/>.

5.4.2 Baseline model

5.4.2.1 Tissue lay-out

We started with a highly simplified, rectangular root model, similar to that used in earlier modeling studies (Grieneisen et al., 2007, Laskowski et al., 2008, Mahonen et al., 2014). Root tissue was simulated with a spatial resolution of 2 μm on an $80 \times 925 \mu\text{m}^2$ grid. Individual grid points correspond to cytoplasm, membrane or cell wall. We assume an average cell width of 8 μm , and simulate a total of eight columns of cells across the width of our 2D root model, incorporating from outermost to innermost epidermal (blue), cortical (green), endodermal (yellow) and vasculature cells (red). The vasculature is connected to the quiescent center (QC, gray), and the lowest part of the root represents the columella (cyan) (Fig. 5.1A, left panel).

Given that tissue growth occurs on a substantially longer timescale of days relative to the minute to hours timescale on which changes in PIN2, AUX1 and auxin patterns occur in response to salt stress, we ignored tissue growth in the current model. We incorporated a subdivision of the root into a meristematic (MZ), expansion (EZ) and differentiation zone (DZ) (Fig. 5.1A) containing cells with a height of 8 μm , 60 μm and 100 μm , respectively. Similar to previous modeling studies, we incorporated the PIN polarity patterns typical for each cell type and zone (Grieneisen et al., 2007, Laskowski et al., 2008, Mahonen et al., 2014) (Fig. 5.1A). Together, this results in a reverse fountain auxin flux pattern that generates an auxin maximum in the QC (Grieneisen et al., 2007).

5.4.2.2 Auxin dynamics

Auxin dynamics were modeled on a grid point level, in a manner similar to earlier studies (Grieneisen et al., 2007, Mahonen et al., 2014, Mitchison, 1980). For an intracellular grid point i,j , auxin dynamics are described as:

$$\frac{\partial A_{i,j}}{\partial t} = p_A - d_A A_{i,j} + \sum_{i',j'} i_{pas+act} + A_{i,j} - \sum_{i',j'} (e_{pas} + e_{PIN}) A_{i,j} + D_{c,w} \Delta A$$

In Eqn 1 p_A is the rate of auxin production per grid point, and d_A the rate of auxin degradation per rate grid point, which are zero for wall points and non-zero for cellular grid points (membrane, cytoplasm). $i_{pas+act}$ represents the lumped, active and passive import of auxin from all extracellular grid points i',j' that are neighboring the cellular grid point i,j , and e_{pas} and e_{PIN} correspond to the passive and active export of auxin from cellular grid point (i,j) to neighboring extracellular points (i',j') , respectively.

These transport reaction terms only exist for membrane and wall grid points. Auxin fluxes were modeled using linear mass action kinetics. Finally, $D_{c,w}$ represents the diffusion constant for auxin inside the cell (c), or inside the wall (w) and diffusion occurs only among neighboring cellular or wall grid points, but not between cellular and wall points.

Note that $e_{PIN} = a_{PIN} \times PIN_{mem}$, i.e. rather than being a constant parameter, the rate of PIN-mediated active auxin transport depends on membrane PIN protein levels. Furthermore, $PIN_{mem} = PIN_{pat} \times PIN_{exp}$, that is, PIN membrane levels depend on the product of the PIN pre-pattern determining maximum relative PIN level at a particular membrane grid point (PIN_{pat}) and the cellular PIN gene expression level (PIN_{exp}) (Mahonen et al., 2014).

To model the connection of the explicitly modeled root section to the not-explicitly modeled rest of the plant we incorporate a shoot derived influx into the vasculature and efflux from the root to the shoot from the non-vasculature tissues, similar to earlier studies (Grieneisen et al., 2007, Mahonen et al., 2014). Parameter values are listed in Table 1.

5.4.3 Extended model

5.4.3.1 Tissue lay-out

We also developed an extended model incorporating a more realistic, wedge-shaped root tip and root cap tissue (Fig. 5.1A, middle panel). The root tip template was generated by developing an idealized, perfectly symmetric, generalized description based on microscopic root tip pictures. The part of the root tip shootward of the lateral root cap was assumed to be perfectly straight and have constant width. In the part of the root containing the root cap, idealized parabolic functions were used to describe the outer boundary of the root cap, and the boundary between different root cap layers, between lateral root cap and epidermis, epidermis and cortex, cortex and endodermis, endodermis and pericycle, and pericycle and the rest of the vasculature. In the lower half of this part of the root, a central point was chosen, through which several radial lines were drawn that were used to describe cell walls in the columella, and lower parts of the lateral root cap, epidermis, ground tissue and vasculature.

Based on experimental data, root cap tissue has a similar PIN protein polarity pattern as epidermal tissue, but with lower maximum membrane PIN protein levels (Ditengou et al., 2008). In the extended model, cell types differ not only in PIN polarity patterns, but also have a cell type-specific width of 18 μm for epidermal, 20 μm for cortical, 12 μm for endodermal, 8 μm for the outermost vascular and 6 μm for the remaining vascular cells, in agreement with experimental data and similar to earlier models (Laskowski et al., 2008). Zone-dependent cell height was the same as in the baseline model, except for the curved part of the root tip where columella and lateral root cap cell height increases towards the tip of the root. In the extended model, to create sufficient resolution for the curved cell walls and membranes, a spatial resolution of 1 μm was used.

Table 5.1. Model parameter values

Parameter	Baseline model	Extended model	Units
D_{wall}	40	40	$\mu\text{m}^2 \text{s}^{-1}$
p_A	0.0005	0.0005	$[\] \text{s}^{-1}$
d_A	0.00005	0.0000725	s^{-1}
D_{cell}	600	600	$\mu\text{m}^2 \text{s}^{-1}$
AUX/LAX _{exp}	100	100	$[\]$
$i_{\text{pas+act}}$	10	10	$\mu\text{m}^2 \text{s}^{-1}$
i_{pas}	–	2.5	$\mu\text{m}^2 \text{s}^{-1}$
$a_{\text{AUX/LAX}}$	–	0.05	$\mu\text{m}^2 \text{s}^{-1}$
e_{pas}	1	1	$\mu\text{m}^2 \text{s}^{-1}$
A_{PIN}	0.2	0.2	$\mu\text{m}^2 \text{s}^{-1}$
PIN _{pat,max_apical}	1	1	Dimensionless
PIN _{pat,max_basal}	1	1	Dimensionless
PIN _{pat,max_lateral}	0.35	0.35	Dimensionless
PIN _{pat,max_lateral} (endodermal and cortex cells)	0.1	0.1	Dimensionless
PIN _{exp}	max 100 (auxin dependent)	100	$[\]$
basal _{PINmem}	–	0.1	Dimensionless
fb _{PINmem}	–	1.5	Dimensionless
sat _{PINmem}	–	10	$[\]$
max _{AUX1}	–	0.01	$[\] \text{s}^{-1}$
sat _{AUX1}	–	50	$[\]$
d_{AUX1}	–	0.0001	s^{-1}

To test the effect of left-right distances between epidermis and lateral root cap on the potential to generate auxin asymmetries, we also developed a variation of the extended model in which these distances were increased (Fig. 5.1A, right). Increased distances between the epidermal tissues were generated by increasing the size of the outermost vascular cells to 10 μm and of the remaining vascular cells to 8 μm , increasing the distance between left and right epidermis with 16 μm . In addition, to also increase the distance between left and right epidermis and root cap in the tip of the root where cell files curve inward the leftmost and rightmost columella cells in each tier were increased in size.

5.4.3.2 AUX/LAX pre-pattern

In the baseline model, we assumed a constant, homogeneous distribution of auxin importers, and modeled this using a single lumped permeability value for passive and active auxin import $i_{\text{pas+act}}$. However, it is well known that the AUX/LAX proteins involved in active auxin uptake have cell type- and root zone-specific patterns (Bennett et al., 1996, Swarup et al., 2001, Swarup et al., 2005, Péret et al., 2012). Therefore, we distinguish passive and active auxin import in the extended model. For simplicity, we incorporated a single generalized AUX/LAX protein, whose domain of expression is the sum of the experimentally reported expression domains for the distinct AUX/LAX genes (Fig. S5.2). Similar to active efflux, the rate of active influx is then described by

$i_{AUX/LAX} = a_{AUX/LAX} \times AUX/LAX_{mem}$, with $AUX/LAX_{mem} = AUX/LAX_{pat} \times AUX/LAX_{exp}$, where AUX/LAX_{pat} is the predefined spatial presence/absence pattern for where AUX/LAX can be expressed and AUX/LAX_{exp} is the actual cellular gene expression. In addition to this spatially heterogeneous active influx we also incorporate a constant, low level of passive auxin influx, i_{pas} , in all cells. Parameter values are listed in Table 1.

5.4.3.3 Auxin-dependent gene expression of AUX/LAX

In a subset of simulations, we incorporate the auxin dependence of AUX/LAX gene expression (Laskowski et al., 2006, Laskowski et al., 2008). We do this by replacing constant AUX/LAX expression levels (AUX/LAX_{exp}) by the following cell-level equation for gene expression dynamics:

$$\frac{dAUX/LAX}{dt} = \max_{AUX/LAX} \frac{A_{meancell}^2}{A_{meancell}^2 + sat_{AUX/LAX}^2} - d_{AUX/LAX}$$

Here, $\max_{AUX/LAX}$ is the maximum gene expression rate of AUX/LAX, $sat_{AUX/LAX}$ is the auxin level at which AUX/LAX expression is at its half maximum rate and $d_{AUX/LAX}$ is the degradation rate of AUX/LAX. Parameter values can be found in Table 1.

5.4.3.4 Auxin feedback on PIN localization

PIN levels on the membrane not only depend on PIN gene expression levels but also on PIN membrane cycling dynamics. PIN proteins are constantly recycled by internalization from the membrane and subsequent secretion to the membrane (Adamowski and Friml, 2015, Steinmann et al., 1999). Auxin influences this subcellular trafficking by limiting the rate of internalization, thus stimulating its own efflux from the cell (Paciorek et al., 2005). This results in a positive feedback between external auxin and membrane PIN levels.

In a subset of simulations, we incorporated this positive feedback on levels of PIN in the membrane. We restricted this positive feedback to the epidermal and root cap tissues that are considered of primary importance for generating the auxin asymmetry underlying root bending. For these cells, the PIN membrane equation ($PIN_{mem} = PIN_{pat} \times PIN_{exp}$) is replaced by the following grid-level equation:

$$PIN_{mem} = PIN_{pat} PIN_{exp} \left(basal_{PIN_{mem}} + fb_{PIN_{mem}} \left(\frac{A_{i,j+1}^2}{A_{i,j+1}^2 + sat_{PIN_{mem}}^2} \right) \right)$$

Here $basal_{PIN_{mem}}$ is the minimal fraction of PINs on the membrane in the absence of auxin, and $fb_{PIN_{mem}}$ is the maximal additional fraction of PINs on the membrane in presence of high levels of auxin. $sat_{PIN_{mem}}$ is the auxin level at which this auxin-dependent fraction attains its half maximum value. Parameter values can be found in Table 1.

5.4.4 Simulating halotropism

Currently, no quantitative data is available showing how changes in PIN2 levels depend on the longitudinal position of a root cell (i.e. distance to the root tip). For simplicity, we therefore assume the same constant response to salt along the first third of the simulated root tissue, while above this part, no response to salt is assumed to occur (Fig. 5.1A). The salt gradient was assumed to be localized to the left of the root tip. We considered two different halotropism scenarios. In the first, apical PIN2

levels were decreased by 20% in the epidermis and (if present) root cap at the salt-exposed side of the root. In the second scenario, concomitant with a reduction of apical PIN2 levels, a 20% upregulation of lateral PIN2 levels was assumed to occur. Both scenarios were based on the experimental data from (Galvan-Ampudia et al., 2013). Simulations were run without salt stress until auxin concentrations reached an equilibrium, after which salt stress was applied.

5.4.5 Analysis methods

Auxin levels may vary both because of the imposed salt gradient as well as due to different model settings. To faithfully compare the extent of auxin asymmetry resulting from a salt gradient under different model settings, we compare auxin levels in the left and right epidermis under salt stress with auxin levels under normal, non-stressed conditions with the same model settings. Furthermore, we compute percentage rather than absolute differences relative to these normal auxin levels. Formally, this can be written as:

$$\Delta auxin_{salt,l/r} = 100 \frac{auxin_{salt,\frac{l}{r}} - auxin_{normal}}{auxin_{normal}}$$

5.4.6 Numerical integration and run-time performance

Owing to the very fast auxin dynamics, stable integration using simple forward Euler schemes would require very small temporal integration steps ($\Delta t = 0.0001$ s) making simulations prohibitively slow. Therefore, a semi-implicit alternating direction integration scheme (Peaceman and Rachford, 1955) was used that allows for integration time steps of $\Delta t = 0.2$ s. This approach has been extensively validated in earlier studies (Grieneisen et al., 2007, Mahonen et al., 2014).

All simulations were run on a dell Precision T7500 workstation with Intel Xeon X5680 processor. The code for the model was written in C++. Run time for simulations were typically around 24 h (corresponding to a biological time of a few days) to reach steady state gene expression and auxin levels in absence of salt stress, and 3-6 h for simulating salt stress (biological time of 10-36 h).

5.4.7 Experiments

5.4.7.1 Growth conditions and treatments

We used *Arabidopsis thaliana* PIN1-GFP (Benková et al., 2003), PIN3-GFP (Zadnikova et al., 2010), *pin1* (SALK_047613) and AUX1-mVenus (Band et al., 2014) lines, all in the Col-0 background. Seeds were sterilized using a 50% bleach solution. After 2 days of stratification the seeds were germinated on 0.5 MS plates with 0.1% MES buffer, 1% sucrose, 1% Daishin agar after which the pH was adjusted to 5.8 (using KOH). The plates were placed at an angle of 70° and placed in a climate chamber (22°C at long-day conditions, 16 h of light at 130 $\mu\text{mol}/\text{m}^2/\text{s}$). After 4 days, the plants were transferred to new 0.5 MS plates. On day 5, the treatment was started. Salt gradients were created starting at 0.5 cm from the root tip by cutting the left lower corner of the square 0.5 MS plate and replacing this with fresh 0.5 MS medium containing 125 mM, 200 mM or 300 mM NaCl, depending on the experiment (for control plates medium was replaced with fresh 0.5 MS medium without salt). The plates were dried for 15 min and placed back into the climate chamber. Microscopy slides were prepared by cutting

a rectangle around the seedling and placing it upside down on a microscopy slide while maintaining an angle of 70°. The slides were imaged within 5 min of removing the plates from the climate chamber.

5.4.7.2 Confocal laser-scanning microscopy

The images were acquired using a Nikon Ti inverted microscope in combination with an A1 spectral confocal scanning head. For GFP, the excitation wavelength used was 488 nm, the emission wavelength detected was 505-555 nm. For mVenus (YFP), the excitation wavelength used was 514 nm and the emission wavelength used was 525-555 nm. The analysis of the images was performed using Fiji (<http://fiji.sc>) software.

5.4.8 Analysis

5.4.8.1 PIN1 and PIN3 response to salt gradient

Plants were exposed to a 300 mM NaCl gradient and imaged at different time points (0.5, 1, 2, 3 and 6 h). For control plants, no significant differences between time points were found. Therefore, all control plants could be pooled into a single control group. Three biological replicates were performed for both PIN1 and PIN3, each time with newly grown *A. thaliana* seedlings. In each experiment, six roots were imaged for the control condition, two roots for the 0.5 h of salt gradient and four roots for the other treatments (1 h, 2 h, 3 h and 6 h). Five cells from each root were used for the quantification of PIN membrane levels. We dismissed images in which an insufficient number of cells could be used for quantifying PIN membrane levels. This could be due to an unfortunate root angle, bad confocal plane or air bubbles near the root while imaging. Five cells of each imaged root were used to determine the average GFP intensity of the pixels by drawing a region of interest (ROI) around one side of the membrane or the intracellular part of the cell and using Fiji software to calculate the average. These values were then corrected for background fluorescence by subtracting the average value of a part of the root which does not express the specific PIN protein. Significance levels between control and salt conditions and the different time points were tested by using ANOVA (using SPSS software).

5.4.8.2 AUX1 response to salt gradient

Plants were imaged 3 h after exposure to a 300 mM salt gradient or control conditions. Three biological replicates were performed for the salt gradient and for control conditions. For the salt gradient a total of 13 plants were analyzed (5, 4 and 4 for the individual replicates), for control conditions a total of 9 plants were analyzed (4, 3 and 2 for the individual replicates). For each root, a line transverse to the longitudinal axis of the root was drawn to indicate the position at which the lateral root cap ends. Next, two lines were drawn following the outer lateral membranes of the epidermal cells starting from the end of the rootcap in the shootward direction (see Fig. 5.3C, right). YFP intensity levels of the pixels composing these lines were determined using ImageJ software (<https://imagej.nih.gov/ij/>). For each root, we computed the ratios between left and right epidermal AUX1 levels as a function of distance from the lateral root cap by determining the ratio of YFP intensity levels for pixel pairs consisting of a pixel at the left and a pixel at the right outer epidermal membrane located at the same distance from the end of the lateral root cap. For the salt treatment, one root was discarded from our analysis, for the control conditions, two roots were discarded from our analysis because of bad confocal planes resulting in highly uneven fluorescence levels at the left and right sides of the root prohibiting the proper application of the above explained analysis method. In addition, for control conditions, one root was discarded from our analysis because of the high level of root bending observed. It has been previously shown that root bending may induce local elevation of

AUX1 levels (Laskowski et al., 2008). Ratios computed for salt gradient and control roots were binned per 5 μm length segments. Significance levels between control and salt gradient exposed roots were computed per bin using a double sided t-test (using R software).

5.4.8.3 Effect of *pin1* on halotropism

Seeds from a heterozygous *pin1* mutants (SALK_047613) [the homozygous *pin1* mutant is sterile (Okada et al., 1991)] were plated and grown to 5 days, as described above (growth conditions and treatment). A difference relative to the above described experiments is that the plants were not transferred after 4 days to new 0.5 MS plates but were germinated on the final treatment plates. On day 5, the treatment was started, as described above. The 5-day-old seedlings were then analyzed for their halotropic response according to Galvan-Ampudia et al. (2013). Ten seeds were used per plate and 20 plates for each treatment (0, 125 and 200 mM NaCl). All seedlings were genotyped to identify seedlings homozygous for the tDNA insertion [forward genomic primer: acggtatagtcctctataact, reverse genomic primer: gctgcaaaagagtgcataaa and insertion primer (LBb1.3): atttgcccatttcggaac]. Significance levels between genotypes at different time points were tested with SPSS software by using MANOVA (post hoc Bonferroni $P < 0.01$).

Acknowledgements

We would like to thank Paulien Hogeweg for helpful discussions, and Laurens Kraai and Daniel Weisse for their advice on AUX1 analysis. We thank Teva Vernoux (PIN1-GFP), Eva Benkova (PIN3-GFP), Remko Offringa (*pin1*) and Malcolm Bennett (AUX1-mVenus) for published and unpublished materials. We would also like to thank Remko Offringa and Chris van Schie for advice on the *pin1* experiment.

Competing interests

The authors declare no competing or financial interests.

Author contributions

T.v.d.B. constructed the code for halotropism simulations, conceived and conducted the computer simulations, and wrote the manuscript. R.A.K. conceived and conducted the halotropism experiments. C.T. conceived the halotropism experiments and wrote the manuscript. K.H.W.J.t.T. constructed the main simulation code, conceived the halotropism simulations, and wrote the manuscript.

Funding

This work was supported by the Netherlands Scientific Organization (Nederlandse Organisatie voor Wetenschappelijk Onderzoek) [864.14.003 to T.v.d.B. and K.H.W.J.t.T.; 711.014.002 to R.A.K. and C.T.]. Deposited in PMC for immediate release.

Data deposition

The source code for the simulation models is available at: <http://bioinformatics.bio.uu.nl/khwjtuss/HaloRoot/>.

5.5 Supplementary information

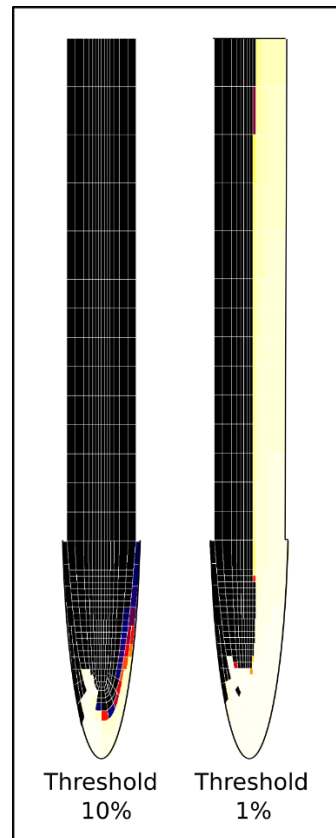


Figure S5.1: Influence of measurement threshold on displayed auxin rerouting. Auxin rerouting maps for auxin elevations of 10% or more (same as in Figure 2C, right) (left) and for auxin elevations of 1% or more (right).

distance from lateral root cap (μm)	significance value
2.5	0.000193054
7.5	0.157423
12.5	0.0118692
17.5	1.18449×10^{-8}
22.5	3.61994×10^{-7}
27.5	1.38665×10^{-8}
32.5	0.000122297
37.5	7.38984×10^{-9}
42.5	3.1453×10^{-10}
47.5	3.44796×10^{-11}
52.5	6.1504×10^{-8}
57.5	0.0000609791
62.5	4.14202×10^{-13}
67.5	9.73117×10^{-12}
72.5	2.40387×10^{-20}
77.5	9.78448×10^{-15}
82.5	5.25836×10^{-15}
87.5	2.01565×10^{-17}
92.5	2.02167×10^{-14}
97.5	1.80546×10^{-10}
102.5	4.7292×10^{-10}
107.5	1.61581×10^{-12}
112.5	2.65674×10^{-10}
117.5	2.95543×10^{-7}
122.5	1.39511×10^{-8}
127.5	6.17551×10^{-6}
132.5	0.0000357128

Table S5.1: Significance values for AUX1 asymmetry in salt-gradient exposed versus non exposed roots. Significance values were computed for a double sided T-test performed on AUX1 fluorescence level ratios between salt-exposed and non-salt exposed plants. Ratios were binned per 5 μm intervals, indicated distances represent the midpoint of the bin.

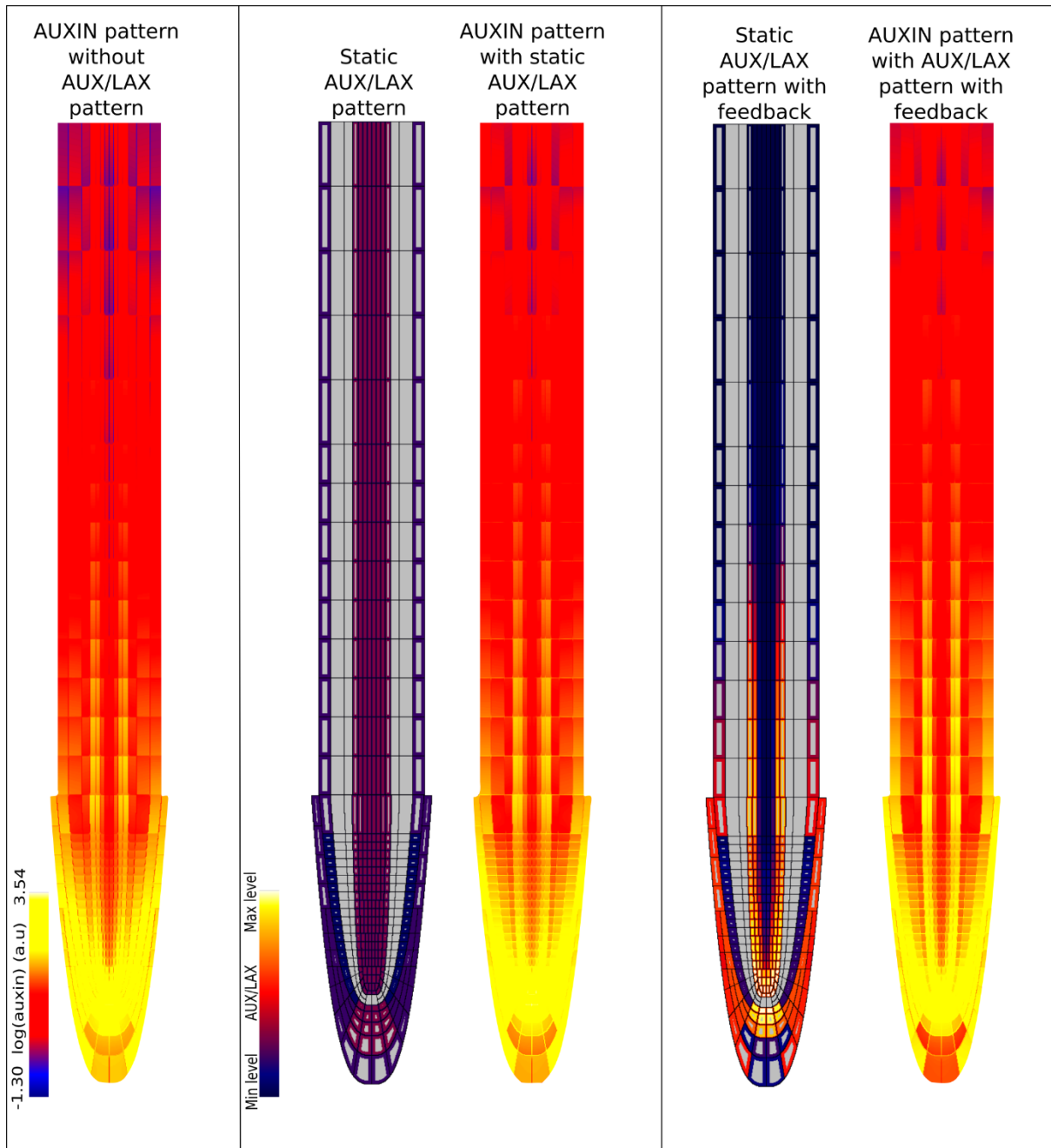


Figure S5.2: Influence of AUX/LAX on root tip auxin pattern. Left: auxin pattern in absence of AUX/LAX prepattern; Middle: AUX/LAX pattern with static AUX/LAX levels and resulting auxin pattern; Right: AUX/LAX pattern with auxin dependent AUX/LAX expression and resulting auxin pattern.

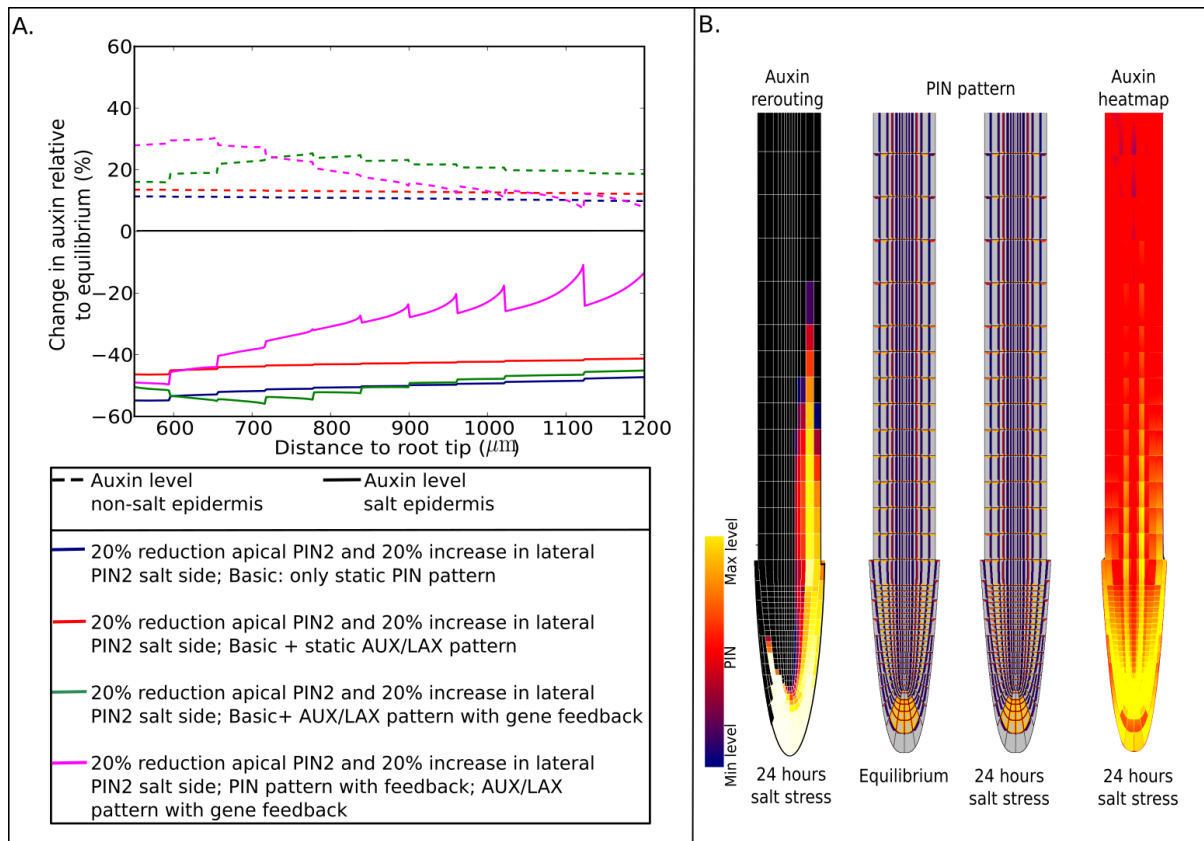


Figure S5.3: Influence of auxin feedback on PIN2. **A** Impact of positive feedback of auxin on PIN2 membrane occupancy on epidermal auxin asymmetry after 24 hours of applying salt stress by reducing apical and increasing lateral PIN2 levels. For comparison purposes auxin asymmetry under several other conditions are also shown. We can see that while auxin induced upregulation of AUX/LAX expression substantially elevated the auxin asymmetry, the added effect of auxin feedback on PIN2 appears more subtle, increasing auxin asymmetry in the lower part and reducing asymmetry in the higher parts of the elongation zone. Important to consider here is that we take the PIN2 situation as observed after 6 hours of salt stress as a starting point for our simulations. As a consequence, we start our simulations from a situation in which most if not all PIN2 dynamics, directly salt induced as well as secondary auxin-feedback dependent- has most likely already taken place. In retrospect, adding auxin dependent feedback of PIN2 on top of this should not be expected to have too much effect. Indeed, auxin dependence of PIN2 might be more important for the initial establishment of the PIN2 asymmetry. **B** Auxin rerouting, change in PIN membrane occupancy pattern and resulting auxin asymmetry in presence of auxin feedback on both AUX/LAX expression and PIN2 membrane occupancy.

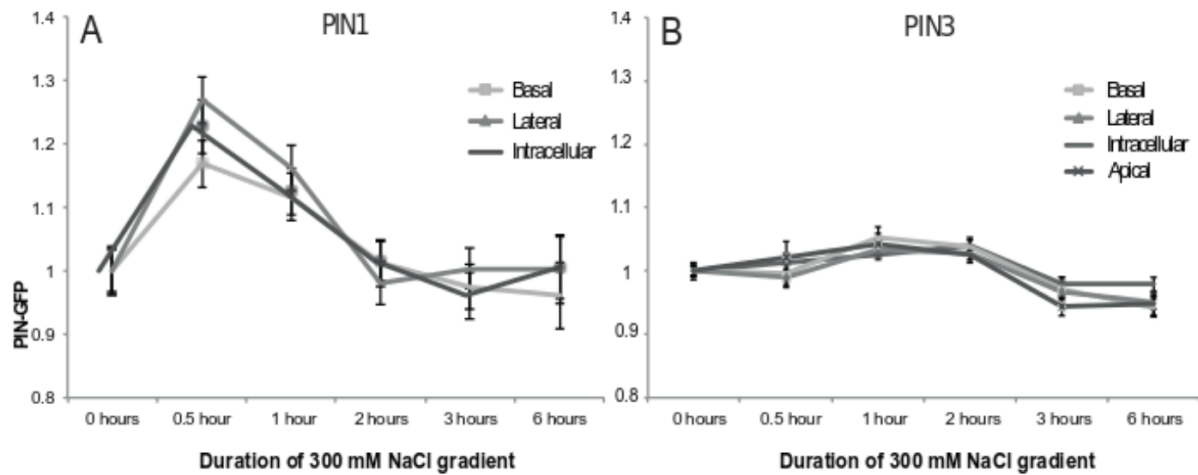


Figure S5.4: *PIN1* and no *PIN3* re-distribution during a 300 mM NaCl gradient. **A** *PIN1*-GFP and **B** *PIN3*-GFP intensities compared to control on the basal and lateral sides of the membrane and inside of the cell. GFP-intensities on the individual membranes and cell interior follow the same pattern as the total GFP-intensity (Fig 4), implying that no redistribution of *PIN1* or *PIN3* occurs during 6 hours of exposure to a 300mM NaCl gradient. Note that in our earlier work we found substantial upregulation of both *PIN1* and *PIN3*. The differences in salt-induced upregulation of *PIN1* and *PIN3* found in our current and earlier experiments can be explained by differences in experimental set-up. In the Galvan-Ampudia et al. study roots were dipped in liquid 100 mM NaCl medium for an hour, generating a uniform and severe salt stress for the root. In contrast, in the current study roots were grown in solid medium containing a salt-gradient with a maximum of 300 mM NaCl. These conditions are more representative for naturally occurring growth conditions. Extrapolating from measurements of similar gradients in our earlier study (Galvan-Ampudia et al. Curr Biol 2013), we derive that salt concentrations at the tip of the root will not exceed 75 mM after 24 hours. Thus, in the current experiments roots are exposed to non-uniform and considerably lower salt-stress, explaining the reduced upregulation of *PIN1* and *PIN3*.

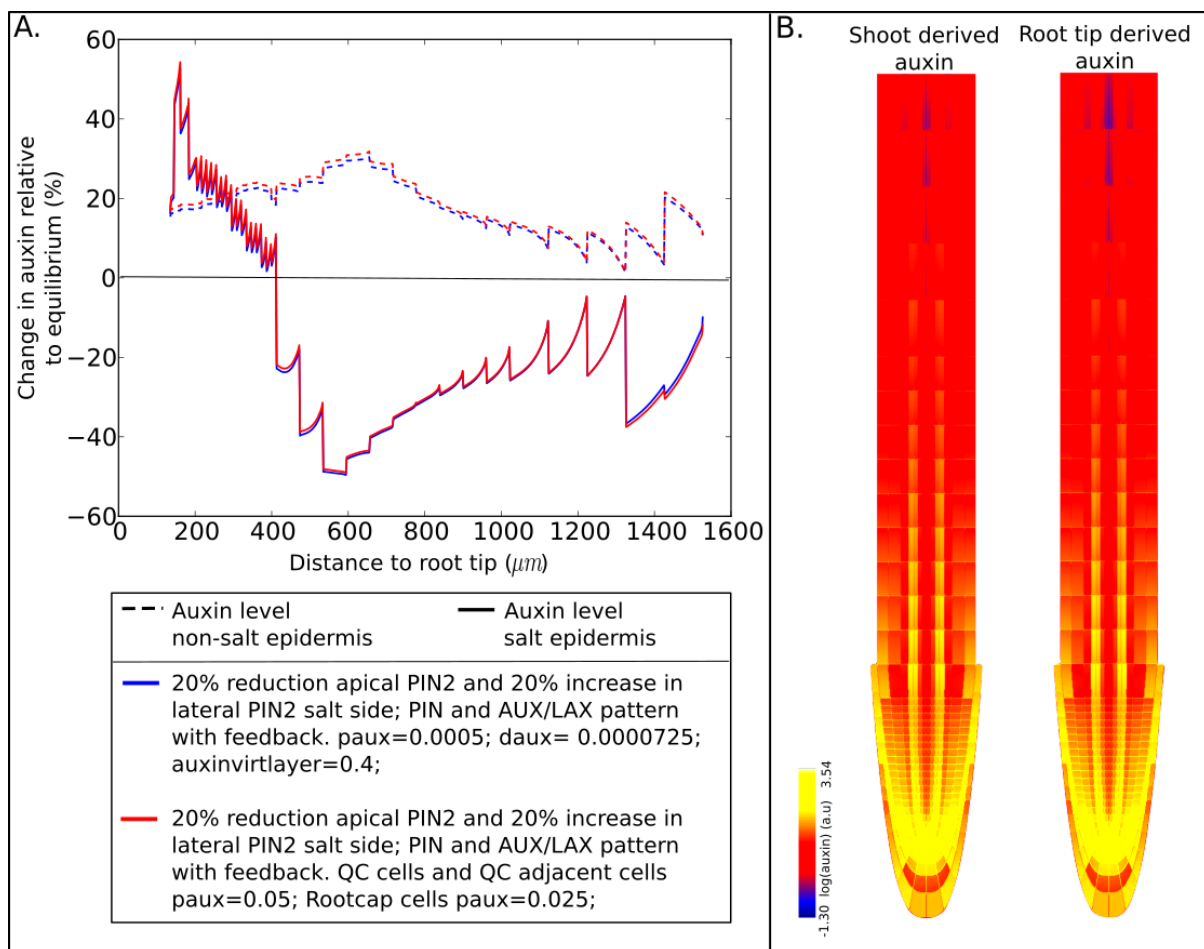


Figure S5.5: Robustness to variation in location of major auxin source. In the default model, all cells have a similar capacity to produce and degrade auxin and there is a substantial flux of auxin from the shoot. Here we reduced shoot derived auxin influx by a factor 2, while increasing auxin production in the QC by a factor 100 and in the root cap increasing auxin production a factor 50 and decreasing degradation by a factor 2. We compare the epidermal auxin asymmetry and overall auxin pattern generated during halotropism with that of the default model.

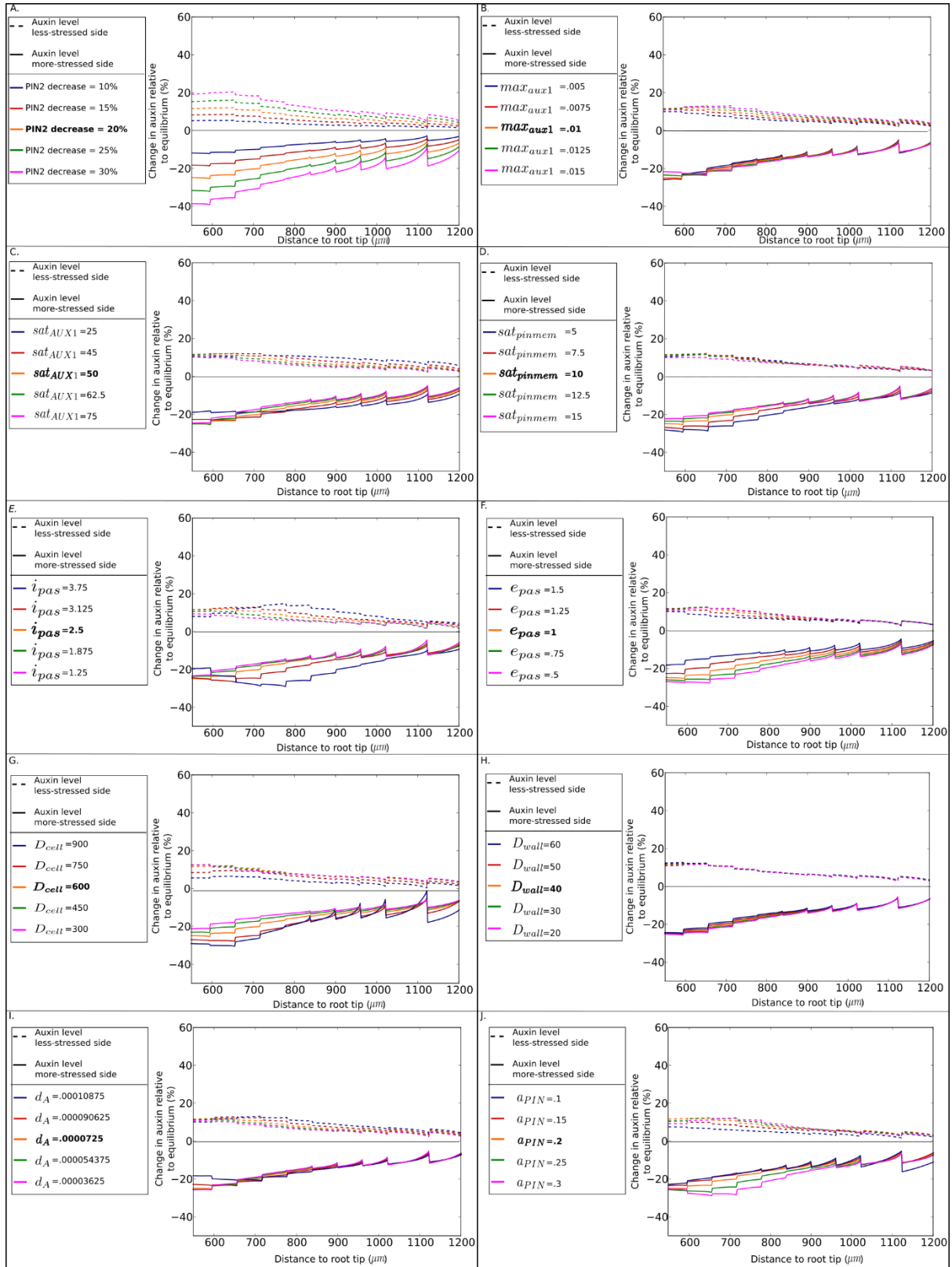


Figure S5.6: Robustness to variation in parameter values. Robustness of simulation outcomes for changes in the reduction of apical PIN2 at the salt-stressed side (A), changes in maxAUX1 (B), changes in satAUX1 (C), changes in satpinmem (D), changes in ipas (E), changes in epas (F), changes in Dcell (G), changes in Dwall (H), changes in da (I) and changes in aPIN (J). Parameter values were varied within a range of a factor 0.5 to 1.5 of the original values. All simulations were performed with the an apical PIN2 reduction of 20%, and without AUX/LAX prepattern and feedback on auxin transporters. Simulations were run for 24 hours, auxin levels during stress were compared to equilibrium levels, and plotted for the elongation zone.

6

Halotropism requires phospholipase D ζ 1-mediated modulation of cellular polarity of auxin transport carriers

Ruud A. Korver, Thea van den Berg, A. Jessica Meyer, Carlos S. Galvan-Ampudia, Kirsten H.W.J. ten Tusscher, Christa Testerink

Plant, Cell & Environment (2019)

Abstract

Endocytosis and relocalization of auxin carriers represent important mechanisms for adaptive plant growth and developmental responses. Both root gravitropism and halotropism have been shown to be dependent on relocalization of auxin transporters. Following their homology to mammalian phospholipase Ds (PLDs), plant PLD ζ -type enzymes are likely candidates to regulate auxin carrier endocytosis. We investigated root tropic responses for an *Arabidopsis pld ζ 1*-KO mutant and its effect on the dynamics of two auxin transporters during salt stress, that is, PIN2 and AUX1. We found altered root growth and halotropic and gravitropic responses in the absence of PLD ζ 1 and report a role for PLD ζ 1 in the polar localization of PIN2. Additionally, irrespective of the genetic background, salt stress induced changes in AUX1 polarity. Utilizing our previous computational model, we found that these novel salt-induced AUX1 changes contribute to halotropic auxin asymmetry. We also report the formation of “osmotic stress-induced membrane structures.” These large membrane structures are formed at the plasma membrane shortly after NaCl or sorbitol treatment and have a prolonged presence in a *pld ζ 1* mutant. Taken together, these results show a crucial role for PLD ζ 1 in both ionic and osmotic stress-induced auxin carrier dynamics during salt stress.

6.1 Introduction

Soil conditions are one of the major decisive factors whether particular crops can be cultivated. For example, water and nutrient availability, pH, salinity, and heavy metals, but also the microbiome, all represent important factors influencing plant growth and survival (Berendsen et al., 2012, Kochian et al., 2015, Munns and Gilliam, 2015). As a result of climate change, soil drought and salinization are encountered more frequently and are more extreme in recent years. Consequently, salt-affected soils, present on all continents, are expected to increase, causing a decline in the amount of arable land (Wicke et al., 2011). Importantly, even moderate levels of soil salinity already cause a significant decrease in yield. Therefore, improving the salt tolerance of crops is important to secure our food supply in the near future, where we face an increasing population and decreasing amount of arable land.

Roots in a saline soil have to cope with both Na^+ toxicity and osmotic stress. Early responses to salt include a short-term arrest of root growth, called the quiescence phase (Geng et al., 2013). Eventually, growth reinitiates at a lower rate as before the stress (Geng et al., 2013, Julkowska and Testerink, 2015). Main root and lateral roots are affected differently by soil salinity, resulting in differences in overall root system architecture (RSA) as compared with control conditions (Julkowska et al., 2014, Julkowska et al., 2017). Besides adaptation of overall RSA to saline soils, plants are also capable of changing their direction of root growth, that is, away from salt, a phenomenon called halotropism (Galvan-Ampudia et al., 2013).

A major player in root development, growth, and tropisms is the plant hormone auxin. Auxin maxima have been shown to promote stem cell status with somewhat lower levels supporting division (Sabatini et al., 1999), whereas auxin minima have been shown to regulate the transition from cell division to cell differentiation (Di Mambro et al., 2017). Additionally, elevation of auxin levels in elongating root cells has been shown to reduce cell expansion rate, and auxin asymmetry is the main mechanism through which growth asymmetries are established during tropisms. Tissue level auxin patterning critically depends on membrane auxin carriers of the PIN family, exporting auxins out of cells (Blilou et al., 2005), and the AUX/LAX family, importing auxin into cells (Band et al., 2014, Bennett et al., 1996). It is particularly the cell-type-specific expression patterns and polarity of the auxin-exporting PINs that give rise to the so-called polar auxin transport that shape root tip auxin patterns (Grieneisen et al., 2007). Feedback of auxin on its own transporters, either through affecting PIN and AUX/LAX transcription (Laskowski et al., 2008, Vieten et al., 2005), PIN degradation (Abas et al., 2006, Kleine-Vehn et al., 2008), or PIN membrane cycling dynamics (Paciorek et al., 2005), are assumed to play key roles in patterning auxin distribution.

Salt stress induces endocytosis, thereby enabling salt to affect auxin carriers and thus root tip auxin patterning. Clathrin-mediated endocytosis (CME) has been proposed as the endocytic pathway involved in the internalization of auxin carriers during salt stress. Phospholipase Ds (PLDs) hydrolyse structural phospholipids, such as phosphatidylcholine, to produce phosphatidic acid (PA) that can function as lipid second messenger (for reviews, see (McDermott et al., 2004, Testerink and Munnik, 2011)). PA is known to play a regulatory role during CME (Antonescu et al., 2010). The regulation of CME by PA is putatively achieved through different modes of action. On the one hand, PA acts as a signal for cytosolic proteins to be recruited to the plasma membrane (PM; (Testerink and Munnik, 2011)); on the other hand, PA increases the negative curvature at the cytoplasmic leaflet of membranes thereby facilitating membrane fusion and fission (Kooijman et al., 2003, Yao and Xue, 2018).

In plants, an increase in PLD-generated PA is measured in response to water deficit (Frank et al., 2000, Jacob et al., 1999) and during osmotic and salt stress (Darwish et al., 2009). For *Arabidopsis*, genetic evidence for the involvement of PLD α 1 and PLD δ in salt stress has been shown (Bargmann et al., 2009). Meanwhile, several candidate PA-binding proteins have been found in the peripheral membrane fraction of salt-stressed roots (McLoughlin et al., 2013). Treatment with an inhibitor of mammalian PLDs, 5-fluoro-2-indolyl des-chlorohalopemide (Su et al., 2009), hampered clathrin localization to the membrane (Galvan-Ampudia et al., 2013). Consequently, PIN2 localization during salt treatment was altered in the presence of 5-fluoro-2-indolyl des-chlorohalopemide. However, *pld ζ 2* mutants only exhibited a weak halotropic response, indicating the possible involvement of other PLDs in the process. Yet, so far, a possible role for the other ζ -type PLD, PLD ζ 1, in plant salt stress responses or tropisms has remained elusive. Inducible RNAi inhibition of PLD ζ 1 resulted in deformed root hairs and an altered root hair patterning (Ohashi et al., 2003). Similarly, involvement of PLD ζ 1 in root development during phosphate starvation has been described (Li et al., 2006). Under phosphate limiting conditions, the *pld ζ 1/pld ζ 2*-double mutant, but not the single mutants, exhibited shorter main roots and longer lateral roots. The PLD ζ s stand out from the other 10 plant PLDs, as they lack a Ca²⁺-dependent C2-binding domain, making them Ca²⁺ independent. Instead, they contain a pleckstrin homology domain and a Phox domain, similar to mammalian PLDs, which bind phosphatidylinositol lipids in membranes (Qin and Wang, 2002) and have been linked to several endocytosis and membrane recycling pathways (Donaldson, 2009).

During the halotropic response, we previously reported a salt-induced increase in internalization and subsequent relocation of the auxin transporter PIN2 on the salt-exposed side of the root, thus asymmetrically impacting auxin flow (Galvan-Ampudia et al., 2013). Through a combination of computational modelling and *in planta* experiments, we subsequently demonstrated that these changes in PIN2 alone would be insufficient to generate an effective auxin asymmetry (van den Berg et al., 2016). Auxin-dependent regulation of AUX1 was required to amplify the auxin asymmetry. In addition, a transient increase of PIN1 that was observed in the stele was found to be essential for a rapid build-up of this asymmetry (van den Berg et al., 2016).

We set out to investigate a putative role for PLD ζ 1 in salt stress responses of the root and halotropism, based on its homology to PLD ζ 2 and mammalian PLDs. We show that both halotropism and gravitropism are affected in the *pld ζ 1* mutant. In addition, we observed defects in auxin carrier localization in root epidermal cells during salt stress. Using computational modelling, we identify the PLD ζ 1-dependent salt-induced relocation of PIN2 to lateral membranes as a key event in mounting an effective halotropic response. At the same time, PLD ζ 1 appears to promote general membrane internalization induced by the osmotic component of salt. Thus, we identify PLD ζ 1 as an essential component of root tropisms and reveal their cellular role in auxin carrier and membrane relocation in response to salinity.

6.2 Methods

6.2.1 Plant materials and growth conditions

The wild type used was *Arabidopsis thaliana*, ecotype Columbia-0 (Col-0). The *pldζ1* mutant is a T-DNA insertion line (SALK_083090). The PIN2-GFP/*pldζ1*, AUX1-mVenus/*pldζ1*, RabF2b-RFPxPIN2-GFP, SYP32-RFPxPIN2-GFP, RabA1e-RFPxPIN2-GFP, VHA1-RFPxPIN2-GFP, RabF2b-RFPxPIN2-GFP/*pldζ1*, SYP32-RFPxPIN2-GFP/*pldζ1*, RabA1e-RFPxPIN2-GFP/*pldζ1*, VHA1-RFPxPIN2-GFP/*pldζ1*, and PLDζ1-YFP/*pldζ1* were created by crossing the following published lines: PIN2-GFP (Xu and Scheres, 2005), AUX1-mVenus (Band et al., 2014), RabF2b-RFP, SYP32-RFP, RabA1e-RFP (Geldner et al., 2009), and VHA1-RFP (Dettmer et al., 2006). Primers used for *pldζ1* genotyping are forward, tgaaaagcatggaattttcg, and reverse, gtgatcgtctctgtctctcgc. General growth conditions on agar plates (half strength MS supplemented with 0.1% 2(*N*-morpholino) ethanesulphonic acid buffer and 0.5% sucrose and 1% agar) were in a climate chamber with long day period (16 hr light at 130 $\mu\text{mol m}^{-2} \text{s}^{-1}$) at 22°C and 70% humidity. Seeds were sterilized using 50% bleach and stratified for at least 2 days at 4°C. For soil experiments, seeds sterilized with 50% bleach were stratified in 0.1% agar in the dark for at least 2 days and then placed on sieved sowing ground. Plants were then grown in a climate chamber with short day period (11 hr light at 130 $\mu\text{mol m}^{-2} \text{s}^{-1}$) at 22°C and 70% humidity.

6.2.2 Halotropism plate assays and gravitropism plate assays

For the halotropism plate assays (both during time-lapse imaging and long-term halotropism assays), 10 seeds were germinated in a diagonal line on half strength MS plates. When the seedlings were 5 days old, the bottom corner (in diagonal line 0.5 cm below the root tips) of the agar was removed and replaced by control half strength MS agar without salt or half strength MS agar containing 200 mM of NaCl. For the time-lapse experiment, the plates were placed in a climate chamber containing the time-lapse set-up. Here, all plates were imaged every 20 min by infrared photography. Images were then analysed using ImageJ. For the long-term halotropism assay, a dot was placed immediately after replacing the agar and every 24 hr after the start of the treatment. After 4 days of growth, the plates were scanned, and the images were analysed using ImageJ. In the gravitropism assay, 12 plants were germinated on half strength MS plates, and after 5 days of growth, the plates were reorientated by turning 90° and placed in the climate chamber containing the time-lapse set-up. All plates were imaged every 20 min by infrared photography. Images were analysed using ImageJ.

6.2.3 Confocal microscopy

The images were acquired using a Nikon Ti inverted microscope in combination with an A1 spectral confocal scanning head. For all GFP fusion proteins, excitation/emission wavelengths used were 488 nm/505–555 nm. For mVenus, excitation/emission wavelengths were 514 nm/525–555 nm. For mCherry and RFP, excitation/emission wavelengths were 561 nm/570–620 nm. The analysis of the images was performed using Fiji (<http://fiji.sc>) software. Using a confocal microscope with a 60× objective did not yield a resolution high enough to distinguish between the apical membrane of one cell and the basal membrane of the neighbouring cell. For AUX1-mVenus, we measured both and added them up to create the apical/basal component. All images were corrected for background signal.

Membrane intensity quantification was done using ImageJ, for all cells the average pixel intensity for the apical side (or apical/basal in the case of AUX1 and Plasma Membrane Proton ATPase 2 [PMA2]),

and both lateral sides of the PM and the intracellular signal were measured by drawing a region of interest by hand.

Osmotic stress-induced membrane structures (OSIMS) quantification was done using ImageJ; a structure was classified as an OSIM structure when it was attached to the PM but clearly on the cytosolic side of the PM and larger than 300 nm. Drug treatments were performed as follows: For filipin, seedlings were treated/stained with 10 $\mu\text{g ml}^{-1}$ of filipin for 1 hr after which 120 mM of NaCl was added and plants were stressed for 60 min. For methyl-beta-cyclodextrin, seedlings were treated with 10 mM of methyl-beta-cyclodextrin for 1 hr after which 120 mM of NaCl was added and plants were stressed for 60 min.

6.2.4 Model adjustments

Our current study makes use of a previously developed model described in detail in van den Berg et al. (2016). Briefly, the model consists of a detailed two-dimensional cross section of the Arabidopsis root tip, incorporating cell-type and developmental zone-specific differences in cell sizes and patterns of the auxin-exporting PIN and auxin-importing AUX/LAX proteins. Auxin dynamics, production, degradation, intracellular and apoplast diffusion, and across membrane fluxes are computed on a subcellular grid level resolution, whereas gene expression is simulated at the level of individual cells. In addition, we include that for AUX/LAX, gene expression is auxin dependent whereas for PIN2 membrane, occupancy levels are auxin dependent.

Relative to this earlier study, a few minor changes were implemented. First, to increase computational precision, simulations were performed with a spatial integration step of 1 rather than 2 μm , resulting in a factor 4 increase in the number of simulated grid points together constituting the root tissue. Second, to increase physiological realism, a more gradual increase in the size of cells in the early elongation zone was incorporated. For further details, we refer to our earlier study.

6.2.5 Main modelling assumptions

To apply the experimentally obtained data to our (halo)tropism model, we needed to make two key assumptions. First, salt-induced effects on intracellular and membrane protein patterns were measured under experimental conditions in which salt was uniformly applied to the plant roots. To extrapolate these findings to halotropism where salt stress occurs (predominantly) at a single side of the root, we assumed that the experimentally observed changes in PIN2 and AUX1 occur in a similar manner but only at the salt-exposed side of the root.

Second, in contrast to our earlier work, microscopic images were obtained using a longitudinal epidermal top view rather than a longitudinal cross section of the root. As a consequence, in addition to apical and basal membranes, radial rather than transversal lateral membrane faces were imaged. To extrapolate the thus obtained data to our halotropism model, which describes a longitudinal cross section, we assumed that PIN2 and AUX1 patterns on radial and transversal lateral membranes are similar. Support for this assumption can be derived from the observation that similar to what we previously observed for wild-type PIN2 on transversal lateral membranes (Galvan-Ampudia et al., 2013), wild-type PIN2 on radial lateral membranes was observed to decrease approximately 20% in response to salt exposure.

6.2.6 Simulating *pldζ1* mutants

Our experimental data indicate that *pldz1* mutants have an approximately 15% reduction in apical PIN2 levels and an approximately 10% increase in (inward) lateral PIN2 levels under control conditions. As we model standard wild-type epidermal cells under control conditions to have a ratio of PIN2 apical:lateral of 1:0.1, we thus simulated *pldz1* epidermal cells under control conditions as having a ratio of apical PIN2:lateral PIN2 of 0.85:0.11 (Figure 6.S3). Notably, this results in a less polar PIN2 pattern, as well as a lower overall PIN2 level. These differences in PIN2 pattern result in minor changes in the default, nonhalotropic auxin pattern of *pldζ1* as compared with wild-type roots (Figure 6.S3).

Our experimental data indicate that in addition to changes in PIN2, cellular AUX1 patterns also change in response to salt exposure, with apical/basal levels recovering after a transient change and lateral levels showing a longer term, approximately 20% decrease. Therefore, in most halotropism simulations (indicated), we incorporated a 20% reduction of AUX1 on the lateral membranes of epidermal cells on the salt-exposed side of the root.

6.2.7 RSA assay

pldζ1 and wild-type plants were germinated on half strength MS plates. Four days after germination, the seedlings were transferred to half strength MS plates with either 0 or 75 mM of NaCl. Four seedlings were transferred to each plate, resulting in 20 replicates per line per treatment. Plates were placed in the climate chamber following a randomized order. After 6 days, the plates were scanned using an Epson Perfection V800 scanner at a resolution of 400 dpi. Root phenotypes were quantified using the SmartRoot (Lobet et al., 2011) plugin for ImageJ. Statistical analysis was performed in R with RStudio using a two-way ANOVA with Tukey's post hoc test for significance.

6.3 Results

6.3.1 PLD ζ 1 is involved in altering the root growth direction during tropisms

To assess the putative role of PLD ζ 1 during halotropism, roots from a *pld ζ 1*-KO mutant were followed for 1 day on vertical agar plates, containing either control medium or a salt gradient induced by 200 mM of NaCl (Galvan-Ampudia et al., 2013). On control plates, *pld ζ 1* seedlings were found to display a stronger skewing effect to the right than wild type (Figure 6.S1A, B). On salt, the *pld ζ 1* seedlings exhibited a slower halotropism response, and they did not reach the same angle of bending as the wild type within 24 hr (Figure 6.1a,b). During the long-term halotropic response, no difference between wild type and *pld ζ 1* was found until Day 4, where even a slightly larger angle away from the salt gradient was observed (Figure 6.S1C). To determine whether *pld ζ 1* roots were also impaired in the gravitropic response, seedlings were grown on vertical agar plates, and the root growth direction was monitored after changing the orientation of the plates by 90°. Surprisingly, *pld ζ 1* roots were found to display an exaggerated gravitropic response compared with the wild type (Figure 6.2a,b). Although wild-type roots remained at an angle of about 10° 5 hr after reorientation, the *pld ζ 1* roots kept bending towards gravity. The difference was found up to 7 hr after reorientation. Skewing during normal growth was not seen until 15 hr after reorientation of the plate (Figure 6.2b). The slower halotropic response and the exaggerated gravitropic response were both rescued by expression of pPLD ζ 1::PLD ζ 1-YFP in the *pld ζ 1* mutant background (Figures 6.1a,b and 6.2a,b). In conclusion, PLD ζ 1 is involved in both the halotropic and gravitropic responses.

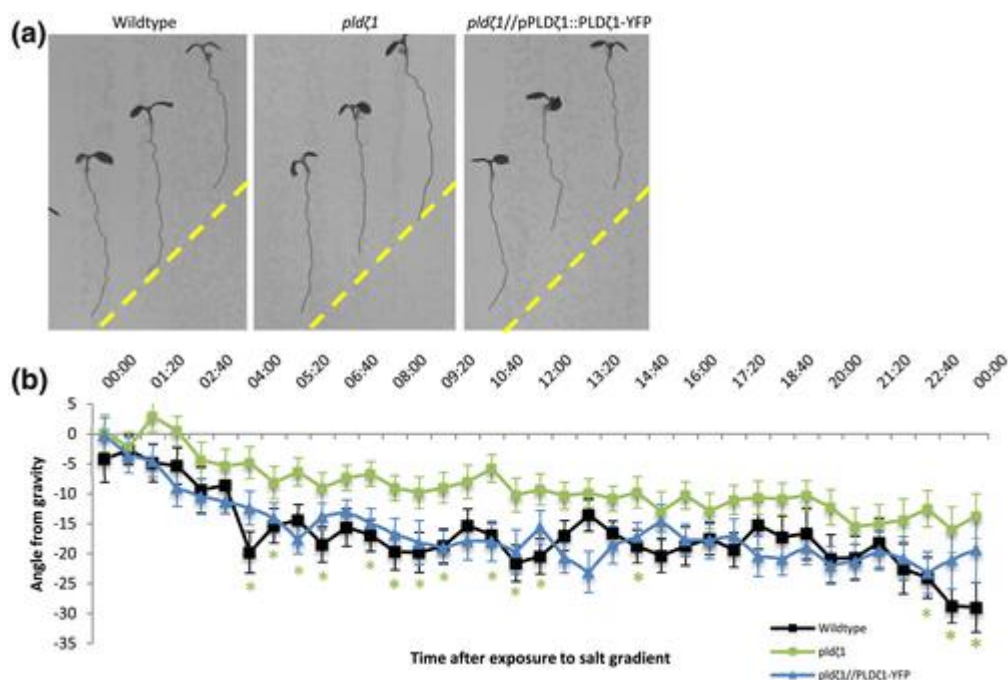


Figure 6.1. *pld ζ 1* mutant plant roots show a delayed halotropism response. (a) Representative images of WT (*Col-0*), *pld ζ 1*, and *pld ζ 1*//pPLD ζ 1::PLD ζ 1-YFP seedlings 24 hr after exposure to a 200-mM NaCl gradient in a time-lapse set-up. Yellow dashed lines show the start of gradient. (b) Quantification of the growth angle over the first 24 hr after exposure to the 200-mM salt gradient (combined data of two biological replicates, WT n = 34, *pld ζ 1* n = 38, and *pld ζ 1*//pPLD ζ 1::PLD ζ 1-YFP n = 32). Asterisks show significant differences (P < .05 in a univariate ANOVA, Tukey's post hoc test); the colour of the asterisks corresponds to the line with a significant difference from wild type

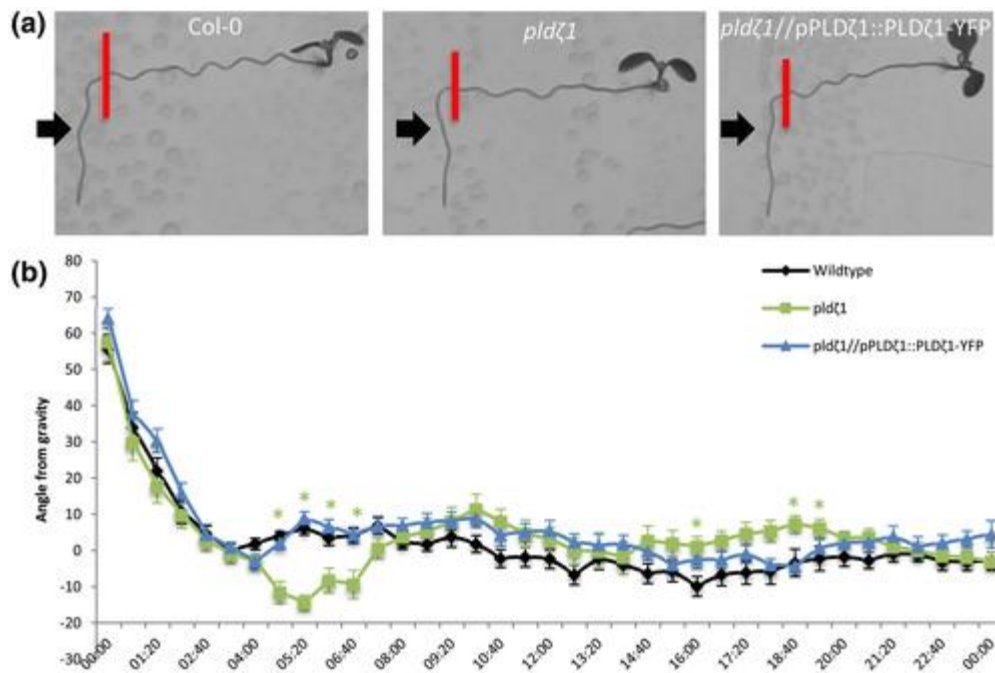


Figure 6.2. *pldζ1* roots show an exaggerated gravitropic response. (a) Representative images of WT (*Col-0*), *pldζ1*, and *pldζ1//pPLDζ1::PLDζ1-YFP* seedlings 24 hr after a 90° reorientation. Red bars show the position of the root tip immediately after reorientation. Black arrows point at the 4:00 time point. (b) Quantification of root growth angle over 24 hr after 90° reorientation (two biological replicates, WT $n = 22$, *pldζ1* $n = 24$, and *pldζ1//pPLDζ1::PLDζ1-YFP* $n = 30$). Asterisks show significant differences ($P < .05$ in a univariate ANOVA, Tukey's post hoc test); the colour of the asterisks corresponds to the line with a significant difference from wild type

6.3.2 AUX1 is internalized from the lateral side of the PM during salt stress

Our earlier work demonstrated the importance of the interplay between auxin-influx and auxin-efflux carriers during halotropism (van den Berg et al., 2016). Auxin-induced changes in AUX1 expression were shown to be crucial to amplify the auxin asymmetry required for bending. To further investigate the cellular dynamics of AUX1 during salt stress, we imaged AUX1-mVenus during control and salt treatments over time. As expected, AUX1 showed a less polar distribution than PIN2-GFP in control conditions (Band et al., 2014), which was similar for wild-type and *pldζ1* roots (Figure 6.3a,b). After 5 min of 120 mM of NaCl, AUX1-mVenus was observed to cluster in what appeared to be punctate structures at the PM. In wild-type plants, this clustering occurred simultaneously with a decrease in the combined apical and basal signal (apical/basal component), whereas its combined lateral abundance did not change. In contrast, in *pldζ1* plants, mostly the lateral rather than apical/basal AUX1 abundance decreased in response to salt (Figure 6.3b). After 60 min of salt treatment, the apical/basal AUX1-mVenus signal recovered to mock treatment levels for both wild type and *pldζ1*, whereas the lateral signal was still decreased, the intracellular signal increased, and less clustering at the PM was found than in the control situation (Figure 6.3c). These results suggest an involvement of PLDζ1 in the early (minutes) salt-induced AUX1 relocalization, but not in the long-term AUX1 response. Additionally, these results indicate that longer salt exposure (hours) leads to a reduction in lateral AUX1 levels, irrespective of genetic background.

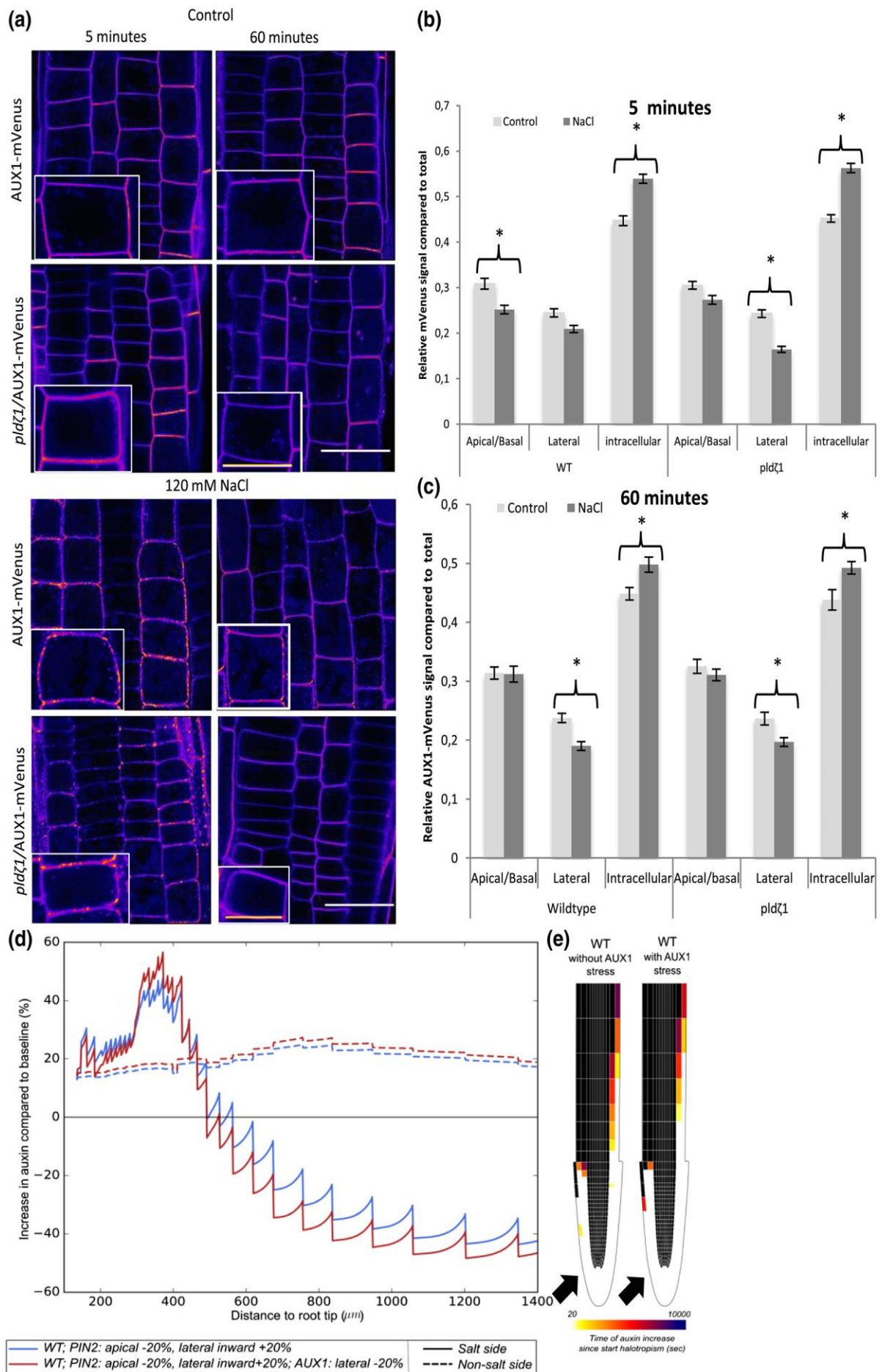


Figure 6.3. After short-term differences in AUX1 dynamics between wild type and *pldζ* during salt stress, cells show less AUX1 on the lateral side of the PM upon salt stress after 60 min. (a) Representative pictures of AUX1-mVenus in wild type and *pldζ1* during control and salt stress conditions (shown in fire look up table). (b) Relative AUX1-mVenus signal abundance at the different sides of the PM compared with total signal in control and salt stress conditions after 5 min of treatment. Apical/basal is the combined signal of the adjacent apical and basal membranes because they are indistinguishable (*N* is, respectively, 88, 80, 88, and 80 cells for WT control, WT salt, *pldζ1* control, and *pldζ1* salt). Asterisks show significant differences between control and salt ($P < .05$ using *t* test in SPSS 24). (c) Relative AUX1-mVenus signal abundance at the different sides of the PM compared with total signal in control and salt stress conditions after 60 min of treatment (*N* is, respectively, 88, 64, 96, and 80 cells for WT control, WT salt, *pldζ1* control, and *pldζ1* salt). Asterisks show significant differences between control and salt ($P < .05$ using *t* test in SPSS 24). (d) Percentage change in epidermal auxin levels at the salt and nonsalt-exposed side of the root as a function of distance from the root tip for simulated halotropism in wild-type roots, thus a 20% reduction in apical PIN2 and a 20% increase in lateral PIN2 in the root epidermal and root cap cells on the salt-exposed side of the root. Changes were shown both for a situation not incorporating and a situation incorporating salt-induced AUX1 changes. Changes in auxin levels were shown for a time point 3 hr after the start of halotropism. (e) Halotropism-induced rerouting of auxin in the two corresponding situations. Rerouting is shown if cells experience a 10% or more increase in auxin; colour coding indicates the time after the start of halotropism when this rise in auxin levels occurs. Black arrows show the direction of the salt gradient. Scale bar = 20 μm, scale bar inlay = 10 μm

6.3.3 Modelling shows how salt-induced changes in AUX1 patterning contribute to root halotropism

To investigate the effects of the altered AUX1 patterning during salt stress on halotropic auxin asymmetry, we took advantage of our previously developed computational model (van den Berg et al., 2016). Our experimental data indicated that after 60 min, roots showed restored apical/basal AUX1 levels and an approximately 20% reduction in lateral AUX1 levels. Interestingly, incorporating this 20% reduction of lateral AUX1 in our model gave rise to a 10% elevated increase in auxin at the nonsalt-exposed side of the root (Figure 6.3d), whereas an even larger change in auxin decrease at the salt-exposed side occurred. Additionally, auxin rerouting occurred in a shorter time frame, whereas the rerouting also extended further shootward (Figure 6.3e).

6.3.4 NaCl and sorbitol induce large membrane structures at the PM in epidermal and lateral root cap cells

Following the observation that AUX1 clusters to punctate structures upon root exposure to salt, we tested whether similar clustering is observed for PIN2-GFP. Indeed, within 5 min after exposure of roots to NaCl or sorbitol, root cap and epidermal cells in wild-type roots were observed to form large, punctate structures at the PM (Figure 6.4a). With an apparent size of ~600 nm (Figure 6.4c), these structures are too large to be any known type of PM-associated vesicle (Heuser, 1980, Homann, 1998). In wild-type seedlings, both number and size of these OSIMS dramatically decreased after 15 min of stress treatment (Figure 6.4b), and after 60 min, almost all OSIMS were gone. In contrast, the OSIMS in *pldζ1* roots build up over a much longer time (up to 15 min), whereas the average size increased to 700 nm after 15 min in the *pldζ1* roots (Figure 6.4c), and still half of the OSIMS remained present after 60 min of salt stress. In addition to these differences in temporal dynamics, also the subcellular localization of OSIMS showed a different pattern between wild type and *pldζ1* (Figure 6.4d). In wild type, ~55% of the OSIMS were located at the apical side of the membrane, whereas ~35% resided in the corner region (undistinguishable whether located on the lateral or apical side) after 5 min of salt stress. In *pldζ1* cells, less OSIMS were found at the apical side of the membrane (~45%) and more at the corners (~45%). Besides, in *pldζ1* cells, this spatial distribution did not differ between different time points, yet in wild-type cells, even more OSIMS were found at the apical side (~64%) after 15 min of salt stress.

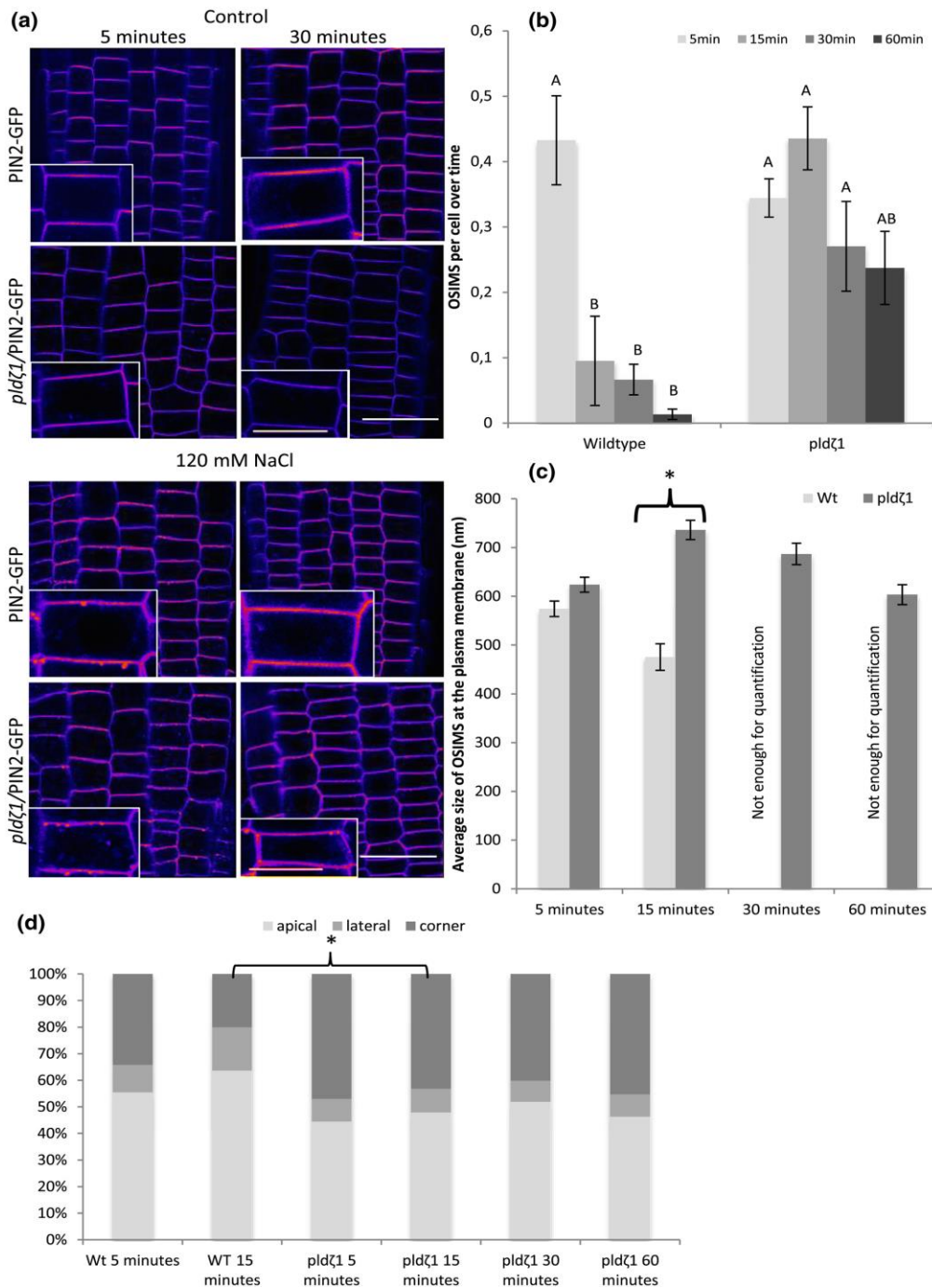


Figure 6.4. *pldζ1* mutant plants have delayed processing of OSIMS at the plasma membrane, which are bigger after 30 min and localize more often to cell corners. (a) Representative images showing PIN2-GFP in WT and *pldζ1* in control and salt stress conditions after 5 and 60 min (shown in fire look up table). (b) Quantification of amount of osmotic stress-induced membrane structures (OSIMS) at the plasma membrane in WT and *pldζ1* mutant plant epidermal cells in the lower elongation zone (data are from three biological replicates combined: $n =$ between 350 and 500 cells per time point). (c) Average structure size in WT and *pldζ1* mutant plant epidermal cells in the lower elongation zone. Letters show significant groups, $P < .05$ in a univariate ANOVA, Tukey's post hoc test in SPSS 24 (data are from three biological replicates combined: $n = 50$ for Col-0 15 min, for Col-0 5 min, and all *pldζ1* n is between 150 and 250. For Col-0 30 and 60 min, $N < 10$, and they were not quantified). Asterisks show significant difference between Col-0 and *pldζ1*. $P < .05$ in a t test using SPSS 24. (d) Subcellular localization of the NaCl-induced structures at the plasma membrane. Structures scored as localized in the corner could not be scored as either apical or lateral (the same images were used for both size and location, and the n is the same). Asterisks show significant differences between WT and *pldζ1* for a time point ($P < .05$ using a chi-square test in SPSS 24). Scale bar = 20 μm , scale bar inlay = 10 μm

Next, we investigated whether a membrane protein unrelated to auxin, the PM H⁺-ATPase PMA2, would also occur in OSIMS after salt application. Indeed, PMA2-GFP appeared in OSIMS 5 min after salt application similar to PIN2-GFP and AUX1-mVenus (Figure 6.S2A). Moreover, no significant difference in the number of OSIMS between PMA2- and PIN2-GFP-expressing lines was found 5 min after salt stress (Figure 6.S2B). Imaging PIN2-GFP after treatment with 240 mM of sorbitol also revealed OSIMS (Figure 6.S2C), and no significant difference in the number of OSIMS was observed compared with salt. Similar to salt stress, these OSIMS were rarely observed after 60 min of sorbitol treatment (Figure 6.S2D).

To test whether these OSIMS are larger forms of known endosomal structures, colocalization experiments with PIN2 and known endosomal markers were performed in wild-type and *pldζ1* background. These include RabF2b-RFP (ARA7) for multivesicular bodies, SYP32-RFP for the golgi network, RabA1e-RFP for recycling endosomes, and VHA1-RFP for early endosomes (Dettmer et al., 2006, Geldner et al., 2009). However, none of the markers showed colocalization with the PIN2-containing OSIMS after 5 min of NaCl treatment (Figure 6.S3). If OSIMS represent excess membrane material, the styryl dye FM4-64, used to label PM, should colocalize with the PIN2-GFP found in the OSIMS. Hence, Arabidopsis seedlings expressing PIN2-GFP were stained with FM4-64 (Figure 6.S4E,F). Indeed, PIN2-GFP and FM4-64 were found to colocalize in the OSIMS, indicating that OSIMS are of membranous origin.

To investigate whether OSIMS are part of an endocytic pathway, we tested their association with clathrin (CME) and their response to pharmacological drugs that inhibit membrane microdomain-associated endocytosis (MMAE). For clathrin, we used a PIN2-GFP × CLC-mCherry line to image the subcellular localization of both proteins during early salt stress responses, and no clathrin was found to associate with OSIMS (Figure 6.S4A,B). For MMAE, two inhibitors were tested, that is, methyl-β-cyclodextrin and filipin (Ovecka et al., 2010, Valitova et al., 2014), neither of which affected the formation of OSIMS (Figure 6.S4C,D), and no colocalization was found with the fluorescent filipin (Figure 6.S4E,F). Together, these results suggest that OSIMS represent excess membrane material but not enlarged clathrin-coated vesicles or internalized microdomains.

6.3.5 The PIN2 auxin-efflux carrier is more apolarly distributed in a *pldζ1* line

Next to the influx carrier AUX1, cellular polarity of the efflux carrier PIN2 has been reported to be affected by salt during the halotropism response (Galvan-Ampudia et al., 2013). Thus, we investigated differences in the subcellular localization of PIN2 in root epidermal cells between wild type and *pldζ1* with and without salt in the root elongation zone. Under control conditions, *pldζ1* mutants exhibited a more apolar distribution of PIN2-GFP compared with wild-type roots, with more PIN2 at the lateral membranes and less at the apical membranes (Figures 6.4a and 6.5a). In salt-stressed wild type, apical PIN2 abundance decreased, and intracellular PIN increased compared with total PIN2, whereas lateral PIN2 abundance increased after 30 min (Figure 6.5c), in accordance with our earlier work (Galvan-Ampudia et al., 2013). As OSIMS were already formed at 5 min after treatment with salt, we next investigated early changes in polarity and found a PIN2 decrease at both apical and lateral sides of the membrane after 5 min, whereas the intracellular pool increased (Figure 6.5b). Thus, although initially, PIN2 at all membranes decreases in response to salt, at later stages, PIN2 is relocalized to the lateral membrane. In contrast, a membrane protein unrelated to auxin transport, that is, PMA2, displayed no such polarity change (Figure 6.S5). The *pldζ1* mutant showed similar changes to wild type in cellular PIN2 patterning after 5 min of salt stress (Figure 6.5b) but failed to relocalize PIN2 to the lateral membrane at later stages after salt stress (Figure 6.5c).

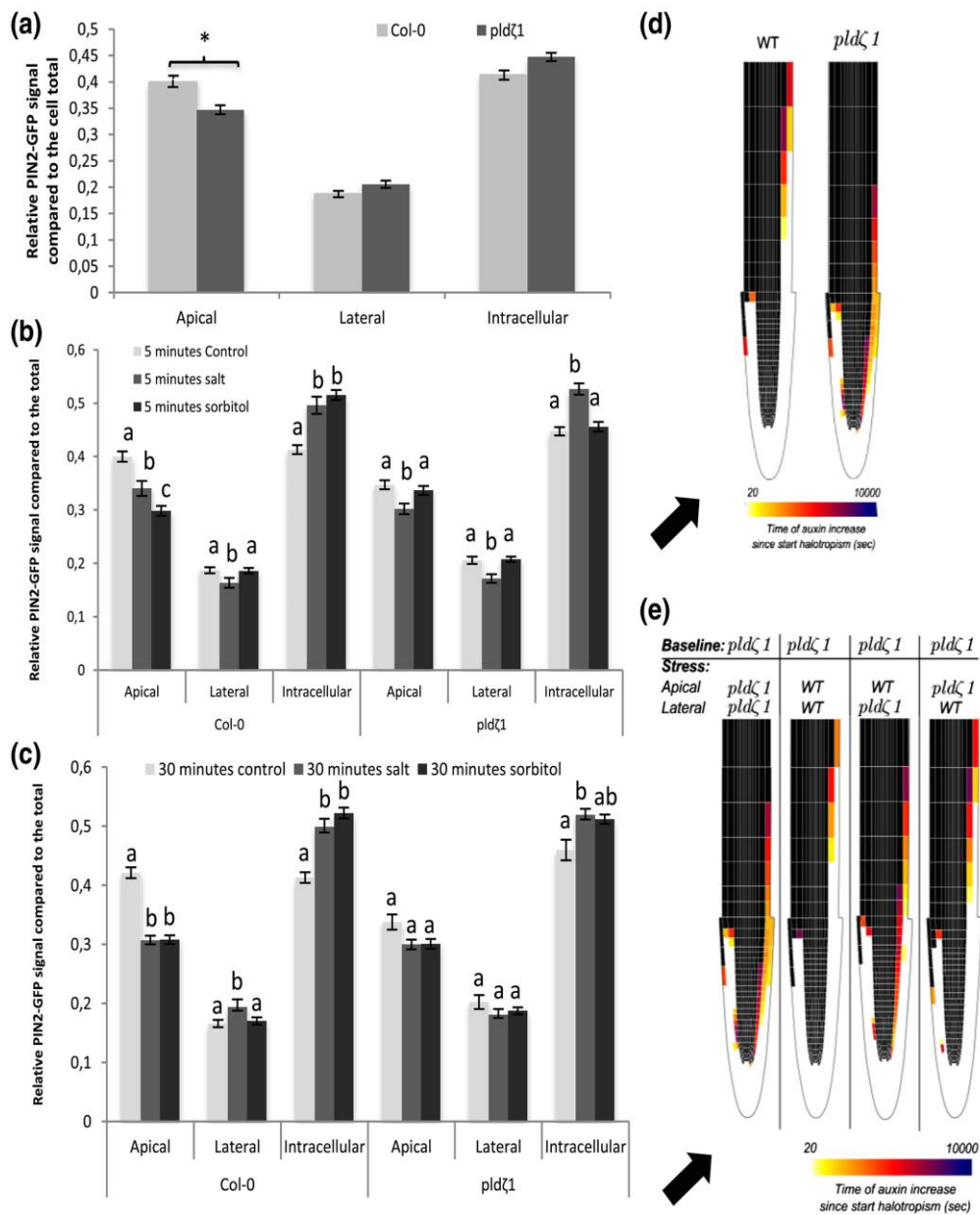


Figure 6.5. Loss of PLD ζ 1 results in a more apolar PIN2 distribution and altered PIN2 relocation upon salt stress. Using a PIN2-GFP fusion protein in both wild-type (*Col-0*) and *pldζ1* background, the intensity of the GFP signal on the apical and lateral sides of the membrane was measured next to the intracellular signal. (a) PIN2 polarity in normal conditions shows a significant lower signal at the apical membrane in the *pldζ1* background (three biological replicates, $n = 96$ cells from 12 roots). (b) Quantification of PIN2-GFP signal at the different cell compartments after 5 min of control, salt or sorbitol treatment (three biological replicates, $n > 80$, from 10 roots or more). (c) Quantification of PIN2-GFP signal at the different cell compartments after 30 min of control, salt or sorbitol treatment (three biological replicates, $n > 80$ from 10 roots or more). (d) Heat maps showing halotropism-induced auxin rerouting for wild-type and *pldζ1* settings. When a cell changes from black to coloured, this indicates an auxin increase of at least 10%. The colour indicates the timing of the auxin increase with lighter colours for short time periods. Black arrow indicates direction of the salt gradient. (e) Changes in auxin rerouting for the different stress settings in the *pldζ1* mutant. The apical or lateral distribution of PIN2 using either the *pldζ1* settings or the wild-type stress settings in the model is indicated. When a cell changes from black to coloured, this indicates an auxin increase of at least 10%. The colour indicates the timing of the auxin increase with lighter colours for short time periods. Black arrow indicates direction of the salt gradient

Next, we investigated whether the differences in PIN2 polarity during NaCl treatment were salt specific or caused by osmotic shock. In order to answer this question, roots were treated with an equal osmolality of sorbitol (240 mM), and the polarity of PIN2 was determined after 5 and 30 min. Similar to 120 mM of NaCl, the apical component of the PIN2-GFP signal in wild-type root epidermal cells decreased after 5 min (Figure 6.5b). The abundance of PIN2 at the lateral sides of the membrane, however, did not change, whereas the intracellular signal increased. After 30 min, the apical, lateral, and intracellular signals all remained at the same level as the 5-min sorbitol treatment. Thus, no significant PIN2 relocation to the lateral sides of the PM in case of osmotic stress treatment was observed. No differences were found between the *pldζ1* mutant and wild type with regard to PIN2 internal signal and lateral relocation in response to sorbitol (Figure 6.5c). On the other hand, the *pldζ1* mutant showed a different response from the wild type to sorbitol with respect to the apical PIN2 signal, which did not decrease in response to sorbitol treatment. This result indicates that osmotic stress-induced PIN2-GFP internalization from the apical side of the PM is impaired in the *pldζ1* (Figure 6.5b,c), whereas the observed PIN2 relocation to the lateral sides of the PM upon salt stress is salt specific and PLDζ1 dependent.

6.3.6 Modelling demonstrates how differences in salt-induced PIN2 response can delay root halotropism

Because our experimental results showed that next to salt-induced changes in PIN2 polarity also the baseline PIN2 pattern differed between wild-type and the *pldζ1* mutant roots, we investigated whether the observed differences in basal PIN2 patterning and those induced by salt could explain the observed response differences during halotropism. To simulate auxin patterning in the *pldζ1* mutant, we first applied the somewhat less polarized *pldζ1* mutant baseline PIN2 pattern in all lateral root cap and epidermal cells at both sides of our two-dimensional root tip model (wild type–apical PIN2:lateral PIN2 ratio = 1:0.1; *pldζ1*–apical PIN2:lateral PIN2 ratio = 0.85:0.11; based on Figure 6.5a). We tested whether our model would predict differences in epidermal auxin levels in control conditions due to these changes. Apart from modestly elevated auxin levels between 250 and 500 μm from the root tip, overall root auxin patterning was largely unaffected (Figure 6.S6). To simulate auxin patterning during halotropism in the *pldζ1* mutant, we applied the altered *pldζ1*-type PIN2 salt responses in the higher lateral root cap and epidermal cells of only the salt-exposed side of the root. On the basis of our data (Figure 6.5b), we applied a smaller reduction in apical PIN2 levels and no increase in lateral PIN2 levels as compared with wild-type halotropism (wild-type halotropism = apical PIN2:lateral PIN2 ratio = 0.8:0.12; *pldζ1* halotropism = apical PIN2:lateral PIN2 ratio = 0.775:0.11). The model also included the salt-induced transient increase of PIN1, which was shown to be important for auxin asymmetry timing, and the auxin-induced expression of AUX1, important for auxin asymmetry amplification found earlier (van den Berg et al., 2016), as well as the above discussed reduction in lateral AUX1 levels in response to salt (Figure 6.3c). Consistent with the experimentally observed slower halotropic response, the model predicted that *pldζ1* has a slower, less distal rerouting of auxin to the nonsalt-exposed side of the root and achieves substantially less pronounced auxin asymmetry levels (18% vs. 27% increase at the nonsalt-exposed side and 17% vs. 54% decrease at the salt-exposed side; Figures 6.5d and 6.S7d).

Making use of the freedom that a mathematical model offers in separating and combining conditions not easily created *in planta*, we then decided to investigate to what extent differences in *pldζ1* halotropism response depend on differences in basal PIN2 patterns and differences in salt-induced PIN2 responses. First, we investigated the effect of the differences in baseline conditions. For this, we combined the *pldζ1* type of salt-induced PIN2 changes with different baseline conditions: wild

type, *pldζ1*, or hybrid combinations (Figure 6.S7A). Differences in baseline PIN2 patterns appear to have a small effect on the auxin increase at the nonsalt-exposed side, a somewhat larger effect on the auxin decrease on the salt-exposed side, as well as a small effect on the timing of auxin rerouting (Figure 6.S7B). The slightly larger asymmetry and rerouting speed arising in wild type as compared with *pldζ1* baseline PIN2 conditions are predominantly caused by the difference in baseline apical PIN2 levels (Figure 6.S6A). Next, we combined *pldζ1* baseline PIN2 settings with different salt-induced PIN2 changes: wild type, *pldζ1*, or hybrid combinations. We find that it is predominantly the increase in lateral PIN2 levels that occurs in the wild type but not *pldζ1*, under salt, that is critical for both the level of auxin asymmetry (Figures 6.5e and 6S7c) and the speed with which this asymmetry is being build-up (Figure 6.5e). The higher salt-induced apical PIN2 levels in wild type relative to *pldζ1* only play a minor role in both location and timing of the auxin asymmetry.

In conclusion, although the baseline PIN2 differences cause a mild-slowing down and reduction of auxin rerouting during halotropism in the *pldζ1* mutant, it is predominantly the difference in salt-induced PIN2 localization changes relative to wild type that causes a slower halotropic response due to slower, less spatially extended but foremost reduced auxin rerouting.

6.3.7 *pldζ1* root epidermal cells in the elongation zone lose turgor during the early response to mild salt stress

As PLDζ1 is involved in membrane trafficking during salt and osmotic stress, the loss of PLDζ1 may lead to defective maintenance of PM surface area. In guard cells, which shrink and swell through ABA regulation, it has been shown that membrane material is internalized and remobilized back during shrinking and swelling (Meckel et al., 2004, Shope et al., 2003). We investigated root epidermal cell shrinking in the elongation zone of *pldζ1*. Interestingly, the *pldζ1* mutant appears to show a mild reduction in epidermal protoplast size after 5 min of 120 mM of NaCl treatment, whereas in wild-type cells, this concentration does not lead to plasmolysis (Figure 6.6a). The size reduction was only transient and was restored after 60 min (Figure 6.6a). Thus, the putative mild transient plasmolysis and reduced cell size in the *pldζ1* mutant suggest a slower recovery of PM surface area in response to osmotic stress.

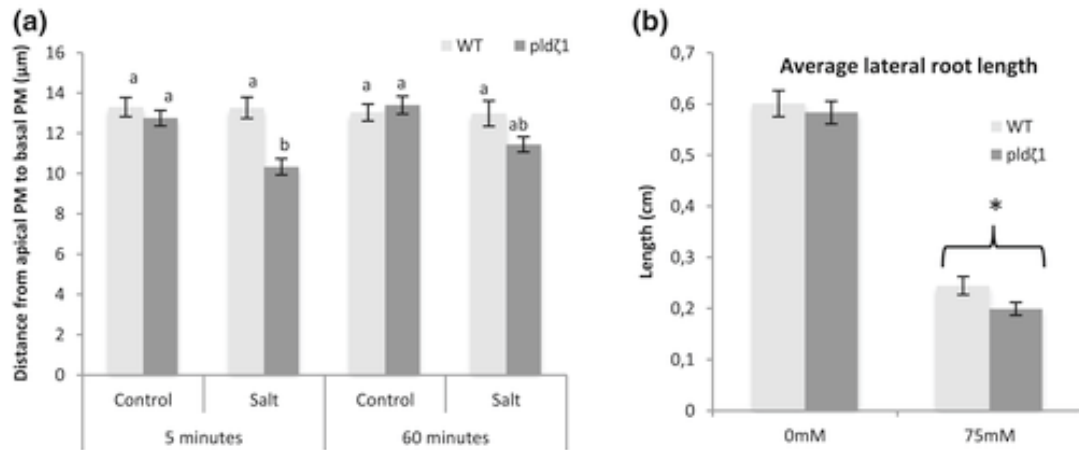


Figure 6.6. The *pldζ1* mutant exhibits a transient decrease in root epidermal protoplast size in the elongation zone and shorter lateral roots upon exposure to salt stress. (a) Five-day-old WT and *pldζ1* seedlings expressing *pAUX1::AUX1-mVenus* were exposed to a control or 120-mM salt treatment for either 5 or 60 min. Using confocal microscopy, cells were imaged, and distance from apical PM to basal PM was measured (data are from three biological replicates combined, for 5 min, *n* is, respectively, 88, 80, 88, and 80 cells for WT control, WT salt, *pldζ1* control, and *pldζ1* salt, and for 60 min, *n* is, respectively, 88, 64, 96, and 80 cells for WT control, WT salt, *pldζ1* control, and *pldζ1* salt). Letters show significant group determined by ANOVA followed by Tukey's post hoc test ($P < .05$). (b) *pldζ1* seedlings have shorter average lateral root length during mild salt stress. Result are from two biological replicates, total $n \pm 40$. Asterisks show significant differences between *Col-0* and *pldζ1* according to a univariate ANOVA followed by Tukey's post hoc test with $P < .05$.

6.3.8 Loss of PLDζ1 has a mild effect on RSA response to salt

The difference in baseline PIN2 polarity and salt-induced AUX1 and PIN2 relocalization has been predicted by our model to result in altered auxin dynamics during halotropism in *pldζ1* roots. To determine whether the changes in auxin transporter dynamics of *pldζ1* roots result in changes in RSA on uniform salt media (no gradient), we compared root growth parameters of wild-type and *pldζ1* seedlings transferred to agar plates containing 0 or 75 mM of NaCl (Figure 6.S8A–E). No differences were found between wild type and *pldζ1* for main root length (Figure 6.S8A), number of lateral roots (Figure 6.S8B), or lateral root density (Figure 6.S8C) in both control and mild salt stress conditions. However, *pldζ1* plants were found to have on average shorter lateral roots in salt (Figure 6.6b), suggesting a role for PLDζ1 in outgrowth of lateral roots under salt stress.

6.4 Discussion

Changes in polar auxin transport in plant roots during development and in response to environmental stimuli are essential for plant survival. The endocytic pathways responsible for internalization of auxin carriers to change polar auxin transport upon stress remain elusive. For the response to salt, both clathrin-dependent and clathrin-independent pathways have been proposed (Baral et al., 2015, Galvan-Ampudia et al., 2013). Mammalian PLD-type enzymes are known to be involved in endocytosis and cell polarity, and their closest homologues in plants are PLD ζ s, in Arabidopsis represented by PLD ζ 1 and 2. Thus, PLD ζ s are potential candidates for regulating the internalization and cellular polarity of auxin carriers during root responses to salt stress. Previously, we demonstrated the involvement of PLD ζ 2 in PIN2 internalization during root halotropism, a directional growth response away from the region of the highest salt stress (Galvan-Ampudia et al., 2013). Yet a role for PLD ζ 1 in salt-induced auxin carrier internalization has never been addressed.

Our results reveal a role for PLD ζ 1 in tropic responses and salt stress. Furthermore, we observed the formation of large structures at the PM (OSIMS) shortly after hyperosmotic stress with NaCl or sorbitol. These OSIMS essentially disappeared in wild-type roots within 30 min but were still found in *pld ζ 1* after 60 min of hyperosmotic stress. Moreover, the salt-specific lateral relocalization of PIN2 in root epidermal cells observed in wild-type roots was defective in a *pld ζ 1* mutant, whereas lateral AUX1 abundance was found to decrease irrespective of genetic background. Using our previously developed model for root halotropism simulations (van den Berg et al., 2016), we demonstrate how salt-induced AUX1 changes could enhance halotropism-induced auxin asymmetry. Additionally, we show that the observed PIN2 auxin carrier changes in the *pld ζ 1* mutant lead to a slower build-up of auxin asymmetry during halotropism. Finally, our modelling results predict that it is predominantly the absence of an increase in lateral PIN2 in mutants as compared with wild-type seedlings that reduces auxin asymmetry build-up, explaining the observed delayed halotropism phenotype of the *pld ζ 1* mutant.

6.4.1 PLD ζ 1 is involved in the halotropic and gravitropic responses

For PLD ζ 2, a role during halotropism (Galvan-Ampudia et al., 2013), gravitropism (Li and Xue, 2007), and hydrotropism (Taniguchi et al., 2010) has been shown. For PLD ζ 1, only a role in root hair formation (Ohashi et al., 2003) and root development during phosphate starvation had been described (Li et al., 2006), but the underlying cellular mechanisms remain unknown. Here, we report a slower halotropic response of the *pld ζ 1* mutant. Although *pld ζ 2* had a repressed halotropic response after 24 hr of growth on a salt gradient (Galvan-Ampudia et al., 2013), for *pld ζ 1*, a smaller angle away from the salt gradient compared with wild type after 5–7 hr was found but no difference after 24 hr. Additionally, in contrast to the *pld ζ 2* mutant (Li and Xue, 2007), which showed a repressed gravitropic response, we found a normal initial yet a defective attenuation of the long-term gravitropic response for the *pld ζ 1* mutant. This indicates distinct roles for PLD ζ 1 and PLD ζ 2 in the plant root during tropisms. The apparently contrasting result that the *pld ζ 1* mutant exhibits a repressed early-halotropic response and an exaggerated long-term gravitropic response might be explained by a shared importance of PIN2 relocalization during the early salt response to shift auxin to the nonsalt-exposed side and during the late-gravitropic response to shift back auxin to attenuate gravitropism. In this way, the dysfunctional PIN2 cycling in *pld ζ 1* would cause both the slow start of halotropism and the slow ending of gravitropism, underlining the importance of appropriate timing for the distinct roles of PIN2 during tropisms.

6.4.2 PLD ζ 1 regulates PIN2 polarity and auxin carrier polarity shifts during salt stress

It is believed that membrane protein polarity is dependent on constitutive cycling, which requires endocytosis, and PLD ζ 2 has been found to be involved in the endocytosis of PIN2 under normal conditions (Li and Xue, 2007). Additionally, it has been shown that PLD ζ 2-derived PA regulates PIN1 polar localization through an interaction with the scaffolding A1 subunit of protein phosphatase 2A, which mediates PIN1 dephosphorylation (Gao et al., 2013). We report altered polarity of PIN2 in a *pld ζ 1* mutant under control conditions and in addition aberrant PIN2 and AUX1 distribution during, respectively, later and initial salt stress. This is in agreement with previously shown involvement of PLD ζ 2 in auxin carrier relocalization during halotropism (Galvan-Ampudia et al., 2013). Also, we found similar initial sorbitol-induced internalization of PIN2 compared with previously reported PIN2 dynamics after a 10-min mannitol treatment (Zwiewka et al., 2015). However, although salt induces a relocalization of PIN2 to the lateral membrane compartment, osmotic stress does not have this effect. These differences in auxin carrier relocalization during salt and osmotic treatments suggest that the relocalization during salt treatment is not due to the osmotic component of the salt stress and might explain why an osmotic gradient does not lead to a tropic (directional) response, whereas a salt gradient does (Galvan-Ampudia et al., 2013). In support, computational modelling established that relocalization of PIN2 to the lateral side of the membrane in cells on the salt-facing side during halotropism is required for a sufficient difference in auxin concentration between the salt-facing and nonsalt-facing side of the root (van den Berg et al., 2016).

PLD ζ 2 has been proposed to function in PIN endocytosis through the recruitment of components of the clathrin machinery to the PM by binding PLD-derived PA (McLoughlin et al., 2013). Interaction between Clathrin Heavy Chain and Epsin-like Clathrin Adaptor 1 and Epsin-like Clathrin Adaptor 4 and PA was observed shortly after initiation of salt stress. The finding by McLoughlin and colleagues is consistent with other studies showing involvement of CME in internalization of auxin carriers (Galvan-Ampudia et al., 2013, Kleine-Vehn et al., 2010, Rakusova et al., 2015, Shinohara et al., 2013, Zwiewka et al., 2015) and aquaporins (Martiniere et al., 2012) during tropic responses or stress by using the CME inhibitor tyrphostin A23 (TyrA23). However, recently, it has been shown that TyrA23 treatment results in acidification of the cytoplasm (Dejonghe et al., 2016), raising serious questions on the specificity of CME inhibition by TyrA23. Other evidence pointing towards clathrin-independent endocytosis during salt stress comes from auxin carriers that are internalized in the presence of NAA, a known inhibitor of CME (Baral et al., 2015). Moreover, ABCB19 was found to interact with PIN1 in association with sterols and sphingolipids (Titapiwatanakun et al., 2009). PIN1 was found in detergent-resistant membrane fractions after Triton X-100 treatment in wild-type plants, whereas in *abcb19* mutants, PIN1 abundance in the detergent-resistant membrane fraction was much lower. This suggests that PIN1 internalization could occur through MMAE. So, until today, no strong evidence exists for one specific endocytosis pathway induced during salt stress, and several pathways could contribute. Here, we report unknown structures arising upon salt and osmotic stress, with an apparent size of approximately 500–700 nm, containing membrane proteins, that we named OSIMS. No evidence for involvement of clathrin or microdomains in affecting these OSIMS was found.

6.4.3 Loss of PLD ζ 1 results in a defect in maintaining PM surface area

We describe novel OSIMS in Arabidopsis seedling roots when treated with NaCl or sorbitol. Interestingly, these osmotic stress-induced membrane compartments were never observed detached from the PM. Therefore, we speculate that OSIMS represent excess membrane material due to osmotic stress. Invaginations or folds upon hyperosmotic stress have been observed in yeast (Morris et al.,

1986), and it has been proposed that in stomatal guard cell protoplasts, changes in membrane surface area are associated with removal and incorporation of membrane material (Homann, 1998). The fact that OSIMS were only observed in the first 30 min after NaCl or sorbitol treatment in wild-type plants and that Arabidopsis epidermal root cells have been shown to recover turgor pressure within 40 min after hyperosmotic stress (Shabala and Lew, 2002) supports this theory. To test whether OSIMS are enlarged, growing vesicles, we performed colocalization experiments with markers for known endocytosis pathways. The OSIMS were not found to colocalize with CLC2 (marker for clathrin-coated vesicles) or filipin (a marker for membrane microdomains), suggesting that they are not enlarged vesicles. Consistently, two drugs commonly used to inhibit MMAE did not affect the presence of OSIMS. These results support the hypothesis that the OSIMS are excess PM material induced by hyperosmotic treatment. Additionally, AUX1-mVenus was found to form punctate structures in the PM, which appear to reside longer in the PM in wild-type cells than *pldζ1* cells, indicating that besides OSIMS, other structures may influence auxin carrier dynamics during osmotic stress. The observation that loss of PLDζ1 leads to a slight decrease in protoplast size of root epidermal cells indicates slow recovery of PM surface area after osmotic stress and thus involvement of PLDζ1 in membrane fission or restoration of osmotic potential.

6.4.4 Loss of PLDζ1 affects root remodelling during salt stress

Recently, the growth rate of a *pldζ1* mutant in soil containing 75 mM of NaCl was found to be more affected than in wild type (Ben Othman et al., 2017), but root architecture was not addressed in this study. Different strategies have been described for Arabidopsis accessions in RSA adaptations to salinity (Julkowska et al., 2014). For the wild-type accession Col-0, it is known that lateral root length contribution towards total root size increases upon an increase in salt concentration (Julkowska et al., 2014). Thus, a shorter main root and longer laterals might be a response to cope with higher salinity. In the current study, we observed in the *pldζ1* mutant a decreased lateral root length to main root length ratio during mild salt stress. Because this represents a reversal of the wild-type salinity response, this supports the idea of defective remodelling in this mutant and could underlie the observed slightly reduced coping capacity of *pldζ1* plants in saline soil (Ben Othman et al., 2017).

6.4.5 Lateral AUX1 decrease, PLDζ1, and OSIMS affect the salt response in Arabidopsis roots

Concluding, we report salt-induced changes in AUX1 localization, and through mathematical modelling, we predict that the observed decrease of lateral AUX1 enhances auxin asymmetry during halotropism. Moreover, this work confirms a role for PLDζ1 in halotropic and gravitropic responses. A *pldζ1* mutant exhibited both permanently altered PIN2 polarity and changes in salt-induced PIN2 relocalization. Simulations in our updated mathematical root model show how these differences can result in delayed and weaker build-up of auxin asymmetry in the *pldζ1* mutant, thus explaining its halotropism phenotype. Finally, we discovered novel OSIMS. The hampered processing of OSIMS in the *pldζ1* mutant coincides with the absence of PIN2 relocalization to the lateral side of the PM during salt stress and thus indicates a role for OSIMS in the auxin carrier dynamics during salt stress. Together, these results further our knowledge on auxin carrier internalization and relocalization during the salt stress response.

Acknowledgments

We thank Remko Offringa (PIN2-GFP), Malcolm Bennet (AUX1-mVenus), Niko Geldner (wavelines W2R, W22R, and W34R; Geldner et al., 2009), Karin Schumacher (VHA1-RFP and PMA2-GFP), and Eva Benkova (PIN3-GFP) for kindly sharing published materials. We thank Michel Haring and Teun Munnik for critical reading. This project was funded by NWO (CW 711.014.002 and Vidi 864.14.003).

Author contributions

R.A.K., T.v.d.B., K.H.W.J.t.T., and C.T. conceptualized the study. T.v.d.B. and K.H.W.J.t.T. contributed to the software. R.A.K., A.J.M., and T.v.d.B. contributed to the investigation of the study. C.S.G.A. contributed to the resources. R.A.K. and C.T. wrote the original draft. All authors reviewed and edited the study. C.T. and K.H.W.J.t.T contributed to the supervision and funding acquisition.

6.5 Supporting information

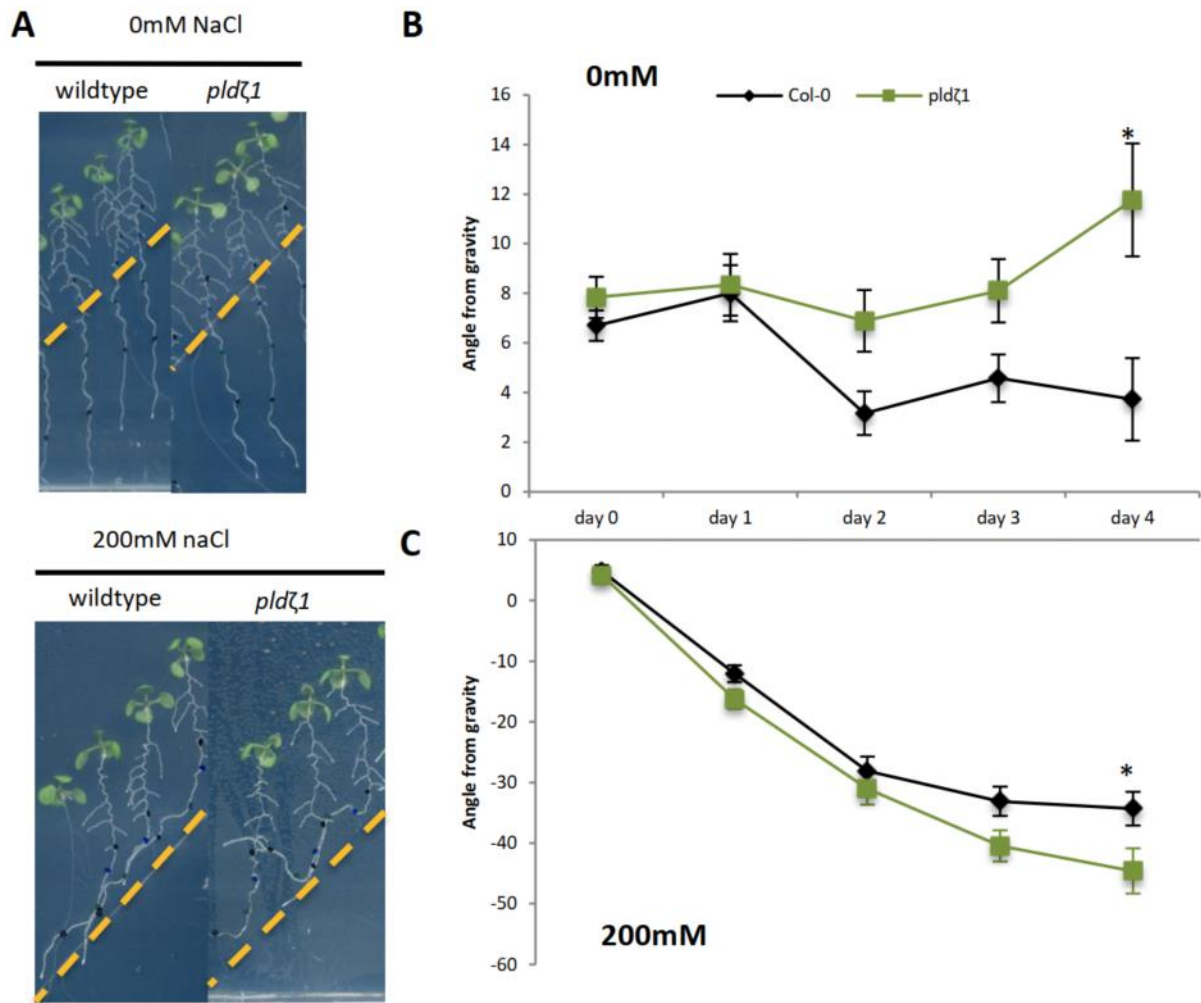


Figure S6.1: Long term effects on halotropic response show delayed attenuation of the halotropic response. (A) Images showing 5 days of growth of WT and the *pldζ1* mutant on gradient plates with 0 mM or 200 mM of NaCl. (B,C) Quantification of halotropism plate assay over multiple days shows more skewing of *pldζ1* mutant roots in control conditions (B) (3 biological replicates: WT $n = 68$, *pldζ1* $n = 62$) and more avoidance after 4 days of growth on a salt medium (C) (3 biological replicates: WT $n = 67$, *pldζ1* $n = 66$). Asterisks show significant differences, an univariate ANOVA was used followed by a Tukey post-hoc test ($p < 0.05$)

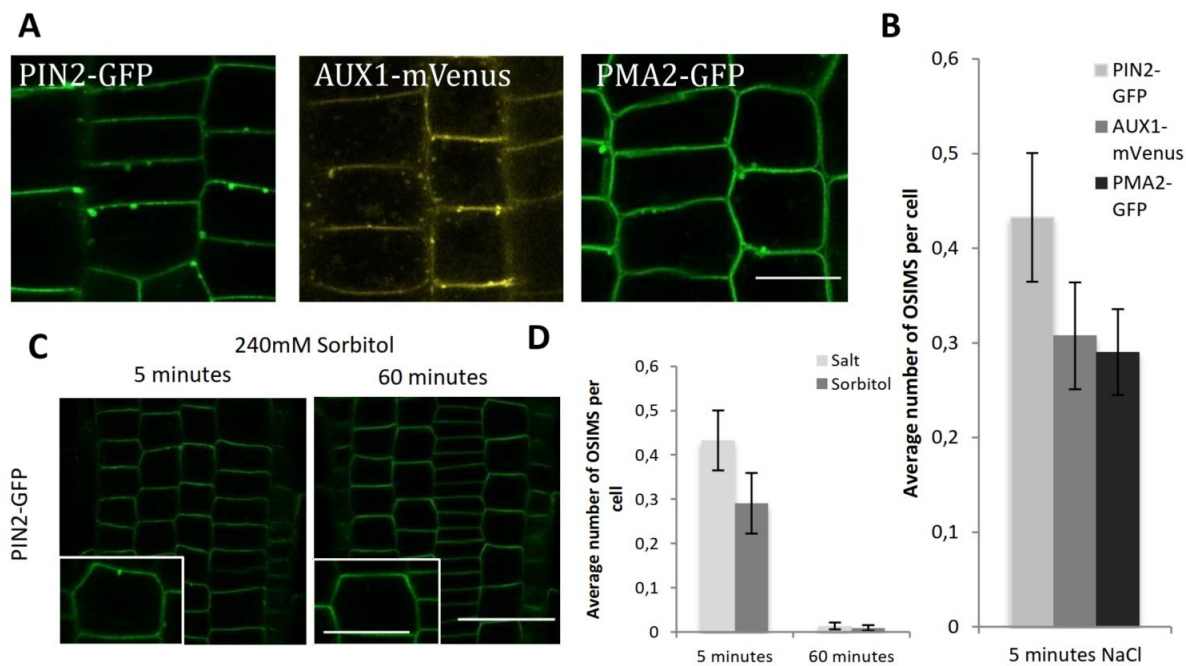


Figure S6.2: OSIMS contain multiple plasma membrane proteins and are induced by osmotic stress. (A) Comparison of the amount of OSIMS in a PIN2-GFP, AUX1-mVenus and PMA2-GFP line after 5 minutes of a 120 mM salt stress. No significant differences were found using a univariate ANOVA with Tukey post hoc in SPSS 24. (B) Representative images of OSIMS in Arabidopsis roots expressing PIN2-GFP, AUX1-mVenus and PMA2-GFP after a 5 minute 120 mM NaCl treatment. (C) Representative pictures of PIN2-GFP sub-cellular localization after 5 or 60 minutes of 240 mM Sorbitol treatment. Inlays show an enlargement of one cell. (D) Quantification of the average number of OSIM structures per cell after 5 and 60 minutes of 240 mM Sorbitol treatment, salt treatment data is shown for comparison. No significant differences using a univariate ANOVA followed by a Tukey post-hoc test ($p < 0.05$) were found for either time point. Scale bar = 10 μ m in (A), 20 μ m in (C) and 10 μ m in the inlay.

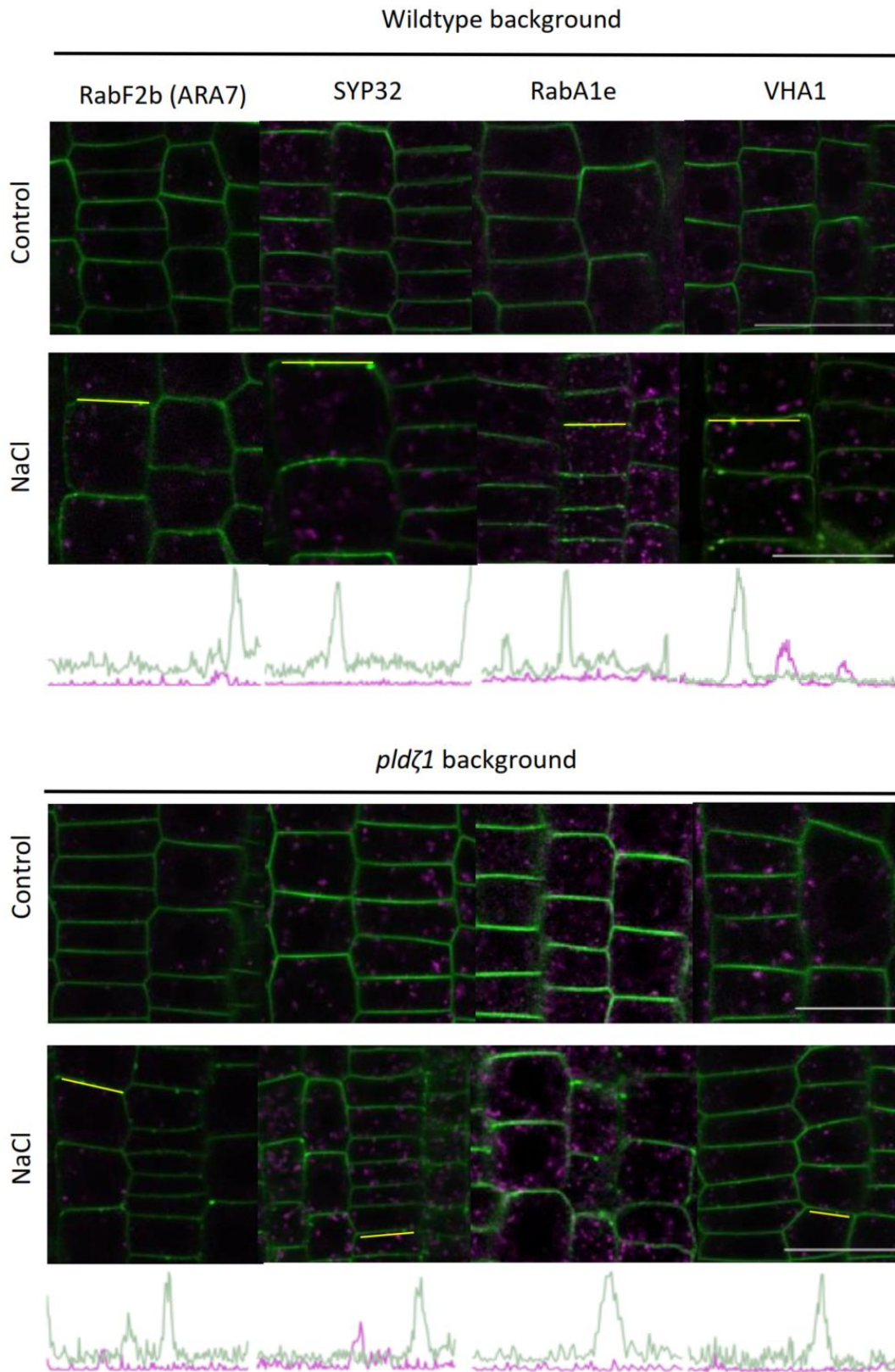


Figure S6.3: OSIMS do not co-localize with known endosomal markers. Representative images showing PIN2-GFP in wildtype and *pldζ1* background in combination with either RabF2b-RFP (ARA7) for multi-vesicular bodies, SYP32-RFP for the golgi network, RabA1e-RFP for recycling endosomes and VHA1-RFP for early endosomes after 5 minutes of salt stress. Yellow lines are the lines used for the profile plot through the OSIMS. Green line shows PIN2-GFP signal and the magenta line shows the endosomal marker RFP signal. No OSIMS are found in control conditions so no profile plots are shown. Scale bar = 20 μ m

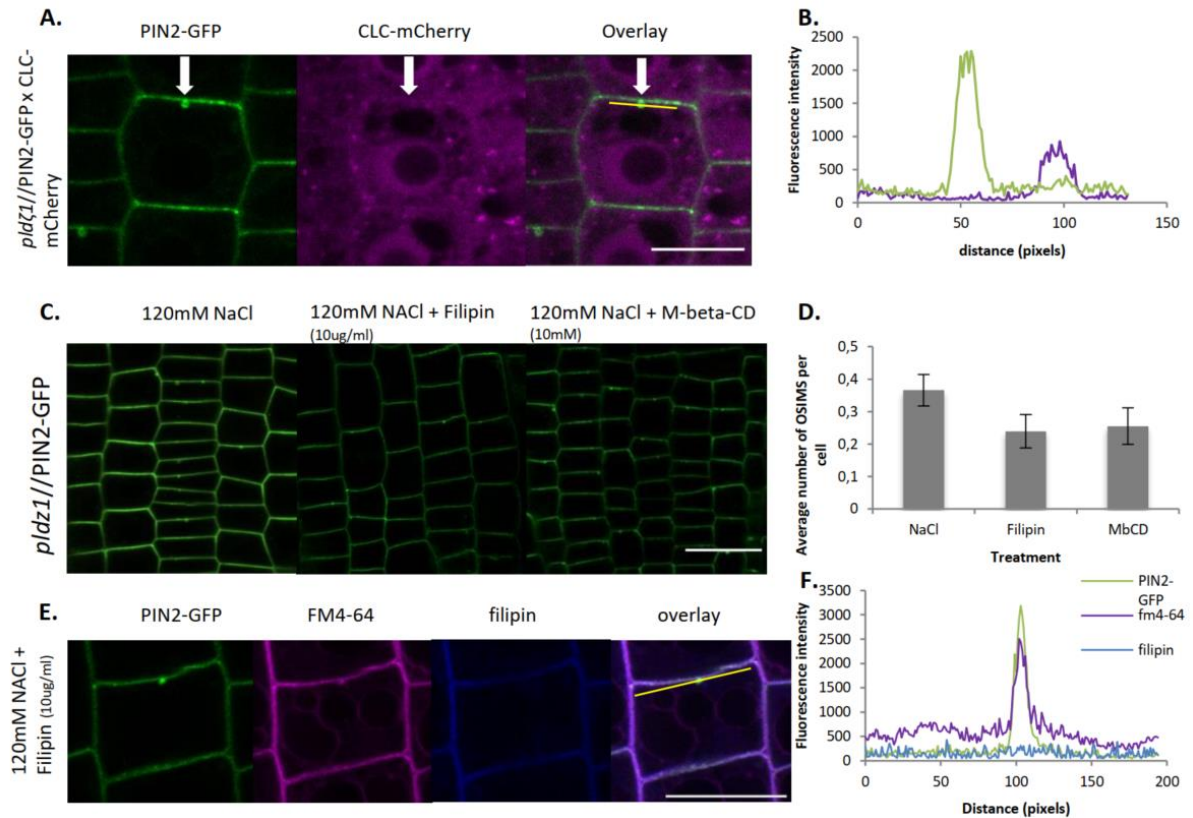


Figure S6.4: OSIMS do not co-localize with clathrin light chain and are not inhibited by membrane micro-domain inhibiting drugs. (A) Representative image of a *pld1* line expressing PIN2-GFP and CLC-mCherry during a salt treatment. (B) Profile plot of the yellow line in (A) showing PIN2-GFP and CLC-mCherry intensities just below the apical side of the PM crossing through one OSIMS. (C) Representative images showing a *pld1* line expressing PIN2-GFP during salt stress with either no drug, 10ug/ml Filipin or 10 mM of Methyl-beta-Cyclodextrin. (D) Quantification of average number of OSIMS per cell during no drug treatment ($n = 12$), Filipin treatment ($n = 8$) and M-b-CD treatment ($N = 14$). No significant differences were found ($p < 0.05$ in a univariate ANOVA, Tukey post hoc using SPSS 24). (E) Enlargements of one cell expressing PIN2-GFP and stained with fm4-64 and filipin showing one OSIMS. (F) Profile plot the yellow line in (E) showing the OSIMS contains PIN2-GFP, fm4-64 but not filipin. Scale bar = 10 μm in (A), 20 μm in (B) and 10 μm in (C)

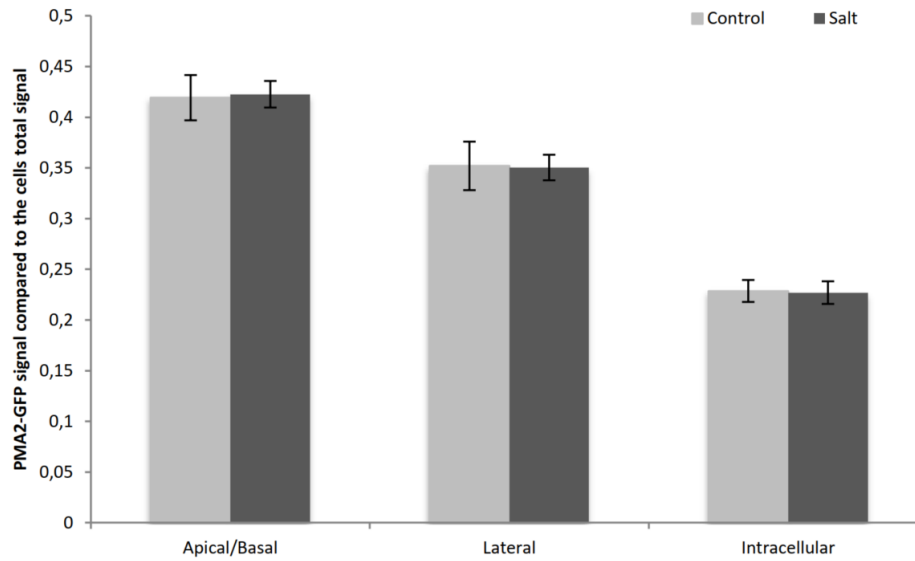


Figure S6.5: No change in PMA2 cellular polarity during salt stress. PMA2-GFP expressing seedlings were treated with either control or salt containing (120 mM NaCl) medium. After 5 minutes the PMA2-GFP signal was measured on the apical and lateral side of the PM as well as the intracellular signal. No differences between the treatments were observed, an univariate ANOVA followed by a Tukey post-hoc was used. $N = 32$ cells from 2 biological replicates.

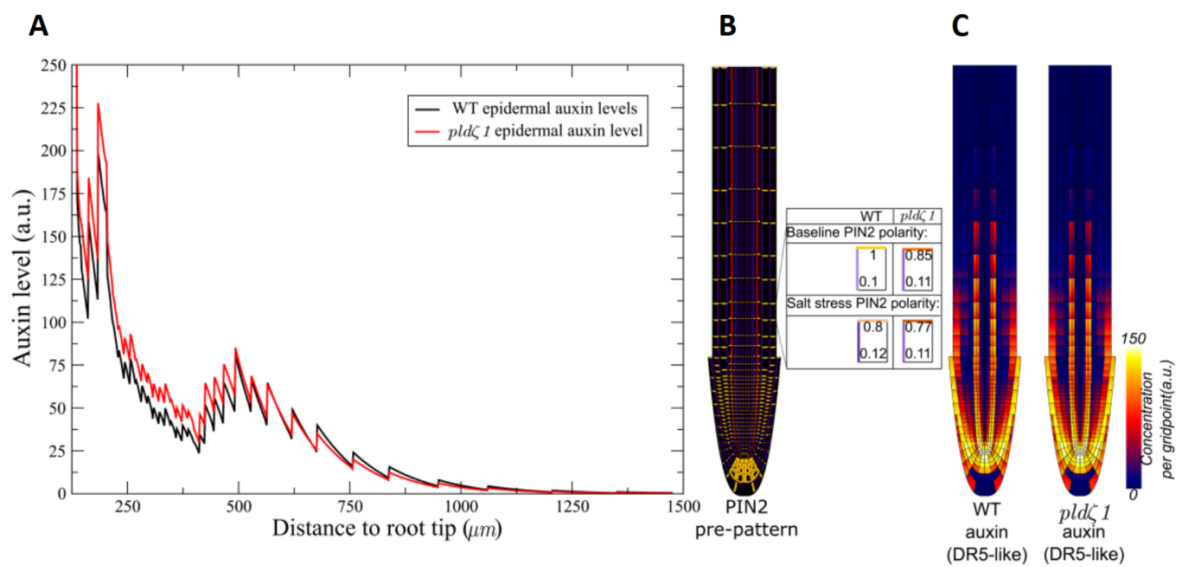


Figure S6.6: Comparison of default, non-halotropic simulated auxin patterns in wildtype and *pldζ1* plants. (A) Epidermal auxin levels as a function of distance from the root tip in wildtype and *pldζ1* plants. (B) Model PIN pattern, highlighting differences between wildtype and *pldζ1* in PIN2 patterning under both baseline and salt stress conditions. (C) Simulated DR5 auxin marker pattern for wildtype and *pldζ1* plants. Colors depict auxin concentration.

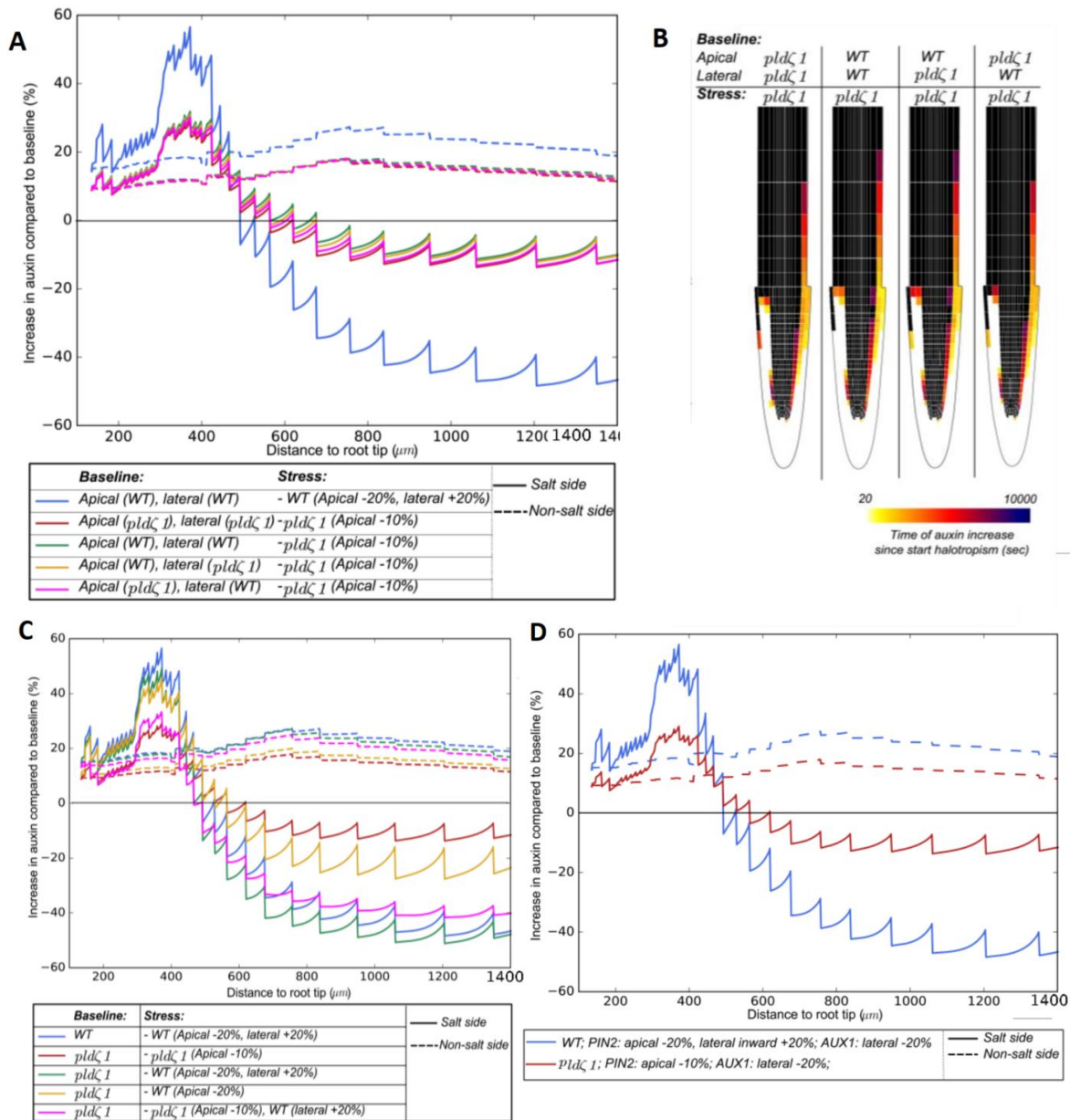


Figure S6.7: Effect of baseline differences and salt induced differences in PIN2 polarity on epidermal auxin levels during halotropism. (A) Changes in epidermal auxin levels when combining *pldζ1* type halotropic PIN2 patterning changes with different baseline PIN2 patterns, wildtype, *pldζ1* or hybrid combinations over the lower part of the root after 24 hours. For comparison purposes also the auxin dynamics in wildtype plants are shown. (B) Changes in auxin rerouting for the different settings. A colored cell has an auxin increase of at least 10% the different colors depict different times. (C) Changes in epidermal auxin levels when combining *pldζ1* baseline PIN2 patterns with different salt induced changes in PIN2 patterning, wildtype, *pldζ1* or hybrid combinations. For comparison purposes also the auxin dynamics in wildtype plants are shown over the lower part of the root after 24 hours. (D) Changes in epidermal auxin levels for *pldζ1* and wildtype plants over the lower part of the root during halotropism after 24 hours.

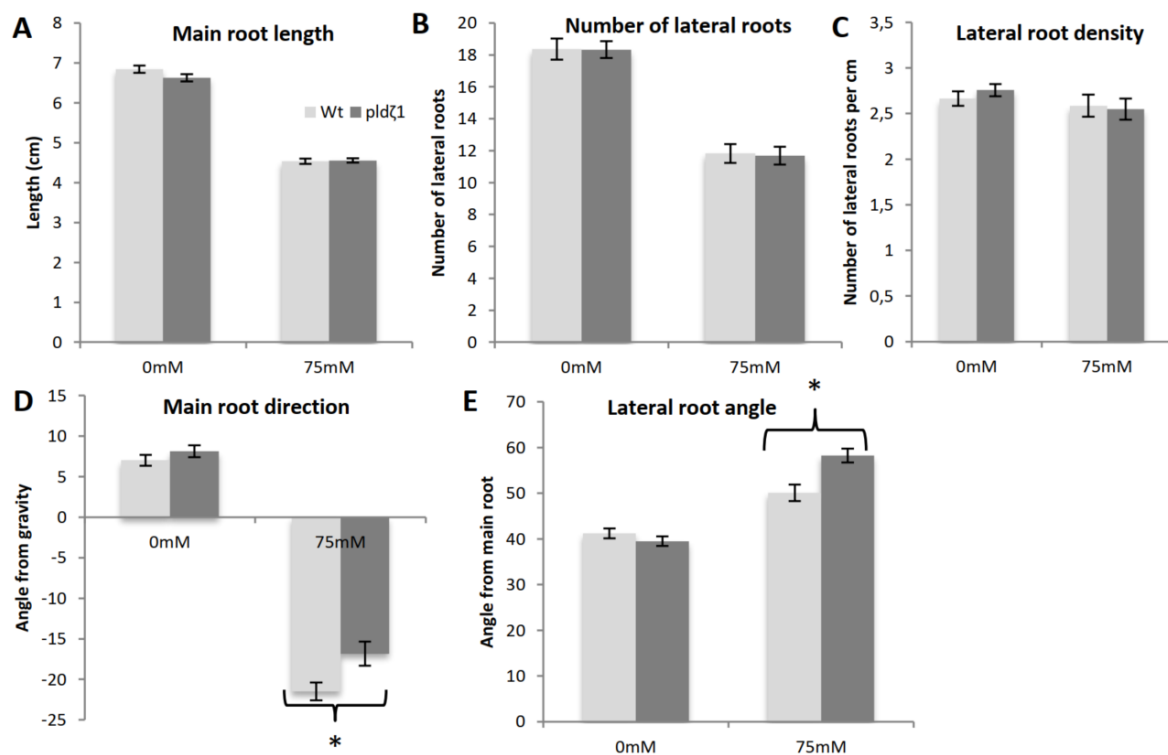


Figure S6.8: *pldζ1* has shorter lateral roots and both main root and lateral roots grow in a different angle during salt stress. *pldζ1* and WT plants were germinated on half strength MS plates. Four days after germination the seedlings were transferred plates with either 0 mM or 75 mM NaCl. Four seedlings were transferred to each plate, after six days of growth roots were analyzed. *pldζ1* has no change in main root length (A), number of lateral roots (B) or lateral root density (C). Significant differences that are found are; main root direction (D), and lateral root direction (E). Result are from 2 biological replicates, total $n \pm 40$. Asterisks show significant differences between Col-0 and *pldζ1* according to an univariate ANOVA followed by a Tukey post hoc test with $p < 0.05$.

7

Discussion

7. 1 Summary

In this thesis we studied decision making processes in plant roots in the context of pre-patterning of lateral root branching sides and directional growth. In **chapter 2** we reviewed the multipurpose nature of auxin and highlighted several studies that have shown that there are ways beyond the well-known TIR/AFB, AUX/IAA and ARF factor combinatorics to achieve auxin specificity (Weijers and Wagner, 2016). These studies have shown how the integration of multiple processes with distinct temporal and spatial scales in a model can elucidate how plant roots obtain additional information from the functional context of an auxin signal to achieve a robust yet sensitive response.

In **chapter 3** we aimed to uncover the mechanism underlying lateral root priming. Specifically, we investigated the hypothesis that an interplay between root tip auxin transport and growth dynamics gives rise to auxin oscillations. Our hypothesis suggested that priming is an emergent property involving processes at spatio-temporal scales ranging from cell level auxin import and export to overall root growth dynamics. Therefore, we developed a multi-scale root growth model enabling us to simultaneously track auxin dynamics at the single cell, tissue and whole root organ level, while independently varying different aspects of auxin and growth dynamics. Confirming previous observations of the importance of auxin carriers for lateral root numbers, a readout of priming amplitude, we showed that a functional auxin reflux loop is necessary to create an auxin loading zone at the proximal boundary of the meristem where the priming occurs. Furthermore, again in agreement with experimental data we showed that also sufficient auxin production is needed to generate a signal of significant amplitude. Nevertheless, different from the previously proposed strong dependence of the priming signal's amplitude on LRC derived auxin production (Xuan et al., 2015) we showed that the exact auxin production location is not relevant due to fast auxin transport. We next demonstrated that vascular origin of the priming signal emerges from the narrowness of cells in these inner tissues, causing a high surface to volume ratio and therefore enhanced auxin uptake. Additionally, to this shape benefit, vasculature cells are relatively long at the start of the elongation zone due to their premature division exit in the meristem giving them a head start in enlarged auxin loading potential. Our results on the importance of cell shape and growth dynamics for auxin loading are in line with previous research showing that a bending induced increase in cell size can induce the formation of a lateral root (Laskowski et al., 2008).

After understanding the role of the auxin reflux loop and the location of the signal, we continue with elucidating the mechanism underlying the oscillatory nature of the priming signal. Our simulations showed that growth of the tissue where the priming signal occurs, and not the previously suggested LRC shedding (Xuan et al., 2016), is necessary and sufficient for priming to occur. We use our model to demonstrate how root growth dynamics result in periodic variations in the height of cells arriving in the TZ, with a large cell followed by small cell receiving the highest auxin levels and hence becoming primed. This preferential auxin loading results from the increased passive auxin loading potential of large cells due to their increased membrane surface area and the enhanced loading time facilitated by the reduced local replacement of the slow growing below cell. Large cells had a relative long growth time, around $\sim .75$ - $.99$ cell cycle time, between their final division and TZ arrival. This defines a temporal-spatial window in the meristem with cell dividing in this region arriving large and becoming primed and cells dividing above this window being small upon TZ arrival. Subsequently, the occurrence of a large-small cell pair in TZ depends on the amount of independent divisions in the window and thus depends on the clone density in the meristem, since asynchronous division exclusively occur on the border of two clones. We found that the size of the window will depend on the meristem size, while the occurrence of a final division event of a cell there will depend on the

division rate. At the same time both meristem size and division rate will have a negative effect on the clone density, thereby decreasing the occurrence of independent division events (Fig. 7.1). Since division rate and meristem size are in this way both a factor in the priming frequency as well as the spacing between the primed sites the proposed mechanism can be distinguished from a Turing pattern or a clock-and-wavefront model that would predict solely a change priming frequency or priming site spacing, respectively, upon a change in division rate or meristem size (Laskowski and Ten Tusscher, 2017). Together with our experimental collaborators we set out to test our model predictions, confirming that priming frequency and priming site spacing both positively scale with cell production, the product of meristem size and division rate.

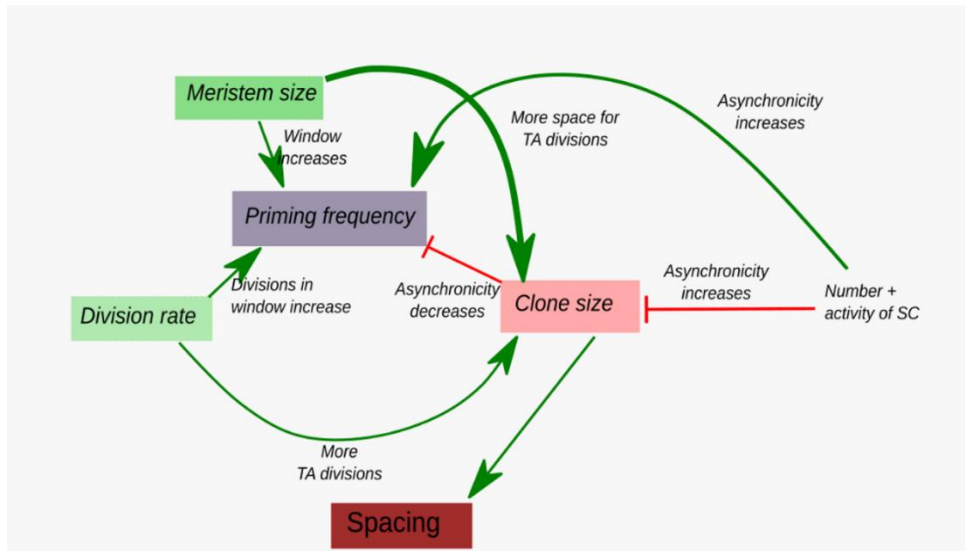


Figure 7.1. Overview of the reflux-and-growth mechanism illustrating the complex interrelationships between meristem size, transit amplifying division rate and stem cell activity and priming frequency and spacing.

In **chapter 4** we further explored the details and implications of the reflux-loop and growth mechanism uncovered in chapter 3. We determined the theoretical boundaries of the priming morphospace by deriving an analytical formula describing priming frequency as a function of meristem growth properties. This formula enabled us to predict how priming frequency and priming site spacing fall in between theoretical upper and lower boundaries. In addition to validating these predicted boundaries, our *in planta* data analysis revealed an interdependency of meristem size, division frequency and stem cell activity that causes a bias towards high priming frequency and low priming site spacing. Surprisingly, we found that although globally priming frequency and priming site spacing increases with cell production, locally this relationship can be reversed when clone size becomes limiting for priming frequency. Specifically, we found that for high cell production rates a decreased cell division rate, and hence decreased cell production, increased priming frequency. Since environmental or developmental changes often impinge on core components of meristem growth dynamics, division rate, meristem size and stem cell activity, we explored what the effect of such changes on priming frequency and priming site spacing would be. Our analysis indicates that while often effects on both priming frequency and spacing occur the precise effect on priming dynamics of a change in root growth dynamics depends on the exact combination of meristem size, division rate and stem cell activity at the moment the growth transition occurs. Finally, we showed that combining in our model the increase in meristem size and accelerating stem cell activity occurring during the first 6 days after germination enables us to explain the observed increase in priming frequency during early root development.

In **chapter 5** we change the focus from decision making processes on when to branch to deciding where to grow. Previous research had observed that roots bend away from salinity, a process called halotropism (Galvan-Ampudia et al., 2013). It was shown that levels of the PIN2 transporters at the salt facing side of the root were reduced, while an increase in auxin could be observed on the other side of the root facilitating reduced elongation rates and hence bending. By using a visualisation of the temporal-spatial displacement of auxin we elucidated that a realistic root topology is necessary to generate an initial small shift of the auxin that accumulates due to the reduced PIN2 activity at the salt facing side to the other side of the root (Fig. 7.2). Besides the realistic root shape, a relative increase in lateral PIN2 localisation, i.e., a reduction in PIN2 polarity, on the salt facing side was found to be essential for redirecting auxin to the non-salt side of the root. Furthermore, we showed in the model that the auxin self-feedback on the AUX1 importer is needed to amplify this initial asymmetry and predicted that this amplification would induce an asymmetric AUX1 distribution during halotropism (Fig. 7.2). In planta experiments confirmed an asymmetric AUX1 distribution upon halotropism induced auxin asymmetry confirming model predictions. Besides changes in PIN2 and AUX1, membrane levels of the vascular PIN1 transporter were also found to increase but only in a transient manner during the initial stages of the halotropic response. Model simulations showed that although a transient PIN1 increase did not influence the final auxin asymmetry, it did speed up the amplification of the auxin asymmetry, enabling a more rapid induction of the bending response (Fig. 7.2). Indeed, when experimentally comparing *pin1* and WT halotropic responses, *pin1* mutants showed a delayed halotropic response.

In **chapter 6** we extended our findings from chapter 5 and focussed on the *pldζ1* mutant that has a delayed halotropic response yet an aggravated gravitropic response. PLDζ1 was found to regulate auxin carrier endocytosis, affecting the localisation of the auxin carrier AUX1 and PIN2 during halotropism and the general levels and localisation of PIN2. Since the results in chapter 5 showed an important role for PIN2 polarity in redirecting auxin fluxes during halotropism we investigated the effect of a *pldζ1*-mutant like PIN2 distribution on the halotropic and gravitropic response in the root model. We found that the more apolarly distributed PIN2 in the *pldζ1* mutant, with relatively more lateral transport, facilitated a faster redirection of auxin to the opposite root side explaining the exaggerated gravitropic response. However, due to the impaired PIN2 cycling in the *pldζ1* mutant, salt induced changes in PIN2 levels and localisation were less efficient explaining the slower halotropic response.

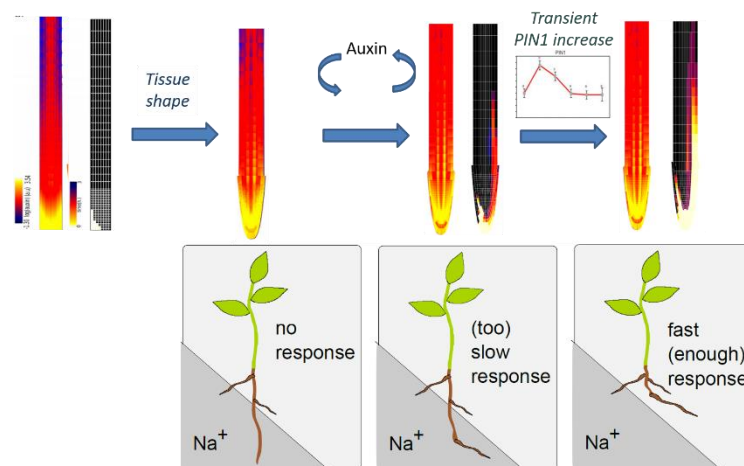


Figure 7.2. Halotropic response. Top row left to right, realistic root topology is essential to shift auxin, auxin feedback on its own transporters amplifies the initial auxin response and a transient upregulation of vascular PIN1 results in an increased build-up of the auxin asymmetry. Bottom row; corresponding plant root response to the top row figures, from left to right: small auxin asymmetry results in no bending, a slow build-up of auxin result in a slow bending response and growth into the salt area, a fast build-up of a sufficient auxin asymmetry result in a timely bending response.

7.2 The many roles of auxin in emergent decision making in plant roots

We started out this thesis in chapter 2 with the question how the plant root knows what to decide on when perceiving an auxin signal, since auxin regulates virtually all developmental and adaptive processes. We showed that there are players beyond the nuclear signalling pathway factors TIR/AFB, AUX/IAA and ARF that influence auxin sensitivity and illustrated the role of dynamical modelling to elucidate these factors. For example, in a study by Mahonen et al. (2014) it was shown how protein stability and the presence of plasmodesmata facilitate the separation of the fast direct effect of auxin on cellular developmental rates from the much more slower effect of auxin via PLT expression on developmental zonation (Mahonen et al., 2014). Such a separation of time scales is most likely not limited to PLT actions, during a tropism like halotropism the fast effect of auxin is to reduce the elongation speed, yet prolonged increases in auxin have also been shown to reduce PIN2 expression (Retzer et al., 2019) and possibly in this way terminate the asymmetry. Even transient subprocesses can influence the outcome of the overall process, like in chapter 5 where we showed that a transient PIN1 increase helps to speed up the auxin asymmetry enabling a timely halotropic response.

For lateral root priming we demonstrated in chapter 3 that large narrow vasculature cells have optimal auxin loading capacity, thereby explaining the location of the priming signal. Additionally, we showed how the frequency of the periodic cell size alterations that underly the oscillatory nature of the auxin signal is determined by the combination of stem cell and transit amplifying division rates and meristem size. To understand the mechanism driving lateral root priming we had to zoom in on local cell size patterns arising due to unidirectional stem cell driven growth in plant roots. We found that a differential spatial-temporal position of the final division a cell undergoes in the meristem translates to differential cell sizes in the priming zone. As a result of this differential cell sizes, differential auxin uptake as well as local displacement rate differences arise, with large cells followed by a small cell having both the advantage of increased auxin loading because of cell height and increased loading time because of low local displacement caused by the small lower neighbour.

The many roles of auxin are particularly relevant in our priming mechanism. First, auxin availability determined the amplitude of the priming signal thereby influencing priming success, explaining the reduced lateral root numbers in mutants affecting auxin production or the auxin reflux loop (Strader and Bartel, 2011, Xuan et al., 2015, Lewis et al., 2011, Swarup et al., 2008, De Smet et al., 2007). Secondly, although not explicitly incorporated in our model, auxin regulates elongation rate, which via affecting auxin loading potential also affect priming success rate. Finally, although also not explicitly integrated in our model, auxin impacts cellular division rates and meristem size, and is therefore also influencing priming frequency. Importantly, both changes in priming amplitude and hence success rate and changes in priming frequency translate into changes in lateral root numbers, complicating the interpretation of experimental observations. For example, a recent study claims that a TEMPERATURE INDUCED LIPOCALIN (TIL) is changing the root clock based on the observed reduction in amplitude in the DR5 oscillations in the priming region. However, TIL in fact strongly affects cell elongation thereby reducing priming amplitude (Dickinson et al., 2021). Thus, not priming frequency but priming success rate is decreased, and the TIL factor does not affect the mechanism underlying priming periodicity. Another recent report by Perianez-Rodriguez et al (2021) demonstrated that an *iaa18* mutant named *potent* results in a large number of prebranch sites, elevated auxin levels yet blocked lateral root formation (Perianez-Rodriguez et al., 2021). Similar results were obtained for an *arf7* mutant. This led the authors to propose that IAA18 and ARF7 together with a hypothetical factor form the long sought-after root clock. Importantly in their simulation model, the *potent* mutation however does not abolish oscillations but instead elevates overall auxin levels. This

instead suggests that for normal patterning of prebranch sites, auxin levels during the valleys of the auxin oscillations should be sufficiently low to not set in motion prebranch site formation. Improved experimental methods and analysis, preferably combining the measurement of priming dynamics, prebranch site and lateral root formation that allow for accurately separating the effect of increases in oscillation amplitude and hence efficiency and changes in frequency are important to further study lateral root priming and accurately interpret the effect of mutants. Still, currently, the vascular localization of the priming signal and the transient nature of the cell sizes differences underlying it form a huge constraint for the *in planta* visualisation of lateral root priming and spacing. Until these methods are available the reflux-and-growth mechanism we describe in this thesis can only be proven in the more indirect manner we employed in chapter 4.

That the roots' auxin response emerges from the sum of many factors is similarly observed in chapter 5 and 6. Here the level of auxin asymmetry arising during halotropism emerges from the interplay between salt-induced primary changes in auxin exporters on two different timescales (PIN1 versus PIN2), auxin-dependent feedback on auxin importers and the state of the reflux loop. While in chapter 5 we explained the initial set-up and subsequent speedup and amplification of the auxin asymmetry, in chapter 6 the complexity of this halotropism system becomes even more apparent. Intriguingly, the experimental data indicated that a *pld ζ 1* mutant has a slower halotropic yet exaggerated gravitropic response, seemingly implying a specific halotropism defect. Upon closer inspection it becomes apparent that the slightly altered reflux loop due to a defect in PIN2 cycling dynamics enables the *pld ζ 1* root to more rapidly set up a gravitropism induced auxin asymmetry, consistent with recent data suggesting an inhibitory role for PIN2 in gravitropism (Retzer et al., 2019). At the same time, due to the key role of PIN2 in halotropism, the hampered PIN2 dynamics result in a less effective build-up of auxin asymmetry under salt stress compared to WT.

7.2.1 When to branch, growth as a deciding factor

The prepatterning mechanism underlying the specification of lateral root prebranch sites has been the topic of a large number of studies. For a long time, the main hypothesis has been that lateral root priming is caused by a clock-and-wavefront mechanism, similar to that observed for vertebrate somitogenesis, with a cell autonomous clock that is entrained by external auxin. The primary support for this root clock hypothesis is the observation of waves of gene expression in the priming region (Moreno-Risueno et al., 2010), yet a molecular network driving gene expression oscillation akin to that found in somitogenesis has so far not been identified. In chapter 3 we show that a clock-and-wavefront mechanism cannot be the mechanism behind lateral root priming since *in planta* both priming site frequency and spacing increase with an increasing cell production, whereas a clock-and-wavefront mechanism would predict an increase in only spacing. Instead, in chapter 3 we uncovered a reflux-and-growth mechanism that explains lateral root priming as an emergent property of auxin transport and meristematic growth, consistent with the observed increase in priming frequency and spacing with cell production rates. Intriguingly, different experimental studies have reported widely varying priming frequencies with observed priming period ranging from ~4-15h (De Smet et al., 2007, Moreno-Risueno et al., 2010, Xuan et al., 2015, Kircher and Schopfer, 2016, Xuan et al., 2016). When studying the detailed experimental setups, we noticed that experimental set up and plant age differ between studies, which will result in substantial differences in root growth dynamics and resulting priming dynamics. As already discussed in the previous section many recent papers still interpret mutants affecting lateral root numbers in terms of a root clock mechanism. Importantly, the mutants reported in these papers affect elongation rate, cell wall modification and polarity (Dickinson et al., 2021, Perianez-Rodriguez et al., 2021, Wachsman et al., 2020). Following our reflux-and-growth

mechanisms, these mutants are predicted to reduce oscillation amplitude and hence priming efficiency, which is fully consistent with the observed reduction in lateral root numbers in these studies. Additionally, changes in cell division rate, predicted to result in different priming frequencies, were shown to impact lateral root production rate (Xie et al., 2019, Li et al., 2021).

The highly emergent nature of the priming mechanism described in chapter 3 will also have implications for the interpretation of environmentally induced changes in RSA. Currently adjustments in main root growth and lateral root production observed during abiotic stress and varying nutrient conditions are often interpreted as a main root or lateral root specific response of the plant in response to the changing conditions (Gruber et al., 2013, Julkowska and Testerink, 2015, Koevoets et al., 2016). However, in chapter 4, albeit an explorative study, we demonstrate that the implications of the reflux-and-growth priming mechanism are that changes in main root meristem growth dynamics affect the numbers and spacing of priming sites. Thus, changes in RSA and lateral root formation, at least to some extent, arise from similar mechanisms as those affecting main root growth. Previously proposed priming mechanisms such as the clock-and-wavefront or Turing model only predict a change in priming site spacing or priming frequency, respectively. In contrast the reflux-and-growth mechanism indicates that adjustments in main root growth properties, division rate, stem cell activity and meristem size affect the plant's position in morphospace in a complex non-linear manner. As a consequence, both changes in spacing and frequency occur, with their relative sizes depending on the prior morphospace position, particularly meristem size. As a consequence, meaningful comparisons of the effect of environmental factors on RSA changes can only be performed between plants of similar developmental age and prior growth conditions. Finally, in chapter 4 we uncovered an interdependency of stem cell activity, meristem size and TA division rate, these findings imply that an environmentally induced change in root meristem growth dynamics likely often affects multiple instead of a single meristem growth parameter. In order to be able to understand how environmental changes affect RSA, and which part of lateral root patterning changes arise from -complex- changes in main root growth dynamics and which parts involve separate control mechanisms is thus essential to combine detailed DR5-LUC assays mapping out priming dynamics combined with measurements of the various main root growth parameters.

Future experimental and modelling research is needed to understand how dynamic adjustments in stem cell activity, possibly combined with changes in TA division rate and meristem size, translate into RSA adjustments. Finally, while in this thesis we focussed on the nature of the priming signal itself, the prepatterning of cells competent for future lateral root formation is more complicated than just this initial signal and likely to involve additional mechanisms (Laskowski and Ten Tusscher, 2017). A recent study shows that up to $\frac{2}{3}$ of all the primed sites will fade in time and even those primed cells that eventually will become a stable prebranch side show a decrease in signal before becoming a lateral root founder cell (Kircher and Schopfer, 2018). It is therefore up to future research to elucidate how the primed cells interpret the high but transient auxin signal, and how they translate this into a type of memory enabling them to later on become a founder cell.

7.2.2 Where to grow, distributed decision making

In chapter 5 and 6 we focussed on the directional movement of plant roots in response to a salt gradient. In chapter 5 we showed how asymmetric changes of PIN2 auxin carriers in response to salinity causes a shift of auxin to the non-salt side and that via auxin-dependence of the AUX1 importer positive feedback was created that enabled this initial difference to become amplified into an auxin symmetry sufficient to drive bending. In chapter 6 we elucidated that both the levels as well as the speed of the response of the transporter are essential for the asymmetry to be sufficient in both timing and strength to induce root bending. The role of PINs in translating graded environmental signals is not limited to root halotropism, during root phototropism light radiation was shown to cause PIN3 polarisation and PIN2 degradation at the irradiated side causing an auxin flux toward and bending away from the light (Kleine-Vehn et al., 2008, Wan et al., 2012, Zhang et al., 2013) and on a similar note PIN2 has been shown to mediate thigmotropism (Lee et al., 2020). Recent studies have indicated an important role for phosphorylation in the swift response of PIN proteins to environmental fluctuations (Han et al., 2021, Tan et al., 2020).

In essence, in chapters 5 and 6 we demonstrated how, starting from an initial unisided limited size response to high salt levels at one side of the root plants can effectively respond through building up a significant auxin elevation at the opposing side of the root via the auxin reflux loop. However, due to its high diffusivity salt is not simply present on one side of the root and absent on the other, rather, the salt concentration is slightly higher on one side relative to the other. As a consequence, rather than a single side of the root experiencing salt stress both sides will experience salt stress albeit of somewhat different intensity. For instance, for the model plant *Arabidopsis thaliana*, with a root width of only 150 μm and the experimental conditions applied to evoke a halotropic responses, salt concentrations between left and right sides of the root can be computed to only differ in the order of 5-10% (van den Berg et al., 2016). To respond to such a signal with a robust directional response, the plant root should be able to somehow amplify initial small amplitude, noisy signal differences to generate a form of directional sensing, i.e., determine the direction where salt concentration is highest and hence from which the salt is coming.

Directional sensing is a common trait throughout the tree of life, many organisms are capable of a directional adaptive response in reaction to sensing a graded or more discrete difference in signal intensity containing spatial and/or temporal directional information. For example, prokaryotes use chemotaxis to move towards food sources or away from toxic substances (Adler, 1966). Due to their limited size, across cell concentration differences are assumed to be insufficient and prokaryotes typically use temporal information to direct their motion (Macnab and Koshland, 1972). In multicellular eukaryotes chemotaxis is also used for directional movement of individually moving cells. For instance, white blood cells respond to cytokines to navigate towards an infection source (De Oliveira et al., 2016). Here, due to the substantially larger cell sizes, spatial information of across cell concentration differences is typically used. Additionally, complex, multicellular animals, typically have paired sensory systems: 2 ears, 2 eyes, and 2 nose holes, that allow them to perceive differences in intensity, timing and location of signals by integrating them in a central nervous system.

Plants are neither unicellular nor have a central processing unit combined with a clear pair of sensors on two sides, so an interesting question is how they achieve directional responses. Based on our results from chap 5 and 6, we suggest that similar to light impacting cAMP dynamics and thereby wave orientation in *Dictyostelium*, the effect of salt on auxin transporters enables for emergent, self-organized auxin asymmetry generation and thereby directional responses (Maree and Hogeweg, 2001,

Maree and Hogeweg, 2002). Preliminary simulation results indicate that when applying stress on both sides of the root an auxin asymmetry arises with an auxin increase at the least stressed side (Figure 7.3). Additionally, these results show that the level of asymmetry scales both with overall salt level as across root salt concentration differences, indicating that the root can not only respond to a gradient through alterations in the reflux loop, but can do so in a quantitative manner (Figure 7.3). In this preliminary model, although now both sides are stressed, a relatively large between sides difference is needed to build up an auxin asymmetry sufficient to induce bending. Thus, while it provides a proof of principle that from two stressed sides the more stressed one can be determined, our initial model is likely still missing some essential aspects. For example, in the current model the factors that might influence the auxin asymmetry are limited to PIN auxin exporters and the AUX1 auxin importer. The addition of factors such as regulated auxin biosynthesis, ABCB transporters, plasmodesmata aperture, PH, and other hormones such as cytokinin and gibberellin, of which a subset has already been implicated in gravitropism (Barbez et al., 2017, Han et al., 2014, Lofke et al., 2013), may improve the sensitivity of the system to a graded signal. This would be in line with a recent study showing that multicellular organisms are better at sensing a gradient than a single cell as long as the change in environmental conditions are not faster than the communication amongst the cells (Colizzi et al., 2020).

Understanding how the different factors involved in the auxin reflux loop facilitate a robust directional response to a graded signal will also help to answer an important remaining question in halotropism, namely how the initial PIN2 asymmetry is set up. Additionally, in chapter 5 we also elucidated the importance of a transient increase in PIN1 in building up a timely auxin asymmetry. On a similar note, the continuous diffusion of salt and bending of the plant root will both affect the perceived salt gradient shape, which should be taken into account in future work to investigate their role in establishing, maintaining and finally terminating the auxin asymmetry.

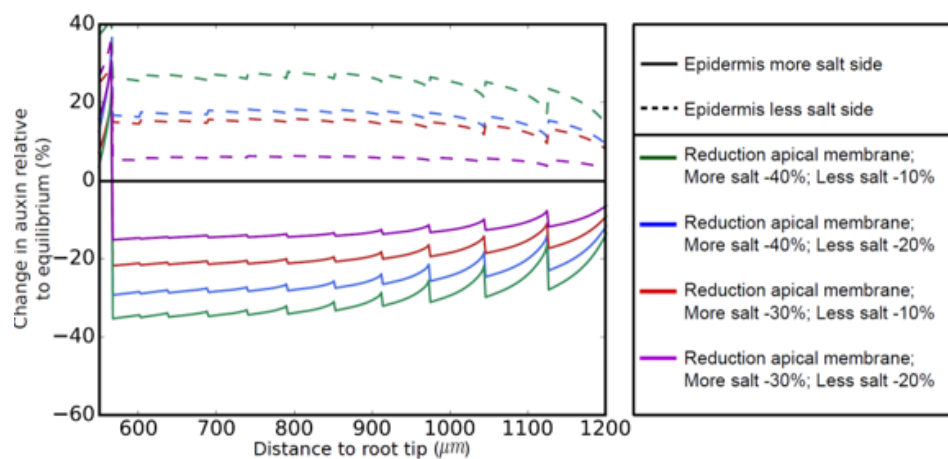


Figure 7.3. Simulation with salt stress on both sides of the root. Percentage change in auxin levels in the elongation zone of the epidermis as a function of distance from the root tip after 2 hours of simulating halotropism. Simulations were ran to auxin equilibrium was reached before reducing apical PIN2 levels in the epidermis at both sides of the root.

7.3 The dynamic interaction between models and experiments and the rise of data

The role of computational dynamical models is increasing in biology. With the increase in computational power and the rise of systems over reductionist approaches more and more complex multilevel models, integrating multiple processes and scales in a single model, are being created. These computational models can help to create insight in the complexity of biology with all its scales,

interactions and non-linear responses. Indeed, models have proven extremely powerful in elucidating the necessary and sufficient factors underlying complex properties, revealing the mechanistic basis of processes and uncovering the emergent nature of particular characteristics. However, computational models should also be used with some caution. With increasing model complexity it becomes increasingly difficult to find meaningful values for the many free parameters. Therefore close collaboration with experimental research is needed to challenge the model and validate findings and hypotheses. The research in chapter 5 and 6 is a beautiful example of such collaboration, where through iteration between model and experiments the mechanism of halotropism could be elucidated. Without the modelling the role of auxin feedback on the AUX1 and PIN2 transporters could not have been understood, nor would the relevance of a transient upregulation of PIN1 during the first hours of halotropism be uncovered. The model allowed us to study the contribution of the different factors of halotropism independently as well as their interaction with each other to get a clear insight in what is necessary and sufficient during a halotropic response. The experiments on the other hand were essential in the discovery of halotropism, delineating the initial PIN2 asymmetries and quantification of auxin asymmetry, as well as validating the predicted asymmetric distribution of the AUX1 and the relevance of PIN1 for early but not later phases of halotropism.

In studies combining experiments with modelling, computational models are most often used to validate experimental findings or confirm whether particular factors are necessary and sufficient to reproduce a particular process. The use of multilevel computational models, however, is not limited to this type of approach and with the rise of more complex and realistic developmental models these can be used the other way around with experiments confirming model findings. In chapter 3 and 4 we took such an approach and used the model to explore the mechanism behind lateral root priming before confirming our hypothesis *in planta*. It is to our knowledge unique in the field of plant root development that a study is designed in such a ‘model first experiments later’ setup in which the experiments were used to confirm model findings rather than the other way around. Interestingly, this model driven approach is instead common in e.g., physics research, where factors such as the Higgs boson or the radiation testifying of a long ago big bang were predicted decades before they could be experimentally determined. Based on the work on lateral root priming described in chapter 3 and 4, we argue that also within biology modelling should be used more extensively as a valuable, independent research tool particularly for the unravelling of highly complex, emergent properties for which available experimental tools are limited.

With the increase of computational power and tools to generate data fast and in large quantities, the role of data analysis and statistical modelling is quickly increasing. Particularly machine learning is a promising research area where developments and applications follow each other quickly. Exploring these data sets combined with new modelling approaches and computational techniques, offers exciting future potential but also requires us to ask the right questions and identify the right approach to display the enormous amount of data in an interpretable way. With the availability of large amounts of data and rapid developments in tools like deep learning we will increasingly be capable of predicting with great quantitative detail how a particular plant species will respond to particular conditions. This may beg the question of whether we still need mechanistic models that enable us to decipher underlying mechanisms or that we could simply make do with the more black box type models generated by machine learning. Importantly, big data does not come for free, and instead consumes large amounts of money, energy and time. Without mechanistic understanding, extrapolation of findings to other conditions or plant species will each time demand the same amount of data and effort, which we hardly have in the light of climate change and a growing world population. Therefore, we

should not ever take the focus from the question: “how does it work, how was the decision by the plant made?” and instead combine mechanistic modelling and machine learning approaches.

7.4 Conclusion

In this thesis we studied decision making processes in plant roots with respect to patterning of lateral root priming sites and directional growth responses. To decipher the distributed, emergent nature of information processing in plant root growth and development we used a computational modelling approach combined with experimental confirmation. Through using visualization techniques that allow interpretation of a combination of temporal and spatial information, kymographs (chapter 3 and 4) and auxin increase tracking (chapter 5 and 6) it was possible to elucidate the highly dynamic nature of lateral root priming and halotropism respectively. Additionally, for both lateral root priming and halotropism the results of this thesis show a vital role for the auxin reflux loop as an integrator of the information flow. In case of lateral root priming auxin availability sets the oscillation amplitude, yet may also influence division rate, stem cell activity and meristem size, all influencing priming dynamics. For halotropism, the auxin dependence of levels, polarity pattern and cellular cycling rates of the auxin transporters together determine the amplitude and speed of generation of the auxin asymmetry. The origin of tropisms, root branching and auxin response in land plants (Mutte et al., 2018) suggest that these processes might have coevolved to facilitate a robust as well as adaptive root system.

References

- ABAS, L., BENJAMINS, R., MALENICA, N., PACIOREK, T., WISNIEWSKA, J., MOULINIER-ANZOLA, J. C., SIEBERER, T., FRIML, J. & LUSCHNIG, C. 2006. Intracellular trafficking and proteolysis of the Arabidopsis auxin-efflux facilitator PIN2 are involved in root gravitropism. *Nat Cell Biol*, 8, 249-56.
- ADAMOWSKI, M. & FRIML, J. 2015. PIN-dependent auxin transport: action, regulation, and evolution. *Plant Cell*, 27, 20-32.
- ADLER, J. 1966. Chemotaxis in bacteria. *Science*, 153, 708-716.
- ADLER, J. 1969. Chemoreceptors in bacteria. *Science*, 166, 1588-1597.
- AIDA, M., BEIS, D., HEIDSTRA, R., WILLEMSEN, V., BLILOU, I., GALINHA, C., NUSSAUME, L., NOH, Y.-S., AMASINO, R. & SCHERES, B. 2004. The PLETHORA genes mediate patterning of the Arabidopsis root stem cell niche. *Cell*, 119, 109-120.
- ALARCON, M. V., SALGUERO, J. & LLORET, P. G. 2019. Auxin Modulated Initiation of Lateral Roots Is Linked to Pericycle Cell Length in Maize. *Front Plant Sci*, 10, 11.
- ANTONESCU, C. N., DANUSER, G. & SCHMID, S. L. 2010. Phosphatidic acid plays a regulatory role in clathrin-mediated endocytosis. *Mol Biol Cell*, 21, 2944-52.
- ANTONIADI, I., PLAČKOVÁ, L., SIMONOVIK, B., DOLEŽAL, K., TURNBULL, C., LJUNG, K. & NOVÁK, O. 2015. Cell-type-specific cytokinin distribution within the Arabidopsis primary root apex. *The Plant Cell*, 27, 1955-1967.
- AQUEA, F., FEDERICI, F., MOSCOSO, C., VEGA, A., JULLIAN, P., HASELOFF, J. & ARCE-JOHNSON, P. 2012. A molecular framework for the inhibition of Arabidopsis root growth in response to boron toxicity. *Plant Cell Environ*, 35, 719-34.
- ARMSTRONG, N. J., PAINTER, K. J. & SHERRATT, J. A. 2009. Adding adhesion to a chemical signaling model for somite formation. *Bull Math Biol*, 71, 1-24.
- BAKER, R. E., SCHNELL, S. & MAINI, P. K. 2006. A clock and wavefront mechanism for somite formation. *Dev Biol*, 293, 116-26.
- BAND, L. R., WELLS, D. M., FOZARD, J. A., GHETIU, T., FRENCH, A. P., POUND, M. P., WILSON, M. H., YU, L., LI, W., HIJAZI, H. I., OH, J., PEARCE, S. P., PEREZ-AMADOR, M. A., YUN, J., KRAMER, E., ALONSO, J. M., GODIN, C., VERNOUX, T., HODGMAN, T. C., PRIDMORE, T. P., SWARUP, R., KING, J. R. & BENNETT, M. J. 2014. Systems Analysis of Auxin Transport in the Arabidopsis Root Apex. *The Plant Cell*, 26, 862-875.
- BAND, L. R., WELLS, D. M., LARRIEU, A., SUN, J., MIDDLETON, A. M., FRENCH, A. P., BRUNOUD, G., SATO, E. M., WILSON, M. H., PERET, B., OLIVA, M., SWARUP, R., SAIRANEN, I., PARRY, G., LJUNG, K., BEECKMAN, T., GARIBALDI, J. M., ESTELLE, M., OWEN, M. R., VISSENBERG, K., HODGMAN, T. C., PRIDMORE, T. P., KING, J. R., VERNOUX, T. & BENNETT, M. J. 2012. Root gravitropism is regulated by a transient lateral auxin gradient controlled by a tipping-point mechanism. *Proc Natl Acad Sci U S A*, 109, 4668-73.
- BANDA, J., BELLANDE, K., VON WANGENHEIM, D., GOH, T., GUYOMARCH, S., LAPLAZE, L. & BENNETT, M. J. 2019. Lateral Root Formation in Arabidopsis: A Well-Ordered L-Rexit. *Trends Plant Sci*, 24, 826-839.
- BAO, Y., AGGARWAL, P., ROBBINS, N. E., 2ND, STURROCK, C. J., THOMPSON, M. C., TAN, H. Q., THAM, C., DUAN, L., RODRIGUEZ, P. L., VERNOUX, T., MOONEY, S. J., BENNETT, M. J. & DINNENY, J. R. 2014. Plant roots use a patterning mechanism to position lateral root branches toward available water. *Proc Natl Acad Sci U S A*, 111, 9319-24.
- BARAL, A., IRANI, N. G., FUJIMOTO, M., NAKANO, A., MAYOR, S. & MATHEW, M. K. 2015. Salt-induced remodeling of spatially restricted clathrin-independent endocytic pathways in Arabidopsis root. *Plant Cell*, 27, 1297-315.
- BARBEZ, E., DUNSER, K., GAIDORA, A., LENDL, T. & BUSCH, W. 2017. Auxin steers root cell expansion via apoplastic pH regulation in Arabidopsis thaliana. *Proc Natl Acad Sci U S A*, 114, E4884-E4893.

- BARBOSA, I. C., ZOURELIDOU, M., WILLIGE, B. C., WELLER, B. & SCHWECHHEIMER, C. 2014. D6 PROTEIN KINASE activates auxin transport-dependent growth and PIN-FORMED phosphorylation at the plasma membrane. *Dev Cell*, 29, 674-85.
- BARGMANN, B. O., LAXALT, A. M., TER RIET, B., VAN SCHOOTEN, B., MERQUIOL, E., TESTERINK, C., HARING, M. A., BARTELS, D. & MUNNIK, T. 2009. Multiple PLDs required for high salinity and water deficit tolerance in plants. *Plant Cell Physiol*, 50, 78-89.
- BASTER, P., ROBERT, S., KLEINE-VEHN, J., VANNESTE, S., KANIA, U., GRUNEWALD, W., DE RYBEL, B., BEECKMAN, T. & FRIML, J. 2013. SCF(TIR1/AFB)-auxin signalling regulates PIN vacuolar trafficking and auxin fluxes during root gravitropism. *EMBO J*, 32, 260-74.
- BAYER, E. M., SMITH, R. S., MANDEL, T., NAKAYAMA, N., SAUER, M., PRUSINKIEWICZ, P. & KUHLEMEIER, C. 2009. Integration of transport-based models for phyllotaxis and midvein formation. *Genes & development*, 23, 373-384.
- BEECKMAN, T., BURSSSENS, S. & INZE, D. 2001. The peri-cell-cycle in Arabidopsis. *J Exp Bot*, 52, 403-11.
- BEECHSTER, G. T. & BASKIN, T. I. 1998. Analysis of cell division and elongation underlying the developmental acceleration of root growth in Arabidopsis thaliana. *Plant Physiol*, 116, 1515-26.
- BEN OTHMAN, A., ELLOUZI, H., PLANCHAIS, S., DE VOS, D., FAIYUE, B., CAROL, P., ABDELLY, C. & SAVOURE, A. 2017. Phospholipases Dzeta1 and Dzeta2 have distinct roles in growth and antioxidant systems in Arabidopsis thaliana responding to salt stress. *Planta*, 246, 721-735.
- BENKOVÁ, E., MICHNIEWICZ, M., SAUER, M., TEICHMANN, T., SEIFERTO VÁ, D., JÜRGENS, G. & FRIML, J. 2003. Local, Efflux-Dependent Auxin Gradients as a Common Module for Plant Organ Formation. *Cell*, 115, 591-602.
- BENNETT, M. J., MARCHANT, A., GREEN, H. G., MAY, S. T., WARD, S. P., MILLNER, P. A., WALKER, A. R., SCHULZ, B. & FELDMANN, K. A. 1996. Arabidopsis AUX1 gene: a permease-like regulator of root gravitropism. *Science*, 273, 948-950.
- BENNETT, S. R. M., ALVAREZ, J., BOSSINGER, G. & SMYTH, D. R. 1995. Morphogenesis in pinoid mutants of Arabidopsis thaliana. *The Plant Journal*, 8, 505-520.
- BENNETT, T., VAN DEN TOORN, A., SANCHEZ-PEREZ, G. F., CAMPILHO, A., WILLEMSSEN, V., SNEL, B. & SCHERES, B. 2010. SOMBRERO, BEARSKIN1, and BEARSKIN2 regulate root cap maturation in Arabidopsis. *Plant Cell*, 22, 640-54.
- BERCKMANS, B., VASSILEVA, V., SCHMID, S. P., MAES, S., PARIZOT, B., NARAMOTO, S., MAGYAR, Z., ALVIM KAMEI, C. L., KONCZ, C., BOGRE, L., PERSIAU, G., DE JAEGER, G., FRIML, J., SIMON, R., BEECKMAN, T. & DE VEYLDER, L. 2011. Auxin-dependent cell cycle reactivation through transcriptional regulation of Arabidopsis E2Fa by lateral organ boundary proteins. *Plant Cell*, 23, 3671-83.
- BERENDSEN, R. L., PIETERSE, C. M. & BAKKER, P. A. 2012. The rhizosphere microbiome and plant health. *Trends Plant Sci*, 17, 478-86.
- BESSHO, Y., HIRATA, H., MASAMIZU, Y. & KAGEYAMA, R. 2003. Periodic repression by the bHLH factor Hes7 is an essential mechanism for the somite segmentation clock. *Genes Dev*, 17, 1451-6.
- BHALERAO, R. P., EKLOF, J., LJUNG, K., MARCHANT, A., BENNETT, M. & SANDBERG, G. 2002. Shoot-derived auxin is essential for early lateral root emergence in Arabidopsis seedlings. *Plant J*, 29, 325-32.
- BIEDRON, M. & BANASIAK, A. 2018. Auxin-mediated regulation of vascular patterning in Arabidopsis thaliana leaves. *Plant Cell Rep*, 37, 1215-1229.
- BIELACH, A., PODLESÁKOVA, K., MARHAVY, P., DUCLERCQ, J., CUESTA, C., MULLER, B., GRUNEWALD, W., TARKOWSKI, P. & BENKOVA, E. 2012. Spatiotemporal regulation of lateral root organogenesis in Arabidopsis by cytokinin. *Plant Cell*, 24, 3967-81.
- BIZET, F., HUMMEL, I. & BOGEAT-TRIBOULOT, M. B. 2015. Length and activity of the root apical meristem revealed in vivo by infrared imaging. *J Exp Bot*, 66, 1387-95.

- BLILOU, I., XU, J., WILDWATER, M., WILLEMSSEN, V., PAPONOV, I., FRIML, J., HEIDSTRA, R., AIDA, M., PALME, K. & SCHERES, B. 2005. The PIN auxin efflux facilitator network controls growth and patterning in Arabidopsis roots. *Nature*, 433, 39-44.
- BOER, D. R., FREIRE-RIOS, A., VAN DEN BERG, W. A., SAAKI, T., MANFIELD, I. W., KEPINSKI, S., LÓPEZ-VIDRIO, I., FRANCO-ZORRILLA, J. M., DE VRIES, S. C. & SOLANO, R. 2014. Structural basis for DNA binding specificity by the auxin-dependent ARF transcription factors. *Cell*, 156, 577-589.
- BRUNOUD, G., WELLS, D. M., OLIVA, M., LARRIEU, A., MIRABET, V., BURROW, A. H., BEECKMAN, T., KEPINSKI, S., TRAAS, J., BENNETT, M. J. & VERNOUX, T. 2012. A novel sensor to map auxin response and distribution at high spatio-temporal resolution. *Nature*, 482, 103-6.
- CALDERON VILLALOBOS, L. I., LEE, S., DE OLIVEIRA, C., IVETAC, A., BRANDT, W., ARMITAGE, L., SHEARD, L. B., TAN, X., PARRY, G., MAO, H., ZHENG, N., NAPIER, R., KEPINSKI, S. & ESTELLE, M. 2012. A combinatorial TIR1/AFB-Aux/IAA co-receptor system for differential sensing of auxin. *Nat Chem Biol*, 8, 477-85.
- CAMPILHO, A., GARCIA, B., TOORN, H. V., WIJK, H. V., CAMPILHO, A. & SCHERES, B. 2006. Time-lapse analysis of stem-cell divisions in the Arabidopsis thaliana root meristem. *Plant J*, 48, 619-27.
- CASPAR, T. & PICKARD, B. G. 1989. Gravitropism in a starchless mutant of Arabidopsis : Implications for the starch-statolith theory of gravity sensing. *Planta*, 177, 185-97.
- CASSAB, G. I., EAPEN, D. & CAMPOS, M. E. 2013. Root hydrotropism: an update. *American journal of botany*, 100, 14-24.
- CAUSIER, B., ASHWORTH, M., GUO, W. & DAVIES, B. 2012. The TOPLESS interactome: a framework for gene repression in Arabidopsis. *Plant Physiol*, 158, 423-38.
- CAVALLARI, N., ARTNER, C. & BENKOVA, E. 2021. Auxin-Regulated Lateral Root Organogenesis. *Cold Spring Harb Perspect Biol*, 13.
- CHANDLER, J. W. & WERR, W. 2015. Cytokinin–auxin crosstalk in cell type specification. *Trends in plant science*, 20, 291-300.
- CHAPMAN, N., WHALLEY, W. R., LINDSEY, K. & MILLER, A. J. 2011. Water supply and not nitrate concentration determines primary root growth in Arabidopsis. *Plant Cell Environ*, 34, 1630-8.
- CHEN, Q., SUN, J., ZHAI, Q., ZHOU, W., QI, L., XU, L., WANG, B., CHEN, R., JIANG, H., QI, J., LI, X., PALME, K. & LI, C. 2011. The basic helix-loop-helix transcription factor MYC2 directly represses PLETHORA expression during jasmonate-mediated modulation of the root stem cell niche in Arabidopsis. *Plant Cell*, 23, 3335-52.
- CHEN, R., HILSON, P., SEDBROOK, J., ROSEN, E., CASPAR, T. & MASSON, P. H. 1998. The arabidopsis thaliana AGRAVITROPIC 1 gene encodes a component of the polar-auxin-transport efflux carrier. *Proc Natl Acad Sci U S A*, 95, 15112-7.
- CHRISTIE, J. M. & MURPHY, A. S. 2013. Shoot phototropism in higher plants: new light through old concepts. *American journal of botany*, 100, 35-46.
- COLIZZI, E. S., VROOMANS, R. M. & MERKS, R. M. 2020. Evolution of multicellularity by collective integration of spatial information. *Elife*, 9, e56349.
- CONLON, R. A., REAUME, A. G. & ROSSANT, J. 1995. Notch1 is required for the coordinate segmentation of somites. *Development*, 121, 1533-1545.
- COOKE, J. & ZEEMAN, E. C. 1976. A clock and wavefront model for control of the number of repeated structures during animal morphogenesis. *J Theor Biol*, 58, 455-76.
- CRUZ-RAMIREZ, A., DIAZ-TRIVINO, S., BLILOU, I., GRIENEISEN, V. A., SOZZANI, R., ZAMIOUDIS, C., MISKOLCZI, P., NIEUWLAND, J., BENJAMINS, R., DHONUKSHE, P., CABALLERO-PEREZ, J., HORVATH, B., LONG, Y., MAHONEN, A. P., ZHANG, H., XU, J., MURRAY, J. A., BENFEY, P. N., BAKO, L., MAREE, A. F. & SCHERES, B. 2012. A bistable circuit involving SCARECROW-RETINOBLASTOMA integrates cues to inform asymmetric stem cell division. *Cell*, 150, 1002-15.
- DAHL, T. W. & ARENS, S. K. 2020. The impacts of land plant evolution on Earth's climate and oxygenation state—An interdisciplinary review. *Chemical Geology*, 547, 119665.

- DARWIN, C. 1859. *On the Origin of Species by Means of Natural Selection, or the Preservation of Favoured Races in the Struggle for Life*, London, John Murray.
- DARWISH, E., TESTERINK, C., KHALIL, M., EL-SHIHY, O. & MUNNIK, T. 2009. Phospholipid signaling responses in salt-stressed rice leaves. *Plant Cell Physiol*, 50, 986-97.
- DATTA, S., KIM, C. M., PERNAS, M., PIRES, N. D., PROUST, H., TAM, T., VIJAYAKUMAR, P. & DOLAN, L. 2011. Root hairs: development, growth and evolution at the plant-soil interface. *Plant and Soil*, 346, 1-14.
- DAVIDSON, E. 2006. *The Regulatory Genome*.
- DAVIS, G. K. & PATEL, N. H. 1999. The origin and evolution of segmentation. *Trends in Cell Biology*, 9, M68-M72.
- DE OLIVEIRA, S., ROSOWSKI, E. E. & HUTTENLOCHER, A. 2016. Neutrophil migration in infection and wound repair: going forward in reverse. *Nature Reviews Immunology*, 16, 378-391.
- DE RYBEL, B., AUDENAERT, D., XUAN, W., OVERVOORDE, P., STRADER, L. C., KEPINSKI, S., HOYE, R., BRISBOIS, R., PARIZOT, B., VANNESTE, S., LIU, X., GILDAY, A., GRAHAM, I. A., NGUYEN, L., JANSEN, L., NJO, M. F., INZE, D., BARTEL, B. & BEECKMAN, T. 2012. A role for the root cap in root branching revealed by the non-auxin probe naxillin. *Nat Chem Biol*, 8, 798-805.
- DE RYBEL, B., VASSILEVA, V., PARIZOT, B., DEMEULENAERE, M., GRUNEWALD, W., AUDENAERT, D., VAN CAMPENHOUT, J., OVERVOORDE, P., JANSEN, L., VANNESTE, S., MOLLER, B., WILSON, M., HOLMAN, T., VAN ISTERDAEL, G., BRUNOUD, G., VUYLSTEKE, M., VERNOUX, T., DE VEYLDER, L., INZE, D., WEIJERS, D., BENNETT, M. J. & BEECKMAN, T. 2010. A novel aux/IAA28 signaling cascade activates GATA23-dependent specification of lateral root founder cell identity. *Curr Biol*, 20, 1697-706.
- DE SMET, I., TETSUMURA, T., DE RYBEL, B., FREI DIT FREY, N., LAPLAZE, L., CASIMIRO, I., SWARUP, R., NAUDTS, M., VANNESTE, S., AUDENAERT, D., INZE, D., BENNETT, M. J. & BEECKMAN, T. 2007. Auxin-dependent regulation of lateral root positioning in the basal meristem of Arabidopsis. *Development*, 134, 681-90.
- DEJONGHE, W., KUENEN, S., MYLLE, E., VASILEVA, M., KEECH, O., VIOTTI, C., SWERTS, J., FENDRYCH, M., ORTIZ-MOREA, F. A., MISHEV, K., DELANG, S., SCHOLL, S., ZARZA, X., HEILMANN, M., KOURELIS, J., KASPROWICZ, J., NGUYEN LE, S. L., DROZDZECKI, A., VAN HOUTTE, I., SZATMARI, A. M., MAJDA, M., BAISA, G., BEDNAREK, S. Y., ROBERT, S., AUDENAERT, D., TESTERINK, C., MUNNIK, T., VAN DAMME, D., HEILMANN, I., SCHUMACHER, K., WINNE, J., FRIML, J., VERSTREKEN, P. & RUSSINOVA, E. 2016. Mitochondrial uncouplers inhibit clathrin-mediated endocytosis largely through cytoplasmic acidification. *Nat Commun*, 7, 11710.
- DELLO IOIO, R., LINHARES, F. S., SCACCHI, E., CASAMITJANA-MARTINEZ, E., HEIDSTRA, R., COSTANTINO, P. & SABATINI, S. 2007. Cytokinin Determine Arabidopsis Root-Meristem Size by Controlling Cell Differentiation. *Current Biology*, 17, 678-682.
- DELLO IOIO, R., NAKAMURA, K., MOUBAYIDIN, L., PERILLI, S., TANIGUCHI, M., MORITA, M. T., AOYAMA, T., COSTANTINO, P. & SABATINI, S. 2008. A genetic framework for the control of cell division and differentiation in the root meristem. *Science*, 322, 1380-4.
- DEQUEANT, M. L., GLYNN, E., GAUDENZ, K., WAHL, M., CHEN, J., MUSHEGIAN, A. & POURQUIE, O. 2006. A complex oscillating network of signaling genes underlies the mouse segmentation clock. *Science*, 314, 1595-8.
- DETTMER, J., HONG-HERMESDORF, A., STIERHOF, Y. D. & SCHUMACHER, K. 2006. Vacuolar H⁺-ATPase activity is required for endocytic and secretory trafficking in Arabidopsis. *Plant Cell*, 18, 715-30.
- DI MAMBRO, R., DE RUVO, M., PACIFICI, E., SALVI, E., SOZZANI, R., BENFEY, P. N., BUSCH, W., NOVAK, O., LJUNG, K., DI PAOLA, L., MAREE, A. F. M., COSTANTINO, P., GRIENEISEN, V. A. & SABATINI, S. 2017. Auxin minimum triggers

- the developmental switch from cell division to cell differentiation in the Arabidopsis root. *Proc Natl Acad Sci U S A*, 114, E7641-E7649.
- DICKINSON, A. J., ZHANG, J., LUCIANO, M., WACHSMAN, G., SANDOVAL, E., SCHNERMANN, M., DINNENY, J. R. & BENFEY, P. N. 2021. A plant lipocalin promotes retinal-mediated oscillatory lateral root initiation. *Science*, 373, 1532-1536.
- DIDONATO, R. J., ARBUCKLE, E., BUKER, S., SHEETS, J., TOBAR, J., TOTONG, R., GRISAFI, P., FINK, G. R. & CELENZA, J. L. 2004. Arabidopsis ALF4 encodes a nuclear-localized protein required for lateral root formation. *Plant J*, 37, 340-53.
- DING, M. & CHEN, Z. J. 2018. Epigenetic perspectives on the evolution and domestication of polyploid plant and crops. *Current Opinion in Plant Biology*, 42, 37-48.
- DITENGOU, F. A., TEALE, W. D., KOCHERSPERGER, P., FLITTNER, K. A., KNEUPER, I., VAN DER GRAAFF, E., NZIENGUI, H., PINOSA, F., LI, X., NITSCHKE, R., LAUX, T. & PALME, K. 2008. Mechanical induction of lateral root initiation in Arabidopsis thaliana. *Proc Natl Acad Sci U S A*, 105, 18818-23.
- DOLAN, L., JANMAAT, K., WILLEMSSEN, V., LINSTEAD, P., POETHIG, S., ROBERTS, K. & SCHERES, B. 1993. Cellular organisation of the Arabidopsis thaliana root. *Development*, 119, 71-84.
- DOLLE, P., IZPISUA-BELMONTE, J. C., FALKENSTEIN, H., RENUCCI, A. & DUBOULE, D. 1989. Coordinate expression of the murine Hox-5 complex homeobox-containing genes during limb pattern formation. *Nature*, 342, 767-72.
- DONALDSON, J. G. 2009. Phospholipase D in endocytosis and endosomal recycling pathways. *Biochim Biophys Acta*, 1791, 845-9.
- DOUADY, S. & COUDER, Y. 1996. Phylloclaxis as a Dynamical Self Organizing Process Part II: The Spontaneous Formation of a Periodicity and the Coexistence of Spiral and Whorled Patterns. *Journal of Theoretical Biology*, 178, 275-294.
- DU, Y. & SCHERES, B. 2017. PLETHORA transcription factors orchestrate de novo organ patterning during Arabidopsis lateral root outgrowth. *Proc Natl Acad Sci U S A*, 114, 11709-11714.
- DU, Y. & SCHERES, B. 2018. Lateral root formation and the multiple roles of auxin. *Journal of Experimental Botany*, 69, 155-167.
- DUBCOVSKY, J. & DVORAK, J. 2007. Genome plasticity a key factor in the success of polyploid wheat under domestication. *Science*, 316, 1862-1866.
- DUBEY, S. M., SERRE, N. B. C., OULEHLOVA, D., VITTAL, P. & FENDRYCH, M. 2021. No Time for Transcription-Rapid Auxin Responses in Plants. *Cold Spring Harb Perspect Biol*, 13.
- DUBROVSKY, J. G., GAMBETTA, G. A., HERNANDEZ-BARRERA, A., SHISHKOVA, S. & GONZALEZ, I. 2006. Lateral root initiation in Arabidopsis: developmental window, spatial patterning, density and predictability. *Ann Bot*, 97, 903-15.
- DUBROVSKY, J. G., SAUER, M., NAPSUCIALY-MENDIVIL, S., IVANCHENKO, M. G., FRIML, J., SHISHKOVA, S., CELENZA, J. & BENKOVA, E. 2008. Auxin acts as a local morphogenetic trigger to specify lateral root founder cells. *Proc Natl Acad Sci U S A*, 105, 8790-4.
- DUBRULLE, J., MCGREW, M. J. & POURQUIE, O. 2001. FGF signaling controls somite boundary position and regulates segmentation clock control of spatiotemporal Hox gene activation. *Cell*, 106, 219-32.
- DUBRULLE, J. & POURQUIÉ, O. 2002. From head to tail: links between the segmentation clock and antero-posterior patterning of the embryo. *Current Opinion in Genetics & Development*, 12, 519-523.
- EL-SHOWK, S., HELP-RINTA-RAHKO, H., BLOMSTER, T., SILIGATO, R., MAREE, A. F., MAHONEN, A. P. & GRIENEISEN, V. A. 2015. Parsimonious Model of Vascular Patterning Links Transverse Hormone Fluxes to Lateral Root Initiation: Auxin Leads the Way, while Cytokinin Levels Out. *PLoS Comput Biol*, 11, e1004450.
- ESHEL, A. & BEECKMAN, T. 2013. *Plant roots: the hidden half*, CRC press.

- EVANS, M. L., ISHIKAWA, H. & ESTELLE, M. A. 1994. Responses of Arabidopsis roots to auxin studied with high temporal resolution: comparison of wild type and auxin-response mutants. *Planta*, 194, 215-222.
- FENDRYCH, M., AKHMANOVA, M., MERRIN, J., GLANC, M., HAGIHARA, S., TAKAHASHI, K., UCHIDA, N., TORII, K. U. & FRIML, J. 2018. Rapid and reversible root growth inhibition by TIR1 auxin signalling. *Nat Plants*, 4, 453-459.
- FISCHER, U., IKEDA, Y., LJUNG, K., SERRALBO, O., SINGH, M., HEIDSTRA, R., PALME, K., SCHERES, B. & GREBE, M. 2006. Vectorial information for Arabidopsis planar polarity is mediated by combined AUX1, EIN2, and GNOM activity. *Curr Biol*, 16, 2143-9.
- FOX, D. T., SOLTIS, D. E., SOLTIS, P. S., ASHMAN, T.-L. & VAN DE PEER, Y. 2020. Polyploidy: a biological force from cells to ecosystems. *Trends in cell biology*, 30, 688-694.
- FRANK, W., MUNNIK, T., KERKMANN, K., SALAMINI, F. & BARTELS, D. 2000. Water deficit triggers phospholipase D activity in the resurrection plant *Craterostigma plantagineum*. *Plant Cell*, 12, 111-24.
- FRENCH, A. P., WILSON, M. H., KENOBI, K., DIETRICH, D., VOSS, U., UBEDA-TOMAS, S., PRIDMORE, T. P. & WELLS, D. M. 2012. Identifying biological landmarks using a novel cell measuring image analysis tool: Cell-o-Tape. *Plant Methods*, 8, 7.
- FRIML, J., BENKOVÁ, E., BLILOU, I., WISNIEWSKA, J., HAMANN, T., LJUNG, K., WOODY, S., SANDBERG, G., SCHERES, B., JÜRGENS, G. & PALME, K. 2002a. AtPIN4 Mediates Sink-Driven Auxin Gradients and Root Patterning in Arabidopsis. *Cell*, 108, 661-673.
- FRIML, J., VIETEN, A., SAUER, M., WEIJERS, D., SCHWARZ, H., HAMANN, T., OFFRINGA, R. & JURGENS, G. 2003. Efflux-dependent auxin gradients establish the apical-basal axis of Arabidopsis. *Nature*, 426, 147-53.
- FRIML, J., WISNIEWSKA, J., BENKOVA, E., MENDGEN, K. & PALME, K. 2002b. Lateral relocation of auxin efflux regulator PIN3 mediates tropism in Arabidopsis. *Nature*, 415, 806-9.
- FU, J. & WANG, S. 2011. Insights into auxin signaling in plant-pathogen interactions. *Front Plant Sci*, 2, 74.
- GALINHA, C., HOFHUIS, H., LUIJTEN, M., WILLEMSSEN, V., BLILOU, I., HEIDSTRA, R. & SCHERES, B. 2007. PLETHORA proteins as dose-dependent master regulators of Arabidopsis root development. *Nature*, 449, 1053-1057.
- GALVAN-AMPUDIA, C. S., CERUTTI, G., LEGRAND, J., BRUNOUD, G., MARTIN-AREVALILLO, R., AZAIS, R., BAYLE, V., MOUSSU, S., WENZL, C., JAILLAIS, Y., LOHMANN, J. U., GODIN, C. & VERNOUX, T. 2020. Temporal integration of auxin information for the regulation of patterning. *Elife*, 9.
- GALVAN-AMPUDIA, C. S., JULKOWSKA, M. M., DARWISH, E., GANDULLO, J., KORVER, R. A., BRUNOUD, G., HARING, M. A., MUNNIK, T., VERNOUX, T. & TESTERINK, C. 2013. Halotropism is a response of plant roots to avoid a saline environment. *Curr Biol*, 23, 2044-50.
- GALWAY, M. E., MASUCCI, J. D., LLOYD, A. M., WALBOT, V., DAVIS, R. W. & SCHIEFELBEIN, J. W. 1994. The TTG gene is required to specify epidermal cell fate and cell patterning in the Arabidopsis root. *Dev Biol*, 166, 740-54.
- GAO, H. B., CHU, Y. J. & XUE, H. W. 2013. Phosphatidic acid (PA) binds PP2AA1 to regulate PP2A activity and PIN1 polar localization. *Mol Plant*, 6, 1692-702.
- GAO, Y., ZHANG, Y., ZHANG, D., DAI, X., ESTELLE, M. & ZHAO, Y. 2015. Auxin binding protein 1 (ABP1) is not required for either auxin signaling or Arabidopsis development. *Proceedings of the National Academy of Sciences*, 112, 2275-2280.
- GELDNER, N., DENERVAUD-TENDON, V., HYMAN, D. L., MAYER, U., STIERHOF, Y. D. & CHORY, J. 2009. Rapid, combinatorial analysis of membrane compartments in intact plants with a multicolor marker set. *Plant J*, 59, 169-78.
- GENG, Y., WU, R., WEE, C. W., XIE, F., WEI, X., CHAN, P. M., THAM, C., DUAN, L. & DINNENY, J. R. 2013. A spatio-temporal understanding of growth regulation during the salt stress response in Arabidopsis. *Plant Cell*, 25, 2132-54.
- GIBLING, M. R. & DAVIES, N. S. 2012. Palaeozoic landscapes shaped by plant evolution. *Nature Geoscience*, 5, 99-105.

- GOH, T., JOI, S., MIMURA, T. & FUKAKI, H. 2012. The establishment of asymmetry in Arabidopsis lateral root founder cells is regulated by LBD16/ASL18 and related LBD/ASL proteins. *Development*, 139, 883-893.
- GONZALEZ-GARCIA, M. P., VILARRASA-BLASI, J., ZHIPONOVA, M., DIVOL, F., MORA-GARCIA, S., RUSSINOVA, E. & CANO-DELGADO, A. I. 2011. Brassinosteroids control meristem size by promoting cell cycle progression in Arabidopsis roots. *Development*, 138, 849-59.
- GRIENEISEN, V. A., XU, J., MARÉE, A. F., HOGEWEG, P. & SCHERES, B. 2007. Auxin transport is sufficient to generate a maximum and gradient guiding root growth. *Nature*, 449, 1008-1013.
- GRUBER, B. D., GIEHL, R. F., FRIEDEL, S. & VON WIREN, N. 2013. Plasticity of the Arabidopsis root system under nutrient deficiencies. *Plant Physiol*, 163, 161-79.
- HA, M., LU, J., TIAN, L., RAMACHANDRAN, V., KASSCHAU, K. D., CHAPMAN, E. J., CARRINGTON, J. C., CHEN, X., WANG, X.-J. & CHEN, Z. J. 2009. Small RNAs serve as a genetic buffer against genomic shock in Arabidopsis interspecific hybrids and allopolyploids. *Proceedings of the National Academy of Sciences*, 106, 17835-17840.
- HAMANN, T., MAYER, U. & JURGENS, G. 1999. The auxin-insensitive bodenlos mutation affects primary root formation and apical-basal patterning in the Arabidopsis embryo. *Development*, 126, 1387-95.
- HAN, H., ADAMOWSKI, M., QI, L., ALOTAIBI, S. S. & FRIML, J. 2021. PIN-mediated polar auxin transport regulations in plant tropic responses. *New Phytol*, 232, 510-522.
- HAN, X., HYUN, T. K., ZHANG, M., KUMAR, R., KOH, E. J., KANG, B. H., LUCAS, W. J. & KIM, J. Y. 2014. Auxin-callose-mediated plasmodesmal gating is essential for tropic auxin gradient formation and signaling. *Dev Cell*, 28, 132-46.
- HARDTKE, C. S. & BERLETH, T. 1998. The Arabidopsis gene MONOPTEROS encodes a transcription factor mediating embryo axis formation and vascular development. *EMBO J*, 17, 1405-11.
- HARDTKE, C. S., DORCEY, E., OSMONT, K. S. & SIBOUT, R. 2007. Phytohormone collaboration: zooming in on auxin-brassinosteroid interactions. *Trends Cell Biol*, 17, 485-92.
- HARPER, J. L. 1980. Plant demography and ecological theory. *Oikos*, 244-253.
- HAYASHI, K., HASEGAWA, J. & MATSUNAGA, S. 2013. The boundary of the meristematic and elongation zones in roots: endoreduplication precedes rapid cell expansion. *Sci Rep*, 3, 2723.
- HEISLER, M. G. & JÖNSSON, H. 2006. Modeling auxin transport and plant development. *Journal of Plant Growth Regulation*, 25, 302-312.
- HEISLER, M. G., OHNO, C., DAS, P., SIEBER, P., REDDY, G. V., LONG, J. A. & MEYEROWITZ, E. M. 2005. Patterns of auxin transport and gene expression during primordium development revealed by live imaging of the Arabidopsis inflorescence meristem. *Current biology*, 15, 1899-1911.
- HESTER, S. D., BELMONTE, J. M., GENS, J. S., CLENDENON, S. G. & GLAZIER, J. A. 2011. A multi-cell, multi-scale model of vertebrate segmentation and somite formation. *PLoS Comput Biol*, 7, e1002155.
- HETHERINGTON, A. J. & DOLAN, L. 2018. Stepwise and independent origins of roots among land plants. *Nature*, 561, 235-238.
- HEUSER, J. 1980. Three-dimensional visualization of coated vesicle formation in fibroblasts. *J Cell Biol*, 84, 560-83.
- HIMANEN, K., VUYLSTEKE, M., VANNESTE, S., VERCRUYSSSE, S., BOUCHERON, E., ALARD, P., CHRIQUI, D., VAN MONTAGU, M., INZE, D. & BEECKMAN, T. 2004. Transcript profiling of early lateral root initiation. *Proc Natl Acad Sci U S A*, 101, 5146-51.
- HOFHUIS, H., LASKOWSKI, M., DU, Y., PRASAD, K., GRIGG, S., PINON, V. & SCHERES, B. 2013. Phyllotaxis and rhizotaxis in Arabidopsis are modified by three PLETHORA transcription factors. *Curr Biol*, 23, 956-62.
- HOMANN, U. 1998. Fusion and fission of plasma-membrane material accommodates for osmotically induced changes in the surface area of guard-cell protoplasts. *Planta*, 206, 329-333.

- HORIKAWA, K., ISHIMATSU, K., YOSHIMOTO, E., KONDO, S. & TAKEDA, H. 2006. Noise-resistant and synchronized oscillation of the segmentation clock. *Nature*, 441, 719-23.
- IBANES, M., KAWAKAMI, Y., RASSKIN-GUTMAN, D. & BELMONTE, J. C. I. 2006. Cell lineage transport: a mechanism for molecular gradient formation. *Molecular systems biology*, 2, 57.
- IKEDA, Y., MEN, S., FISCHER, U., STEPANOVA, A. N., ALONSO, J. M., LJUNG, K. & GREBE, M. 2009. Local auxin biosynthesis modulates gradient-directed planar polarity in Arabidopsis. *Nat Cell Biol*, 11, 731-8.
- ISHIDA, T., ADACHI, S., YOSHIMURA, M., SHIMIZU, K., UMEDA, M. & SUGIMOTO, K. 2010. Auxin modulates the transition from the mitotic cycle to the endocycle in Arabidopsis. *Development*, 137, 63-71.
- ISHIDA, T., KURATA, T., OKADA, K. & WADA, T. 2008. A genetic regulatory network in the development of trichomes and root hairs. *Annu Rev Plant Biol*, 59, 365-86.
- IVANOV, V. B. & DUBROVSKY, J. G. 2013. Longitudinal zonation pattern in plant roots: conflicts and solutions. *Trends Plant Sci*, 18, 237-43.
- JACOB, T., RITCHIE, S., ASSMANN, S. M. & GILROY, S. 1999. Abscisic acid signal transduction in guard cells is mediated by phospholipase D activity. *Proc Natl Acad Sci U S A*, 96, 12192-7.
- JAIN, A., POLING, M. D., KARTHIKEYAN, A. S., BLAKESLEE, J. J., PEER, W. A., TITAPIWATANAKUN, B., MURPHY, A. S. & RAGHOTHAMA, K. G. 2007. Differential effects of sucrose and auxin on localized phosphate deficiency-induced modulation of different traits of root system architecture in Arabidopsis. *Plant Physiol*, 144, 232-47.
- JANSEN, L., ROBERTS, I., DE RYCKE, R. & BEECKMAN, T. 2012. Phloem-associated auxin response maxima determine radial positioning of lateral roots in maize. *Philos Trans R Soc Lond B Biol Sci*, 367, 1525-33.
- JÁSIK, J., BOKOR, B., STUHLÍK, S., MIČIETA, K., TURŇA, J. & SCHMELZER, E. 2016. Effects of auxins on PIN-FORMED2 (PIN2) dynamics are not mediated by inhibiting PIN2 endocytosis. *Plant Physiology*, 172, 1019-1031.
- JENSEN, P. J., HANGARTER, R. P. & ESTELLE, M. 1998. Auxin transport is required for hypocotyl elongation in light-grown but not dark-grown Arabidopsis. *Plant Physiol*, 116, 455-62.
- JIANG, T. X., JUNG, H. S., WIDELITZ, R. B. & CHUONG, C. M. 1999. Self-organization of periodic patterns by dissociated feather mesenchymal cells and the regulation of size, number and spacing of primordia. *Development*, 126, 4997-5009.
- JIANG, Y. J., AERNE, B. L., SMITHERS, L., HADDON, C., ISH-HOROWICZ, D. & LEWIS, J. 2000. Notch signalling and the synchronization of the somite segmentation clock. *Nature*, 408, 475-9.
- JOHN C. LARKIN, JASON D. WALKER, AGNESE C. BOLOGNESI-WINFIELD, GRAY, J. C. & WALKER, A. R. 1999. Allele-Specific Interactions Between *ttg* and *gl1* During Trichome Development in Arabidopsis thaliana. *Genetics*, 151, 1591-1604.
- JONES, A. R., KRAMER, E. M., KNOX, K., SWARUP, R., BENNETT, M. J., LAZARUS, C. M., LEYSER, H. M. & GRIERSON, C. S. 2009. Auxin transport through non-hair cells sustains root-hair development. *Nat Cell Biol*, 11, 78-84.
- JONSSON, H., HEISLER, M. G., SHAPIRO, B. E., MEYEROWITZ, E. M. & MJOLSNES, E. 2006. An auxin-driven polarized transport model for phyllotaxis. *Proc Natl Acad Sci U S A*, 103, 1633-8.
- JULKOWSKA, M. M., HOEFSLOOT, H. C., MOL, S., FERON, R., DE BOER, G. J., HARING, M. A. & TESTERINK, C. 2014. Capturing Arabidopsis root architecture dynamics with ROOT-FIT reveals diversity in responses to salinity. *Plant Physiol*, 166, 1387-402.
- JULKOWSKA, M. M., KOEVOETS, I. T., MOL, S., HOEFSLOOT, H., FERON, R., TESTER, M. A., KEURENTJES, J. J. B., KORTE, A., HARING, M. A., DE BOER, G. J. & TESTERINK, C. 2017. Genetic Components of Root Architecture Remodeling in Response to Salt Stress. *Plant Cell*, 29, 3198-3213.
- JULKOWSKA, M. M. & TESTERINK, C. 2015. Tuning plant signaling and growth to survive salt. *Trends Plant Sci*, 20, 586-94.

- KAZAN, K. 2013. Auxin and the integration of environmental signals into plant root development. *Annals of botany*, 112, 1655-1665.
- KENRICK, P. & STRULLU-DERRIEN, C. 2014. The origin and early evolution of roots. *Plant physiology*, 166, 570-580.
- KEPINSKI, S. & LEYSER, O. 2005. The Arabidopsis F-box protein TIR1 is an auxin receptor. *Nature*, 435, 446-51.
- KERSTENS, M., STRAUSS, S., SMITH, R. & WILLEMSSEN, V. 2020. From Stained Plant Tissues to Quantitative Cell Segmentation Analysis with MorphoGraphX. *Methods Mol Biol*, 2122, 63-83.
- KHARE, D., MITSUDA, N., LEE, S., SONG, W. Y., HWANG, D., OHME-TAKAGI, M., MARTINOIA, E., LEE, Y. & HWANG, J. U. 2017. Root avoidance of toxic metals requires the GeBP-LIKE 4 transcription factor in Arabidopsis thaliana. *New Phytol*, 213, 1257-1273.
- KIRCHER, S. & SCHOPFER, P. 2016. Priming and positioning of lateral roots in Arabidopsis. An approach for an integrating concept. *J Exp Bot*, 67, 1411-20.
- KIRCHER, S. & SCHOPFER, P. 2018. The plant hormone auxin beats the time for oscillating light-regulated lateral root induction. *Development*, 145.
- KLEINE-VEHN, J., DING, Z., JONES, A. R., TASAKA, M., MORITA, M. T. & FRIML, J. 2010. Gravity-induced PIN transcytosis for polarization of auxin fluxes in gravity-sensing root cells. *Proc Natl Acad Sci U S A*, 107, 22344-9.
- KLEINE-VEHN, J., LEITNER, J., ZWIEWKA, M., SAUER, M., ABAS, L., LUSCHNIG, C. & FRIML, J. 2008. Differential degradation of PIN2 auxin efflux carrier by retromer-dependent vacuolar targeting. *Proc Natl Acad Sci U S A*, 105, 17812-7.
- KOCHIAN, L. V., PINEROS, M. A., LIU, J. & MAGALHAES, J. V. 2015. Plant Adaptation to Acid Soils: The Molecular Basis for Crop Aluminum Resistance. *Annu Rev Plant Biol*, 66, 571-98.
- KOEVOETS, I. T., VENEMA, J. H., ELZENGA, J. T. & TESTERINK, C. 2016. Roots Withstanding their Environment: Exploiting Root System Architecture Responses to Abiotic Stress to Improve Crop Tolerance. *Front Plant Sci*, 7, 1335.
- KOOIJMAN, E. E., CHUPIN, V., DE KRUIJFF, B. & BURGER, K. N. 2003. Modulation of membrane curvature by phosphatidic acid and lysophosphatidic acid. *Traffic*, 4, 162-74.
- KROUK, G., MIROWSKI, P., LECUN, Y., SHASHA, D. E. & CORUZZI, G. M. 2010. Predictive network modeling of the high-resolution dynamic plant transcriptome in response to nitrate. *Genome biology*, 11, 1-19.
- KUTSCHERA, U. & BRIGGS, W. R. 2012. Root phototropism: from dogma to the mechanism of blue light perception. *Planta*, 235, 443-452.
- LABANDEIRA, C. C. 2013. A paleobiologic perspective on plant–insect interactions. *Current Opinion in Plant Biology*, 16, 414-421.
- LAI, F., THACKER, J., LI, Y. & DOERNER, P. 2007. Cell division activity determines the magnitude of phosphate starvation responses in Arabidopsis. *Plant J*, 50, 545-56.
- LASKOWSKI, M. 2013. Lateral root initiation is a probabilistic event whose frequency is set by fluctuating levels of auxin response. *J Exp Bot*, 64, 2609-17.
- LASKOWSKI, M., BILLER, S., STANLEY, K., KAJSTURA, T. & PRUSTY, R. 2006. Expression profiling of auxin-treated Arabidopsis roots: toward a molecular analysis of lateral root emergence. *Plant Cell Physiol*, 47, 788-92.
- LASKOWSKI, M., GRIENEISEN, V. A., HOFHUIS, H., HOVE, C. A., HOGEWEG, P., MAREE, A. F. & SCHERES, B. 2008. Root system architecture from coupling cell shape to auxin transport. *PLoS Biol*, 6, e307.
- LASKOWSKI, M. & TEN TUSSCHER, K. H. 2017. Periodic Lateral Root Priming: What Makes It Tick? *Plant Cell*, 29, 432-444.
- LAUX, T., WURSCHEM, T. & BREUNINGER, H. 2004. Genetic regulation of embryonic pattern formation. *Plant Cell*, 16 Suppl, S190-202.
- LAVENUS, J., GOH, T., ROBERTS, I., GUYOMARC'H, S., LUCAS, M., DE SMET, I., FUKAKI, H., BEECKMAN, T., BENNETT, M. & LAPLAZE, L. 2013. Lateral root development in Arabidopsis: fifty shades of auxin. *Trends in plant science*, 18, 450-458.

- LAVREKHA, V. V., PASTERNAK, T., IVANOV, V. B., PALME, K. & MIRONOVA, V. V. 2017. 3D analysis of mitosis distribution highlights the longitudinal zonation and diarch symmetry in proliferation activity of the *Arabidopsis thaliana* root meristem. *Plant J*, 92, 834-845.
- LAXMI, A., PAN, J., MORSY, M. & CHEN, R. 2008. Light plays an essential role in intracellular distribution of auxin efflux carrier PIN2 in *Arabidopsis thaliana*. *PLoS One*, 3, e1510.
- LEE, H. J., KIM, H. S., PARK, J. M., CHO, H. S. & JEON, J. H. 2020. PIN-mediated polar auxin transport facilitates root-obstacle avoidance. *New Phytol*, 225, 1285-1296.
- LEVINE, M. & TJIAN, R. 2003. Transcription regulation and animal diversity. *Nature*, 424, 147-51.
- LEWIS, D. R., NEGI, S., SUKUMAR, P. & MUDAY, G. K. 2011. Ethylene inhibits lateral root development, increases IAA transport and expression of PIN3 and PIN7 auxin efflux carriers. *Development*, 138, 3485-95.
- LEWIS, J. 2003. Autoinhibition with Transcriptional Delay. *Current Biology*, 13, 1398-1408.
- LI, G. & XUE, H. W. 2007. *Arabidopsis* PLDzeta2 regulates vesicle trafficking and is required for auxin response. *Plant Cell*, 19, 281-95.
- LI, M., QIN, C., WELTI, R. & WANG, X. 2006. Double knockouts of phospholipases Dzeta1 and Dzeta2 in *Arabidopsis* affect root elongation during phosphate-limited growth but do not affect root hair patterning. *Plant Physiol*, 140, 761-70.
- LI, Y., SHAO, J., XIE, Y., JIA, L., FU, Y., XU, Z., ZHANG, N., FENG, H., XUN, W. & LIU, Y. 2021. Volatile compounds from beneficial rhizobacteria *Bacillus* spp. promote periodic lateral root development in *Arabidopsis*. *Plant, cell & environment*, 44, 1663-1678.
- LINKIES, A., GRAEBER, K., KNIGHT, C. & LEUBNER-METZGER, G. 2010. The evolution of seeds. *New Phytol*, 186, 817-831.
- LINKOHR, B. I., WILLIAMSON, L. C., FITTER, A. H. & LEYSER, H. M. 2002. Nitrate and phosphate availability and distribution have different effects on root system architecture of *Arabidopsis*. *Plant J*, 29, 751-60.
- LISCUM, E. & BRIGGS, W. R. 1996. Mutations of *Arabidopsis* in potential transduction and response components of the phototropic signaling pathway. *Plant Physiology*, 112, 291-296.
- LISCUM, E. & REED, J. 2002. Genetics of Aux/IAA and ARF action in plant growth and development. *Plant molecular biology*, 49, 387-400.
- LIU, W., LI, R. J., HAN, T. T., CAI, W., FU, Z. W. & LU, Y. T. 2015. Salt stress reduces root meristem size by nitric oxide-mediated modulation of auxin accumulation and signaling in *Arabidopsis*. *Plant Physiol*, 168, 343-56.
- LJUNG, K., HULL, A. K., CELENZA, J., YAMADA, M., ESTELLE, M., NORMANLY, J. & SANDBERG, G. 2005. Sites and regulation of auxin biosynthesis in *Arabidopsis* roots. *Plant Cell*, 17, 1090-104.
- LOBET, G., PAGES, L. & DRAYE, X. 2011. A novel image-analysis toolbox enabling quantitative analysis of root system architecture. *Plant Physiol*, 157, 29-39.
- LOFKE, C., ZWIEWKA, M., HEILMANN, I., VAN MONTAGU, M. C., TEICHMANN, T. & FRIML, J. 2013. Asymmetric gibberellin signaling regulates vacuolar trafficking of PIN auxin transporters during root gravitropism. *Proc Natl Acad Sci U S A*, 110, 3627-32.
- LUSCHNIG, C., GAXIOLA, R. A., GRISAFI, P. & FINK, G. R. 1998. EIR1, a root-specific protein involved in auxin transport, is required for gravitropism in *Arabidopsis thaliana*. *Genes Dev*, 12, 2175-87.
- MACNAB, R. M. & KOSHLAND, D. E. 1972. The gradient-sensing mechanism in bacterial chemotaxis. *Proceedings of the National Academy of Sciences*, 69, 2509-2512.
- MAHONEN, A. P., TEN TUSSCHER, K., SILIGATO, R., SMETANA, O., DIAZ-TRIVINO, S., SALOJARVI, J., WACHSMAN, G., PRASAD, K., HEIDSTRA, R. & SCHERES, B. 2014. PLETHORA gradient formation mechanism separates auxin responses. *Nature*, 515, 125-129.
- MARCHANT, A., BHALERAO, R., CASIMIRO, I., EKLOF, J., CASERO, P. J., BENNETT, M. & SANDBERG, G. 2002. AUX1 promotes lateral root formation by facilitating indole-3-acetic acid distribution between sink and source tissues in the *Arabidopsis* seedling. *Plant Cell*, 14, 589-97.

- MAREE, A. F. & HOGEWEG, P. 2001. How amoeboids self-organize into a fruiting body: multicellular coordination in *Dictyostelium discoideum*. *Proc Natl Acad Sci U S A*, 98, 3879-83.
- MAREE, A. F. & HOGEWEG, P. 2002. Modelling *Dictyostelium discoideum* morphogenesis: the culmination. *Bull Math Biol*, 64, 327-53.
- MARTINIERE, A., LI, X., RUNIONS, J., LIN, J., MAUREL, C. & LUU, D. T. 2012. Salt stress triggers enhanced cycling of Arabidopsis root plasma-membrane aquaporins. *Plant Signal Behav*, 7, 529-32.
- MASSA, G. D. & GILROY, S. 2003. Touch modulates gravity sensing to regulate the growth of primary roots of *Arabidopsis thaliana*. *The Plant Journal*, 33, 435-445.
- MATSUZAKI, Y., OGAWA-OHNISHI, M., MORI, A. & MATSUBAYASHI, Y. 2010. Secreted peptide signals required for maintenance of root stem cell niche in *Arabidopsis*. *Science*, 329, 1065-1067.
- MCDERMOTT, M., WAKELAM, M. J. & MORRIS, A. J. 2004. Phospholipase D. *Biochem Cell Biol*, 82, 225-53.
- MCGINNIS, W. & KRUMLAUF, R. 1992. Homeobox genes and axial patterning. *Cell*, 68, 283-302.
- MCLOUGHLIN, F., ARISZ, S. A., DEKKER, H. L., KRAMER, G., DE KOSTER, C. G., HARING, M. A., MUNNIK, T. & TESTERINK, C. 2013. Identification of novel candidate phosphatidic acid-binding proteins involved in the salt-stress response of *Arabidopsis thaliana* roots. *Biochem J*, 450, 573-81.
- MECKEL, T., HURST, A. C., THIEL, G. & HOMANN, U. 2004. Endocytosis against high turgor: intact guard cells of *Vicia faba* constitutively endocytose fluorescently labelled plasma membrane and GFP-tagged K-channel KAT1. *Plant J*, 39, 182-93.
- MIRONOVA, V. V., OMELYANCHUK, N. A., YOSIPHON, G., FADEEV, S. I., KOLCHANOV, N. A., MJOLSNESS, E. & LIKHOSHVAI, V. A. 2010. A plausible mechanism for auxin patterning along the developing root. *BMC Syst Biol*, 4, 98.
- MITCHISON, G. 1980. A model for vein formation in higher plants. *Proceedings of the Royal Society of London. Series B. Biological Sciences*, 207, 79-109.
- MITCHISON, G. J. 1977. Phyllotaxis and the fibonacci series. *Science*, 196, 270-5.
- MOCKAITIS, K. & ESTELLE, M. 2008. Auxin receptors and plant development: a new signaling paradigm. *Annual review of cell and developmental biology*, 24.
- MONSHAUSEN, G. B., MILLER, N. D., MURPHY, A. S. & GILROY, S. 2011. Dynamics of auxin-dependent Ca²⁺ and pH signaling in root growth revealed by integrating high-resolution imaging with automated computer vision-based analysis. *The Plant Journal*, 65, 309-318.
- MORENO-RISUENO, M. A., VAN NORMAN, J. M., MORENO, A., ZHANG, J., AHNERT, S. E. & BENFEY, P. N. 2010. Oscillating gene expression determines competence for periodic *Arabidopsis* root branching. *Science*, 329, 1306-11.
- MORRIS, G. J., WINTERS, L., COULSON, G. E. & CLARKE, K. J. 1986. Effect of osmotic stress on the ultrastructure and viability of the yeast *Saccharomyces cerevisiae*. *J Gen Microbiol*, 132, 2023-2034.
- MOTTE, H. & BEECKMAN, T. 2019. The evolution of root branching: increasing the level of plasticity. *Journal of Experimental Botany*, 70, 785-793.
- MOUBAYIDIN, L., DI MAMBRO, R., SOZZANI, R., PACIFICI, E., SALVI, E., TERPSTRA, I., BAO, D., VAN DIJKEN, A., IOIO, R. D. & PERILLI, S. 2013. Spatial coordination between stem cell activity and cell differentiation in the root meristem. *Developmental cell*, 26, 405-415.
- MULLEN, J. L., ISHIKAWA, H. & EVANS, M. L. 1998. Analysis of changes in relative elemental growth rate patterns in the elongation zone of *Arabidopsis* roots upon gravistimulation. *Planta*, 206, 598-603.
- MULLER, A., GUAN, C., GALWEILER, L., TANZLER, P., HUIJSER, P., MARCHANT, A., PARRY, G., BENNETT, M., WISMAN, E. & PALME, K. 1998. AtPIN2 defines a locus of *Arabidopsis* for root gravitropism control. *EMBO J*, 17, 6903-11.

- MULLER, M. & SCHMIDT, W. 2004. Environmentally induced plasticity of root hair development in Arabidopsis. *Plant Physiology*, 134, 409-419.
- MUNNS, R. & GILLIHAM, M. 2015. Salinity tolerance of crops - what is the cost? *New Phytol*, 208, 668-73.
- MUTTE, S. K., KATO, H., ROTHFELS, C., MELKONIAN, M., WONG, G. K.-S. & WEIJERS, D. 2018. Origin and evolution of the nuclear auxin response system. *Elife*, 7, e33399.
- NACRY, P., CANIVENC, G., MULLER, B., AZMI, A., VAN ONCKELEN, H., ROSSIGNOL, M. & DOUMAS, P. 2005. A role for auxin redistribution in the responses of the root system architecture to phosphate starvation in Arabidopsis. *Plant Physiology*, 138, 2061-2074.
- NAULIN, P. A., ARMIJO, G. I., VEGA, A. S., TAMAYO, K. P., GRAS, D. E., DE LA CRUZ, J. & GUTIERREZ, R. A. 2020. Nitrate Induction of Primary Root Growth Requires Cytokinin Signaling in Arabidopsis thaliana. *Plant Cell Physiol*, 61, 342-352.
- NAVARRO, L., DUNOYER, P., JAY, F., ARNOLD, B., DHARMASIRI, N., ESTELLE, M., VOINNET, O. & JONES, J. D. 2006. A plant miRNA contributes to antibacterial resistance by repressing auxin signaling. *Science*, 312, 436-439.
- NEWMAN, S. A. & FRISCH, H. L. 1979. Dynamics of skeletal pattern formation in developing chick limb. *Science*, 205, 662-8.
- NIEUWLAND, J., MAUGHAN, S., DEWITTE, W., SCOFIELD, S., SANZ, L. & MURRAY, J. A. 2009. The D-type cyclin CYCD4;1 modulates lateral root density in Arabidopsis by affecting the basal meristem region. *Proc Natl Acad Sci U S A*, 106, 22528-33.
- NIU, Y., JIN, G., LI, X., TANG, C., ZHANG, Y., LIANG, Y. & YU, J. 2015. Phosphorus and magnesium interactively modulate the elongation and directional growth of primary roots in Arabidopsis thaliana (L.) Heynh. *J Exp Bot*, 66, 3841-54.
- NOVAK, D., KUCHAROVA, A., OVECKA, M., KOMIS, G. & SAMAJ, J. 2016. Developmental Nuclear Localization and Quantification of GFP-Tagged EB1c in Arabidopsis Root Using Light-Sheet Microscopy. *Front Plant Sci*, 6, 1187.
- OHASHI, Y., OKA, A., RODRIGUES-POUSADA, R., POSSENTI, M., RUBERTI, I., MORELLI, G. & AOYAMA, T. 2003. Modulation of phospholipid signaling by GLABRA2 in root-hair pattern formation. *Science*, 300, 1427-30.
- OKADA, K., UEDA, J., KOMAKI, M. K., BELL, C. J. & SHIMURA, Y. 1991. Requirement of the Auxin Polar Transport System in Early Stages of Arabidopsis Floral Bud Formation. *Plant Cell*, 3, 677-684.
- OMELYANCHUK, N. A., KOVRIZHNYKH, V. V., OSHCHEPKOVA, E. A., PASTERNAK, T., PALME, K. & MIRONOVA, V. V. 2016. A detailed expression map of the PIN1 auxin transporter in Arabidopsis thaliana root. *BMC Plant Biol*, 16 Suppl 1, 5.
- OROSA-PUENTE, B., LEFTLEY, N., VON WANGENHEIM, D., BANDA, J., SRIVASTAVA, A. K., HILL, K., TRUSKINA, J., BHOSALE, R., MORRIS, E., SRIVASTAVA, M., KUMPERS, B., GOH, T., FUKAKI, H., VERMEER, J. E. M., VERNOUX, T., DINNENY, J. R., FRENCH, A. P., BISHOPP, A., SADANANDOM, A. & BENNETT, M. J. 2018. Root branching toward water involves posttranslational modification of transcription factor ARF7. *Science*, 362, 1407-1410.
- ORTEGA-MARTINEZ, O., PERNAS, M., CAROL, R. J. & DOLAN, L. 2007. Ethylene modulates stem cell division in the Arabidopsis thaliana root. *Science*, 317, 507-10.
- OTTENSCHLÄGER, I., WOLFF, P., WOLVERTON, C., BHALERAO, R. P., SANDBERG, G., ISHIKAWA, H., EVANS, M. & PALME, K. 2003. Gravity-regulated differential auxin transport from columella to lateral root cap cells. *Proceedings of the National Academy of Sciences*, 100, 2987-2991.
- OVECKA, M., BERSON, T., BECK, M., DERKSEN, J., SAMAJ, J., BALUSKA, F. & LICHTSCHEIDL, I. K. 2010. Structural sterols are involved in both the initiation and tip growth of root hairs in Arabidopsis thaliana. *Plant Cell*, 22, 2999-3019.
- PACIOREK, T., ZAZIMALOVA, E., RUTHARDT, N., PETRASEK, J., STIERHOF, Y. D., KLEINE-VEHN, J., MORRIS, D. A., EMANS, N., JURGENS, G., GELDNER, N. & FRIML, J. 2005. Auxin inhibits endocytosis and promotes its own efflux from cells. *Nature*, 435, 1251-6.

- PALMEIRIM, I., HENRIQUE, D., ISH-HOROWICZ, D. & POURQUIE, O. 1997. Avian hairy gene expression identifies a molecular clock linked to vertebrate segmentation and somitogenesis. *Cell*, 91, 639-48.
- PANGANIBAN, G., IRVINE, S. M., LOWE, C., ROEHL, H., CORLEY, L. S., SHERBON, B., GRENIER, J. K., FALLON, J. F., KIMBLE, J., WALKER, M., WRAY, G. A., SWALLA, B. J., MARTINDALE, M. Q. & CARROLL, S. B. 1997. The origin and evolution of animal appendages. *Proc Natl Acad Sci U S A*, 94, 5162-6.
- PAPONOV, I. A., TEALE, W. D., TREBAR, M., BLILOU, I. & PALME, K. 2005. The PIN auxin efflux facilitators: evolutionary and functional perspectives. *Trends Plant Sci*, 10, 170-7.
- PARKINSON, J. S. 1993. Signal transduction schemes of bacteria. *Cell*, 73, 857-871.
- PEACEMAN, D. W. & RACHFORD, J., HENRY H 1955. The numerical solution of parabolic and elliptic differential equations. *Journal of the Society for industrial and Applied Mathematics*, 3, 28-41.
- PÉRET, B., SWARUP, K., FERGUSON, A., SETH, M., YANG, Y., DHONDT, S., JAMES, N., CASIMIRO, I., PERRY, P. & SYED, A. 2012. AUX/LAX genes encode a family of auxin influx transporters that perform distinct functions during Arabidopsis development. *The Plant Cell*, 24, 2874-2885.
- PÉREZ-TORRES, C.-A., LÓPEZ-BUCIO, J., CRUZ-RAMÍREZ, A., IBARRA-LACLETTE, E., DHARMASIRI, S., ESTELLE, M. & HERRERA-ESTRELLA, L. 2008. Phosphate Availability Alters Lateral Root Development in Arabidopsis by Modulating Auxin Sensitivity via a Mechanism Involving the TIR1 Auxin Receptor. *The Plant Cell*, 20, 3258-3272.
- PERIANEZ-RODRIGUEZ, J., RODRIGUEZ, M., MARCONI, M., BUSTILLO-AVENDAÑO, E., WACHSMAN, G., SANCHEZ-CORRIONERO, A., DE GERNIER, H., CABRERA, J., PEREZ-GARCIA, P. & GUDE, I. 2021. An auxin-regulable oscillatory circuit drives the root clock in Arabidopsis. *Science Advances*, 7, eabd4722.
- PERROT-RECHENMANN, C. 2010. Cellular responses to auxin: division versus expansion. *Cold Spring Harbor perspectives in biology*, 2, a001446.
- PETERSSON, S. V., JOHANSSON, A. I., KOWALCZYK, M., MAKOVEYCHUK, A., WANG, J. Y., MORITZ, T., GREBE, M., BENFEY, P. N., SANDBERG, G. & LJUNG, K. 2009. An auxin gradient and maximum in the Arabidopsis root apex shown by high-resolution cell-specific analysis of IAA distribution and synthesis. *The Plant Cell*, 21, 1659-1668.
- PETRASEK, J., MRAVEC, J., BOUCHARD, R., BLAKESLEE, J. J., ABAS, M., SEIFERTOVA, D., WISNIEWSKA, J., TADELE, Z., KUBES, M., COVANOVA, M., DHONUKSHE, P., SKUPA, P., BENKOVA, E., PERRY, L., KRECEK, P., LEE, O. R., FINK, G. R., GEISLER, M., MURPHY, A. S., LUSCHNIG, C., ZAZIMALOVA, E. & FRIML, J. 2006. PIN proteins perform a rate-limiting function in cellular auxin efflux. *Science*, 312, 914-8.
- PLIKUS, M. V., MAYER, J. A., DE LA CRUZ, D., BAKER, R. E., MAINI, P. K., MAXSON, R. & CHUONG, C. M. 2008. Cyclic dermal BMP signalling regulates stem cell activation during hair regeneration. *Nature*, 451, 340-4.
- PRUSINKIEWICZ, P. & LINDENMAYER, A. 2012. *The algorithmic beauty of plants*, Springer Science & Business Media.
- QIN, C. & WANG, X. 2002. The Arabidopsis Phospholipase D Family. Characterization of a Calcium-Independent and Phosphatidylcholine-Selective PLD ζ 1 with Distinct Regulatory Domains. *Plant Physiology*, 128, 1057-1068.
- QUIRK, J., LEAKE, J. R., JOHNSON, D. A., TAYLOR, L. L., SACCONI, L. & BEERLING, D. J. 2015. Constraining the role of early land plants in Palaeozoic weathering and global cooling. *Proceedings of the Royal Society B: Biological Sciences*, 282, 20151115.
- RADEMACHER, E. H., MÖLLER, B., LOKERSE, A. S., LLAVATA-PERIS, C. I., VAN DEN BERG, W. & WEIJERS, D. 2011. A cellular expression map of the Arabidopsis AUXIN RESPONSE FACTOR gene family. *The Plant Journal*, 68, 597-606.
- RAHNI, R. & BIRNBAUM, K. D. 2019. Week-long imaging of cell divisions in the Arabidopsis root meristem. *Plant Methods*, 15, 30.
- RAKUSOVA, H., FENDRYCH, M. & FRIML, J. 2015. Intracellular trafficking and PIN-mediated cell polarity during tropic responses in plants. *Curr Opin Plant Biol*, 23, 116-23.

- RAKUSOVA, H., GALLEGU-BARTOLOME, J., VANSTRAELEN, M., ROBERT, H. S., ALABADI, D., BLAZQUEZ, M. A., BENKOVA, E. & FRIML, J. 2011. Polarization of PIN3-dependent auxin transport for hypocotyl gravitropic response in *Arabidopsis thaliana*. *Plant J*, 67, 817-26.
- RASPOPOVIC, J., MARCON, L., RUSSO, L. & SHARPE, J. 2014. Modeling digits. Digit patterning is controlled by a Bmp-Sox9-Wnt Turing network modulated by morphogen gradients. *Science*, 345, 566-70.
- RAVEN, J. A. & EDWARDS, D. 2001. Roots: evolutionary origins and biogeochemical significance. *Journal of experimental botany*, 52, 381-401.
- REINHARDT, D., PESCE, E. R., STIEGER, P., MANDEL, T., BALTENSBERGER, K., BENNETT, M., TRAAS, J., FRIML, J. & KUHLEMEIER, C. 2003. Regulation of phyllotaxis by polar auxin transport. *Nature*, 426, 255-60.
- RETZER, K., AKHMANOVA, M., KONSTANTINOVA, N., MALÍNSKÁ, K., LEITNER, J., PETRÁŠEK, J. & LUSCHNIG, C. 2019. Brassinosteroid signaling delimits root gravitropism via sorting of the *Arabidopsis* PIN2 auxin transporter. *Nature Communications*, 10, 5516.
- RICHTER, G. L., MONSHAUSEN, G. B., KROL, A. & GILROY, S. 2009. Mechanical stimuli modulate lateral root organogenesis. *Plant Physiol*, 151, 1855-66.
- ROBERT, S., KLEINE-VEHN, J., BARBEZ, E., SAUER, M., PACIOREK, T., BASTER, P., VANNESTE, S., ZHANG, J., SIMON, S. & ČOVANOVÁ, M. 2010. ABP1 mediates auxin inhibition of clathrin-dependent endocytosis in *Arabidopsis*. *Cell*, 143, 111-121.
- ROGERS, E. D. & BENFEY, P. N. 2015. Regulation of plant root system architecture: implications for crop advancement. *Curr Opin Biotechnol*, 32, 93-98.
- RUNIONS, A., SMITH, R. S. & PRUSINKIEWICZ, P. 2014. Computational models of auxin-driven development. *Auxin and its role in plant development*. Springer.
- RUTSCHOW, H. L., BASKIN, T. I. & KRAMER, E. M. 2014. The carrier AUXIN RESISTANT (AUX1) dominates auxin flux into *Arabidopsis* protoplasts. *New Phytol*, 204, 536-544.
- RUTTEN, J. P. & TEN TUSSCHER, K. H. 2021. Bootstrapping and Pinning down the Root Meristem; the Auxin-PLT-ARR Network Unites Robustness and Sensitivity in Meristem Growth Control. *Int J Mol Sci*, 22.
- SABATINI, S., BEIS, D., WOLKENFELT, H., MURFETT, J., GUILFOYLE, T., MALAMY, J., BENFEY, P., LEYSER, O., BECHTOLD, N., WEISBEEK, P. & SCHERES, B. 1999. An Auxin-Dependent Distal Organizer of Pattern and Polarity in the *Arabidopsis* Root. *Cell*, 99, 463-472.
- SACHS, T. 1981. The control of the patterned differentiation of vascular tissues. *Advances in botanical research*, 9, 151-262.
- SACHS, T. 1991. Cell polarity and tissue patterning in plants. *Development*, 113, 83-93.
- SAINI, S., SHARMA, I., KAUR, N. & PATI, P. K. 2013. Auxin: a master regulator in plant root development. *Plant cell reports*, 32, 741-757.
- SALAZAR-HENAO, J. E., VÉLEZ-BERMÚDEZ, I. C. & SCHMIDT, W. 2016. The regulation and plasticity of root hair patterning and morphogenesis. *Development*, 143, 1848-1858.
- SALVI, E., RUTTEN, J. P., DI MAMBRO, R., POLVERARI, L., LICURSI, V., NEGRI, R., DELLO IOIO, R., SABATINI, S. & TEN TUSSCHER, K. 2020. A Self-Organized PLT/Auxin/ARR-B Network Controls the Dynamics of Root Zonation Development in *Arabidopsis thaliana*. *Dev Cell*, 53, 431-443 e23.
- SANCHEZ-CALDERON, L., LOPEZ-BUCIO, J., CHACON-LOPEZ, A., CRUZ-RAMIREZ, A., NIETO-JACOBO, F., DUBROVSKY, J. G. & HERRERA-ESTRELLA, L. 2005. Phosphate starvation induces a determinate developmental program in the roots of *Arabidopsis thaliana*. *Plant Cell Physiol*, 46, 174-84.
- SARRAZIN, A. F., PEEL, A. D. & AVEROF, M. 2012. A segmentation clock with two-segment periodicity in insects. *Science*, 336, 338-41.
- SASSI, M., LU, Y., ZHANG, Y., WANG, J., DHONUKSHE, P., BLILOU, I., DAI, M., LI, J., GONG, X., JAILLAIS, Y., YU, X., TRAAS, J., RUBERTI, I., WANG, H., SCHERES, B., VERNOUX, T. & XU, J. 2012. COP1 mediates the coordination of root and shoot growth

- by light through modulation of PIN1- and PIN2-dependent auxin transport in Arabidopsis. *Development*, 139, 3402-12.
- SAUNDERS, J. W., JR. 1948. The proximo-distal sequence of origin of the parts of the chick wing and the role of the ectoderm. *J Exp Zool*, 108, 363-403.
- SAUNDERS, P. T. 1992. *Collected Works of A.M. Turing: Morphogenesis*, Amsterdam, Elsevier.
- SAUQUET, H., VON BALTHAZAR, M., MAGALLON, S., DOYLE, J. A., ENDRESS, P. K., BAILES, E. J., BARROSO DE MORAIS, E., BULL-HERENU, K., CARRIVE, L., CHARTIER, M., CHOMICKI, G., COIRO, M., CORNETTE, R., EL OTTRA, J. H. L., EPICOCO, C., FOSTER, C. S. P., JABBOUR, F., HAEVERMANS, A., HAEVERMANS, T., HERNANDEZ, R., LITTLE, S. A., LOFSTRAND, S., LUNA, J. A., MASSONI, J., NADOT, S., PAMPERL, S., PRIEU, C., REYES, E., DOS SANTOS, P., SCHOONDERWOERD, K. M., SONTAG, S., SOULEBEAU, A., STAEDLER, Y., TSCHAN, G. F., WING-SZE LEUNG, A. & SCHONENBERGER, J. 2017. The ancestral flower of angiosperms and its early diversification. *Nat Commun*, 8, 16047.
- SCHEITZ, K., LUTHEN, H. & SCHENCK, D. 2013. Rapid auxin-induced root growth inhibition requires the TIR and AFB auxin receptors. *Planta*, 238, 1171-6.
- SCHERES, B., BENFEY, P. & DOLAN, L. 2002. Root development. *Arabidopsis Book*, 1, e0101.
- SCHINDELIN, J., ARGANDA-CARRERAS, I., FRISE, E., KAYNIG, V., LONGAIR, M., PIETZSCH, T., PREIBISCH, S., RUEDEN, C., SAALFELD, S., SCHMID, B., TINEVEZ, J. Y., WHITE, D. J., HARTENSTEIN, V., ELICEIRI, K., TOMANCAK, P. & CARDONA, A. 2012. Fiji: an open-source platform for biological-image analysis. *Nat Methods*, 9, 676-82.
- SEAGO JR, J. L. & FERNANDO, D. D. 2013. Anatomical aspects of angiosperm root evolution. *Annals of Botany*, 112, 223-238.
- SHABALA, S. N. & LEW, R. R. 2002. Turgor regulation in osmotically stressed Arabidopsis epidermal root cells. Direct support for the role of inorganic ion uptake as revealed by concurrent flux and cell turgor measurements. *Plant Physiol*, 129, 290-9.
- SHAHZAD, Z. & AMTMANN, A. 2017. Food for thought: how nutrients regulate root system architecture. *Curr Opin Plant Biol*, 39, 80-87.
- SHI, C. L., VON WANGENHEIM, D., HERRMANN, U., WILDHAGEN, M., KULIK, I., KOPF, A., ISHIDA, T., OLSSON, V., ANKER, M. K., ALBERT, M., BUTENKO, M. A., FELIX, G., SAWA, S., CLAASSEN, M., FRIML, J. & AALEN, R. B. 2018. The dynamics of root cap sloughing in Arabidopsis is regulated by peptide signalling. *Nat Plants*, 4, 596-604.
- SHIMIZU-MITAO, Y. & KAKIMOTO, T. 2014. Auxin sensitivities of all Arabidopsis Aux/IAAs for degradation in the presence of every TIR1/AFB. *Plant and Cell Physiology*, 55, 1450-1459.
- SHINOHARA, N., TAYLOR, C. & LEYSER, O. 2013. Strigolactone can promote or inhibit shoot branching by triggering rapid depletion of the auxin efflux protein PIN1 from the plasma membrane. *PLoS Biol*, 11, e1001474.
- SHKOLNIK, D., KRIEGER, G., NURIEL, R. & FROMM, H. 2016. Hydrotropism: root bending does not require auxin redistribution. *Molecular plant*, 9, 757-759.
- SHOPE, J. C., DEWALD, D. B. & MOTT, K. A. 2003. Changes in surface area of intact guard cells are correlated with membrane internalization. *Plant Physiol*, 133, 1314-21.
- SHYER, A. E., RODRIGUES, A. R., SCHROEDER, G. G., KASSIANIDOU, E., KUMAR, S. & HARLAND, R. M. 2017. Emergent cellular self-organization and mechanosensation initiate follicle pattern in the avian skin. *Science*, 357, 811-815.
- SICK, S., REINKER, S., TIMMER, J. & SCHLAKE, T. 2006. WNT and DKK determine hair follicle spacing through a reaction-diffusion mechanism. *Science*, 314, 1447-50.
- SMITH, R. S., GUYOMARCH, S., MANDEL, T., REINHARDT, D., KUHLEMEIER, C. & PRUSINKIEWICZ, P. 2006. A plausible model of phyllotaxis. *Proc Natl Acad Sci U S A*, 103, 1301-6.
- STEINMANN, T., GELDNER, N., GREBE, M., MANGOLD, S., JACKSON, C. L., PARIS, S., GALWEILER, L., PALME, K. & JURGENS, G. 1999. Coordinated polar localization of auxin efflux carrier PIN1 by GNOM ARF GEF. *Science*, 286, 316-8.

- STEPANOVA, A. N., ROBERTSON-HOYT, J., YUN, J., BENAVENTE, L. M., XIE, D. Y., DOLEZAL, K., SCHLERETH, A., JURGENS, G. & ALONSO, J. M. 2008. TAA1-mediated auxin biosynthesis is essential for hormone crosstalk and plant development. *Cell*, 133, 177-91.
- STOMA, S., LUCAS, M., CHOPARD, J., SCHAEDEL, M., TRAAS, J. & GODIN, C. 2008. Flux-based transport enhancement as a plausible unifying mechanism for auxin transport in meristem development. *PLoS computational biology*, 4, e1000207.
- STRADER, L. C. & BARTEL, B. 2011. Transport and metabolism of the endogenous auxin precursor indole-3-butyric acid. *Mol Plant*, 4, 477-86.
- STRADER, L. C. & ZHAO, Y. 2016. Auxin perception and downstream events. *Current Opinion in Plant Biology*, 33, 8-14.
- SU, W., YEKU, O., OLEPU, S., GENNA, A., PARK, J. S., REN, H., DU, G., GELB, M. H., MORRIS, A. J. & FROHMAN, M. A. 2009. 5-Fluoro-2-indolyl des-chlorohalopemide (FIPI), a phospholipase D pharmacological inhibitor that alters cell spreading and inhibits chemotaxis. *Mol Pharmacol*, 75, 437-446.
- SUKUMAR, P., EDWARDS, K. S., RAHMAN, A., DELONG, A. & MUDAY, G. K. 2009. PINOID kinase regulates root gravitropism through modulation of PIN2-dependent basipetal auxin transport in Arabidopsis. *Plant Physiol*, 150, 722-35.
- SUN, F., ZHANG, W., HU, H., LI, B., WANG, Y., ZHAO, Y., LI, K., LIU, M. & LI, X. 2008. Salt modulates gravity signaling pathway to regulate growth direction of primary roots in Arabidopsis. *Plant Physiol*, 146, 178-88.
- SWARUP, K., BENKOVA, E., SWARUP, R., CASIMIRO, I., PERET, B., YANG, Y., PARRY, G., NIELSEN, E., DE SMET, I., VANNESTE, S., LEVESQUE, M. P., CARRIER, D., JAMES, N., CALVO, V., LJUNG, K., KRAMER, E., ROBERTS, R., GRAHAM, N., MARILLONNET, S., PATEL, K., JONES, J. D., TAYLOR, C. G., SCHACHTMAN, D. P., MAY, S., SANDBERG, G., BENFEY, P., FRIML, J., KERR, I., BEECKMAN, T., LAPLAZE, L. & BENNETT, M. J. 2008. The auxin influx carrier LAX3 promotes lateral root emergence. *Nat Cell Biol*, 10, 946-54.
- SWARUP, R., FRIML, J., MARCHANT, A., LJUNG, K., SANDBERG, G., PALME, K. & BENNETT, M. 2001. Localization of the auxin permease AUX1 suggests two functionally distinct hormone transport pathways operate in the Arabidopsis root apex. *Genes & development*, 15, 2648-2653.
- SWARUP, R., KRAMER, E. M., PERRY, P., KNOX, K., LEYSER, H. M., HASELOFF, J., BEEMSTER, G. T., BHALERAO, R. & BENNETT, M. J. 2005. Root gravitropism requires lateral root cap and epidermal cells for transport and response to a mobile auxin signal. *Nat Cell Biol*, 7, 1057-65.
- TAM, P. P. & LOEBEL, D. A. 2007. Gene function in mouse embryogenesis: get set for gastrulation. *Nat Rev Genet*, 8, 368-81.
- TAN, S., ZHANG, X., KONG, W., YANG, X. L., MOLNAR, G., VONDRAKOVA, Z., FILEPOVA, R., PETRASEK, J., FRIML, J. & XUE, H. W. 2020. The lipid code-dependent phosphoswitch PDK1-D6PK activates PIN-mediated auxin efflux in Arabidopsis. *Nat Plants*, 6, 556-569.
- TANIGUCHI, Y. Y., TANIGUCHI, M., TSUGE, T., OKA, A. & AOYAMA, T. 2010. Involvement of Arabidopsis thaliana phospholipase D ζ 2 in root hydrotropism through the suppression of root gravitropism. *Planta*, 231, 491-7.
- TESTERINK, C. & MUNNIK, T. 2011. Molecular, cellular, and physiological responses to phosphatidic acid formation in plants. *J Exp Bot*, 62, 2349-61.
- THIMANN, K. V. 1936. Auxins and the Growth of Roots. *American Journal of Botany*, 23.
- TIAN, H., WABNIK, K., NIU, T., LI, H., YU, Q., POLLMANN, S., VANNESTE, S., GOVAERTS, W., ROLCÍK, J., GEISLER, M., FRIML, J. & DING, Z. 2014. WOX5-IAA17 feedback circuit-mediated cellular auxin response is crucial for the patterning of root stem cell niches in Arabidopsis. *Molecular Plant*, 7, 277-289.
- TICCONI, C. A., LUCERO, R. D., SAKHONWASEE, S., ADAMSON, A. W., CREFF, A., NUSSAUME, L., DESNOS, T. & ABEL, S. 2009. ER-resident proteins PDR2 and LPR1

- mediate the developmental response of root meristems to phosphate availability. *Proc Natl Acad Sci U S A*, 106, 14174-9.
- TIMILSINA, R., KIM, J. H., NAM, H. G. & WOO, H. R. 2019. Temporal changes in cell division rate and genotoxic stress tolerance in quiescent center cells of Arabidopsis primary root apical meristem. *Sci Rep*, 9, 3599.
- TITAPIWATANAKUN, B., BLAKESLEE, J. J., BANDYOPADHYAY, A., YANG, H., MRAVEC, J., SAUER, M., CHENG, Y., ADAMEC, J., NAGASHIMA, A., GEISLER, M., SAKAI, T., FRIML, J., PEER, W. A. & MURPHY, A. S. 2009. ABCB19/PGP19 stabilises PIN1 in membrane microdomains in Arabidopsis. *Plant J*, 57, 27-44.
- TIWARI, S. B., HAGEN, G. & GUILFOYLE, T. 2003. The roles of auxin response factor domains in auxin-responsive transcription. *The Plant Cell*, 15, 533-543.
- TOYOKURA, K., GOH, T., SHINOHARA, H., SHINODA, A., KONDO, Y., OKAMOTO, Y., UEHARA, T., FUJIMOTO, K., OKUSHIMA, Y., IKEYAMA, Y., NAKAJIMA, K., MIMURA, T., TASAKA, M., MATSUBAYASHI, Y. & FUKAKI, H. 2019. Lateral Inhibition by a Peptide Hormone-Receptor Cascade during Arabidopsis Lateral Root Founder Cell Formation. *Dev Cell*, 48, 64-75 e5.
- TURING, A. M. 1952. The chemical basis of morphogenesis. *Philosophical Transactions of the Royal Society of London. Series B, Biological Sciences*, 237, 37-72.
- UBEDA-TOMAS, S., SWARUP, R., COATES, J., SWARUP, K., LAPLAZE, L., BEEMSTER, G. T., HEDDEN, P., BHALERAO, R. & BENNETT, M. J. 2008. Root growth in Arabidopsis requires gibberellin/DELLA signalling in the endodermis. *Nat Cell Biol*, 10, 625-8.
- ULMASOV, T., HAGEN, G. & GUILFOYLE, T. J. 1999a. Activation and repression of transcription by auxin-response factors. *Proc Natl Acad Sci U S A*, 96, 5844-9.
- ULMASOV, T., HAGEN, G. & GUILFOYLE, T. J. 1999b. Dimerization and DNA binding of auxin response factors. *The plant journal*, 19, 309-319.
- URIU, K., MORISHITA, Y. & IWASA, Y. 2010. Random cell movement promotes synchronization of the segmentation clock. *Proc Natl Acad Sci U S A*, 107, 4979-84.
- VALITOVA, J., SULKARNAYEVA, A., KOTLOVA, E., PONOMAREVA, A., MUKHITOVA, F. K., MURTAZINA, L., RYZHKINA, I., BECKETT, R. & MINIBAYEVA, F. 2014. Sterol binding by methyl-beta-cyclodextrin and nystatin--comparative analysis of biochemical and physiological consequences for plants. *FEBS J*, 281, 2051-60.
- VAN BERKEL, K., DE BOER, R. J., SCHERES, B. & TEN TUSSCHER, K. 2013. Polar auxin transport: models and mechanisms. *Development*, 140, 2253-2268.
- VAN DEN BERG, T., KORVER, R. A., TESTERINK, C. & TEN TUSSCHER, K. H. 2016. Modeling halotropism: a key role for root tip architecture and reflux loop remodeling in redistributing auxin. *Development*, 143, 3350-62.
- VAN DEN BERG, T., YALAMANCHILI, K., DE GERNIER, H., SANTOS TEIXEIRA, J., BEECKMAN, T., SCHERES, B., WILLEMSSEN, V. & TEN TUSSCHER, K. 2021. A reflux-and-growth mechanism explains oscillatory patterning of lateral root branching sites. *Dev Cell*, 56, 2176-2191 e10.
- VEEN, A. H. & LINDENMAYER, A. 1977. Diffusion mechanism for phyllotaxis: theoretical physico-chemical and computer study. *Plant Physiol*, 60, 127-39.
- VERMEER, J. E. M., VON WANGENHEIM, D., BARBERON, M., LEE, Y., STELZER, E. H. K., MAIZEL, A. & GELDNER, N. 2014. A spatial accommodation by neighboring cells is required for organ initiation in Arabidopsis. *Science (New York, N.Y.)*, 343, 178-183.
- VERNOUX, T., BRUNOUD, G., FARCOT, E., MORIN, V., VAN DEN DAELE, H., LEGRAND, J., OLIVA, M., DAS, P., LARRIEU, A. & WELLS, D. 2011. The auxin signalling network translates dynamic input into robust patterning at the shoot apex. *Molecular systems biology*, 7, 508.
- VERNOUX, T., KRONENBERGER, J., GRANDJEAN, O., LAUFS, P. & TRAAS, J. 2000. PIN-FORMED 1 regulates cell fate at the periphery of the shoot apical meristem. *Development*, 127, 5157-5165.
- VERT, G., WALCHER, C. L., CHORY, J. & NEMHAUSER, J. L. 2008. Integration of auxin and brassinosteroid pathways by Auxin Response Factor 2. *Proceedings of the National Academy of Sciences*, 105, 9829-9834.

- VIETEN, A., VANNESTE, S., WISNIEWSKA, J., BENKOVA, E., BENJAMINS, R., BEECKMAN, T., LUSCHNIG, C. & FRIML, J. 2005. Functional redundancy of PIN proteins is accompanied by auxin-dependent cross-regulation of PIN expression. *Development*, 132, 4521-31.
- VILARRASA-BLASI, J., GONZALEZ-GARCIA, M. P., FRIGOLA, D., FABREGAS, N., ALEXIOU, K. G., LOPEZ-BIGAS, N., RIVAS, S., JAUNEAU, A., LOHMANN, J. U., BENFEY, P. N., IBANES, M. & CANO-DELGADO, A. I. 2014. Regulation of plant stem cell quiescence by a brassinosteroid signaling module. *Dev Cell*, 30, 36-47.
- VILLALOBOS, L. I. A. C., LEE, S., DE OLIVEIRA, C., IVETAC, A., BRANDT, W., ARMITAGE, L., SHEARD, L. B., TAN, X., PARRY, G. & MAO, H. 2012. A combinatorial TIR1/AFB–Aux/IAA co-receptor system for differential sensing of auxin. *Nature chemical biology*, 8, 477-485.
- VON WANGENHEIM, D., HAUSCHILD, R., FENDRYCH, M., BARONE, V., BENKOVA, E. & FRIML, J. 2017. Live tracking of moving samples in confocal microscopy for vertically grown roots. *Elife*, 6.
- WACHSMAN, G., ZHANG, J., MORENO-RISUENO, M. A., ANDERSON, C. T. & BENFEY, P. N. 2020. Cell wall remodeling and vesicle trafficking mediate the root clock in Arabidopsis. *Science*, 370, 819-823.
- WAN, Y., JASIK, J., WANG, L., HAO, H., VOLKMANN, D., MENZEL, D., MANCUSO, S., BALUSKA, F. & LIN, J. 2012. The signal transducer NPH3 integrates the phototropin1 photosensor with PIN2-based polar auxin transport in Arabidopsis root phototropism. *Plant Cell*, 24, 551-65.
- WEI, N., CRONN, R., LISTON, A. & ASHMAN, T. L. 2019. Functional trait divergence and trait plasticity confer polyploid advantage in heterogeneous environments. *New Phytologist*, 221, 2286-2297.
- WEIJERS, D., BENKOVA, E., JÄGER, K. E., SCHLERETH, A., HAMANN, T., KIENTZ, M., WILMOTH, J. C., REED, J. W. & JÜRGENS, G. 2005. Developmental specificity of auxin response by pairs of ARF and Aux/IAA transcriptional regulators. *The EMBO journal*, 24, 1874-1885.
- WEIJERS, D. & JURGENS, G. 2004. Funneling auxin action: specificity in signal transduction. *Curr Opin Plant Biol*, 7, 687-93.
- WEIJERS, D. & WAGNER, D. 2016. Transcriptional Responses to the Auxin Hormone. *Annu Rev Plant Biol*, 67, 539-74.
- WENDRICH, J. R., MOLLER, B. K., LI, S., SAIGA, S., SOZZANI, R., BENFEY, P. N., DE RYBEL, B. & WEIJERS, D. 2017. Framework for gradual progression of cell ontogeny in the Arabidopsis root meristem. *Proc Natl Acad Sci U S A*, 114, E8922-E8929.
- WENT, F. W. 1974. Reflections and Speculations. *Annual Review of Plant Physiology*, 25, 1-27.
- WEST, G., INZE, D. & BEEMSTER, G. T. 2004. Cell cycle modulation in the response of the primary root of Arabidopsis to salt stress. *Plant Physiol*, 135, 1050-8.
- WHITFORD, R., FERNANDEZ, A., TEJOS, R., PEREZ, A. C., KLEINE-VEHN, J., VANNESTE, S., DROZDZECKI, A., LEITNER, J., ABAS, L., AERTS, M., HOOGWIJS, K., BASTER, P., DE GROODT, R., LIN, Y. C., STORME, V., VAN DE PEER, Y., BEECKMAN, T., MADDER, A., DEVREESE, B., LUSCHNIG, C., FRIML, J. & HILSON, P. 2012. GOLVEN secretory peptides regulate auxin carrier turnover during plant gravitropic responses. *Developmental cell*, 22, 678-85.
- WICKE, B., SMEETS, E., DORNBURG, V., VASHEV, B., GAISER, T., TURKENBURG, W. & FAAIJ, A. 2011. The global technical and economic potential of bioenergy from salt-affected soils. *Energy & Environmental Science*, 4, 2669-2681.
- WILLEMSEN, V., WOLKENFELT, H., DE VRIEZE, G., WEISBEEK, P. & SCHERES, B. 1998. The HOBBIT gene is required for formation of the root meristem in the Arabidopsis embryo. *Development*, 125, 521-531.
- WISNIEWSKA, J., XU, J., SEIFERTOVA, D., BREWER, P. B., RUZICKA, K., BLILOU, I., ROUQUIE, D., BENKOVA, E., SCHERES, B. & FRIML, J. 2006. Polar PIN localization directs auxin flow in plants. *Science*, 312, 883.

- WOLVERTON, C., MULLEN, J. L., ISHIKAWA, H. & EVANS, M. L. 2002. Root gravitropism in response to a signal originating outside of the cap. *Planta*, 215, 153-7.
- XIAO, T. T., VAN VELZEN, R., KULIKOVA, O., FRANKEN, C. & BISSELING, T. 2019. Lateral root formation involving cell division in both pericycle, cortex and endodermis is a common and ancestral trait in seed plants. *Development*, 146.
- XIE, Y., WANG, J., ZHENG, L., WANG, Y., LUO, L., MA, M., ZHANG, C., HAN, Y., BEECKMAN, T. & XU, G. 2019. Cadmium stress suppresses lateral root formation by interfering with the root clock. *Plant, cell & environment*, 42, 3182-3196.
- XU, J. & SCHERES, B. 2005. Dissection of Arabidopsis ADP-RIBOSYLATION FACTOR 1 function in epidermal cell polarity. *Plant Cell*, 17, 525-36.
- XU, T., WEN, M., NAGAWA, S., FU, Y., CHEN, J.-G., WU, M.-J., PERROT-RECHENMANN, C., FRIML, J., JONES, A. M. & YANG, Z. 2010. Cell surface-and rho GTPase-based auxin signaling controls cellular interdigitation in Arabidopsis. *Cell*, 143, 99-110.
- XUAN, W., AUDENAERT, D., PARIZOT, B., MOLLER, B. K., NJO, M. F., DE RYBEL, B., DE ROP, G., VAN ISTERDAEL, G., MAHONEN, A. P., VANNESTE, S. & BEECKMAN, T. 2015. Root Cap-Derived Auxin Pre-patterns the Longitudinal Axis of the Arabidopsis Root. *Curr Biol*, 25, 1381-8.
- XUAN, W., BAND, L. R., KUMPF, R. P., VAN DAMME, D., PARIZOT, B., DE ROP, G., OPDENACKER, D., MOLLER, B. K., SKORZINSKI, N., NJO, M. F., DE RYBEL, B., AUDENAERT, D., NOWACK, M. K., VANNESTE, S. & BEECKMAN, T. 2016. Cyclic programmed cell death stimulates hormone signaling and root development in Arabidopsis. *Science*, 351, 384-7.
- XUAN, W., OPDENACKER, D., VANNESTE, S. & BEECKMAN, T. 2018. Long-Term In Vivo Imaging of Luciferase-Based Reporter Gene Expression in Arabidopsis Roots. *Methods Mol Biol*, 1761, 177-190.
- YAMAGUCHI, M., YOSHIMOTO, E. & KONDO, S. 2007. Pattern regulation in the stripe of zebrafish suggests an underlying dynamic and autonomous mechanism. *Proc Natl Acad Sci U S A*, 104, 4790-3.
- YANG, L., ZHANG, J., HE, J., QIN, Y., HUA, D., DUAN, Y., CHEN, Z. & GONG, Z. 2014. ABA-mediated ROS in mitochondria regulate root meristem activity by controlling PLETHORA expression in Arabidopsis. *PLoS Genet*, 10, e1004791.
- YAO, H. Y. & XUE, H. W. 2018. Phosphatidic acid plays key roles regulating plant development and stress responses. *J Integr Plant Biol*, 60, 851-863.
- YOON, E. K., YANG, J. H., LIM, J., KIM, S. H., KIM, S.-K. & LEE, W. S. 2010. Auxin regulation of the microRNA390-dependent transacting small interfering RNA pathway in Arabidopsis lateral root development. *Nucleic acids research*, 38, 1382-1391.
- ZADNIKOVA, P., PETRASEK, J., MARHAVY, P., RAZ, V., VANDENBUSSCHE, F., DING, Z., SCHWARZEROVA, K., MORITA, M. T., TASAKA, M., HEJATKO, J., VAN DER STRAETEN, D., FRIML, J. & BENKOVA, E. 2010. Role of PIN-mediated auxin efflux in apical hook development of Arabidopsis thaliana. *Development*, 137, 607-17.
- ZHANG, H., HAN, W., DE SMET, I., TALBOYS, P., LOYA, R., HASSAN, A., RONG, H., JURGENS, G., PAUL KNOX, J. & WANG, M. H. 2010. ABA promotes quiescence of the quiescent centre and suppresses stem cell differentiation in the Arabidopsis primary root meristem. *Plant J*, 64, 764-74.
- ZHANG, H., JENNINGS, A., BARLOW, P. W. & FORDE, B. G. 1999. Dual pathways for regulation of root branching by nitrate. *Proc Natl Acad Sci U S A*, 96, 6529-34.
- ZHANG, H. T. & HIIRAGI, T. 2018. Symmetry Breaking in the Mammalian Embryo. *Annu Rev Cell Dev Biol*, 34, 405-426.
- ZHANG, K. X., XU, H. H., YUAN, T. T., ZHANG, L. & LU, Y. T. 2013. Blue-light-induced PIN3 polarization for root negative phototropic response in Arabidopsis. *Plant J*, 76, 308-21.
- ZHANG, Y., RODRIGUEZ, L., LI, L., ZHANG, X. & FRIML, J. 2020. Functional innovations of PIN auxin transporters mark crucial evolutionary transitions during rise of flowering plants. *Science advances*, 6, eabc8895.
- ZHANG, Y., XIAO, G., WANG, X., ZHANG, X. & FRIML, J. 2019. Evolution of fast root gravitropism in seed plants. *Nature communications*, 10, 1-10.

- ZHAO, Y., WANG, T., ZHANG, W. & LI, X. 2011. SOS3 mediates lateral root development under low salt stress through regulation of auxin redistribution and maxima in Arabidopsis. *New Phytol*, 189, 1122-1134.
- ZHU, J., ZHANG, K. X., WANG, W. S., GONG, W., LIU, W. C., CHEN, H. G., XU, H. H. & LU, Y. T. 2015. Low temperature inhibits root growth by reducing auxin accumulation via ARR1/12. *Plant Cell Physiol*, 56, 727-36.
- ZHU, T., LUCAS, W. J. & ROST, T. L. 1998. Directional cell-to-cell communication in the Arabidopsis root apical meristem I. An ultrastructural and functional analysis. *Protoplasma*, 203, 35-47.
- ZWIEWKA, M., NODZYNSKI, T., ROBERT, S., VANNESTE, S. & FRIML, J. 2015. Osmotic Stress Modulates the Balance between Exocytosis and Clathrin-Mediated Endocytosis in Arabidopsis thaliana. *Mol Plant*, 8, 1175-87.

Samenvatting

Planten zijn essentieel voor het leven op aarde niet alleen door hun zuurstofproductie, maar ook omdat zij de basis van de voedselketen vormen. Pas nadat planten land koloniseerden, ongeveer 400 miljoen jaar geleden, kon het leven van de dieren op het vasteland evolueren omdat er genoeg zuurstof en voedsel was. De kolonisatie van land door planten was een stapsgewijs proces, een belangrijke factor hierbij was het evolueren van een wortelsysteem dat zorgt voor opname van water en nutriënten en stabiele verankering in de grond. Een optimaal wortelsysteem is erg belangrijk voor een plant, een plant kan zich immers niet verplaatsen en is volledige afhankelijk van de nutriënten en water in de bodem rondom het wortelsysteem. Gedurende evolutie zijn daardoor de ontwikkeling van de plant en de signalen uit het milieu waar de plant groeit nauw verweven geraakt, met als gevolg een grote variatie in wortelsystemen afhankelijk van de nutriënten en water in de bodem. Het begrijpen van deze interactie tussen plantenontwikkeling en het milieu is erg belangrijk om landbouwgewassen te verbeteren, zeker in een tijdperk van globale opwarming van de aarde waar droogte en verzilting van de landbouwgrond een grote invloed hebben op de oogst, alsook het streven naar een meer duurzame landbouw met gebruik van minder water en meststoffen. Voor beide geldt dat landbouwgewassen met sterk adaptieve wortelstelsels, die zelf op zoek gaan naar water en nutriënten, van groot belang zullen zijn bij het veiligstellen van onze voedselvoorziening.

In de afgelopen decennia is er al veel onderzoek gedaan naar plantenwortels, hun verankering in de grond en het vertakken van het wortelstelsel. In deze onderzoeken is gevonden dat het plantenhormoon auxine een belangrijke rol speelt in de wortelontwikkeling en groei. Auxine wordt op bepaalde plekken in de wortel geproduceerd en door eiwitten door de cellen getransporteerd waarbij er op sommige plekken meer auxine terecht komt dan op andere plekken. De hoeveelheid auxine in een cel bepaalt welke processen er actief worden, zoals celdeling of juist celstrekking maar ook de snelheid waarmee dit gebeurt. Bijvoorbeeld, als een wortel horizontaal komt te liggen dan wordt er auxine naar de onderkant van de wortel getransporteerd, de hoge auxine remt dan de cel strekking en daarmee de groei aan de onderkant van de wortel en zorgt ervoor dat de wortel terugbuigt naar een verticale groeirichting. Ook in de vertakking van het wortelstelsel speelt auxine een belangrijke rol, het bepaalt welke cellen later een zijwortel kunnen vormen, aan welke kant de zijwortel komt en wanneer en hoe snel de zijwortel begint te groeien. Door middel van auxine, en ook andere plantenhormonen, kan een plantenwortel zijn ontwikkeling dus sturen afhankelijk van de omgevingsfactoren.

Dit proefschrift heeft als titel: “Ondergrondse beslissingen, welke kant op te groeien en wanneer te vertakken”, deze titel hint naar het feit dat planten geen hersenen hebben, maar toch ‘beslissingen’ maken. In dit proefschrift staan meerdere studies die inzicht proberen te geven in hoe een plant zijn groeirichting aanpast en hoe de plant besluit wanneer een zijwortel te vormen. Dit soort plantenontwikkeling gerelateerde processen integreren informatie op verschillende tijds- en ruimteschalen. Daarom zijn er in deze thesis simulatiemodellen van een plantenwortel gebruikt om te begrijpen hoe veel verschillende kleine stukjes informatie samen tot een coherente plantenreactie kunnen leiden.

Hoofdstuk 2 is een literatuurstudie naar de rol die modellen hebben gespeeld bij het meer begrip krijgen van de invloed van auxine op de plantenwortel. Auxine beïnvloedt heel veel verschillende processen, van de activiteit van de stamcellen tot weefsel differentiatie tot een snelle groeireactie bij een veranderende omgeving, en het is moeilijk te begrijpen hoe één stofje zoveel verschillende processen tegelijk kan beïnvloeden. Het is bekend dat de hoeveelheid auxine in de cel kan bepalen welke processen actief zijn, of cellen gaan groeien en delen, veel water opnemen en strekken, of zich differentiëren tot bijvoorbeeld wortelhaarcellen of vaatcellen. Auxine controleert echter ook hoe snel

cellen delen, strekken of differentiëren en of dit groeien en strekken meer aan een kant gebeurt een wortel een bepaalde kant op buigt. Bijvoorbeeld in de wortelpunt bepaalt auxine waar en hoe groot de ontwikkelingsdomeinen voor celdeling en celstrekking zijn, dit regelt auxine door de hoeveelheid van een belangrijk ontwikkelingseiwit PLETHORA te bepalen. Maar auxine bepaalt ook hoe snel de celdeling of strekking gaat, als er een auxine asymmetrie is wordt aan de ene kant van de wortel de celstrekking sterk geremd, zonder dat de ontwikkelingsdomeinen van plaats of grootte veranderen. Dit lijkt tegenstrijdig, want omdat auxine de PLETHORAS aanstuurt zou de veranderende auxine hoeveelheid gedurende een auxine asymmetrie ook de ontwikkelingsdomeinen moeten veranderen. Doormiddel van een combinatie van modellen en experimenten werd duidelijk dat het aansturen van de hoeveelheid PLETHORAS via auxine een langzaam en indirect proces is, terwijl de groeivertraging een directe reactie op de hoeveelheid auxine is en daarmee een heel snel proces. Deze verschillen in tijdschalen maken het mogelijk dat auxine via de PLETHORAS, in combinatie met een aantal terugkoppelingen en groei, de grootte van de ontwikkelingsdomeinen, kan bepalen en tegelijkertijd binnen die domeinen, via directe terugkoppeling, de snelheid van de daar plaats vindende processen kan bepalen zonder de grootte van het domein te veranderen. Op deze manier kan de paradox van stabiele grootte van de ontwikkelingsdomeinen gedurende snel wisselend omstandigheden begrepen worden. De literatuurstudie laat zien dat door niet alleen in 1 cel te kijken, maar ook naar de communicatie tussen cellen en de verschillende tijdschalen waarop processen plaatsvinden er beter kan worden begrepen hoe veranderingen in auxine in de plantenwortel zoveel verschillende processen kan aansturen.

In **hoofdstuk 3** kijken we ook naar de rol van auxine in plantenwortels, maar in het specifieke geval van zijwortelvorming. In planten met een zogenaamde tapwortelarchitectuur heeft het wortelstels een bepaalde hiërarchie. De hoofdwortel groeit naar beneden, en met een zekere regelmaat ontspringen er zijwortels uit de hoofdwortel. Het ontstaan van zo'n zijwortel is een stapsgewijs proces, en het duurt een aantal dagen voordat een zijwortel zichtbaar uitgroeit. Nieuwe cellen ontstaan in de wortelpunt uit de stamcellen en ondergaan een aantal delingen voordat ze strekken en vervolgens differentiëren. Doordat er vanuit de stamcellen in de wortelpunt steeds nieuwe cellen ontstaan worden oudere cellen vanuit de wortelpunt gezien omhoog geduwd en komen steeds hoger in de wortel te liggen. Tijdens de groei in de hoofdwortel treden er periodieke veranderingen in de hoeveelheid auxine op, aan het begin van de zone waar cellen met celstrekking beginnen. Cellen die een hoge concentratie auxine hebben in deze regio van de wortelpunt ontwikkelen het vermogen om hogerop in de wortel, bij gunstige omstandigheden, een zijwortel te vormen, we zeggen dan dat deze cellen geprimed zijn. Cellen die een lage concentratie auxine ervaren hebben dit vermogen niet. Hoe deze oscillaties in auxine ontstaan wordt niet goed begrepen. Er zijn verschillende mechanismes geopperd maar deze bieden onvolledige verklaringen en ook waren resultaten van experimenten met planten vaak tegenstrijdig met de aangedragen verklaringen.

Om zijwortelvorming, en dan met name het proces van priming, te begrijpen hebben we gebruik gemaakt van een wortel simulatiemodel, dat een realistische wortelvorm, auxine transport dynamiek en gedetailleerde groeiprocessen integreert. Dit is niet de eerste keer dat een computermodel wordt gebruikt om priming te bestuderen, maar dit model is uniek omdat het realistische wortelgroei simuleert met celdeling, strekking en differentiatie. Door zowel een realistische wortelvorm, auxine en groei samen te voegen in een model konden we laten zien hoe auxine transport en groei op elkaar ingrijpen en samen deze auxine oscillaties in de wortelpunt veroorzaken. Met andere woorden, deze periodieke variaties in auxine die een prepatroon vormen voor waar later zijwortels kunnen ontstaan zijn een zogenaamde emergente eigenschap, die nooit door afzonderlijke bestudering van groei of transport begrepen zou kunnen worden. We vonden dat de celdelingen in de wortelpunt aan de basis van de auxine oscillaties staan. Doordat cellen in de wortel in groepjes van zustercellen, ontstaan uit

1 deling van de stamcel, ongeveer tegelijkertijd groeien en delen, maar ook allemaal in 1 richting bewegen is de onderste cel van een groepje zustercellen het grootste wanneer het de delingszone van de wortelpunt verlaat en begint met strekken. Een grote cel heeft meer oppervlakte om auxine op te nemen en zal daardoor een hoge auxine concentratie hebben en het vermogen ontwikkelen om een zijwortel te vormen, kleinere cellen kunnen niet zoveel auxine opnemen en daardoor blijft hun auxine concentratie laag. Door dit mechanisme hangt de hoeveelheid cellen die mogelijk een zijwortel kunnen vormen af van de hoeveelheid groepjes zuster cellen in de wortelpunt en ook hoe vaak er celdelingen zijn in de wortelpunt. Op basis van het met ons model ontdekte mechanisme voor priming van zijwortels hebben we voorspellingen gedaan voor hoe het aantal plekjes waar zijwortels kunnen vormen, de snelheid waarmee ze gemaakt worden en de afstand er tussen afhangen van de grootte van de groeizone in de wortelpunt en het aantal delingen en daarmee de totale celproductie van de wortelpunt. Om deze modeluitkomsten ook in levende planten te testen hebben we experimenten opgezet die door het Scheres-Willemsen laboratorium zijn uitgevoerd. Deze experimenten bevestigden onze voorspellingen en daarmee bleek dat het inderdaad zo is dat de eerste stap van zijwortelvorming ontstaat uit de groei van de hoofdwortel. Met dit model dat is bevestigd door experimenten is er nu een veel completer beeld over de eerste stap van zijwortelvorming.

In **hoofdstuk 4** gaat verder met het onderzoek naar zijwortelvorming. Het priming mechanisme dat we in hoofdstuk 3 hebben gevonden laat zien dat een verandering in groei in de hoofdwortel automatisch tot een verandering in zijwortelvorming leidt. Dit is een nieuwe invalshoek. Tot nu toe zochten plantenbiologen vaak naar een afzonderlijke verklaring voor de verandering in groei in de hoofdwortel en het aantal zijwortels dat optreedt als een plant bijvoorbeeld niet voldoende nutriënten krijgt. De resultaten uit hoofdstuk 3 laten zien dat alhoewel de eerste fase van zijwortelvorming, priming, qua snelheid, aantallen en afstanden goed uit de celproductie van de hoofdwortel kan worden verklaard, er toch nog veel variatie in de hoeveelheid en dichtheid van zijwortels is voor dezelfde groeisnelheid van de hoofdwortel. Dit komt doordat wortelgroei uit verschillende factoren bestaat, celdelingssnelheid, grootte van de celdelingszone en de grootte en hoeveelheid van groepjes cellen met dezelfde delingstijd. Verschillende combinaties van deze factoren kunnen leiden tot een gelijke celproductie maar een andere hoeveelheid en dichtheid van de zijwortels. In het simulatiemodel maken we gebruik van het feit dat we de verschillende factoren van groei onafhankelijk van elkaar kunnen veranderen, iets wat onmogelijk is in planten. Hierdoor kunnen we de invloed van individuele factoren en hun interacties ontrafelen. Door vervolgens analytische wiskundige modellen voor priming op te stellen konden we begrijpen hoe de relatieve bijdrage van de verschillende wortelgroeifactoren in levende planten er toe leidt dat er relatief veel zijwortels zijn en ze dicht op elkaar zitten. Ook lieten de wiskundige modellen en de simulaties zien dat groeiveranderingen in de hoofdwortel er toe kunnen leiden dat de wortels dichter op elkaar komen te zitten. Dit is eerder vaak geïnterpreteerd als een toename van zijwortelvorming en groei die contrasteert met een afname in hoofdwortelgroei. Ons werk suggereert dat de hogere dichtheid aan zijwortels juist een gevolg is van dat de hoofdwortel minder groeit en geen snellere zijwortelvorming vereist. Toekomstige experimenten moeten uitwijzen of dit in levende planten ook daadwerkelijk zo gebeurt. Dit is van belang omdat een beter begrip van wortelvorming essentieel is om in de toekomst de wortelarchitectuur van gewassen aan te kunnen passen zodat er optimale groei is gegeven een bepaalde omgeving.

In **hoofdstuk 5** gaat het over het richtingsgevoel van plantenwortels. Hoewel planten op een vaste plek groeien kunnen ze wel hun groeirichting aanpassen in reactie op omgevingsfactoren zoals, licht, zwaartekracht, voeding of zout. Zo'n verandering van groeirichting wordt een tropisme genoemd, een recent beschreven worteltropisme is halotropisme. Onderzoekers aan de Universiteit van Amsterdam hadden gevonden dat planten hun wortels wegbuigen als reactie op een zoutgradiënt. Zoals al eerder genoemd kunnen plantenwortels buigen door een toename van auxine aan één kant van de wortel.

Deze toename van auxine remt de celstrekking met als gevolg dat de wortel naar de kant met hoge auxine buigt. In dit geval buigt de wortel weg door een auxine ophoging aan de andere kant te vormen dan waar het zout wordt waargenomen, aan de kant waar het zout wordt waargenomen is juist een lichte toename in auxine transporters. Dus aan de ene kant van de wortel wordt er meer auxine getransporteerd en aan de andere kant van de wortel wordt er meer auxine vastgehouden. Door gebruik te maken van een wortel simulatiemodel konden we laten zien dat de u-vormige wortelpunt erg belangrijk is om de auxine van de ene naar de andere kant van de wortel te transporteren. Ook laten de resultaten zien dat de terugkoppeling van auxine op de hoeveelheid transporters in de cel erg belangrijk is voor het versterken van de initiële auxine asymmetrie. Daarnaast is er aan het begin van een zoutreactie een tijdelijke toename van auxine transporters in de vaatbundels in het midden van wortel. Deze toename helpt niet om de grootte van de auxine asymmetrie te versterken maar zorgt ervoor dat deze asymmetrie sneller wordt opgebouwd en zodoende de plantenwortel sneller kan beginnen met buigen. De terugkoppeling van auxine op de hoeveelheid transporters voorspelt dat onder halotropisme niet alleen een auxine asymmetrie maar ook een asymmetrie in deze transporters zal ontstaan, terwijl het belang van een tijdelijke verandering in vaatbundel auxine transporters voorspelt dat mutanten in deze transporter een langzamere buiging laten zien. Beide model voorspellingen zijn experimenteel gevalideerd door collegas in het Testerink laboratorium.

Plantenwortels kunnen dus snel van groeirichting veranderen door als reactie op een omgevings signaal kleine veranderingen in auxine transporters te laten plaatsvinden die vervolgens leiden tot een auxine asymmetrie. Normaal gesproken groeit de plantenwortel richting de zwaartekracht en dezelfde auxine transporters die verantwoordelijk zijn voor de buiging weg van een zoutgradiënt zijn ook betrokken bij het ervoor zorgen dat een horizontaal geplaatste wortel weer verticaal gaat groeien. Een belangrijke vraag is daarmee hoe een zoutstress-sigitaal en zwaartekracht-sigitaal worden geïntegreerd om te besluiten in welke richting de wortel moet groeien. In **hoofdstuk 6** gebruiken we een plant met een mutatie die een versterkte reactie op zwaartekracht, maar juist een vertraagde reactie op een zoutgradiënt heeft om meer inzicht te krijgen in hoe deze twee processen op elkaar ingrijpen. Hiervoor gebruikten we het wortelmodel ontwikkeld in hoofdstuk 5. We breiden dit model vervolgens uit op basis van de observatie dat in de mutant er minder auxine transporters zijn en dat de verdeling van de transporters over de celmembraan anders is, met meer transport in de horizontale richting. Bovendien gaat de herverdeling van de transporters over de celmembraan in reactie op zout wat langzamer. Door deze veranderingen in het model op te nemen konden we laten zien dat het relatief meer horizontale auxine transport er voor zorgt dat de mutant sneller kan reageren met het genereren van een auxine asymmetrie als de wortel verticaal wordt geplaatst en verklaart daarmee het versterkte gravitropisme. De langzamere herverdeling van de transporters over de celmembraan na een zoutreactie zorgt er juist voor dat de plant langzamer op een zoutgradiënt kan reageren. Aan de hand van simulaties en experimenten in planten, uitgevoerd door het Testerink laboratorium, laten we zien dat het voor wortelbuiging belangrijk is hoeveel auxine transporters er zijn in de cel, waar ze op het celmembraan staan en hoe snel ze hun concentratie en positie op het celmembraan kunnen wisselen om snel en efficiënt op een omgevings signaal te kunnen reageren.

De studies in dit proefschrift hebben inzicht gegeven in communicatie in een plantenwortel. In hoofdstuk 3 en 4 hebben we laten zien hoe groeipatronen in de wortelpunt kunnen leiden tot golfpatronen in de wortelpunt die het patroon van zijwortelvorming kunnen verklaren. En in hoofdstuk 5 en 6 hebben we laten zien hoe plantencellen aan weerszijden van een wortel met elkaar kunnen communiceren doormiddel van auxine en een terugkoppeling van auxine op de activiteit van auxine transporters om zo een wortelbuiging in gang te zetten. Deze inzichten konden worden verkregen door het gebruik van computersimulaties die het mogelijk maakten om allerlei processen in tijd en ruimte te integreren, maar ook de mogelijkheid om deze processen die in levende planten sterk interacteren

los te koppelen en individueel te bestuderen. Het gebruik van wortelmodellen in combinatie met experimenten in deze thesis is essentieel geweest om te begrijpen hoe plantenwortels omgevingsignalen en ontwikkelingsprogramma's integreren en hoe deze processen op elkaar inwerken zodat de plantenwortel een coherente response kan geven in groeirichting of zijwortelvorming.

Curriculum vitae



Thea van den Berg was born in Wilnis, the Netherlands, on the 2nd of February 1987. In 2011 she started her studies in Biology at the University of Amsterdam where she developed a strong interest in Theoretical Biology. After receiving her Bachelor's degree in 2013 she continued her studies as a Master's student in the Theoretical Biology and Bioinformatics group in Utrecht. During her masters she conducted a research project under the supervision of prof. Kirsten ten Tusscher, part of the results of this project were published and can be found in chapter 5 of this thesis. After her graduation in 2016 Thea stayed in the Theoretical Biology and Bioinformatics group as a PhD candidate under supervision of prof. Kirsten ten Tusscher and prof. Rob de Boer, the results of her PhD research can be found in this thesis.

Thea is currently employed by KeyGene N.V., Wageningen.

List of publications

Rutten, J., **van den Berg, T.** and Ten Tusscher, K., 2022. Modeling Auxin Signaling in Roots: Auxin Computations. *Cold Spring Harbor Perspectives in Biology*, 14(2), p.a040089.

van den Berg, T., Yalamanchili, K., De Gernier, H., Teixeira, J.S., Beeckman, T., Scheres, B., Willemsen, V. and Ten Tusscher, K., 2021. A reflux-and-growth mechanism explains oscillatory patterning of lateral root branching sites. *Developmental Cell*, 56(15), pp.2176-2191.

Korver, R.A., **van den Berg, T.**, Meyer, A.J., Galvan-Ampudia, C.S., Ten Tusscher, K.H. and Testerink, C., 2020. Halotropism requires phospholipase D ζ 1-mediated modulation of cellular polarity of auxin transport carriers. *Plant, cell & environment*, 43(1), pp.143-158.

Van den Berg, T. and Ten Tusscher, K.H., 2017. Auxin information processing; partners and interactions beyond the usual suspects. *International journal of molecular sciences*, 18(12), p.2585.

van den Berg, T., Korver, R.A., Testerink, C. and Ten Tusscher, K.H., 2016. Modeling halotropism: a key role for root tip architecture and reflux loop remodeling in redistributing auxin. *Development*, 143(18), pp.3350-3362.

Acknowledgements

Understanding the nature of interactions and processes is something that has always kept me busy and even kept me up at night. While some processes and interactions are too hard to grasp, in my PhD I was faced with the interesting process of lateral root priming: a very difficult process to understand, but not so hard that it could not be solved. I really enjoyed doing research and being given the possibility to decipher a process until I truly understood it. I was fortunate enough to be able to do this with a very motivated and inspiring supervisor. Kirsten, I really enjoyed working together with you, and I want to thank you for all your support in both the scientific part of this journey as well as the personal part. I admire your dedication to your work and the never-ending flow of ideas, it really helped me to keep going and explore new directions.

During my PhD research I have collaborated with experimental groups, the combined results of the experiments and modelling have led to the results in this thesis. I want to thank the group of Christa Testerink, and specifically Ruud Korver, for the collaboration on the halotropism project. And also many thanks to group of Ben Scheres, Viola Willemsen and Tom Beeckman for the lively discussions and the investment in many hours of experimental work that have led to the results in chapter 3 and 4 of this thesis. Specifically, I want to thank Kavya Yalamanchili for the all the lab work, analysis and the nice collaboration.

I also want to thank the Theoretical Biology and Bioinformatics group; I have spent many years in the group and it always felt like home: a place where everyone is welcome. I enjoyed the ongoing discussions and debates, the space for different opinions and the passion and dedication of many group members.

Ik wil mijn ouders bedanken voor hun support gedurende mijn studies. Deze thesis is om vele redenen ongedacht, maar niet onmogelijk zo blijkt. Dit is iets wat ik van jullie heb geleerd, doorzetten, opstaan en weer doorgaan, bedankt dat jullie daarin een voorbeeld voor mij zijn geweest, dat zijn lessen die ik op geen enkele universiteit had kunnen leren en aan de basis staan van dit succes.

En ook veel dank aan alle vrienden en familie die er voor mij en Alfred & Aaron waren. Een paar wil ik er in bijzonder noemen: Bauk je hebt heel wat keren voor me gekookt, altijd gezellig en lekker en Fredo's wijsheid heeft mij zeker veel wetenschappelijk inzicht gegeven. Fop & Jeltje, hartelijk dank voor alle keren oppassen zodat ik aan mijn thesis kon werken.

And finally, my AJ's, my biggest fans and favourite distraction. Alfred thank you for your support, your patience and helping me with references and editing, and mostly for believing in me. Now we both have our doctoral degree it's time for new adventures for our family.